

# Comparison of Mitochondrial Phenotypes Across Cancers with Different Tissues of Origin

By

Kelsey L. McLaughlin

December, 2021

Director of Dissertation: Kelsey H. Fisher-Wellman, PhD

Major Department: Physiology

## **ABSTRACT**

Cancer metabolism is typically characterized by aerobic glycolysis, an increase in glucose uptake and lactate production despite adequate sufficient oxygen availability to support mitochondrial oxidative phosphorylation (OXPHOS). The mitochondrial contribution to cancer has remained an important open question, with some suggesting that mitochondrial damage must be present to enable aerobic glycolysis and others suggesting mitochondrial OXPHOS is vital to cancer progression. Recent evidence of the oncogenic consequences to metabolic reprogramming caused by mutations to mitochondria-related genes has increased interest in understanding the interplay between metabolism and cancer, and how this may be targeted to improve therapy. The aim of this dissertation was to determine whether there was a consistent mitochondrial phenotype across several models of two different cancers: acute myeloid leukemia (AML) and hepatocellular carcinoma (HCC). Both AML and HCC have extremely poor prognoses (5-year survival 20-25%), heterogeneous patient populations, and limited curative treatment options. Mitochondrial phenotyping was accomplished through application of a comprehensive, diagnostic biochemical workflow that integrated several assessments of mitochondrial function under physiologically relevant stimuli with mitochondrial-targeted mass spectrometry-based proteomics. The application of this platform was first used to validate a proteomics-based

normalization factor that accounts for mitochondrial content across different preparations to improve comparisons of mitochondrial function between tissues. AML and HCC mitochondria were found to have a common phenotype in which maximal respiratory capacity was similar to their respective noncancer tissues, but respiration was inhibited in the presence of physiological ATP demand states. Different mechanisms contributed to this outcome in either cancer, suggesting that this may be a conserved feature of metabolic reprogramming in cancer. The detection of this phenotype was entirely dependent upon the use of mitochondrial interrogation methods that simulate *in vivo* energy states, supporting the tremendous importance of the integration of bioenergetics with physiology.



COMPARISON OF MITOCHONDRIAL PHENOTYPES ACROSS CANCERS WITH  
DIFFERENT TISSUES OF ORIGIN

A Dissertation

Presented To the Faculty of the Department of Physiology

East Carolina University

In Partial Fulfillment of the Requirements for the Degree

Doctor of Philosophy in Physiology

by

Kelsey L. McLaughlin

December, 2021

© Kelsey L. McLaughlin, 2021

Comparison of Mitochondrial Phenotypes Across Cancers with Different Tissues of Origin

By

Kelsey L. McLaughlin

APPROVED BY:

DIRECTOR OF DISSERTATION

---

Kelsey H. Fisher-Wellman, PhD

COMMITTEE MEMBER

---

P. Darrell Neuffer, PhD

COMMITTEE MEMBER

---

Jessica M. Ellis, PhD

COMMITTEE MEMBER

---

Myles C. Cabot, PhD

COMMITTEE MEMBER

---

Rukiyah T. Van Dross-Anderson, PhD

CHAIR OF THE DEPARTMENT  
OF PHYSIOLOGY

---

Robert M. Lust, PhD

DEAN OF THE  
GRADUATE SCHOOL

---

Paul J. Gemperline, PhD

## TABLE OF CONTENTS

LIST OF SYMBOLS & ABBREVIATIONS.....	viii
CHAPTER 1: INTRODUCTION.....	1
Mitochondria in Cancer Metabolism .....	1
Acute Myeloid Leukemia .....	3
Hepatocellular Carcinoma .....	7
Mitochondrial Functional Assessment.....	9
Central Hypothesis.....	13
CHAPTER 2: PROTEOMICS-BASED QUANTIFICATION OF MITOCHONDRIAL CONTENT .....	14
Abstract .....	16
Introduction .....	17
Results .....	19
Discussion .....	32
Materials and Methods.....	36
Acknowledgements.....	45
Declaration of Interest.....	45
Figures .....	46
Figure 1. Quantification of percent mitochondrial enrichment using subcellular proteomics. ....	46
Figure 2. Intrinsic differences in matrix dehydrogenase activity and expression across tissues. ....	47
Figure 3. Carbon substrate preference and OXPHOS conductance across tissues. .....	48
Figure 4. Intrinsic OXPHOS proteome heterogeneity across mouse tissues.	50
Figure 5. The mitochondrial SLC family of proteins correlate with Pyr/M supported intrinsic phosphorylation efficiency.....	51

Supplementary Figure 1. Comparison of search strategies using the MitoCarta 2.0 Database.....	53
References .....	54
<b>CHAPTER 3: CHARACTERIZATION OF THE MITOCHONDRIAL PHENOTYPE OF ACUTE MYELOID LEUKEMIA .....</b>	<b>60</b>
Abstract .....	62
Introduction .....	63
Results .....	65
Discussion .....	81
Methods .....	85
Acknowledgements.....	99
Ethics Declaration.....	99
Figures .....	100
Figure 1. Leukemia exhibits impaired cellular respiratory capacity amid an increased mitochondrial network.....	100
Figure 2. Impaired OXPHOS kinetics and ATP-dependent inhibition of ETS flux are unique phenotypes of leukemic mitochondria. ....	102
Figure 3. In leukemic mitochondria $\Delta$ GATP regulates ETS flux independent of substrate condition.....	104
Figure 4. Analysis of mitochondrial proteome reveal disparate expression of ANT isoforms in leukemia. ....	105
Figure 5. ETS flux inhibition by $\Delta$ GATP links to matrix ATP consumption in leukemia.....	106
Figure 6. 17-AAG and gamitrinib increase fractional OXPHOS and restore ETS flux in the presence of $\Delta$ GATP.....	108
Figure 7. Human primary leukemia is characterized by low fractional OXPHOS. ....	110
Figure 8. OXPHOS power output is reduced in the setting of venetoclax resistance.....	111

Supplementary Figure 1. Morphology of leukemia and respiratory flux stimulated by BAM15, a mitochondrial uncoupler.....	112
Supplementary Figure 2. Respiratory profile of healthy bone marrow mononuclear cells and primary human myoblasts.....	113
Supplementary Figure 3. Heatmap analysis depicting abundance of subunits and assembly factors that comprise the ETS complexes. ....	114
Supplementary Figure 4. ETS flux in the presence of $\Delta$ GATP is restored by ANT inhibition ANT.....	115
Supplementary Figure 5. Effects of 17-AAG on OXPHOS kinetics.....	116
Supplementary Figure 6. Effects of 17-AAG on OXPHOS kinetics and cell viability in PBMC and healthy bone marrow mononuclear cells. ....	117
References .....	118
<b>CHAPTER 4: CHARACTERIZATION OF THE MITOCHONDRIAL PHENOTYPE OF HEPATOCELLULAR CARCINOMA .....</b>	<b>130</b>
Abstract .....	132
Introduction .....	132
Results .....	135
Discussion .....	150
Methods .....	154
Figures .....	162
Figure 1. Hepatocellular carcinoma-derived (Hepa 1-6) cells display profound impairment in Complex I-supported respiration compared to non-tumorigenic immortalized hepatocytes (AML12).....	162
Figure 2. Induction of hepatocellular carcinoma in C3H mice using diethylnitrosamine (DEN) and the purity of the resultant isolated mitochondrial preparations. ....	164
Figure 3. Broad characterization of DEN-induced tumor mitochondria across diverse biochemical stimuli. ....	165

Figure 4. DEN tumor-derived mitochondria exhibit Complex I-linked respiratory deficiency.....	166
Figure 5. Upregulation of adenylate kinase 4 (AK4) in DEN-induced tumor mitochondria contributes to altered Complex I-linked respiratory flux. ....	168
Supplementary Figure 1. Pairwise mitochondrial proteome volcano plot comparisons. ....	169
Supplementary Figure 2. Trap1 and OXPHOS complex expression and effects of 17AAG and CAT on OXPHOS kinetics.....	170
References .....	171
CHAPTER 5: DISCUSSION.....	179
Mitochondrial Enrichment Factor.....	179
Mitochondrial Phenotype of Acute Myeloid Leukemia .....	179
Mitochondrial Phenotype of Hepatocellular Carcinoma .....	181
Consistencies in Cancer Mitochondrial Phenotype .....	182
Future Directions .....	183
Public Health Significance.....	185
REFERENCES .....	187
APPENDIX A: IACUC Approval Letter.....	204
APPENDIX B: IRB Approval Letters .....	206

## LIST OF SYMBOLS & ABBREVIATIONS

$\Delta G_{\text{ATP}}$  — Free energy of the hydrolysis of ATP

$\Delta\Psi$  — Mitochondrial membrane potential

ACO — Aconitase

ADP — Adenosine diphosphate

ATP — Adenosine triphosphate

AKG —  $\alpha$ -ketoglutarate

AKGDH —  $\alpha$ -ketoglutarate dehydrogenase

AML — Acute myeloid leukemia

ANT — Adenine nucleotide translocase

Ant/Ant A — Antimycin A; Complex III inhibitor

Ap5A — P1, P5-di(adenosine-5') pentaphosphate

Ara-C — Cytarabine

ASXL1 — Additional sex Comb-like 1

BAT — Brown adipose tissue

BCKDH — Branched-chain  $\alpha$ -ketoacid dehydrogenase

BCKDK — Branched-chain  $\alpha$ -ketoacid dehydrogenase kinase

BCL-2 — B-cell lymphoma 2

BDH —  $\beta$ -hydroxybutyrate dehydrogenase

BSA — Bovine serum albumin

CAT — Carboxyatractyloside

CEBPA — CCAAT enhancer-binding protein alpha

CK — Creatine Kinase

CI — Complex I; NADH:ubiquinone oxidoreductase

CII — Complex II; succinate dehydrogenase

CIII — Complex III; coenzyme Q:cytochrome C oxidoreductase

CIV — Complex IV; cytochrome C oxidase

CV — Complex V; ATP synthase

CN — Cyanide

Cr — Creatine

CS — Citrate Synthase

CTNNB1 —  $\beta$ -catenin

Cyt C — Cytochrome C

DEN — Diethylnitrosamine

DHO — Dihydroorotate

DHODH — Dihydroorotate dehydrogenase

DMSO — Dimethyl sulfoxide

DNA — Deoxyribonucleic acid

DTNB — 5',5'-Dithiobis 2-nitrobenzoic acid

DTT — Dithiothreitol

ECAR — Extracellular acidification rate

EGTA — Egtazic acid

ETS — Electron transport system

Cr — Creatine

FADH<sub>2</sub>/FAD — Reduced/oxidized flavin adenine dinucleotide

FBS — Fetal bovine serum

FCCP — Carbonyl cyanide-4-phenylhydrazone

FCCP<sub>ΔG<sub>ATP</sub></sub> — Maximal oxygen consumption rate attained through FCCP titration in the presence of ATP free energy; also denoted as FCCP<sub>CK</sub>

FCCP<sub>HK</sub> — Maximal oxygen consumption rate attained through FCCP titration following a hexokinase clamp experiment

FH — Fumarate hydratase

FLT3 — Feline McDonough Sarcoma-like tyrosine kinase 3

G — Glutamate

G3P — Glycerol-3-phosphate

G6PDH — Glucose-6-phosphate dehydrogenase

GDH — Glutamate dehydrogenase

GOT2 — Glutamic-oxaloacetic transaminase 2

GPD2 — Glycerol-3-phosphate dehydrogenase 2

HADHA — β-hydroxyacyl-CoA dehydrogenase

HCC — Hepatocellular carcinoma

HIF1 — Hypoxia-inducible factor 1

HK — Hexokinase

HMB — Human myoblast

HSCT — Hematopoietic stem cell transplantation

HSP90 — Heat shock protein 90

IDH1/2/3 — Isocitrate dehydrogenase isoform 1/2/3

$JH^+$ <sub>OXPHOS</sub> — Maximal proton conductance stimulated by ATP demand; quantified as the oxygen consumption rate at maximal ΔG<sub>ATP</sub> (-12.94kcal/mol; -54.16kJ/mol)

$JH^+_{TOTAL}$  — Maximal proton conductance capacity of the electron transport system; quantified as the maximal uncoupled oxygen consumption rate; also denoted as  $FCCP_{Alone}$

$JO_2$  — Oxygen consumption rate

$JATP$  — ATP production rate

M — Malate

Malo — Malonate; Complex II inhibitor

MDH — Malate dehydrogenase

ME — Malate enzyme

MEF — Mitochondrial Enrichment Factor

MPTP — Mitochondrial permeability transition pore

mtDNA — Mitochondrial DNA

NADH/NAD<sup>+</sup> — Reduced/oxidized nicotinamide adenine dinucleotide

NADPH/NADP<sup>+</sup> — Reduced/oxidized nicotinamide adenine dinucleotide phosphate

NPM1 — Nucleophosmin 1

O/Oct — Octanoyl-L-carnitine

OCR — Oxygen consumption rate obtained using extracellular flux analysis

OXPHOS — Oxidative phosphorylation

P/Pyr — Pyruvate

PBS — Phosphate-buffered saline

PBMC — Peripheral blood mononuclear cells

PCr — Phosphocreatine

PC — Palmitoyl-carnitine

PDH — Pyruvate dehydrogenase

Q pool — Quinone pool

R/Rot — Rotenone; Complex I inhibitor

ROS — Reactive oxygen species

RUNX1 — Runt-related transcription factor 1

S/Succ — Succinate

S4 — State 4; condition in respiration or fluorometry experiment in which mitochondria are incubated with carbon substrates and no additional respiratory stimulus

SDH — Succinate dehydrogenase

SEER — Surveillance, Epidemiology, and End Results program

shRNA — Short hairpin RNA

SUCLA — Succinyl-CoA ligase

TCA — Tricarboxylic acid

TET — Ten-eleven translocation family of dioxygenases

TERT — Telomerase reverse transcriptase

TF — Teriflunomide

TFA — Trifluoroacetic acid

TMPD — N,N,N',N'-tetramethyl-*p*-phenylenediamine

TMRM — Tetramethyl rhodamine methyl ester

TMT — Tandem mass tag

TP53 — Tumor protein 53

Ucp1 — Uncoupling protein 1

UK5099 — Acyano-(1-phenylindol-3-yl)-acrylate; pyruvate carrier inhibitor

VDAC — Voltage-dependent anion transporter

## CHAPTER 1: INTRODUCTION

### Mitochondria in Cancer Metabolism

Stemming from the original observations of Otto Warburg in 1926, the mitochondrial contribution to tumorigenesis has remained an important open question (Koppenol et al., 2011). The excessive production of lactate by tumor cells in the presence of oxygen, termed aerobic glycolysis, suggested to Warburg that mitochondrial respiration was compromised in tumors. He would go on to propose that impairment of mitochondrial energy transduction was the initiating event of tumor formation (Koppenol et al., 2011; Warburg, 1956). Nearly a century on from this discovery, evidence continues to indicate that mitochondrial reprogramming—though not ‘impairment’ per se—is central to cancer metabolism (Ahn and Metallo, 2015; Bayley and Devilee, 2010; Zong et al., 2016). Indeed, in addition to ATP production, mitochondria have a central role in several other cellular processes with links to tumor metabolism, including lipid and nucleotide synthesis (Hatzivassiliou et al., 2005; Khutornenko et al., 2010), one-carbon metabolism (Newman and Maddocks, 2017), and redox balance (Dai et al., 2016). In a series of elegantly designed studies, manipulation of respiratory complex expression revealed that mitochondrial ubiquinol oxidation (Diebold et al., 2019; Martínez-Reyes et al., 2020), membrane potential (Martínez-Reyes et al., 2016), and tricarboxylic acid (TCA) cycle flux (Martínez-Reyes et al., 2016) were all required for proliferation in tumors and healthy progenitors independent of mitochondrial oxidative phosphorylation. Together, these findings imply that the high glycolytic rate of tumor cells is not due to a mitochondrial deficiency that limits ATP availability but is part of a broad program of redistribution of fluxes across cellular metabolic pathways.

Genes for mitochondrial proteins have also been shown to harbor oncogenic mutations across cancers from different tissues of origin. TCA cycle enzymes such as isocitrate dehydrogenases 1/2 (IDH1/2), fumarate hydratase (FH), and succinate dehydrogenase (SDH) are among the most frequently altered genes (Bayley and Devilee, 2010; King et al., 2006; Yan et al., 2009). Loss of function in these enzymes leads to the accumulation of different TCA cycle intermediates ( $\alpha$ -ketoglutarate and D-2-glutarate, fumarate, and succinate, respectively), and these metabolites have been shown to directly interact with other oncogenes to alter gene transcription and promote tumorigenesis (Figuroa et al., 2010; King et al., 2006). For instance,  $\alpha$ -ketoglutarate, fumarate, and succinate have each been linked to stabilization of hypoxia-inducible factor 1 (HIF1), a transcription factor that is normally activated by low oxygen availability and other cellular stressors (Bayley and Devilee, 2010; Maxwell, 2005a, 2005b). HIF1 activation directly stimulates an upregulation of glycolytic enzymes, leading to a Warburg-like metabolic phenotype. Accumulation of D-2-glutarate has also been linked to epigenetic regulation of gene expression through inhibition of the TET family of  $\alpha$ -ketoglutarate-dependent 5-methylcytosine hydroxylases as well as histone demethylases, which results in a hypermethylated nuclear genome and a shift toward dedifferentiation (Figuroa et al., 2010). Both oncogenic mechanisms described here highlight the ability of shifts in metabolism to influence, rather than just support, tumor development.

In addition to oncogenic mutations to nuclear-encoded genes, mitochondrial reprogramming has been linked to damage to the mitochondrial genome (Gammage and Frezza, 2019). Several groups have noted that mitochondrial DNA (mtDNA) has a greater susceptibility to mutation than nuclear DNA (Shay and Werbin, 1987), with an increased burden of mutations and deletions found within the mtDNA of tumors (Carew and Huang, 2002). In fact, results from

The Cancer Genome Atlas consortium and others have demonstrated that the majority of solid tumors sampled from humans exhibited lower mtDNA copy numbers (Lee et al., 2004; Reznik et al., 2016), along with reduced transcript numbers for the 13 genes encoded by mtDNA (Reznik et al., 2017) compared to healthy surrounding tissue. Mutations to mtDNA were even reported to be among the most common mutations found across human cancers (Gorelick et al., 2021).

The most regularly mutated region in these cancers is the D-loop of the mtDNA, which contains the origin site for replication and transcription (Carew and Huang, 2002; Lee et al., 2004). Mutation to the D-loop sequence has been independently linked to the depletion of mtDNA copy numbers and may also confer resistance to at least one pathway of apoptosis, potentially contributing to the development of tumorigenicity (Higuchi et al., 2006; Lee et al., 2004). Additionally, as the 13 polypeptides encoded by the mtDNA correspond to vital subunits of the respiratory complexes of the mitochondrial electron transport chain (ETC) (Falkenberg et al., 2007), it is possible that both increased mutation rates and decreased mtDNA copy number could alter respiratory function in tumor mitochondria. This idea is attractive as it provides a potential mechanism through which mitochondrial flux could be limited, but not eliminated, to support an increase in glycolytic rate (Higuchi, 2007).

Although these findings have been described to relate to cancer in general, the incidence of each of these mutations is highly variable between different cancers, and even across patients within the same type of cancer (Faubert et al., 2020). To highlight this heterogeneity in human malignancy, two distinct cancers will be reviewed below: acute myeloid leukemia and hepatocellular carcinoma.

### **Acute Myeloid Leukemia**

Acute myeloid leukemia (AML) is a clonal disorder that is characterized by pathological expansion of abnormally differentiated hematopoietic progenitors in the bone marrow and blood. The accumulation of these leukemic blasts will rapidly diminish immune function, and without treatment will lead to death within 1 year (Estey and Döhner, 2006). AML is the most common form of acute leukemia in adults, though it primarily affects older adults with a median age of diagnosis of 68 (Song et al., 2018). There were over 20,000 estimated new cases in the United States in 2021, (Siegel et al., 2021), and incidence has continued to rise steadily since tracking of incidence rates was made possible by the Surveillance, Epidemiology, and End Results program (SEER) in 1973 (Shallis et al., 2019). Most cases of AML develop spontaneously, though other causes include genetic predisposition, previous exposure to chemo- or radiation therapy, environmental exposure to benzene or other carcinogens, and preexisting hematopoietic changes from myelodysplasia (Arber et al., 2016; Shallis et al., 2019).

The overall 5-year survival for AML patients is 24%, which is lower than any other leukemia (Shallis et al., 2019). However, AML is an extremely heterogeneous malignancy, and individual patient survival has been linked to prognostic factors such as etiology, disease comorbidities, specific oncogenic mutations, and age (Döhner et al., 2015; Shallis et al., 2019). For instance, the 5-year survival of patients diagnosed before 40 years of age has been estimated at 58.2%, though this estimate lowered by 10% per every 10 years added to the age of diagnosis (Shallis et al., 2019). These factors also help determine the treatment strategy for each patient. Standard treatment of AML involves two stages, referred to as induction and consolidation (Kirtonia et al., 2020). The induction phase consists of treatment with the chemotherapeutics cytarabine and anthracycline with the goal of killing sufficient leukemic blasts so that they are no longer detectable, defined as complete remission. Additional high doses of cytarabine are then

provided during consolidation to eliminate any remaining blasts and reduce the risk of relapse (Kirtonia et al., 2020). If this treatment fails or the risk of relapse is high, hematopoietic stem cell transplantation (HSCT) may then be used for treatment (Othus et al., 2015; Takami, 2018).

Long term cure rates are relatively low for AML, with treatment success estimated to be between 30-45% in younger patients ( $\leq 60$  years), but only 5-15% in patients over 60 (Döhner et al., 2015). There is an exceptionally high rate of relapse following chemotherapy, which is the most common cause of death in AML (Ding et al., 2012). Relapse is typically caused by the survival of a small number of leukemic blasts which are able to clone themselves to reestablish the disease. The blast population within a single patient has been shown to contain multiple collections of clones, each possessing a unique combination of oncogenic mutations and drivers (The Cancer Genome Atlas Research Network, 2013). Genomic sequencing of AML patient samples has demonstrated that there is commonly one dominant population of clones which may either acquire new mutations or be overtaken by a separate subclone population to cause relapse, referred to as clonal evolution (Ding et al., 2012). As a result, relapsed leukemia is almost always refractory to chemotherapy, and HSCT would be the next best treatment (Döhner et al., 2015).

The genetic etiology of AML is also tremendously varied, with abnormalities found in both chromosomal arrangement (~55% of patients) and specific genes (Gaidzik and Döhner, 2008; Kirtonia et al., 2020; Weltermann et al., 2004). Most AML presents with multiple genetic aberrations, with the most commonly mutated gene, nucleophosmin 1 (*NPM1*), found in 25-35% of patients (Döhner et al., 2015). Several frequently recurrent oncogenic mutations have also been found to have clinical relevance to disease prognosis and treatment outcomes (Döhner et al., 2015; Kirtonia et al., 2020), and are evaluated during clinical diagnosis to determine treatment strategy, including: *NPM1*, CCAAT enhancer-binding protein alpha (*CEBPA*), FMS-like tyrosine kinase 3

(*FLT3*), runt-related transcription factor 1 (*RUNX1*), additional sex Comb-like 1 (*ASXL1*), and tumor protein 53 (*TP53*) (Döhner et al., 2017, 2010). Of the mitochondrial oncogenes mentioned previously, only mutations to *IDH1/2* have been found in AML, affecting 7-14% and 8-19% of patients, respectively (Döhner et al., 2015; Figueroa et al., 2010). *IDH1/2* mutations have been correlated with reduced survival when paired with mutations to *NPM1* in chromosomally normal patients (Kirtonia et al., 2020). In a small study of 200 AML patients, 8% were found to have somatic mutations in one or more of the protein-coding genes of mtDNA, which was linked to decreased survival (S. Wu et al., 2018).

Treatment efficacy for AML has been improving in recent years due to the development of new therapeutics targeted to different aspects of AML physiology as well as recurrent oncogenic mutations, increasing treatment options for patients for whom standard induction/consolidation therapies are contraindicated due to age or other prognostic factors (Döhner et al., 2015; Kirtonia et al., 2020; Shallis et al., 2019). Venetoclax, a B-cell lymphoma 2 (BCL-2) inhibitor, has recently been approved to treat AML in patients over 65 who are ineligible for standard treatment. In clinical trials, venetoclax paired with hypomethylating agents was able to induce complete remission in 67% of these patients (DiNardo et al., 2019). Venetoclax has also been favorably indicated for patients with *IDH1/2* mutations (Kirtonia et al., 2020). Novel inhibitors of mutant *IDH1/2* proteins (ivosidenib and enasidenib, respectively) have also shown positive results for patients with relapsed/refractory AML and mutations to *IDH1/2*, with response rates of 33% and 40% in clinical trials, respectively (Norsworthy et al., 2019; Stein et al., 2017). However, relapse is not fully prevented with these new targeted treatments. For instance, the anti-leukemic effects of *FLT3*-inhibitor quizartinib are reduced over time due to progressive acquisition of new point mutations in *FLT3* that render it ineffective (Cortes et al., 2013; Smith et al., 2012). Additionally,

targeted therapeutics only work for the patients presenting with specific oncogenic profiles, limiting the pool of patients who will see benefit.

## **Hepatocellular Carcinoma**

Hepatocellular carcinoma (HCC) is a malignancy of the liver tissue in which chronically stressed liver cells acquire chromosomal and genetic aberrations following multiple cycles of damage and regeneration that lead to the formation of tumors (Forner et al., 2018; Nault, 2014). HCC is the most common primary liver cancer, and the third leading cause of cancer-related death globally (Sung et al., 2021). In the United States, there was an estimated HCC incidence of 42,230 in 2021, and approximately 71% of these new cases were in men (Siegel et al., 2021). The majority of HCC cases develop in the context of preexisting liver and metabolic diseases such as cirrhosis, hepatitis, non-alcoholic fatty liver disease, and diabetes (Nault, 2014). With increasing incidence of metabolic diseases in developed countries, the burden of HCC will likely continue to increase over time (Dyson et al., 2014).

The 5-year survival for HCC is estimated to be ~20%, making it the second most lethal cancer overall after prostate cancer (Siegel et al., 2021). Late detection of HCC contributes to its poor prognosis, as the presence of multiple tumors and/or comorbid liver disease will limit treatment options (Balogh et al., 2016). As a result, surveillance is recommended to reduce HCC mortality of patients with significant risk factors for HCC, particularly cirrhosis (European Association for the Study of the Liver, 2018; Singal et al., 2014).

Treatment of HCC is dependent upon the stage of the tumor, as defined by the Barcelona Clinic Liver Cancer algorithm (European Association for the Study of the Liver, 2018). There are 5 total stages: very early stage (0), early stage (A), intermediate stage (B), advanced stage (C),

and terminal stage (D). Staging is determined based upon the number and size of tumors present, the underlying liver function, and the degree of invasion to extrahepatic regions (Llovet et al., 1999). For very early or early stage patients with a single lesion and otherwise intact liver function, treatment is typically ablation or resection of the tumor (Ishizawa et al., 2008). Patients with 2-3 small (<3cm) tumors and no spread of malignancy to the microvasculature fall into the intermediate stage, with liver transplantation being the recommended treatment (Mazzaferro et al., 1996). As the typical wait time for transplantation is >6 months, therapies to shrink tumor size are common to prevent tumor progression prior to surgery (Llovet et al., 2002). Advanced stage patients with multiple tumors and extrahepatic spread of malignancy are primarily treated with multi-kinase inhibitors such as sorafenib, though the average survival time is <1 year from the start of treatment (Villanueva, 2019). Only palliative care is provided for terminal stage HCC (European Association for the Study of the Liver, 2018).

Although surgical treatment of HCC conveys the greatest survival benefit, there is still a risk of tumor recurrence. Patients who undergo tumor resection have high 5-year survival rates (>60%), but equally high rates of HCC recurrence within 5 years (~70%) (Ishizawa et al., 2008). However, a second resection has been shown to convey similar survival benefits to the initial resection (Ishizawa et al., 2008). Liver transplantation will cure underlying liver disease, which likely contributes to its superior overall 5-year survival (60-80%) and reduced rate of recurrence (<15%) (Villanueva, 2019). There are currently no therapies with clinically proven effectiveness for preventing tumor recurrence (Villanueva, 2019).

As in AML, recurrent genetic abnormalities have been found to play a role in HCC pathology. However, there is little consistency in oncogene mutation pattern between patients, and most recurrent mutations are found in only small portions of the HCC patient population, ranging

from 1-15%. Accordingly, there are currently no recurrent oncogenic mutations that have been linked with prognostic or treatment outcomes (Villanueva, 2019). The most consistently altered genes include telomerase reverse transcriptase (*TERT*, ~70% of HCC),  $\beta$ -catenin (*CTNNB1*, 30% of HCC), and tumor protein 53 (*TP53*, 30% of HCC), which are found in ~70%, 30%, and 30% of HCC tumors, respectively (Schulze et al., 2015; Totoki et al., 2014). There were no recurrent mutations found in any of the TCA-linked oncogenes *IDH1/2*, *FH*, or *SDH* (Schulze et al., 2016). For the mitochondrial genome, HCC has been associated with low mtDNA copy number (Lee et al., 2004; Yu et al., 2018) and mutations have been found throughout the coding region of the mtDNA, including one truncating mutation to Complex I gene ND1, though these studies included a small number of patients, and the clinical significance is not clear (Yin et al., 2010; Yu et al., 2018).

### **Mitochondrial Functional Assessment**

Acute myeloid leukemia and hepatocellular carcinoma both represent significant health issues whose treatment options and mortality rates remain relatively stagnant despite extensive ongoing research (Shallis et al., 2019; Villanueva, 2019). One important issue for both malignancies is chemotherapeutic resistance. In AML this issue is due to the presence of multiple subclone populations with different growth advantages (Ding et al., 2012), and in HCC this is due to a relative lack of consistent oncogenic targets and complications from underlying liver disease (Llovet et al., 2015). Interestingly, despite almost no overlap between the oncogenic drivers of these two diseases, resistance to chemotherapeutic drugs has been linked to upregulated mitochondrial oxidative phosphorylation (OXPHOS) in both AML (Farge et al., 2017) and HCC (Montero et al., 2008; Sun et al., 2019), as well as other cancers (Faubert et al., 2020; Guièze et

al., 2019a; Viale et al., 2014). This commonality has ignited excitement over the possibility of targeting OXPHOS for cancer therapy and lead to the proposal of several mitochondrial-targeted inhibitors for clinical trials (Faubert et al., 2020; Molina et al., 2018; Wheaton et al., 2014).

One important caveat of these findings is that in every case intact cell respiration measurements were used to determine mitochondrial phenotype (Farge et al., 2017; Guièze et al., 2019b; Sun et al., 2019; Viale et al., 2014; L. Wu et al., 2018). Intact cell respiration measurements have increased in popularity over the last few years due to the availability of high-throughput instruments with relatively simple protocols that allow for rapid and cost-efficient evaluation of oxygen consumption in mitochondria. Although intact cell respiration can be a valuable tool when paired with other assessments of mitochondrial function, by itself it largely constitutes a black box measurement in which the relationship between changes to oxygen consumption rate and the underlying physiology remains nebulous (Schmidt et al., 2021a). Differences in respiration between cells can be caused by a multitude of factors, which require further testing to evaluate. For instance, basal differences in mitochondrial network size could skew respiration results that are normalized to cell number rather than protein or mitochondrial content (Schmidt et al., 2021a). Most importantly, intact cell respiration may not reflect the coupling of respiration to mitochondrial ATP phosphorylation, as damaged mitochondria are still capable of respiring (Brand and Nicholls, 2011). For this reason, the finding that chemoresistant cancer cells were seen to have increased respiration does not necessarily imply that they are more reliant on OXPHOS for energy generation. Application of mitochondrial assessments that quantify function in physiologically meaningful scenarios is necessary to evaluate the implications of increased respiration in chemoresistance, as well as across other models of cancer.

Superior assessments of mitochondrial phenotype can be achieved using *in vitro* modeling of physiological demand states (Fisher-Wellman et al., 2018; Glancy et al., 2013). Mitochondrial OXPHOS is a demand-driven process that is tightly regulated in well-coupled mitochondria by the free energy of ATP hydrolysis, or  $\Delta G_{\text{ATP}}$ . This parameter reflects the balance of ATP, ADP, and  $P_i$  in the cell and the consequent demand for ATP resynthesis (Calderwood et al., 1985). Recently, the enzymatic activity of creatine kinase (CK), has been leveraged to simulate the physiological  $\Delta G_{\text{ATP}}$  for mitochondrial evaluation (Fisher-Wellman et al., 2018; Glancy et al., 2013). CK uses the terminal phosphate of ATP to phosphorylate creatine (Cr), generating phosphocreatine (PCr) and ADP (Teague et al., 1996). Using the equilibrium constant of this reaction ( $K_{\text{CK}}$ ),  $\Delta G_{\text{ATP}}$  can be manipulated in an experimental system by incorporating known amounts of ATP, Cr, and PCr according to the formula:

$$\Delta G'_{\text{ATP}} = \Delta G'^{\circ}_{\text{ATP}} + RT \ln \frac{[\text{Cr}][P_i]}{[\text{PCr}][K'_{\text{CK}}]}$$

where  $\Delta G'^{\circ}_{\text{ATP}}$  is the standard apparent transformed Gibbs energy (under a specified pH, ionic strength, free magnesium, and pressure), R is the gas constant (8.3145J/kmol) and T is temperature in Kelvin (310.15) (Glancy et al., 2013). In a typical cell, values for  $\Delta G_{\text{ATP}}$  will vary dynamically from -56 to -64 kJ/mol (Luptak et al., 2018), with -56 kJ/mol reflecting a high demand for ATP resynthesis (i.e., maximal exercise) and -64kJ/mol reflecting low demand (i.e., rest). By testing mitochondrial function over a range of values within this span, it is possible to gain important information about the ability of mitochondria to adjust their respiration to demand, and thus determine how well they are coupled. Superior control over the conditions of this assay can be achieved by performing the experiments in isolated mitochondria or permeabilized cells, so that the carbon substrates are determined by the investigator and flux through different respiratory complexes and dehydrogenase enzyme systems can be evaluated (Fisher-Wellman et al., 2018).

Additionally, these assay conditions can be used for fluorometric determination of mitochondrial membrane potential and NAD(P)H/NAD(P) redox poise to provide even more insight about the transduction of energy in the mitochondria from carbon fuel sources to electrons entering the ETC, to protons pumped, to ATP generated (Fisher-Wellman et al., 2018).

Intact cell respiration assays also commonly infer ATP synthesis rates from respiration, based on a fixed stoichiometry of the amount of ATP generated per molecule of oxygen consumed, or the ATP/O ratio (Gerencser et al., 2009; Hinkle, 2005). However, ATP/O ratios are dependent upon the substrate that is oxidized to support respiration, with a theoretical ATP/O of 2.7 for NADH-linked substrates and 1.6 for succinate (Watt et al., 2010). In intact models of respiration, it is difficult to determine the carbon substrate that is fueling respiration, as cells may have stored carbons or lipids available to them for oxidation (Schmidt et al., 2021a). In contrast, experiments in permeabilized cells and isolated mitochondria allow for the addition of known combinations of substrates so the appropriate stoichiometry may be applied. Additionally, ATP/O ratios can be determined empirically in both model systems by pairing respirometry with fluorescent determination of ATP generation (*JATP*) (Lark et al., 2016). Determination of *JATP* can be accomplished through pairing the enzymatic activities of hexokinase and glucose-6-phosphate dehydrogenase in the assay buffer such that when ATP that is produced in the mitochondria it is immediately used to phosphorylate glucose, which is then used to generate NADPH. The autofluorescence of NADPH can then be quantified fluorometrically, with the rate of production of NADPH occurring at a 1:1 ratio with the rate of ATP emission from the mitochondrial matrix (Lark et al., 2016). To date, there is only limited information describing  $\Delta G_{ATP}$ -stimulated mitochondrial flux and direct quantification of ATP production across all models of cancer (Schmidt et al., 2021b).

## **Central Hypothesis**

Although there is great heterogeneity in the somatic mutations driving tumorigenesis both across and within different types of cancer, the majority of cancers demonstrate a Warburg-like metabolism involving elevated glucose uptake and lactate production. Despite the burden of evidence suggesting that mitochondria play a central role in malignant metabolic reprogramming and possibly chemoresistance, it remains unclear whether there is a similarly conserved phenotype in cancer mitochondria. The purpose of the work in this dissertation was thus twofold: 1) to comprehensively interrogate the intrinsic mitochondrial phenotype across multiple models within two distinct cancers, acute myeloid leukemia and hepatocellular carcinoma; and 2) to determine whether there are any shared aspects of mitochondrial adaptation between these two cancers. The central hypothesis was that across all models there would be a common functional phenotype of cancer mitochondria that supports malignancy. The identification of such a phenotype would also help to direct the creation of new therapeutics to treat cancer with broad efficacy. In order to complete this work, we additionally had to validate a method to normalize mitochondrial functional data across mitochondria from different preparations and tissues, the results of which are described in Chapter 2.

## **CHAPTER 2: PROTEOMICS-BASED QUANTIFICATION OF MITOCHONDRIAL CONTENT**

Differential centrifugation is a common method used for mitochondrial isolation from cells and tissues. The resultant mitochondrial pellet will inevitably contain nonmitochondrial contaminants of organelles with similar densities (i.e. peroxisomes) or with physical attachments to the mitochondria (i.e. endoplasmic reticulum), leading to variable mitochondrial purity. In order to ensure that comparisons between different tissues, such as tumor and nontumor, reflect true intrinsic alterations to mitochondrial function, normalization of outcome measures must account for potential differences in mitochondrial content. Although previous work in metabolism research has led to the adoption of citrate synthase activity as a marker of mitochondrial content, this has primarily been validated in skeletal muscle tissue. Therefore, we sought to determine whether citrate synthase was a universal marker of mitochondrial content across four distinct tissues: brown adipose, heart, kidney, and liver. Data presented herein demonstrate that mitochondrial content could not be correlated to expression of any single protein across the four tissues but was best quantified using a mass spectrometry-derived mitochondrial enrichment factor. Additionally, thorough assessment of mitochondrial phenotype that included an array of respiratory stimuli, carbon substrates, and mitochondrial proteomic analysis allowed for the identification of intrinsic mitochondrial properties that were unique to each tissue.

**Novel approach to quantify mitochondrial content and intrinsic bioenergetic efficiency across organs. (McLaughlin et al., 2020).**

Kelsey L. McLaughlin<sup>1,3</sup>, James T. Hagen<sup>1,3</sup>, Hannah S. Coalson<sup>1,3</sup>, Margaret A. M. Nelson<sup>1,3</sup>, Kimberly A. Kew<sup>2</sup>, Ashley R. Wooten<sup>2</sup>, and Kelsey H. Fisher-Wellman<sup>1,3,\*</sup>

<sup>1</sup>Department of Physiology, <sup>2</sup>Department of Biochemistry and Molecular Biology, East Carolina University, Brody School of Medicine, Greenville, NC 27834, USA. <sup>3</sup>East Carolina Diabetes and Obesity Institute, Greenville, NC 27834, USA.

\* To whom correspondence should be addressed:

Kelsey H. Fisher-Wellman [fisherwellmank17@ecu.edu](mailto:fisherwellmank17@ecu.edu)

East Carolina Diabetes and Obesity Institute, 115 Heart Drive, Greenville, NC 27834 USA

Telephone: 252-744-2585

Fax: 252-744-0462

## **Abstract**

Human disease pathophysiology commonly involves metabolic disruption at both the cellular and subcellular levels. Isolated mitochondria are a powerful model for separating global cellular changes from intrinsic mitochondrial alterations. However, common laboratory practices for isolating mitochondria (e.g., differential centrifugation) routinely results in organelle preparations with variable mitochondrial purity. To overcome this issue, we developed a mass spectrometry-based method that quantitatively evaluates sample-specific percent mitochondrial enrichment. Sample-specific mitochondrial enrichment was then used to correct various biochemical readouts of mitochondrial function to a ‘fixed’ amount of mitochondrial protein, thus allowing for intrinsic mitochondrial bioenergetics, relative to the underlying proteome, to be assessed across multiple mouse tissues (e.g., heart, brown adipose, kidney, liver). Our results support the use of mitochondrial-targeted nLC-MS/MS as a method to quantitate mitochondrial enrichment on a per-sample basis, allowing for unbiased comparison of functional parameters between populations of mitochondria isolated from metabolically distinct tissues. This method can easily be applied across multiple experimental settings in which intrinsic shifts in the mitochondrial network are suspected of driving a given physiological or pathophysiological outcome.

## **Introduction**

Metabolic dysregulation has been implicated as a key component in the pathophysiology of several diseases, including diabetes, kidney disease, and cancer, among others (Che et al., 2014; Fisher-Wellman and Neuffer, 2012; Gaude and Frezza, 2014). Reflective of this dysregulation, increasing evidence has indicated that mitochondria, the subcellular sites of oxidative phosphorylation (OXPHOS), undergo remodeling in these disease states that may include depressed respiration, increased production of reactive oxygen species, loss of cristae, or loss of mitochondrial volume (Diaz-Vegas et al., 2020). These adaptations occur in addition to the broader physiological consequences of altered metabolism such as shifts in protein expression, deposition of lipid droplets, or increased fibrosis. Together, these interconnected changes result in a tissue that is fundamentally distinct from the healthy ‘normal’ tissue. Furthering our understanding of these diseases thus relies upon comparison of ‘normal’ to ‘diseased’ metabolic states at the cellular and subcellular level, in a multitude of tissue backgrounds.

To separate global changes to metabolism from intrinsic mitochondrial remodeling, investigators commonly use isolated mitochondrial preparations obtained through differential centrifugation (Frezza et al., 2007). This simple process has been reliably implemented in a variety of tissues to produce intact, functional mitochondria for bioenergetic evaluation. For the normalization of data between isolations from the same tissue type, values are typically scaled to the amount of protein used per experiment. However, the crude mitochondrial pellet acquired through differential centrifugation will also contain non-mitochondrial contaminants including lysosomes, peroxisomes, and portions of other subcellular organelles that are of similar density to mitochondria (Glancy and Balaban, 2011; Kappler et al., 2016; van der Walt and Louw, 2020). Further, it is likely that contamination is not uniform across tissues, as each tissue maintains a

different proportion of these organelles (Forner et al., 2006; Johnson et al., 2007; Thor Johnson et al., 2007), presumably to perform specialized functions. Similarly, given the cellular consequences of disease listed above, there will likely be an additional impact of disease state upon the purity of the mitochondrial preparation (Groennebaek et al., 2020). Accordingly, equitable comparison of mitochondrial function across different tissues, as well as between diseased/healthy states, requires reliable normalization that corrects for the mitochondrial purity across subcellular isolations.

One prevailing strategy for normalization is to estimate mitochondrial content through measuring the activity of citrate synthase (CS), an enzyme at the intersection of fuel catalysis and entry of metabolites into the citric acid cycle. Previous work has demonstrated a strong correlation between mitochondrial content and CS activity in skeletal muscle (Larsen et al., 2012). However, to our knowledge, this correlation has not been validated in other tissues, nor in different disease states, potentially limiting its application for evaluating isolation purity for all experimental models. Moreover, as the mitochondrion represents a complex collection of integrated pathways, it seems unlikely that the activity of any single enzyme would be reflective of mitochondrial content across tissues with differing energetic demands or constraints.

The present study sought to address this technical barrier inherent to quantifying inter-mitochondrial differences across organs through the use of label-free, mitochondrial-targeted nanoLC-MS/MS paired with comprehensive bioenergetic phenotyping. By carrying out quantitative proteomic screens on aliquots of mitochondria used for functional analysis, this allowed us to directly compute mitochondrial vs. non-mitochondrial protein on a per-sample basis. Such analyses generated a mitochondrial enrichment factor (MEF) that empirically reflected the mitochondrial purity of a given isolation. We subsequently used this MEF to identify potential protein biomarkers of mitochondrial content shared across tissues, as well as directly compare

mitochondrial bioenergetic fluxes between tissues through differential protein expression, high resolution respirometry, and ATP production profiles. In order to provide experimental contrast, four metabolically diverse tissues were compared: brown adipose tissue, heart, kidney, and liver.

## Results

### *Citrate synthase activity does not reflect mitochondrial content across distinct mouse tissues.*

Comparison of mitochondrial function between tissues requires a reliable normalization factor that corrects for non-mitochondrial protein contamination across subcellular isolations. For example, the activity of citrate synthase (CS) is commonly used as a marker of mitochondrial content for the normalization of a given bioenergetic readout. Although a variety of biochemical and protein biomarkers have been validated to reflect mitochondrial content in skeletal muscle. (Larsen et al., 2012), the validity of these markers across other organs/tissues remains largely unexplored (Groennebaek et al., 2020). To determine potential biomarkers of mitochondrial content shared across organs, we isolated mitochondria from several distinct mouse tissues—brown adipose tissue (BAT), heart, kidney, and liver—and subjected them to label-free, quantitative nanoLC-MS/MS. The purity of each mitochondrial isolation (i.e., the percent contamination by non-mitochondrial proteins) was quantitatively evaluated by comparing the summed abundance of all mitochondrial proteins (i.e., MitoCarta 2.0 positive proteins) to total protein abundance. Note, total abundance reflects both mitochondrial and non-mitochondrial proteins. This allowed for the generation of a ‘mitochondrial enrichment factor’ (MEF) that reflects mitochondrial protein content per unit of crude isolated mitochondrial protein. **Figure 1A** depicts a heatmap of Log<sub>2</sub> protein abundance from each mitochondrial sample (n=5/tissue). In total, 2,212 proteins were identified and quantified across all tissues, with 764 proteins

distinguished as mitochondrial using the MitoCarta 2.0 database. Cluster analysis revealed that replicates from the same tissue type grouped together, demonstrating good reproducibility. Additionally, liver and kidney samples showed similar clustering to one another, as did BAT and heart samples. As expected, mitochondrial proteins accounted for a large percentage of all quantified proteins, yet the MEF varied considerably between tissues (**Fig. 1B-C**). Mitochondrial enrichment was highest in BAT and heart samples (> 90%), compared to kidney (~80%) and liver, with liver having the lowest purity (~65%) (**Fig. 1C**).

Using the same isolated mitochondria samples, we then compared CS activity across the four tissues to determine whether differences in CS activity matched those found in mitochondrial enrichment. The activity of CS was slightly higher in BAT compared to heart, with lower rates apparent in kidney and liver (**Fig. 1D**). A similar pattern was present with respect to CS abundance (**Fig. 1E**). Interestingly, the magnitude of difference in CS activity was much greater than that found for mitochondrial enrichment. This is particularly evident when comparing BAT and liver, for which there was an almost 10-fold difference in CS activity (**Fig. 1D**), but <1.5-fold difference in MEF (**Fig. 1C**). To directly determine whether CS activity predicted mitochondrial enrichment, linear regression was performed between CS activity rates and MEF for each tissue (**Fig. 1F-I**). Surprisingly, with the exception of liver, CS activity was not correlated with mitochondrial enrichment (**Fig. 1F-I**), indicating that CS activity is not a reliable marker of mitochondrial content across organs.

Having failed to validate CS activity as a biomarker of mitochondrial content, we turned our attention back to the proteome in an attempt to identify proteins whose expression correlated with mitochondrial enrichment across tissues. To do this, the expression of each identified/quantified mitochondrial protein was correlated with the sample-specific MEF. Although there were several

proteins that correlated with mitochondrial enrichment among one or more tissues, no proteins were significantly correlated across all four tissues (**Fig. 1J**). Taken together, these data suggest that the activity and/or expression of a single protein is not a useful normalization factor for interpreting differences in mitochondrial physiology across tissues. Thus, throughout the rest of the manuscript, CS activity (**Fig. 1K**), as well as all other indices of bioenergetic flux were normalized to the sample-specific MEF (denoted with a \* following the unit of measurement). For mitochondrial protein expression, nanoLC-MS/MS data were re-searched using the MitoCarta 2.0 database only, as previously described. Using this approach, 795 mitochondrial proteins were identified and quantified across all four tissues. Importantly, we observed nearly identical proteome profiles using either the full mouse proteome database corrected for MitoCarta 2.0 abundance post-hoc or using the MitoCarta 2.0 database exclusively (**Supplementary Fig. 1**).

***Matrix metabolic enzymes display distinct expression and activity profiles across tissues.***

With the technical issue of normalization addressed, we sought to investigate inherent differences in mitochondrial function across tissues, starting with the mitochondrial dehydrogenase network. The dehydrogenase network consists of enzymes that comprise and feed into the citric acid cycle of the mitochondrial matrix (**Fig. 2A**). Therefore, we determined the activity (**Fig. 2B**) and expression (**Fig. 2C**) of matrix dehydrogenases in order to identify the carbon substrates that are most efficiently metabolized within each tissue. **Figure 2C** shows a heatmap of protein abundance for different subunits, isoforms, or regulatory proteins for the matrix enzymes. Each box represents the abundance of the indicated protein scaled to the tissue mean. In several cases, the protein expression data matched the enzymatic activity. For example, the activity and expression levels of both b-hydroxybutyrate dehydrogenase (BDH) and glutamic-oxaloacetic

transaminase (GOT2) were extremely low in BAT. Interestingly, in the case of branched-chain  $\alpha$ -ketoacid dehydrogenase (BCKDH), expression of the catalytic subunits of this enzyme complex were similar across all tissues, but expression of its kinase (BCKDK) was much lower in the liver (**Fig. 2C**, 'BCKDH'). The absence of this regulatory kinase in the liver was reflected in significantly higher BCKDH activity (**Fig. 2B**, 'BCKDH'). Another interesting observation was that the pattern of activity rates seen for pyruvate dehydrogenase (PDH; **Fig. 2B**, 'PDH') mirror those of CS activity (**Fig. 1D**), suggesting that CS activity could in fact be a reliable marker for PDH activity rather than mitochondrial content. This may explain the correlation between mitochondrial content and CS activity that others have observed in skeletal muscle (Larsen et al., 2012), as PDH is highly expressed in skeletal muscle and may happen to be proportionally expressed to mitochondrial number. Of all enzymes evaluated, only malate dehydrogenase (MDH) had equivalent activity rates across all four tissues (**Fig. 2B**, 'MDH'). This may reflect the essential nature of MDH activity given its involvement in several metabolic pathways within the mitochondria.

### ***Heart mitochondria are the most metabolically flexible.***

We then set out to determine how differences in mitochondrial dehydrogenase activity between tissues may influence mitochondrial respiration when exposed to different energetic challenges and substrate conditions. We first probed the substrate preference of each set of tissues using a series of different carbon substrates and specific inhibitors (**Fig. 3A**). Throughout the assay, respiration was stimulated with saturating ADP using the hexokinase enzymatic clamp. The first observation was that heart mitochondria demonstrated a robust inhibition of pyruvate-mediated respiration following the addition of UK5099, an inhibitor of the common pyruvate carrier (**Fig.**

**3A**, ‘Pyr/M’ to ‘UK5099’). Although this effect was most obvious in the heart, Pyr/M supported respiration in BAT, as well as liver and kidney mitochondria was decreased by UK5099 (**Fig. 3A**, inset). Interestingly, relative to heart, percent inhibition by UK5099 in BAT mitochondria respiring on Pyr/M was lower. This may suggest that there is an alternate route for pyruvate transport into the mitochondrial matrix or an increased malate-alone supported rate of oxygen consumption ( $JO_2$ ) in BAT. In the presence of the fatty acid octanoyl-carnitine (**Fig. 3A**, ‘Oct’), further increases in  $JO_2$  were only observed in the heart, suggesting that heart mitochondria are better suited to oxidize fatty acids compared to the other tissues.

Following inhibition of NADH-linked flux with rotenone (Rot or R), glycerol-3-phosphate (**Fig 3A**, ‘G3P’) did not induce an appreciable respiratory response in any of the tissues. This was puzzling, as previous work has shown that BAT typically displays high rates of G3P oxidation (Mráček et al., 2013). Furthermore, our proteomic data supported that the G3P dehydrogenase (GPD2) was highly expressed in BAT mitochondria (**Fig 3B**). Previous work has shown that calcium is necessary for the activation of GPD2 (Clarke and Porter, 2018), and thus the initial G3P oxidation rates observed herein may have been constrained by buffer EGTA. To control for this, respiration assays using G3P as a substrate were repeated in the presence of physiological free calcium ( $\sim 1.5\mu\text{M}$ ). Inclusion of calcium in the assay buffer increased G3P-supported respiration in all tissues and normalized respiration rates aligned well with tissue-specific differences in GPD2 protein expression (**Fig. 3B-C**).

Only through the addition of the complex II substrate succinate (Succ or S) did the respiration rate of kidney approach that of the heart and surpass that of BAT. Although liver mitochondria also achieved a much greater rate with S as a substrate, the  $JO_2$  was comparatively lower with respect to BAT, heart, or kidney. This remained true when complex IV was stimulated directly

using TMPD, a chemical that donates electrons directly to cytochrome C, thus circumventing the inhibition of complex III by antimycin A (Ant). Heart mitochondria had the greatest TMPD-stimulated  $JO_2$ , while BAT and kidney were not different from one another (**Fig. 3A**, ‘TMPD’).

***Substrate preference differences across tissues are maintained across physiological  $\Delta G_{ATP}$  spans.***

Next, we further explored the metabolic flexibility between tissues using a different energetic challenge: the more physiologically relevant creatine kinase (CK) clamp. This assay titrates ATP free energy ( $\Delta G_{ATP}$ ) across a physiological span, from a high demand for ATP re-synthesis ( $\Delta G_{ATP} = -54.16\text{kJ}$ ) to a low demand state in which ATP free energy is highly charged ( $\Delta G_{ATP} = -61.49$ ). If ADP phosphorylation is strongly coupled to respiration in a given tissue, then  $JO_2$  would be expected to be titrated down proportionally to the rise in  $\Delta G_{ATP}$ . Based upon the clear differences in fuel response we observed between tissues (**Fig. 3A**), we performed the CK clamp experiments under five distinct substrate conditions: Pyr/M; glutamate/M (G/M); Oct/M; Succ/Rot;  $\alpha$ -ketoglutarate/G/M/Pyr/Oct/S (Multi). As seen in the substrate preference assay, the heart was able to achieve the highest maximal respiration rates across all substrate conditions (**Fig. 3D**, yellow squares). BAT mitochondria were the only tissue to match the  $JO_2$  of the heart, and this was observed only when fueled by Pyr/M (**Fig. 3D**, red circles). Paired with the results of the substrate preference assay, these data imply that across both the HK and CK clamp systems Pyr/M is the preferred respiratory substrate of BAT. Interestingly, we saw almost no flux in BAT mitochondria under the G/M condition. This observation is in line with our dehydrogenase activity and proteomic data which showed the lowest activity and expression of GOT2 in BAT (**Fig. 2B** and **2C**, respectively). Respiration rates for liver and kidney were lowest across the entire  $\Delta G_{ATP}$

titration under Pyr/M and Oct/M substrate conditions (**Fig. 3D**, green triangles and blue hexagons, respectively). Although this might imply a lower reliance on Complex I-supported respiration in both tissues, the kidney displayed slightly higher respiration when fueled by the Complex-I substrate G/M, approaching the rates of the heart (**Fig. 3D**, 'G/M'). Most interestingly, the response to the CK clamp was altered in kidney mitochondria such that rather than consistently titrating respiration down as the  $\Delta G_{ATP}$  charge was increased, respiration increased at the second titration point. This unexpected result may reflect either an ATP-dependent step in the oxidation pathway for G/M in kidney (i.e., ATP-mediated activation of metabolite oxidation), or possibly a slow activation of the enzymes involved in this pathway.

Beyond the absolute respiration rates themselves, the change in  $JO_2$  relative to the change in  $\Delta G_{ATP}$  can be used to describe the sensitivity of mitochondria to changes in energy demand state. This is referred to as respiratory conductance and is calculated using the slope of the linear portion of the  $JO_2/\Delta G_{ATP}$  relationship (dashed lines in **Fig. 3E**). Conductance was highest in the heart across all four substrate conditions (**Fig. 3E**, yellow bars). BAT mitochondria matched the conductance of heart when fueled by NADH-linked substrates (excluding G/M), though conductance was halved under the Succ/Rot and Multi substrate conditions (**Fig. 3E**, red bars). The kidney also displayed an unusual substrate-dependent pattern to its conductance, in which Succ/Rot evoked the greatest values, but these were not maintained under the Multi substrate condition, in which Succ is present alongside multiple NADH-linked substrates (**Fig. 3E**, green bars). To determine how this might happen, we compared the maximal CK clamp-stimulated respiration rates across 7 substrate conditions (**Fig. 3F**), including  $\alpha$ -ketoglutarate alone (AKG) and AKG/glutamate/M (AKG/G/M). Whereas combining all substrates for the Multi condition produced the greatest  $JO_2$  in heart mitochondria, respiration in kidney mitochondria was

suppressed under the Multi condition compared to S/R alone (**Fig. 3F**). These data suggest that succinate is the predominant respiratory substrate of kidney mitochondria, and the presence of saturating amounts of NADH-linked substrates may restrict succinate uptake and/or oxidation by CII in the kidney.

### ***Respiratory complex expression differs by tissue.***

Given the vast differences in respiratory capacity and sensitivity, we then questioned whether there might also be intrinsic differences in the expression of the respiratory complexes across the four tissues. The mitochondrial OXPHOS system consists of five multi-enzyme complexes which collectively transfer electrons from various NAD- and FAD-linked dehydrogenases to O<sub>2</sub> to form H<sub>2</sub>O. This stepwise transfer releases the energy necessary for complexes I, III, and IV to pump protons across the inner mitochondrial membrane, generating a proton gradient that is harnessed by complex V, ATP synthase, to phosphorylate ADP to ATP. The efficiency of this process depends upon the coordinated action of the various catalytic and accessory subunits that make up these complexes, as depicted in **Figure 4A**. Therefore, changes in the expression of these subunits may have a significant impact upon respiration. To investigate, we searched our proteomics data for all proteins corresponding to components of the OXPHOS system and created separate expression heatmaps based on complex affiliation (**Fig. 4B-F**). As with the dehydrogenase protein expression heatmap (**Fig. 2C**), each box represents the mean abundance of the indicated protein in relation to the tissue mean. We also quantified relative complex expression between tissues by summing the abundance of all proteins related to a given complex and expressing each sum as a percentage of the max abundance across samples (**Fig. 4G**). Supporting the validity of our proteomic results, expression of Cox6a2, a subunit of complex IV specific to striated muscle

(Inoue et al., 2019), was exclusively enriched in heart mitochondrial preparations (**Fig. 4E**). In general, the heart had the greatest expression of the majority of respiratory complexes, while the liver tended to have the lowest expression compared to the other tissues assessed (**Fig. 4G**). The only complex that was not highest in heart mitochondria was complex II, which is also the only complex that does not pump protons. As the tissue with the highest demand for ATP re-synthesis, the heart may not prioritize complex II expression as OXPHOS efficiency is highly dependent upon membrane potential polarization. Interestingly, overall complex I expression was found to be equivalent between BAT and kidney, despite vast differences in  $JO_2$  supported by complex I substrates Pyr/M and Oct/M (**Fig. 4G**). Further, the complex I expression of BAT was found to be approximately half that of heart despite similar Pyr/M-supported respiration rates. This may be reflective of a reserve of complex I that is present specifically in the heart due to its immense energetic demand. BAT also had the lowest expression of complex V of any tissue. The only protein from complex V that was highly expressed in BAT was Atpaf2, an assembly factor for the F1 component of ATP synthase (**Fig. 4F**). This, combined with its enrichment of Ucp1, would suggest that OXPHOS is not the primary role of the electron transport system in BAT, entirely consistent with its known thermogenic function (Harms and Seale, 2013).

***Maximal respiration rates differ by substrate and energetic challenge.***

For a more complete picture of the unique responses to respiratory stimuli between tissues, we compiled the maximal respiration rates attained under several different simulated energetic challenges (**Fig. 5A-B**). To simplify, only two substrate conditions were selected—one primarily feeding complex I (Pyr/M; **Fig. 5A**), and the other feeding complex II (S/Rot; **Fig. 5B**). The state 4 (S4) rate represents  $JO_2$  stimulated by substrates in the absence of an adenylate challenge. In

addition to the CK clamp (reproduced in **Fig. 5A-B**; ‘CK\*’;  $\Delta G_{\text{ATP}} = -54.16\text{kJ}$ ), maximal mitochondrial respiration was elicited through a two-point ADP titration using the HK clamp (‘ADP<sub>10mM</sub>’, ‘ADP<sub>500mM</sub>’) as well as the uncoupler FCCP in the absence of adenylates (‘FCCP<sub>Alone</sub>’) or following the completion of the CK and HK clamp experiments (‘FCCP<sub>CK</sub>’, ‘FCCP<sub>HK</sub>’, respectively).

Across both substrate conditions, the S4 respiration rate of BAT mitochondria was equivalent or greater than the rate attained under all energetic challenges (**Fig. 5A-B**, red bars). As this observation was specific to BAT, it is likely due to the expression of Ucp1, which was enriched in BAT mitochondria. Ucp1 allows reentry of protons from the intermembrane space into the mitochondrial matrix without passing through complex V, inflating the respiration rate through uncoupling (Harms and Seale, 2013). Indeed, the S4 rate was equivalent to the maximal rate achieved by FCCP<sub>Alone</sub> under both substrate conditions, suggesting that the mitochondria were uncoupled prior to the addition of adenylates (**Fig. 5A-B**). The presence of Ucp1 would also explain the stepwise decrease in respiration rate following the addition of increasing amounts of ADP (**Fig. 5A-B**), as ADP is a known inhibitor of Ucp1 (Divakaruni et al., 2012).

Substrate condition had a notable influence over the response to different respiratory challenges in heart mitochondria. When fueled by S/Rot, all maximal energetic challenges (CK, ADP<sub>500mM</sub>, FCCP<sub>Alone</sub>, FCCP<sub>CK</sub>, and FCCP<sub>HK</sub>) evoked equivalent respiration rates (**Fig. 5B**, yellow bars). However, fueling with Pyr/M revealed a different pattern, in which the use of the HK clamp stimulated the greatest  $JO_2$  in the presence of saturating ADP and FCCP (**Fig. 5A**; ‘ADP<sub>500mM</sub>’, ‘FCCP<sub>HK</sub>’). This observation may reflect the different oxidation pathways of these two substrates, as oxidation of succinate by complex II directly feeds the electron transport system while multiple enzyme-mediated steps, including metabolite translocation across the inner mitochondrial

membrane, are needed for the transfer of electrons from pyruvate and malate (Fisher-Wellman et al., 2018). Given that the Pyr/M-supported FCCP<sub>HK</sub> respiration rate was significantly greater than that of FCCP<sub>Alone</sub> and FCCP<sub>CK</sub> (**Fig. 5A**), it is also possible that a supraphysiological concentration of ADP may facilitate the activation of a greater number of respiratory complexes, or put a greater stress on the adenine nucleotide translocator (ANT), which has also been shown to directly transport protons (Bertholet et al., 2019). As this effect is abolished under the S/Rot substrate condition (**Fig. 5B**), proton consumption by the metabolite translocation processes inherent to Pyr/M metabolism is the more likely culprit.

As seen earlier, mitochondria isolated from both the kidney and liver exhibited a clear preference for S/Rot-supported respiration over Pyr/M (**Fig. 5A-B**), likely due to their low PDH activity rates (**Fig. 2B**, PDH). Interestingly, we also observed an unusual bioenergetic phenotype in the kidney in which the S4 rate with Pyr/M, but not S/Rot, was greater than the maximal rate stimulated by the CK energetic clamp (**Fig. 5A-B**, green bars). This may be further evidence of the consumption of the proton gradient by the metabolite exchange processes linked to pyruvate oxidation. Indeed, as in the heart, the highest Pyr/M-supported respiration rates of kidney mitochondria were observed in the presence of the HK clamp and saturating ADP and FCCP (**Fig. 5A**, ‘ADP<sub>500mM</sub>’, ‘FCCP<sub>HK</sub>’). Regardless of substrate, liver mitochondria achieved their highest respiration rates when FCCP was the stimulus, not the adenylate-based CK or HK clamps, indicating that there are limitations to maximal electron transport in the mouse liver that are imposed by the OXPHOS system (**Fig. 5A-B**, blue bars).

*Efficiency of ATP production differs by substrate and tissue.*

We then expanded our interrogation of OXPHOS efficiency across the four tissues by directly quantifying the phosphorylation efficiency using the ratio of ATP production to  $JO_2$  (P/O ratio; **Fig. 5C-D**). ATP production was measured fluorometrically in a parallel HK clamp assay at both ADP concentrations. Both the respiration and fluorometric experiments were performed in the presence of Ap5A, an inhibitor of adenylate kinase (AK). Ap5A was included to eliminate non-OXPHOS-related production of ATP from two molecules of ADP by AK (Lark et al., 2016). The dashed lines represent the theoretical maximum P/O ratios based upon the oxidation of NADH (P/O = 2.7; **Fig. 5C**) and succinate (P/O = 1.6; **Fig. 5D**). As would be expected given the high expression of Ucp1 and low expression of CV previously noted (**Fig. 4F**), BAT demonstrated the lowest P/O ratios across all tissues under both substrate conditions, with ratios at both ADP concentrations far below the theoretical maximum (**Fig. 5C-D**, red bars).

Interestingly, in the heart, substrate condition again played a role in the efficiency of phosphorylation. Under the Pyr/M condition, the P/O ratio attained at  $ADP_{10mM}$  was already at the theoretical maximum, but then significantly dropped in response to an increased concentration of ADP (**Fig. 5B**, yellow bars), despite a large increase in respiration at  $ADP_{500\mu M}$  (**Fig. 5A**). This would suggest that the presence of a saturating amount of ADP may actually make the OXPHOS system less efficient, suggesting a trade-off between maximal respiratory flux and OXPHOS efficiency. The absence of this effect when the mitochondria are fueled by S/Rot (**Fig. 5D**) provides further evidence that there may be other processes involved in Pyr/M metabolism that may be consuming the proton gradient for non-OXPHOS purposes, which may include metabolite transport or proton leak.

Surprisingly, despite their limited respiration under the Pyr/M substrate condition, both kidney and liver appeared to be generating substantial amounts of ATP (**Fig. 5B**, green and blue lines,

respectively). In fact, their Pyr/M-fueled P/O values were greater than those of the heart, as well as the theoretical maximum P/O ratio. As the theoretical maximum was calculated based upon the stoichiometry of the c-subunit composition of the mammalian ATP synthase and the number of protons required for one full turn of the central stalk (Watt et al., 2010), this observation has two possible explanations. One would be that the stoichiometry of the ATP synthase is not fixed, which would imply that there is not a single theoretical maximum. This does not seem likely as the heart, kidney, and liver all displayed similar P/O ratios that were equivalent to the theoretical maximum when supported by S/Rot (**Fig. 5D**). Alternatively, there may have been a contribution of ATP generated through substrate-level phosphorylation rather than OXPHOS. One potential site of substrate-level phosphorylation could be succinyl-CoA synthetase, which is known to have the ability to generate ATP rather than GTP, and this enzyme would not be active in the S/Rot substrate condition. However, this conclusion is not supported by our protein expression data from **Figure 2C**, in which the subunit that favors ADP as a substrate (Sucla2) is shown to be relatively depleted in kidney and liver compared to BAT and heart. Another possibility is that these mitochondrial populations express a version of AK that is insensitive to Ap5A that was responsible for the elevated ATP production. Lastly, given that the  $J_{ATP}$  synthesis and  $J_{O_2}$  assays were run in parallel, rather than being quantified simultaneously (Lark et al., 2016), such conditions may have resulted in slight overestimation of P/O.

*Protein predictors of intrinsic OXPHOS efficiency across tissues are enriched for mitochondrial transporters.*

Given the increased variability in Pyr/M-supported P/O ratios, we sought to determine whether there were any proteins that were predictive of OXPHOS efficiency across tissues. We searched

our proteomic data for the mitochondrial proteins that were most highly correlated with Pyr/M-supported P/O ratio in heart, kidney, and liver tissues. BAT was excluded from this analysis due to the confounding variable of Ucp1 expression. The top 3 most highly correlated proteins are plotted in **Figure 5E**. Ucp3 expression was found to be negatively correlated with the efficiency of OXPHOS (**Fig. 5E**, Ucp3), which would be expected given its role as a mitochondrial uncoupling protein (Mailloux et al., 2011; Toime and Brand, 2010). Lyrn7 expression was also found to be negatively correlated to P/O (**Fig. 5E**, Lyrn7). It functions as an assembly factor that chaperones the insertion of the Rieske iron-sulfur protein Uqcrcfs1 into complex III, a role that may lead to its elevated expression during mitochondrial repair (Hempel et al., 2017). Finally, Slc25A46 belongs to a family of solute carrier proteins, many of which use the mitochondrial proton gradient to transport metabolites in and out of the mitochondria. Given that many of the SLC family of proteins dissipate the proton motive force to do non-OXPHOS work, it is intuitive that they would be negatively correlated with phosphorylation efficiency (**Fig. 5E**, Slc25A46). In fact, as we probed further into the proteomics data for other members of the SLC family, we noted that almost half of the mitochondrial SLC proteins that were identified were significantly correlated with the P/O ratio (**Fig. 5F**; stars denote a significant correlation).

## **Discussion**

Citrate synthase (CS) activity has commonly been the standard strategy for normalization between mitochondrial samples, though, to our knowledge, this has not been validated for comparisons across different tissues. To address this issue, we determined the mitochondrial purity of each sample by calculating the proportion of all nanoLC-MS/MS-quantified proteins that could be identified as mitochondrial using the MitoCarta 2.0 database. This provided a mitochondrial

enrichment factor (MEF) for each sample that could be compared across tissues. Our findings indicate that CS activity was not significantly correlated with the MEF for three out of the four tissues studied. In fact, there were no identified mitochondrial proteins that universally correlated with the MEF. As no protein surrogate was found to be an adequate estimate of mitochondrial purity, the MEF is potentially the optimal method for normalization across tissue types when performing mitochondrial isolations. Although previous work has utilized a similar mass spectrometry-based normalization method in mouse liver (Walheim et al., 2018), this may be the first true comparison of intrinsic mitochondrial respiratory kinetics between several different mammalian tissues.

Collectively, our findings concerning the bioenergetic phenotype of BAT agree with those previously published in the literature (Lidell et al., 2014). Respiration was uniformly high across all substrate conditions (with the exception of glutamate), even in the absence of an adenylate-based stimulus (i.e. state 4 respiration), likely due to the expression of Ucp1 in BAT mitochondria. Interestingly, Ucp1 was only one limitation to the maximal phosphorylation efficiency of BAT, as it was also shown that expression of complex V, or ATP synthase, was significantly depressed in BAT compared to all other tissues. Another curious observation was that expression of complex I-related proteins in BAT was nearly half that of the heart, yet respiration rates for most complex I substrates (including pyruvate, AKG, and octanoyl-carnitine) were generally comparable between BAT and heart. This finding may imply that in the presence of an uncoupling protein, which allows more free cycling of protons across the inner mitochondrial membrane compared to the demand-driven complex V, a smaller number of respiratory complexes may be necessary to achieve the same rate of electron flow.

Mitochondria isolated from the heart, the tissue with the highest energetic demand of the four studied, predictably had the highest maximal respiration rates under nearly every condition. Heart mitochondria were also the only to display an additive effect to respiration when energized by the Multi substrate condition, highlighting the metabolic flexibility of their mitochondrial network. As might be expected, the conductance of the heart, an estimate of bioenergetic efficiency in response to changing  $\Delta G_{ATP}$ , was among the highest under every substrate condition. When phosphorylation efficiency was quantified directly, the heart was able to attain the theoretical maximum P/O values at the lowest concentration of ADP when energized by both Pyr/M and S/Rot. Interestingly, however, the presence of saturating ADP was shown to decrease the P/O ratio below the theoretical maximum when energized by Pyr/M, but not S/Rot. Given that there was a large increase in respiration with the greater concentration of ADP, the decrease in P/O would suggest that this jump in  $J_{O_2}$  was not met with a proportional increase in ATP production. One possibility for this discrepancy is that supra-physiological concentrations of ADP may activate a ‘reserve capacity’ of additional respiratory complexes in order to meet this greater demand, albeit with a lower efficiency. This explanation would align with the discrepancy in complex expression between BAT and heart. Alternatively, such a high ADP concentration may also stress ANT, which is responsible for exchanging ADP and ATP at the inner mitochondrial membrane. This transport process is powered by the proton gradient in the same way as complex V, and ANT has additionally been shown to transport protons into the matrix independently of its ADP/ATP transport activity (Bertholet et al., 2019). Proton movement through ANT would thus mimic the effects of an uncoupling protein.

As an organ whose primary responsibility is to maintain concentration gradients across membranes, the kidney would be expected to have a high demand for ATP re-synthesis. Our results

suggest that succinate is the preferred respiratory substrate for the kidney, across a variety of stimulus conditions, consistent with previous findings (Iuso et al., 2017). However, the kidney was the only tissue to demonstrate significantly depressed respiration under a Multi substrate condition. This may have important implications in the case of diet-induced kidney disease, as it is apparent that their mitochondria may be functionally impaired in the presence of excess NAD-linked carbon substrates (Forbes and Thorburn, 2018). More interestingly, the kidney was the only tissue to demonstrate an increase in respiration in response to the CK clamp-imposed titration of  $\Delta G_{ATP}$ . This effect was only seen when the kidney was fueled by glutamate/malate, which may reflect an ATP-dependent step in the glutamate oxidation pathway. This would not be entirely unusual as a similar phenomenon was recently demonstrated with respect to the oxidation of branched-chain keto-acids (Goldberg et al., 2019).

Although the kidney and liver appear to favor succinate over complex I substrates to support respiration, both displayed P/O values that were greater than the theoretical maximum values when supported by Pyr/M. The theoretical maximum values are based on the stoichiometry of the number of protons that it would take to fully turn the rotor of complex V, which generates three ATP molecules (Watt et al., 2010). This discrepancy may be caused by several different scenarios. First, it is possible that this stoichiometry is not fixed, as has been previously thought. This is unlikely, given that the succinate-supported P/O remained at or below the theoretical maximum for both tissues. Second, a portion of the ATP production that was observed could be through substrate-level phosphorylation. The most likely candidate for this would be SUCLA, which can express an isoform that prefers ADP rather than GDP as its substrate. This possibility is supported by the fact that P/O does not remain above the maximum when fueled by succinate, as SUCLA would no longer be involved in substrate catalysis. From our proteomic data, it appears that liver

and kidney preferentially express the GDP-favoring *Suclg2* isoform. However, it is also possible that these tissues express an enzyme which catalyzes the interconversion from GTP to ATP. Finally, this measurement was obtained using parallel experiments in a respiration chamber and a fluorometer, which may be a technical limitation to obtaining accurate P/O values. Regardless, the pattern that was observed in which the Pyr/M-supported P/O values obtained for liver and kidney were greater than those of heart is intriguing.

One of the most fascinating findings was the high proportion of SLC family proteins (Palmieri and Monné, 2016; Ruprecht and Kunji, 2020) whose expression were significantly correlated to phosphorylation efficiency. This relationship makes sense as many of the SLC proteins as well as complex V consume the proton gradient to perform cellular work. Thus, if both SLC proteins and complex V are active at the same time, some proportion of the  $JO_2$  must be used to power the SLC rather than generate ATP, lowering the P/O.

As studies of bioenergetic function advance, it is becoming more apparent that not all mitochondria are created equal. Full appreciation of the metabolic specialization of different tissues with different energetic demands can only be achieved through normalization that factors in the purity of the mitochondrial sample. Our results support the use of mitochondrial-targeted nanoLC-MS/MS to determine mitochondrial enrichment on a per-sample basis. This method will allow for unbiased comparison of functional parameters between populations of mitochondria isolated from metabolically distinct tissues, as well as in response to a variety of physiological (e.g., exercise, fasting) and pathophysiological (e.g., diabetes, cancer) stressors.

## **Materials and methods**

## ***Animals***

Animal experiments were performed using C3H/HeJ mice (n=10; The Jackson Laboratory, stock #000659) according to the relevant guidelines approved by the East Carolina University Institutional Animal Care and Use Committee. At the time of tissue harvest, 12h-fasted mice were anesthetized with isoflurane, and brown adipose (subscapular; BAT), heart, kidney, and liver tissues were removed and immediately subjected to mitochondrial isolation.

## ***Chemicals and reagents***

Unless otherwise stated, all chemicals were purchased from Sigma-Aldrich.

## ***Mitochondrial isolation***

Mitochondria were isolated from all tissues using differential centrifugation as described previously, with some modifications (McLaughlin et al., 2018). The following buffers were utilized: Buffer A - MOPS (50mM), KCl (100mM), EGTA (1mM), MgSO<sub>4</sub> (5mM), pH=7.1; Buffer B - Buffer A, supplemented with bovine serum albumin (BSA; 2g/L). After removal, all tissues were immediately placed in ice-cold Buffer B, minced, then homogenized via a drill-driven Teflon pestle and borosilicate glass vessel. Homogenates were centrifuged at 800 x g for 10min at 4°C. The supernatant was filtered through gauze and centrifuged at 10,000 x g for 10min at 4°C. The pellets were washed in 1.4mL of Buffer A, transferred to microcentrifuge tubes, and again centrifuged at 10,000 x g for 10min at 4°C. Final mitochondrial pellets were resuspended in 100-200mL of Buffer A. Protein content was determined via the Pierce BCA protein assay. Freshly prepared mitochondria were then used for citrate synthase activity and functional experiments, with a portion of each mitochondrial suspension flash frozen for matrix dehydrogenase activity

and proteomic analyses. Using this method, a single mitochondrial preparation can be used to generate all biochemical outcomes described in this paper.

### ***Citrate synthase activity***

Citrate synthase (CS) activity was determined using a colorimetric plate-based assay in which CoA-SH, a byproduct formed by the CS-mediated reaction of oxaloacetate and acetyl-CoA, interacts with 5', 5'-Dithiobis 2-nitrobenzoic acid (DTNB) to form TNB (OD: 412nm). Assay buffer consisted of Buffer C (105mM potassium-MES, 30mM KCl, 10mM KH<sub>2</sub>PO<sub>4</sub>, 5mM MgCl<sub>2</sub>, and 1mM EGTA; pH=7.2) supplemented with DTNB (0.2mM) and acetyl-CoA (0.5mM). A 96-well round bottom plate was loaded with assay buffer (200µL/well), the permeabilizing agent alamethicin (0.03mg/mL), and isolated mitochondria (10µg/well) and then incubated at 37°C for 5min to deplete endogenous substrates. The assay was initiated by the addition of oxaloacetate (1mM) to sample wells, with absorbance at 412nm recorded every 30s for 20min. The mitochondrial suspension was also added to one control well per sample to account for nonspecific activity, which was later subtracted from the sample rate. CS activity was determined using the Beer-Lambert Law and the molar absorption coefficient of TNB (13.6mM/cm).

### ***Mitochondrial functional assessment***

High-resolution O<sub>2</sub> consumption rate ( $\dot{V}O_2$ ) measurements were conducted using the Oroboros Oxygraph-2K (Oroboros Instruments, Innsbruck, Austria). The base assay buffer was Buffer C (105mM potassium-MES, 30mM KCl, 10mM KH<sub>2</sub>PO<sub>4</sub>, 5mM MgCl<sub>2</sub>, 1mM EGTA, 2.5g/L BSA and 5mM creatine monohydrate; pH=7.2), modified to simulate 3 different energetic challenges: the hexokinase enzymatic clamp (HK clamp); the creatine kinase energetic clamp (CK clamp);

and titration of uncoupling agent carbonyl cyanide-4-(trifluoromethoxy)phenylhydrazone (FCCP). The HK clamp maintained a steady-state ADP concentration by consuming any newly generated ATP to phosphorylate glucose (Lark et al., 2016). The CK clamp titrated the free energy of ATP hydrolysis ( $\Delta G_{\text{ATP}}$ ) as described below. Titration of FCCP was used to stimulate  $JO_2$  independent of the demand for ATP re-synthesis. All respiration experiments were carried out at 37°C in a 1mL reaction volume, with 25-300 $\mu$ g protein loaded per experiment.

*Substrate preference assay:* Substrate preference was assessed by comparing the steady-state  $JO_2$  attained following sequential additions of different carbon substrates and specific inhibitors in the presence of a maximal ADP concentration (500mM) maintained using the HK clamp. Assay buffer was supplemented with HK (1U/ml) and glucose (5mM). Assay was initiated through addition of mitochondria, followed by ADP and pyruvate/malate (P/M; 1mM/2mM). The pyruvate carrier inhibitor acyano-(1-phenylindol-3-yl)-acrylate (UK5099; 1 $\mu$ M) was then added to prevent pyruvate entry, followed by octanoyl-carnitine (Oct; 0.2mM). NADH-linked respiration was then inhibited using rotenone (Rot; 0.05mM), and glycerol-3-phosphate (G3P; 10mM) was added. G3P feeds electrons into the ubiquinone pool through the mitochondrial G3P dehydrogenase located on the outer portion of the inner mitochondrial membrane. Succinate (S; 10mM) was then added to stimulate complex II-linked respiration. Complex III was then inhibited by antimycin A (Ant; 0.005mM), and complex IV was stimulated through the addition of the cytochrome C-specific electron donor N,N,N',N'-tetramethyl-*p*-phenylenediamine (TMPD; 0.5mM dissolved in ascorbate – final ascorbate concentration of 2mM).

In a separate experiment using a subset of five C3H mice, we determined G3P-supported respiration in the presence of calcium, which is necessary to fully activate the G3P dehydrogenase

(Clarke and Porter, 2018). For this experiment, mitochondria were added to Buffer C, followed by an addition of 0.8mM of CaCl<sub>2</sub> (1.5μM free calcium). G3P (10mM) was then added, followed by the HK clamp components and ADP (500 μM).

*Creatine kinase clamp experiments:* As previously described, a modified version of the CK clamp technique was used to determine steady-state  $JO_2$  across a physiological span of  $\Delta G_{ATP}$  using known amounts of creatine (Cr), phosphocreatine (PCr), and ATP in the presence of excess amounts of CK (Fisher-Wellman et al., 2018; Glancy et al., 2013; Messer et al., 2004). For complete details regarding the calculation of  $\Delta G_{ATP}$  at each titration point see (Fisher-Wellman et al., 2018). To begin, mitochondria were added to Buffer C, followed by the addition of respiratory substrates to stimulate State 4 respiration. The CK clamp was then initiated by the addition of ATP (5mM), PCr (1mM), and CK (20U/ml), simulating a ‘maximal’ demand for ATP re-synthesis. Sequential additions of PCr to 6, 15, and 21mM were then performed to gradually lower the ATP demand state back toward baseline. After the final PCr addition, FCCP was titrated (0.5, 1, 2mM) to stimulate respiration back up towards maximal  $JO_2$ . Plotting the calculated  $\Delta G_{ATP}$  against the corresponding steady-state  $JO_2$  reveals a linear force-flow relationship, the slope of which represents the conductance/sensitivity of the entire respiratory system under the specified substrate constraints. Five substrate conditions were used: Pyr/M (5mM/2mM); glutamate/M (G/M; 10mM/2mM); Oct/M (0.2mM/2mM); S/Rot (10mM/0.5mM);  $\alpha$ -ketoglutarate/G/M/Pyr/Oct/S (abbreviated as Multi; 10mM/5mM/2mM/5mM/0.2mM/5mM).

*ATP/O assay:* Parallel respiration and fluorometric ADP titration experiments were carried out in order to generate an ATP/O ratio. Fluorometry experiments were carried out using a

QuantaMaster Spectrofluorometer (QM-400; Horiba Scientific) at 37°C in a 200µL reaction volume with continuous stirring. All experiments were conducted using the HK clamp to maintain the desired ADP concentration. Assay buffer was supplemented with HK (1U/mL), glucose (5mM), glucose-6-phosphate dehydrogenase (2U/mL), and NADP<sup>+</sup> (4mM), as well as P1,P5-di(adenosine-5')pentaphosphate (Ap5A; 0.2mM). Ap5A was included to inhibit adenylate kinase, preventing the generation of ATP from ADP alone (Lark et al., 2016). To begin, mitochondria were added, followed by respiratory substrates. ADP was titrated to 10 and 500mM. Respiration experiments were then continued with an FCCP titration (0.5, 1, 2mM). Fluorometry experiments were conducted in both the presence and absence of oligomycin (0.02mM) to account for fluorescence unrelated to ATP synthase activity. The rate of change in NAD(P)H fluorescence (Ex:Em, 350:450) was equated to the rate of ATP production ( $J_{ATP}$ ), as previously described (Lark et al., 2016). The ATP/O ratio was then calculated as  $J_{ATP}/J_{O_2}$ , divided by 2. Respiratory substrates were limited to complex I-specific Pyr/M (5mM/2mM) or complex II-specific S/Rot (10mM/0.5mM).

### ***Matrix dehydrogenase activity assays***

Enzymatic activities of matrix dehydrogenases were determined via the autofluorescence of NADH or NADPH (Ex:Em 340:450), as described previously (Fisher-Wellman et al., 2018). Evaluated enzymes included aconitase (ACO),  $\alpha$ -ketoglutarate dehydrogenase (AKGDH), branched-chain  $\alpha$ -ketoacid dehydrogenase (BCKDH), b-hydroxybutyrate dehydrogenase (BDH), fumarate hydratase (FH), glutamate dehydrogenase (GDH), glutamic-oxaloacetic transaminase (GOT2), b-hydroxyacyl-CoA dehydrogenase (HADHA), isocitrate dehydrogenase 2 (IDH2), isocitrate dehydrogenase 3 (IDH3), malate dehydrogenase (MDH), malic enzyme (ME), pyruvate

dehydrogenase (PDH), and succinyl-CoA synthetase (SUCLA). With the exception of SUCLA, all activity assays were performed in a 96-well plate in a 200 $\mu$ L volume. SUCLA activity was determined using the same assay volume in the QM-400 fluorometer. Fluorescence was measured every minute for 60 minutes in the plate reader and continuously in the fluorometer. Enzymatic rates were determined using a standard curve performed with NADH standards ranging from 20-50,000 $\mu$ M.

### ***Mitochondrial lysis and sample prep for label-free proteomics***

Isolated mitochondria were lysed in Buffer D (8M urea in 40mM Tris, 30mM NaCl, 1mM CaCl<sub>2</sub>, 1 x cOmplete ULTRA mini EDTA-free protease inhibitor tablet; pH=8.0), as described previously (McLaughlin et al., 2020). The samples were subjected to three freeze-thaw cycles, and sonication with a probe sonicator in three 5s bursts (Q Sonica #CL-188; amplitude of 30). Samples were then centrifuged at 10,000 x g for 10min at 4°C. Protein concentration was determined by BCA protein assay. Equal amounts of protein were reduced with 5mM DTT at 37°C for 30min, and then alkylated with 15mM iodoacetamide at room temperature for 30min in the dark. Unreacted iodoacetamide was quenched with DTT up to 15mM. Initial digestion was performed with Lys C (ThermoFisher Cat# 90307; 1:100 w:w; 2 $\mu$ g enzyme per 200 $\mu$ g protein) for 4hr at 37°C. Following dilution to 1.5M urea with 40mM Tris (pH=8.0), 30mM NaCl, 1mM CaCl<sub>2</sub>, samples were digested overnight with trypsin (Promega; Cat# V5113; 50:1 w/w, protein:enzyme) at 37°C. Samples were acidified to 0.5% TFA and then centrifuged at 4,000 x g for 10min at 4°C. Supernatant containing soluble peptides was desalted, as described previously (McLaughlin et al., 2020) and then eluate was frozen and lyophilized.

### ***nLC-MS/MS for label-free proteomics***

Final peptides were resuspended in 0.1% formic acid, quantified (ThermoFisher Cat# 23275), and then diluted to a final concentration of 0.25 $\mu$ g/ $\mu$ L. Samples were subjected to nanoLC-MS/MS analysis using an UltiMate 3000 RSLCnano system (ThermoFisher) coupled to a Q Exactive Plus Hybrid Quadrupole-Orbitrap mass spectrometer (ThermoFisher) via a nanoelectrospray ionization source. For each injection, 4 $\mu$ L (1 $\mu$ g) of sample was first trapped on an Acclaim PepMap 100 20mm  $\times$  0.075mm trapping column (ThermoFisher Cat# 164535; 5 $\mu$ L/min at 98/2 v/v water/acetonitrile with 0.1% formic acid). Analytical separation was then performed over a 95min gradient (flow rate of 250nL/min) of 4-25% acetonitrile using a 2 $\mu$ m EASY-Spray PepMap RSLC C18 75 $\mu$ m  $\times$  250mm column (ThermoFisher Cat# ES802A) with a column temperature of 45°C. MS1 was performed at 70,000 resolution, with an AGC target of 3 $\times$ 10<sup>6</sup> ions and a maximum injection time (IT) of 100ms. MS2 spectra were collected by data-dependent acquisition (DDA) of the top 15 most abundant precursor ions with a charge greater than 1 per MS1 scan, with dynamic exclusion enabled for 20s. Precursor ions isolation window was 1.5m/z and normalized collision energy was 27. MS2 scans were performed at 17,500 resolution, maximum IT of 50ms, and AGC target of 1 $\times$ 10<sup>5</sup> ions.

### ***Data analysis for label-free proteomics***

As described previously (McLaughlin et al., 2020), with some modification, Proteome Discoverer 2.2 (PDv2.2) was used for raw data analysis, with default search parameters including oxidation (15.995 Da on M) as a variable modification and carbamidomethyl (57.021 Da on C) as a fixed modification. Data were searched against the Uniprot Mus musculus reference proteome (Proteome ID: UP 000000589), as well as the mouse Mito Carta 2.0 database (Calvo et al., 2016).

PSMs were filtered to a 1% FDR and grouped to unique peptides while maintaining a 1% FDR at the peptide level. Peptides were grouped to proteins using the rules of strict parsimony and proteins were filtered to 1% FDR. Peptide quantification was done using the MS1 precursor intensity. Imputation was performed via low abundance resampling. Using only high confidence master proteins, mitochondrial enrichment factor (MEF) was determined by comparing mitochondrial protein abundance (i.e., proteins identified to be mitochondrial by cross-reference with the MitoCarta 2.0 database) to total protein abundance.

### ***Statistical evaluation***

All mass spectrometry samples were normalized to total protein abundance, and the protein tab in the PDv2.2 results was exported as a tab delimited .txt. file and analyzed. Protein abundance was converted to the Log<sub>2</sub> space. For pairwise comparisons, tissue mean, standard deviation, p-value (p; two-tailed Student's t-test, assuming equal variance), and adjusted p-value (Benjamini Hochberg FDR correction) were calculated (Kasen et al., 1990; Lesack and Naugler, 2011). Multi-tissue comparisons were analyzed by 2-way ANOVA (Tissue x Protein) using Tukey's test to correct for multiple comparisons. Where indicated, Pearson correlation coefficients were generated using GraphPad Prism 8 software (Version 8.4.2).

Functional assay results are expressed as the mean ± SEM (error bars). Data were normalized to protein loaded per experiment and then corrected for the mitochondrial enrichment factor (\*) calculated for that sample, with the final values expressed as pmol/s/mg protein\*. Differences between tissues were assessed by one-way ANOVA, followed by Tukey's test where appropriate using GraphPad Prism 8 software (Version 8.4.2). Other statistical tests used are described in the figure legends. Statistical significance in the figures is indicated as follows: \* $p < 0.05$ ; \*\* $p < 0.01$ ;

\*\*\* $p < 0.001$ ; \*\*\*\* $p < 0.0001$ . Unless otherwise stated, figures were generated using GraphPad Prism 8 software (Version 8.4.2).

### ***Data Availability***

All raw data for proteomics experiments are available online using accession number “JPST000908” for jPOST Repository (Deutsch et al., 2017; Okuda et al., 2017).

### **Acknowledgements**

This work was supported in part by DOD-W81XWH-19-1-0213 (K.H.F-W.).

### **Decaration of Interest**

Authors declare that they have no conflicts of interest with the contents of this article.

## Figures

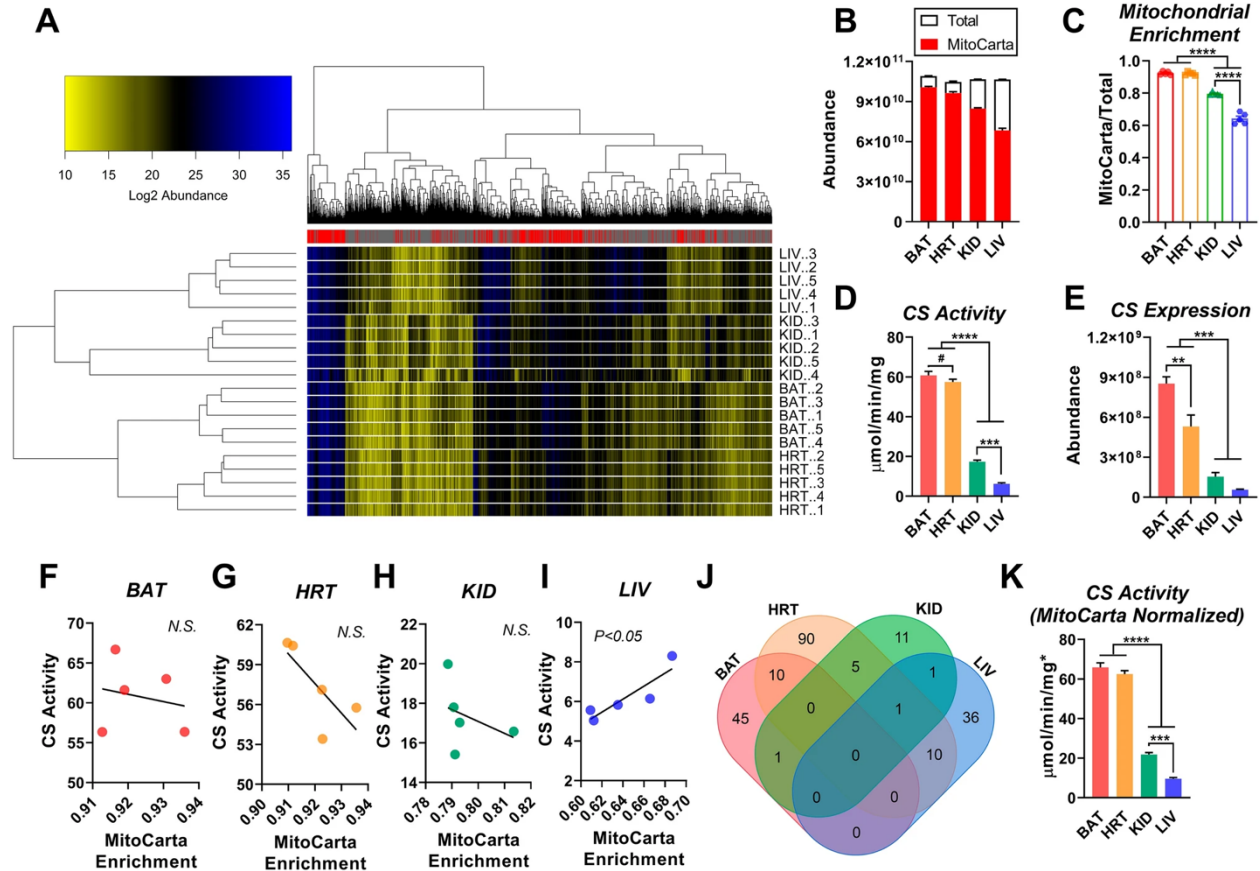


**Figure 1. Quantification of percent mitochondrial enrichment using subcellular proteomics.**

(A) Heatmap displaying abundance (Log<sub>2</sub>) of mitochondrial and non-mitochondrial high confidence proteins from isolated mitochondria samples prepared from BAT, HRT, KID, and LIV. Mitochondrial proteins are indicated in the legend by a ‘red’ mark. Mitochondrial proteins were assigned using the MitoCarta 2.0 database. (B) Summed total abundance of all proteins, relative to mitochondrial proteins. (C) Mitochondrial enrichment factors per tissue, derived from the ratio of mitochondrial to total protein abundance. (D) Citrate synthase (CS) activity in isolated mitochondria, normalized to protein. (E) CS abundance. (F-J) Correlation between CS activity and MitoCarta enrichment. (J) Overlapping proteins per tissue that correlate with MitoCarta

enrichment (Figure generated using <http://bioinformatics.psb.ugent.be/webtools/Venn/>). **(K)** CS activity normalized to protein and corrected for each sample's mitochondrial enrichment factor (MEF). To do this, CS activity displayed in panel **D** was multiplied by the sample-specific MEF. Data are presented as mean  $\pm$  SEM, N=5/group. \*\*P<0.01, \*\*\*P<0.001, \*\*\*\*P<0.0001, #P<0.05 (Student's t-test).

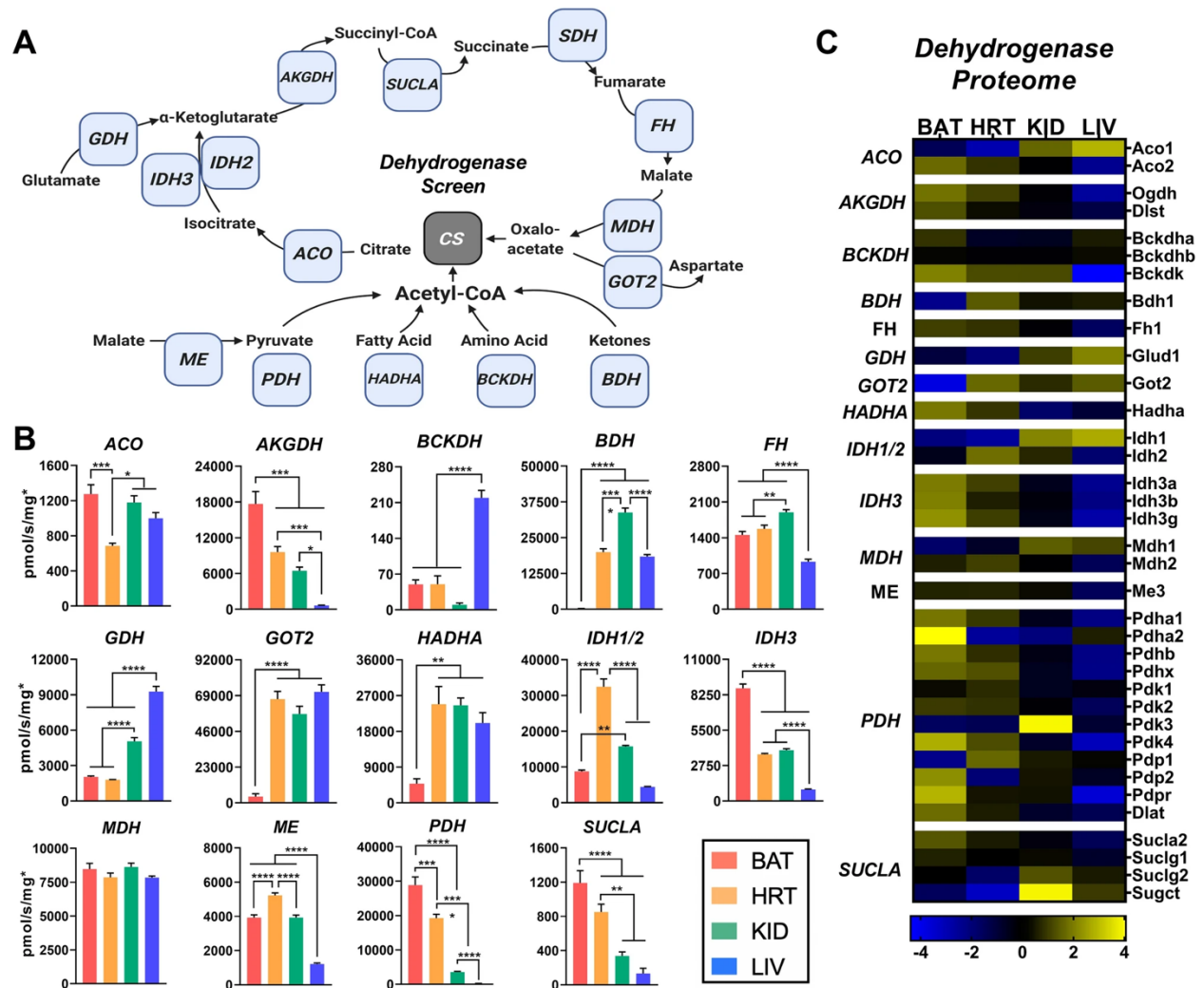


**Figure 2. Intrinsic differences in matrix dehydrogenase activity and expression across tissues.**

**(A)** Cartoon depicting the matrix dehydrogenase, and associated enzymes, network (Figure created

using BioRender.com). **(B)** Enzyme activity normalized to total protein and corrected for each sample's MEF. **(C)** MitoCarta 2.0 normalized protein expression of individual enzyme subunits. Data are presented as mean  $\pm$  SEM, N=5/group. \*P<0.05, \*\*P<0.01, \*\*\*P<0.001, \*\*\*\*P<0.0001.

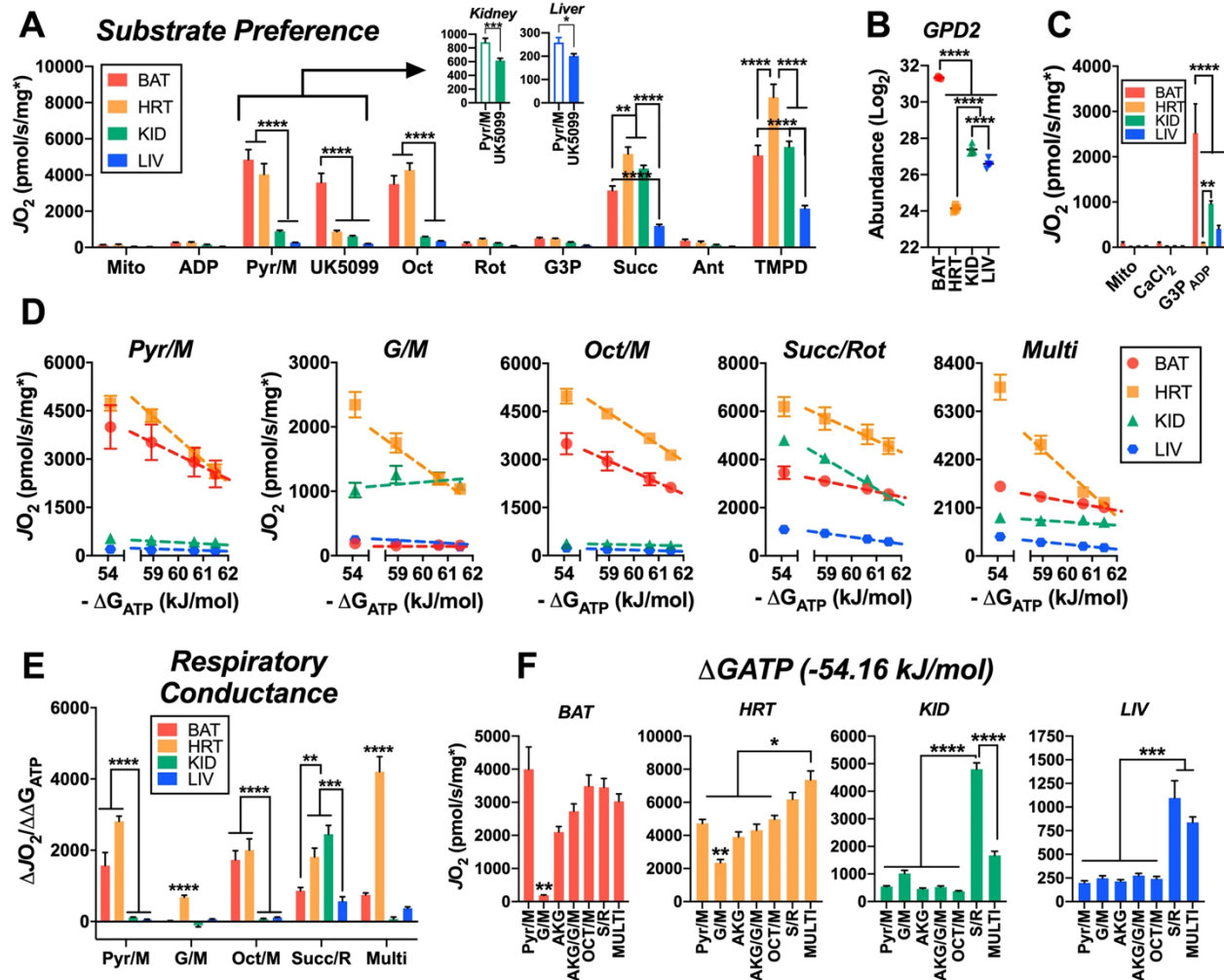


**Figure 3. Carbon substrate preference and OXPHOS conductance across tissues.** (A) Mitochondrial respiratory flux ( $JO_2$ ) stimulated with 0.5mM ADP, clamped throughout the experiment via the hexokinase clamp. Substrate and inhibitor additions were as follows: Pyr/M (1mM/1mM), UK5099 (pyruvate carrier inhibitor – 0.001mM), Oct (0.2mM), Rot (0.0005mM),

G3P (10mM), Succ (10mM), Ant (0.0005mM), TMPD (0.5mM, plus 2mM ascorbate). **(B)** Glycerol-3-phosphate dehydrogenase 2 (GPD2) abundance. **(C)** Mitochondrial  $JO_2$  in the presence of  $CaCl_2$  (1.5 $\mu$ M), stimulated by G3P (10mM) and 0.5mM ADP via the hexokinase clamp ( $G3P_{ADP}$ ). **(D)** Relationship between  $JO_2$  and ATP free energy ( $\Delta G_{ATP}$ ) clamped with the CK clamp in mitochondria energized with Pyr/M, G/M, Oct/M, Succ/Rot, and Multi. **(E)** Respiratory conductance – slope of the relationship between  $JO_2$  and  $\Delta G_{ATP}$ . **(F)** Maximal OXPHOS flux ( $JO_2$  at  $\Delta G_{ATP}$  of -54.16 kJ/mol) in response to various substrate combinations. Data information: **(A, D, F)** Data normalized to protein corrected for each sample's MEF. **(C)** Data normalized to average MEF for that tissue. Data are Mean  $\pm$  SEM, N=5/group. \*P<0.05, \*\*P<0.01, \*\*\*P<0.001, \*\*\*\*P<0.0001.

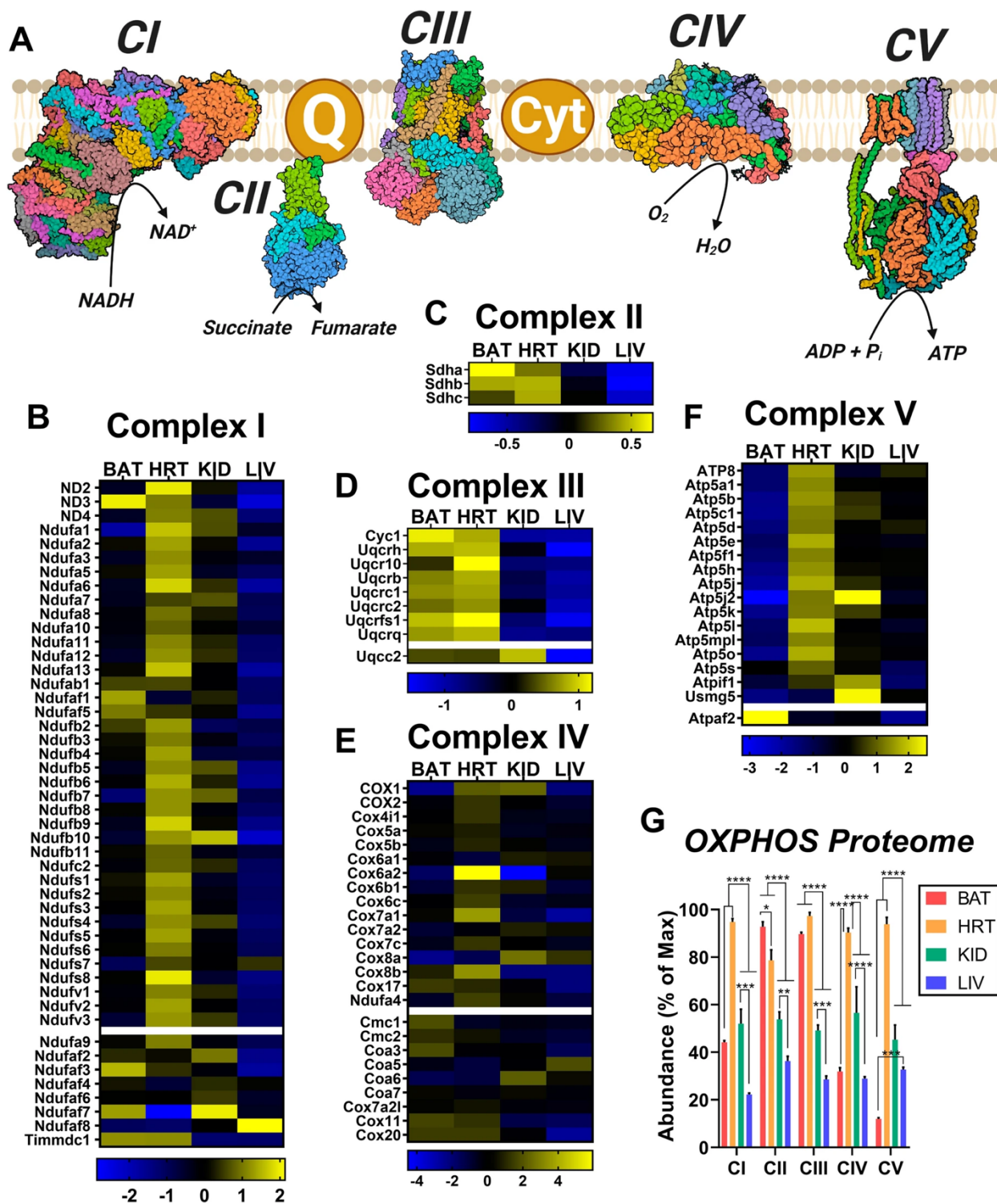


**Figure 4. Intrinsic OXPHOS proteome heterogeneity across mouse tissues.** (A) Cartoon depicting the protein complexes of the electron transport system and ATP synthase (i.e., CV)

(Figure created using BioRender.com). (B-F) MitoCarta 2.0 normalized protein expression of individual protein subunits of CI (B), CII (C), CIII (D), CIV (E), CV (F). (G) Quantification of the OXPHOS protein complexes generated by the summed abundance of all subunits within a given complex. Data are presented as a percentage of the max for each complex. Data are Mean  $\pm$  SEM, N=5/group. \*\*P<0.01, \*\*\*P<0.001, \*\*\*\*P<0.0001.

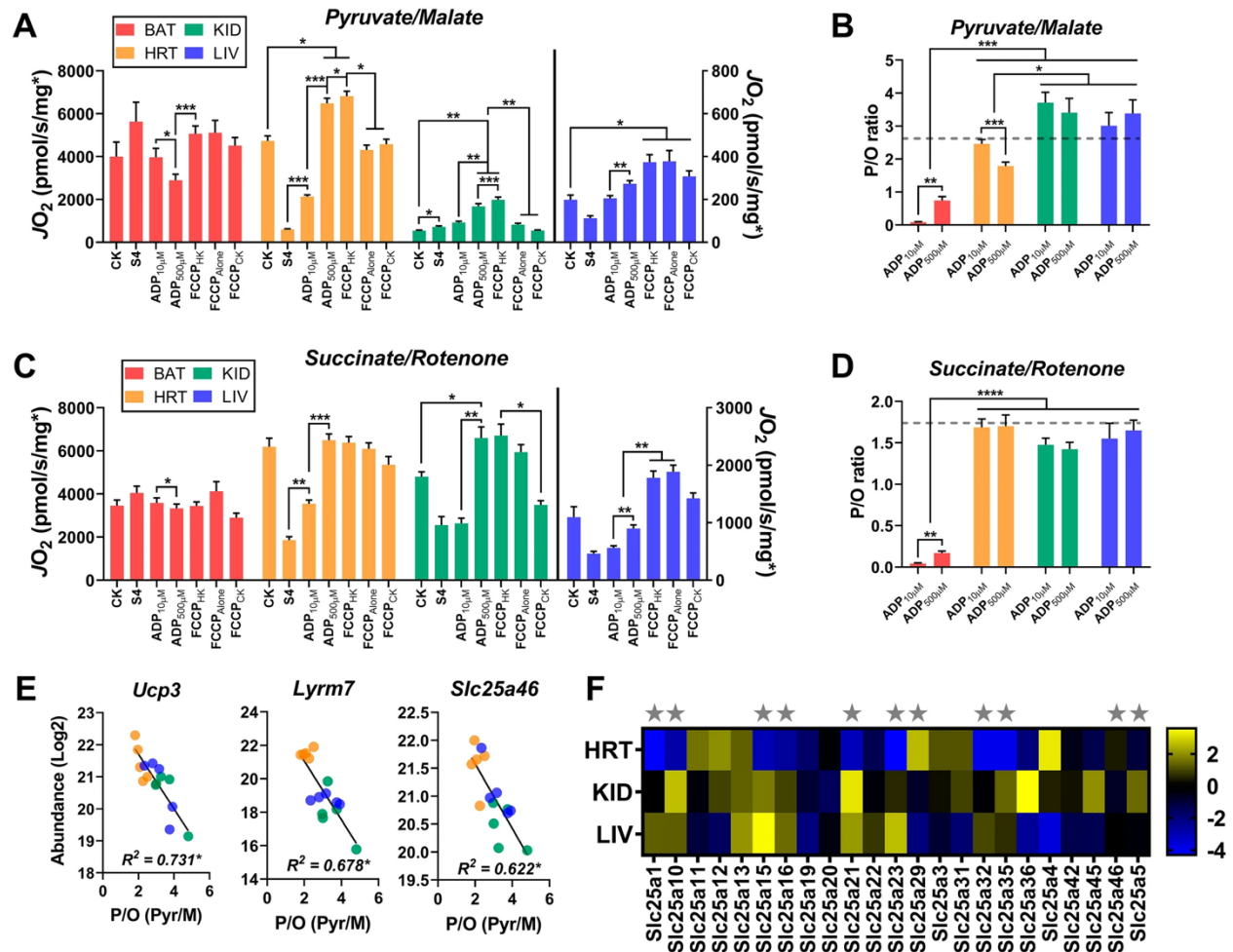
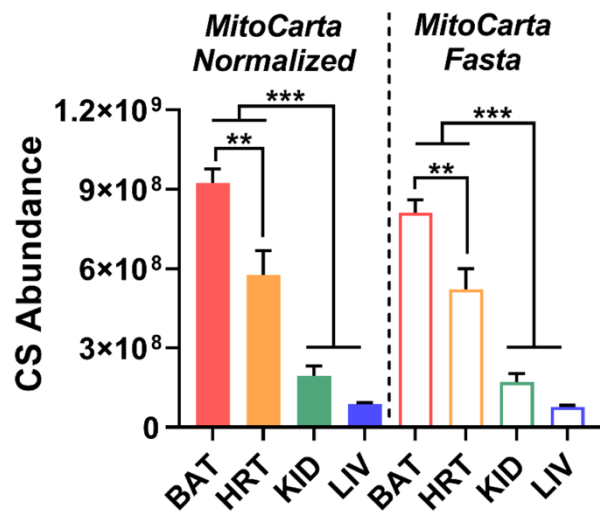


**Figure 5. The mitochondrial SLC family of proteins correlate with Pyr/M supported intrinsic phosphorylation efficiency.** (A) Respiration in isolated mitochondria energized with Pyr/M. Respiration was stimulated with  $\Delta G_{ATP}$  of -54.16 kJ/mol (CK), leak respiration in the absence of

adenylates (S4), 0.01mM ADP (ADP<sub>10μM</sub>), 0.5mM ADP (ADP<sub>500μM</sub>), and FCCP in the presence of 0.5mM ADP (FCCP<sub>HK</sub>), no adenylates (FCCP<sub>Alone</sub>), or  $\Delta G_{ATP}$  (FCCP<sub>CK</sub>). **(B)** Relationship between mitochondrial ATP synthesis and oxygen consumption, a direct measurement of intrinsic phosphorylation efficiency (i.e., P/O ratio). Substrate condition = Pyr/M. Dashed line depicts the theoretical maximum for P/O based on the known mammalian stoichiometry of ATP synthesis. **(C)** Respiration in isolated mitochondria energized with succinate/rotenone. Respiration was stimulated with  $\Delta G_{ATP}$  of -54.16 kJ/mol (CK), leak respiration in the absence of adenylates (S4), 0.01mM ADP (ADP<sub>10μM</sub>), 0.5mM ADP (ADP<sub>500μM</sub>), and FCCP in the presence of 0.5mM ADP (FCCP<sub>HK</sub>), no adenylates (FCCP<sub>Alone</sub>), or  $\Delta G_{ATP}$  (FCCP<sub>CK</sub>). **(D)** Relationship between mitochondrial ATP synthesis and oxygen consumption, a direct measurement of intrinsic phosphorylation efficiency (i.e., P/O ratio). Substrate condition = succinate/rotenone. Dashed line depicts the theoretical maximum for P/O based on the known mammalian stoichiometry of ATP synthesis. **(E)** Correlation of MitoCarta 2.0 normalized protein abundance of Ucp3, Lym7, and Scl25a46 with Pyr/M supported P/O. **(F)** MitoCarta 2.0 normalized protein expression of identified/quantified mitochondrial SLC proteins. Stars indicate SLC proteins found to correlate with Pyr/M mediated P/O. Data are Mean  $\pm$  SEM, N=5/group. \*P<0.05, \*\*P<0.01, \*\*\*P<0.001, \*\*\*\*P<0.0001.



**Supplementary Figure 1. Comparison of search strategies using the MitoCarta 2.0 Database.**

Citrate synthase (CS) abundance. In the closed bars, abundance was determined using the entire mouse proteome database and then results were adjusted for MitoCarta enrichment. The open bars depict MitoCarta 2.0 normalized CS abundance. In this case, the database used for peptide identification was exclusively MitoCarta 2.0. Data are mean ± SEM, N=5, \*\*Adjusted P<0.01, \*\*\*Adjusted P<0.001.

## References

- Bertholet AM, Chouchani ET, Kazak L, Angelin A, Fedorenko A, Long JZ, Vidoni S, Garrity R, Cho J, Terada N, Wallace DC, Spiegelman BM, Kirichok Y. 2019. H<sup>+</sup> transport is an integral function of the mitochondrial ADP/ATP carrier. *Nature* **571**:515–520. doi:10.1038/s41586-019-1400-3
- Calvo SE, Clauser KR, Mootha VK. 2016. MitoCarta2.0: an updated inventory of mammalian mitochondrial proteins. *Nucleic Acids Res* **44**:D1251-7. doi:10.1093/nar/gkv1003
- Che R, Yuan Y, Huang S, Zhang A. 2014. Mitochondrial dysfunction in the pathophysiology of renal diseases. *Am J Physiol - Ren Physiol*. doi:10.1152/ajprenal.00571.2013
- Clarke KJ, Porter RK. 2018. The importance of calcium ions for determining mitochondrial glycerol-3-phosphate dehydrogenase activity when measuring uncoupling protein 1 (UCP1) function in mitochondria isolated from brown adipose tissue *Methods in Molecular Biology*. doi:10.1007/978-1-4939-7831-1\_19
- Deutsch EW, Csordas A, Sun Z, Jarnuczak A, Perez-Riverol Y, Ternent T, Campbell DS, Bernal-Llinares M, Okuda S, Kawano S, Moritz RL, Carver JJ, Wang M, Ishihama Y, Bandeira N, Hermjakob H, Vizcaíno JA. 2017. The ProteomeXchange consortium in 2017: supporting the cultural change in proteomics public data deposition. *Nucleic Acids Res* **45**:D1100–D1106. doi:10.1093/nar/gkw936
- Diaz-Vegas A, Sanchez-Aguilera P, Krycer JR, Morales PE, Monsalves-Alvarez M, Cifuentes M, Rothermel BA, Lavandero S. 2020. Is Mitochondrial Dysfunction a Common Root of Noncommunicable Chronic Diseases? *Endocr Rev*. doi:10.1210/endrev/bnaa005
- Divakaruni AS, Humphrey DM, Brand MD. 2012. Fatty acids change the conformation of uncoupling protein 1 (UCP1). *J Biol Chem*. doi:10.1074/jbc.M112.381780

- Fisher-Wellman KH, Davidson MT, Narowski TM, Lin C-T Te, Koves TR, Muoio DM. 2018. Mitochondrial Diagnostics: A multiplexed assay platform for comprehensive assessment of mitochondrial energy fluxes. *Cell Rep Sep* **25**;24:3593-3606.e10. doi:10.1016/j.celrep.2018.08.091
- Fisher-Wellman KH, Neuffer PD. 2012. Linking mitochondrial bioenergetics to insulin resistance via redox biology. *Trends Endocrinol Metab* **23**. doi:10.1016/j.tem.2011.12.008
- Forbes JM, Thorburn DR. 2018. Mitochondrial dysfunction in diabetic kidney disease. *Nat Rev Nephrol*. doi:10.1038/nrneph.2018.9
- Forner F, Foster LJ, Campanaro S, Valle G, Mann M. 2006. Quantitative proteomic comparison of rat mitochondria from muscle, heart, and liver. *Mol Cell Proteomics*. doi:10.1074/mcp.M500298-MCP200
- Frezza C, Cipolat S, Scorrano L. 2007. Organelle isolation: Functional mitochondria from mouse liver, muscle and cultured fibroblasts. *Nat Protoc* **2**:287–295. doi:10.1038/nprot.2006.478
- Gaude E, Frezza C. 2014. Defects in mitochondrial metabolism and cancer. *Cancer Metab* **2**:1–9. doi:10.1186/2049-3002-2-10
- Glancy B, Balaban RS. 2011. Protein composition and function of red and white skeletal muscle mitochondria. *Am J Physiol Cell Physiol*. doi:10.1152/ajpcell.00496.2010
- Glancy B, Willis WT, Chess DJ, Balaban RS. 2013. Effect of calcium on the oxidative phosphorylation cascade in skeletal muscle mitochondria. *Biochemistry* **52**:2793–2809. doi:10.1021/bi3015983
- Goldberg EJEJ, Buddo KAKA, McLaughlin KL, Fernandez RFRF, Pereyra ASAS, Psaltis CECE, Lin C-TC Te, Hagen JTJT, Boykov ININ, Nguyen TKTK, Gowdy KM, Ellis JMJM, Neuffer PDD, McClung JMJM, Fisher-Wellman KHKH. 2019. Tissue-specific

- characterization of mitochondrial branched-chain keto acid oxidation using a multiplexed assay platform. *Biochem J* **476**. doi:10.1042/BCJ20190182
- Groennebaek T, Nielsen J, Jespersen NR, Bøtker HE, de Paoli F V., Miller BF, Vissing K. 2020. Utilization of biomarkers as predictors of skeletal muscle mitochondrial content after physiological intervention and in clinical settings. *Am J Physiol Endocrinol Metab*. doi:10.1152/ajpendo.00101.2020
- Harms M, Seale P. 2013. Brown and beige fat: Development, function and therapeutic potential. *Nat Med*. doi:10.1038/nm.3361
- Hempel M, Kremer LS, Tsiakas K, Alhaddad B, Haack TB, Löbel U, Feichtinger RG, Sperl W, Prokisch H, Mayr JA, Santer R. 2017. LYRM7 - associated complex III deficiency: A clinical, molecular genetic, MR tomographic, and biochemical study. *Mitochondrion*. doi:10.1016/j.mito.2017.07.001
- Inoue M, Uchino S, Iida A, Noguchi S, Hayashi S, Takahashi T, Fujii K, Komaki H, Takeshita E, Nonaka I, Okada Y, Yoshizawa T, Van Lommel L, Schuit F, Goto Y ichi, Mimaki M, Nishino I. 2019. COX6A2 variants cause a muscle-specific cytochrome c oxidase deficiency. *Ann Neurol*. doi:10.1002/ana.25517
- Iuso A, Repp B, Biagosch C, Terrile C, Prokisch H. 2017. Assessing mitochondrial bioenergetics in isolated mitochondria from various mouse tissues using Seahorse XF96 analyzer Methods in Molecular Biology. doi:10.1007/978-1-4939-6824-4\_13
- Johnson DT, Harris RA, Blair P V, Balaban RS. 2007. Functional consequences of mitochondrial proteome heterogeneity. *Am J Physiol Cell Physiol* **292**:698–707. doi:10.1152/ajpcell.00109.2006.—Potential
- Kappler L, Li J, Häring HU, Weigert C, Lehmann R, Xu G, Hoene M. 2016. Purity matters: A

- workflow for the valid high-resolution lipid profiling of mitochondria from cell culture samples. *Sci Rep*. doi:10.1038/srep21107
- Kasen S, Ouellette R, Cohen P. 1990. Mainstreaming and postsecondary educational and employment status of a rubella cohort. *Am Ann Deaf* **135**:22–6. doi:10.1353/aad.2012.0408
- Lark DS, Torres MJ, Lin C-T Te, Ryan TE, Anderson EJ, Neuffer PD. 2016. Direct real-time quantification of mitochondrial oxidative phosphorylation efficiency in permeabilized skeletal muscle myofibers. *Am J Physiol - Cell Physiol*. doi:10.1152/ajpcell.00124.2016
- Larsen S, Nielsen J, Hansen CN, Nielsen LB, Wibrand F, Stride N, Schroder HD, Boushel R, Helge JW, Dela F, Hey-Mogensen M. 2012. Biomarkers of mitochondrial content in skeletal muscle of healthy young human subjects. *J Physiol* **590**:3349–3360. doi:10.1113/jphysiol.2012.230185
- Lesack K, Naugler C. 2011. An open-source software program for performing Bonferroni and related corrections for multiple comparisons. *J Pathol Inform* **2**:52. doi:10.4103/2153-3539.91130
- Lidell ME, Betz MJ, Enerbäck S. 2014. Brown adipose tissue and its therapeutic potential. *J Intern Med*. doi:10.1111/joim.12255
- Mailloux RJ, Seifert EL, Bouillaud F, Aguer C, Collins S, Harper ME. 2011. Glutathionylation acts as a control switch for uncoupling proteins UCP2 and UCP3. *J Biol Chem* **286**:21865–21875. doi:10.1074/jbc.M111.240242
- McLaughlin KL, Kew KA, McClung JM, Fisher-Wellman KH. 2020. Subcellular proteomics combined with bioenergetic phenotyping reveals protein biomarkers of respiratory insufficiency in the setting of proofreading-deficient mitochondrial polymerase. *Sci Rep* **10**:3603. doi:10.1038/s41598-020-60536-y

- McLaughlin KL, McClung JM, Fisher-Wellman KH. 2018. Bioenergetic consequences of compromised mitochondrial DNA repair in the mouse heart. *Biochem Biophys Res Commun* **504**:742–748. doi:10.1016/j.bbrc.2018.09.022
- Messer JJ, Jackman MR, Willis WT. 2004. Pyruvate and citric acid cycle carbon requirements in isolated skeletal muscle mitochondria. *Am J Physiol Cell Physiol* **286**:C565-572. doi:10.1152/ajpcell.00146.2003
- Mráček T, Drahotka Z, Houštěk J. 2013. The function and the role of the mitochondrial glycerol-3-phosphate dehydrogenase in mammalian tissues. *Biochim Biophys Acta - Bioenerg.* doi:10.1016/j.bbabi.2012.11.014
- Okuda S, Watanabe Y, Moriya Y, Kawano S, Yamamoto T, Matsumoto M, Takami T, Kobayashi D, Araki N, Yoshizawa AC, Tabata T, Sugiyama N, Goto S, Ishihama Y. 2017. jPOSTrepo: an international standard data repository for proteomes. *Nucleic Acids Res* **45**:D1107–D1111. doi:10.1093/nar/gkw1080
- Palmieri F, Monné M. 2016. Discoveries, metabolic roles and diseases of mitochondrial carriers: A review. *Biochim Biophys Acta - Mol Cell Res.* doi:10.1016/j.bbamcr.2016.03.007
- Ruprecht JJ, Kunji ERS. 2020. The SLC25 Mitochondrial Carrier Family: Structure and Mechanism. *Trends Biochem Sci.* doi:10.1016/j.tibs.2019.11.001
- Thor Johnson D, Harris RA, French S, Blair P V, You J, Bemis KG, Wang M, Balaban RS. 2007. Tissue heterogeneity of the mammalian mitochondrial proteome. *Am J Physiol Cell Physiol* **292**:689–697. doi:10.1152/ajpcell.00108.2006.—The
- Toime LJ, Brand MD. 2010. Uncoupling protein-3 lowers reactive oxygen species production in isolated mitochondria. *Free Radic Biol Med* **49**:606–611. doi:10.1016/j.freeradbiomed.2010.05.010

- van der Walt G, Louw R. 2020. Novel mitochondrial and cytosolic purification pipeline for compartment-specific metabolomics in mammalian disease model tissues. *Metabolomics*. doi:10.1007/s11306-020-01697-9
- Walheim E, Wiśniewski JR, Jastroch M. 2018. Respiromics – An integrative analysis linking mitochondrial bioenergetics to molecular signatures. *Mol Metab*. doi:10.1016/j.molmet.2018.01.002
- Watt IN, Montgomery MG, Runswick MJ, Leslie AGW, Walker JE. 2010. Bioenergetic cost of making an adenosine triphosphate molecule in animal mitochondria. *Proc Natl Acad Sci U S A*. doi:10.1073/pnas.1011099107

### **CHAPTER 3: CHARACTERIZATION OF THE MITOCHONDRIAL PHENOTYPE OF ACUTE MYELOID LEUKEMIA**

The previous chapter established methods for mitochondrial assessment that will be used throughout aims 1 and 2 of this dissertation to evaluate the intrinsic mitochondrial properties of acute myeloid leukemia, hepatocellular carcinoma, and their respective healthy tissues of origin. These methods were capable of identifying unique mitochondrial signatures within each tissue that aligned with their physiological role in the body, suggesting that mitochondria are not equivalent from tissue to tissue. The next chapter describes the application of these methods to several models of acute myeloid leukemia. The evidence presented herein primarily supports a model in which respiration in leukemic mitochondria tends to be inhibited by the presence of ATP free energy. Further, leukemic mitochondria appear poised to primarily consume ATP rather than generate it under *in vitro* conditions that simulate physiological ATP demand states. When ATP import was disrupted through the use of inhibitors, proliferation of leukemic blasts was reduced, suggesting that this mitochondrial rewiring is important to the leukemic phenotype.

**Intrinsic OXPHOS limitations underlie cellular bioenergetics in leukemia. (Nelson et al., 2021).**

Margaret A.M. Nelson<sup>1,6,#</sup>, Kelsey L. McLaughlin<sup>1,6,#</sup>, James T. Hagen<sup>1,6</sup>, Hannah S. Coalson<sup>1,6</sup>, Cameron Schmidt<sup>1,6</sup>, Miki Kassai<sup>2,6</sup>, Kimberly A. Kew<sup>2</sup>, Joseph M. McClung<sup>1,3,6</sup>, P. Darrell Neuffer<sup>6</sup>, Patricia Brophy<sup>6</sup>, Nasreen A. Vohra<sup>4</sup>, Darla Liles<sup>5</sup>, Myles C. Cabot<sup>2,6</sup>, and Kelsey H. Fisher-Wellman<sup>1,6\*</sup>

<sup>1</sup>Department of Physiology, <sup>2</sup>Department of Biochemistry and Molecular Biology, <sup>3</sup>Department of Cardiovascular Sciences, <sup>4</sup>Department of Surgery, <sup>5</sup>Department of Internal Medicine. Brody School of Medicine, East Carolina University, Greenville, NC

<sup>6</sup>East Carolina Diabetes and Obesity Institute, East Carolina University, Greenville, NC

<sup>#</sup>Authors contributed equally to this work.

\* To whom correspondence should be addressed:

Kelsey H. Fisher-Wellman [fisherwellmank17@ecu.edu](mailto:fisherwellmank17@ecu.edu)

East Carolina Diabetes and Obesity Institute, 115 Heart Drive, Greenville, NC 27834 USA

Telephone: 252-744-2585

Fax: 252-744-0462

## Abstract

Typified by oxidative phosphorylation (OXPHOS), mitochondria catalyze a wide variety of cellular processes seemingly critical for malignant growth. As such, there is considerable interest in targeting mitochondrial metabolism in cancer. However, notwithstanding the few drugs targeting mutant dehydrogenase activity, nearly all hopeful ‘mito-therapeutics’ cannot discriminate cancerous from non-cancerous OXPHOS and thus suffer from a limited therapeutic index. The present project was based on the premise that the development of efficacious mitochondrial-targeted anti-cancer compounds requires answering two fundamental questions: 1) is mitochondrial bioenergetics in fact different between cancer and non-cancer cells? and 2) If so, what are the underlying mechanisms? Such information is particularly critical for the subset of human cancers, including acute myeloid leukemia (AML), in which alterations in mitochondrial metabolism are implicated in various aspects of cancer biology (e.g., clonal expansion and chemoresistance). Herein, we leveraged an in-house diagnostic biochemical workflow to comprehensively evaluate mitochondrial bioenergetic efficiency and capacity in various hematological cell types, with a specific focus on OXPHOS dynamics in AML. Consistent with prior reports, clonal cell expansion, characteristic of leukemia, was universally associated with a hyper-metabolic phenotype which included increases in basal and maximal glycolytic and respiratory flux. However, despite having nearly 2-fold more mitochondria per cell, clonally expanding hematopoietic stem cells, leukemic blasts, as well as chemoresistant AML were all consistently hallmarked by intrinsic limitations in oxidative ATP synthesis (i.e., OXPHOS). Remarkably, by performing experiments across a physiological span of ATP free energy (i.e.,  $\Delta G_{ATP}$ ), we provide direct evidence that, rather than contributing to cellular  $\Delta G_{ATP}$ , leukemic mitochondria are particularly poised to consume ATP. Relevant to AML biology, acute restoration

of OXPHOS kinetics proved highly cytotoxic to leukemic blasts, suggesting that active OXPHOS repression supports aggressive disease dissemination in AML. Taken together, these findings argue against ATP being the primary output of mitochondria in leukemia and provide proof-of-principle that restoring, rather than disrupting, OXPHOS and/or cellular  $\Delta G_{ATP}$  in cancer may represent an untapped therapeutic avenue for combatting hematological malignancy and chemoresistance.

## **Introduction**

In comparison to normal hematopoietic cells, various human leukemias present with increases in mitochondrial mass and higher basal respiration rates (Farge et al., 2017; Goto et al., 2014b, 2014a; Sriskanthadevan et al., 2015; Sukanuma et al., 2010), the latter of which appears to sensitize them to global disruptions in mitochondrial flux (Kuntz et al., 2017; Lagadinou et al., 2013; Lee et al., 2015; Mirali et al., 2020; Škrtić et al., 2011; Xiang et al., 2015). Although these studies have ignited interest in mitochondrial-targeted chemotherapeutics (Guièze et al., 2019; Panina et al., 2020), experimental rationale for targeting OXPHOS in leukemia is largely based on the assumption that heightened respiration is representative of the cancerous mitochondrial network's attempt to accommodate an increased ATP demand (i.e., increased 'OXPHOS reliance'). However, identical increases in mitochondrial respiration can derive from any number of physiological stimuli, ranging from increased demand for ATP resynthesis to decreased OXPHOS efficiency. Distinguishing between these potential outcomes is critical, as such insight likely demarcates targeted drug efficacy from undesirable systemic toxicity. For example, it is currently unclear how targeting increased 'OXPHOS reliance' in leukemia can specifically disrupt

leukemic oxidative metabolism without impacting OXPHOS in other highly metabolic organs (e.g., brain, heart, muscle).

Given the ubiquitous necessity of OXPHOS for healthy cellular metabolism, a major barrier to mitochondrial-targeted drugs in leukemia relates to the need for cancer-cell selectivity (Cohen, 2010; Dykens and Will, 2007). The current project was based on the premise that establishing cause and effect between mitochondrial bioenergetics and cancer is one of the keys to developing targeted and more effective therapies. As a first step, this will undoubtedly require advanced technical approaches capable of quantifying the interplay among the major mitochondrial thermodynamic free energy driving forces to distinguish between changes in bioenergetic demand versus efficiency. To this end, our group recently developed a diagnostic biochemical workflow that quantifies the changes in free energy driving forces over the entire range of respiratory demand, thus providing a comprehensive profile of mitochondrial bioenergetic efficiency and capacity, relative to the underlying proteome (Fisher-Wellman et al., 2019, 2018; McLaughlin et al., 2018).

Herein, we leveraged our mitochondrial diagnostics workflow across several hematological cell types, including AML cell lines, primary human leukemias, and AML cells made refractory to the chemotherapeutic venetoclax. Clonal cell expansion in leukemia, including chemoresistant AML, was universally associated with two primary phenotypes; 1) higher basal respiration driven by increased cellular mitochondrial content, and 2) intrinsic OXPHOS repression. Parallel assessment of the underlying mitochondrial proteome linked this unique ability to bolster cellular mitochondrial content while simultaneously constraining oxidative ATP synthesis to shifts in adenine nucleotide translocase (ANT) isoform expression. Specifically, decreased ANT1 and increased ANT2/ANT3 appears to prime leukemic mitochondria for ATP

uptake, rather than export, that, in turn directly inhibits the ability of mitochondrial OXPHOS to contribute to the cellular ATP free energy ( $\Delta G_{\text{ATP}}$ ). These findings are consistent with recent evidence demonstrating that mitochondrial OXPHOS is dispensable for tumor growth (Martínez-Reyes et al., 2020), and raise the intriguing possibility that the requirement for mitochondria in leukemia may have little to do with oxidative ATP production but instead reflect a requirement for unimpeded mitochondrial flux to support other aspects of anabolic growth (e.g.,  $\text{NAD}^+$  regeneration (Luengo et al., 2020), nucleotide synthesis (Martínez-Reyes et al., 2020)). Critically however, accommodating such a flux demand, at least in leukemia, appears to require intrinsic mitochondrial remodeling that allows for forward electron transport/oxygen consumption to occur alongside ATP consumption. Given that acute restoration of OXPHOS kinetics in AML proved highly cytotoxic to leukemic blasts, the present findings provide proof-of-principle that interventions designed to restore, rather than disrupt, OXPHOS may impart therapeutic efficacy across various hematological malignancies.

## **Results**

### ***Mitochondrial bioenergetic profiling of acute leukemia reveals respiratory flux limitations.***

To begin to characterize the mitochondrial network in leukemia, we selected three commercially available acute leukemia cell lines – HL-60, KG-1, MV-4-11 – and comprehensively evaluated their bioenergetic profiles. These cells arise from unique precursors along the hematopoietic lineage, express a diverse array of cell surface markers, and have distinct underlying genetics (Inoue et al., 2014; Mrózek et al., 2003; Rucker et al., 2006). Results were compared to peripheral blood mononuclear cells (PBMC) isolated from healthy volunteers. The decision to use PBMC as a control was based on the assumption that comprehensive bioenergetic phenotyping of

non-proliferative PBMC compared to various AML cell lines would provide sufficient experimental design contrast to reveal fundamental mitochondrial bioenergetic phenotypes potentially required for clonal cell expansion.

Using intact PBMC and leukemia cell lines, respiratory flux ( $JO_2$ ) was assessed under basal conditions, as well as in response to ATP synthase inhibition (oligomycin), and FCCP titration (i.e., mitochondrial uncoupler). All experiments were performed in bicarbonate free IMDM growth media, supplemented with 10% FBS. Following FCCP titration, respiration was inhibited with a combination of rotenone (inhibits complex I) and antimycin A (inhibits complex III). Consistent with prior work in human leukemia (Jitschin et al., 2014; Sriskanthadevan et al., 2015), basal respiration normalized to cell count was elevated above PBMC across all leukemia lines and maximal respiratory flux was higher in KG-1 and MV-4-11 (**Figure 1A**). When normalized to basal respiration, oligomycin similarly inhibited respiration across groups and the fold change induced by FCCP was consistently blunted in leukemia (**Figure 1B**).

Given the large differences in cell size between PBMC and leukemia (**Supplementary Figure 1A**), we reasoned that normalization to total protein would likely provide the most accurate index of absolute respiratory kinetics across groups. Interestingly, upon normalization to total protein, although basal respiration remained higher in KG-1 and MV-4-11, differences in maximal respiratory flux were eliminated, particularly at higher FCCP concentrations (**Figure 1C**). In fact, maximal FCCP-supported  $JO_2$  was nearly two-fold lower in HL-60 compared to PBMC when normalized to total protein (**Figure 1C**). Relative to PBMC, maximal respiration induced by FCCP occurred at much lower concentrations in leukemia (i.e., lower  $K_m$ ; **Figure 1D**), with increasing FCCP concentrations leading to an overt bioenergetic collapse (i.e., diminishing respiration rates; **Figure 1C**; compare  $JO_2$  at FC [2.0 $\mu$ M] vs FC [5.0 $\mu$ M]). Similar findings were observed using

the mitochondrial uncoupler BAM15 (**Supplementary Figure 1B-C**). Measurements of extracellular acidification (ECAR), an indirect readout of glycolytic flux, revealed higher extracellular acidification and a rightward shift in ECAR relative to oxygen consumption rate (OCR) in AML cell lines, consistent with prior reports detailing a hyper-metabolic phenotype in leukemia (**Supplementary Figure 1E-F**) (Suganuma et al., 2010).

To determine if flux differences in leukemia could be explained by differences in mitochondrial content, nuclear and mitochondrial volumes were assessed independently by tetramethylrhodamine methyl ester (TMRM) or MitoTracker fluorescence and confocal microscopy (**Figure 1E-I, Supplementary Figure 1D**). Absolute nuclear and mitochondrial volumes were higher in all leukemia lines (**Figure 1E-H**), consistent with leukemia's larger cell size (**Supplementary Figure 1A**). However, when normalized to nuclear volume, mitochondrial content was elevated above PBMC only in HL-60 and MV-4-11 (**Figure 1I**). Interestingly, across all cell types, considerable discrepancies were apparent when protein-normalized maximal respiratory flux (**Figure 1C**) was compared to mitochondrial content (**Figure 1I**). This was particularly evident in HL-60 cells where mean maximal respiration, relative to the size of the underlying mitochondrial network, was ~5-fold lower compared to PBMC (**Figure 1J**). Together, these data suggested that at least a portion of the expansive mitochondrial network in AML may be biochemically constrained and thus unable to contribute to oxidative metabolism under basal conditions.

#### ***Intrinsic limitations to OXPHOS characterize the mitochondrial network in leukemia cell lines.***

To directly test OXPHOS kinetics in leukemia, two complementary assays were designed. Both assays used digitonin-permeabilized cells energized with identical carbon substrates, and

respiratory flux was stimulated with either FCCP or ATP free energy. In the first assay, the maximal capacity of the electron transport system (ETS) was assessed by energizing permeabilized cells with saturating carbon substrates (P/M/G/S/O) and titrating in FCCP (**Figure 2A-B**). The use of multiple substrates was intended to saturate carbon substrate availability such that maximal ETS flux could be quantified. Using this approach, absolute respiration in substrate-replete permeabilized cells was comparable to that observed using intact cells treated with FCCP (**Figure 2C**), confirming maximal ETS flux in the permeabilized system. Note, maximum FCCP-supported flux under these conditions is indicated throughout as  $JH^+_{\text{Total}}$  (**Figure 2A**). Relative to PBMC,  $JH^+_{\text{Total}}$  was lower in HL-60, unchanged in KG-1, and higher in MV-4-11 (**Figure 2B**).

In mammalian cells, the vast majority of the adenylate pool is represented by ATP (i.e.,  $\Delta G_{\text{ATP}}$ ), with typical values for ATP free energy ranging from -56 to -64 kJ/mol (Luptak et al., 2018; Roth and Weiner, 1991; Veech et al., 2002). Thus, to evaluate OXPHOS kinetic efficiency in leukemia across a physiological range of ATP resynthesis demands, we utilized the creatine kinase (CK) energetic clamp (Fisher-Wellman et al., 2018; Glancy et al., 2013; Messer et al., 2004). This technique leverages the enzymatic activity of CK, which couples the interconversion of ATP and ADP to that of phosphocreatine (PCR) and free creatine (CR) such that extramitochondrial ATP free energy (i.e.,  $\Delta G_{\text{ATP}}$ ) can be empirically titrated using PCR. Using this approach, permeabilized cells were energized with the same carbon substrate mix used for the ETS capacity assay and respiration was stimulated at minimal ATP free energy. Note,  $\Delta G_{\text{ATP}}$  equal to -54.16 kJ/mol reflects an ATP/ADP ratio *in vivo* that would be expected to induce ‘maximal’ OXPHOS flux and is thus referred to throughout as ‘ $JH^+_{\text{OXPHOS}}$ ’ (**Figure 2D**). Cytochrome C (Cyt C) was added to assess the integrity of the mitochondrial outer-membrane, and  $\Delta G_{\text{ATP}}$  was then titrated via sequential additions of PCR. With respect to the ETS capacity assay, respiration

stimulated by  $\Delta G_{\text{ATP}}$  partially normalized  $J_{\text{O}_2}$  between MV-4-11 and PBMC and revealed decreased respiratory kinetics in both HL-60 and KG-1 (**Figure 2E**).

In both assays, the utilization of identical substrates ('P/M/G/S/O') allowed us to directly quantitate absolute OXPHOS kinetics (' $J_{\text{H}^+_{\text{OXPHOS}}}$ '), relative to the maximal capacity of the electron transport system, (' $J_{\text{H}^+_{\text{Total}}}$ '). Together,  $J_{\text{H}^+_{\text{OXPHOS}}}$  and  $J_{\text{H}^+_{\text{Total}}}$  provide a quantitative index of fractional OXPHOS capacity as the ratio of the two reflects the proportion of the entire respiratory system that can be used for OXPHOS (**Figure 2F**). A ratio of '1' reflects maximal OXPHOS reliance, whereas a ratio of '0' indicates that the mitochondrial proton current cannot be utilized for ATP synthesis. Strikingly, calculated fractional OXPHOS in leukemic mitochondria was consistently decreased compared to PBMC, corresponding to a factor of  $\sim 0.5$  (**Figure 2G**), indicating that only half of the available ETS capacity in leukemia can be dedicated to OXPHOS under physiological ATP free energy constraints. Given that the OXPHOS network is responsible for driving ATP/ADP disequilibrium to establish cellular  $\Delta G_{\text{ATP}}$ , low fractional OXPHOS was interpreted to reflect reduced bioenergetic efficiency in leukemia. Moreover, such findings indicate that traditional measurements of 'OXPHOS' capacity using intact cells (e.g., extracellular flux analysis) woefully underestimate true OXPHOS kinetics.

To differentiate between bioenergetic signatures inherent to proliferating cells and those which are unique to leukemia, experiments were repeated in mononuclear cells isolated from bone marrow aspirates collected from healthy volunteers. In these experiments, fractional OXPHOS in healthy bone marrow cells was comparable to PBMC and once again elevated above all leukemia cell lines (**Figure 2G**; ' $\text{BM}_{\text{Healthy}}$ ', **Supplementary Figure 2A-B**). As an additional control, identical experiments were carried out in primary human muscle precursor cells (human myoblasts – ' $\text{HMB}$ ' **Supplementary Figure 2C-D**). These cells were cultured from muscle biopsies

uniformly collected from the gastrocnemius muscle (10 cm distal to the tibial tuberosity) of healthy human subjects and were intended to serve as a non-cancerous, proliferative human progenitor control. Importantly, fractional OXPHOS was elevated above leukemia in human muscle progenitor cells (**Figure 2G: 'HMB'**), indicating that decreased bioenergetic efficiency is not an absolute requirement of cellular proliferation, but rather a unique bioenergetic feature of leukemic mitochondria.

***Exposure to physiological  $\Delta G_{ATP}$  reveals direct inhibition of ETS flux by ATP in leukemic mitochondria.***

To gain insight into the mechanism of OXPHOS limitations in leukemia, at the end of the  $\Delta G_{ATP}$  titration, oligomycin was added to inhibit ATP synthesis and maximal uncoupled respiration was stimulated with FCCP titration. Maximal FCCP-supported flux under these conditions is denoted as ' $FCCP_{\Delta G_{ATP}}$ ' (**Figure 2D**). In the intact cell assay (**Figure 1C**), increased glycolytic flux is presumed to maintain cellular  $\Delta G_{ATP}$  during FCCP titration. Thus, the continued presence of extra-mitochondrial  $\Delta G_{ATP}$  in our permeabilized cell system was intended to model the adenylate constraints present in intact cells. By comparing maximal OXPHOS flux (' $JH^+_{OXPHOS}$ ') to maximum FCCP-stimulated respiration in the presence of  $\Delta G_{ATP}$  (' $FCCP_{\Delta G_{ATP}}$ '), it becomes possible to quantitate any flux limitations imposed by physiological ATP/ADP. Importantly, ATP synthase is not functional during the assay, thus any flux limitations imposed by  $\Delta G_{ATP}$  would be interpreted to reflect direct ETS regulation (e.g., allostery). In PBMC and human muscle progenitor cells, the addition of FCCP at the end of the  $\Delta G_{ATP}$  titration restored respiration to levels obtained under low (-54.16 kJ/mol) ATP free energy (**Supplementary Figure 2D-E**), indicating minimal ETS flux inhibition by  $\Delta G_{ATP}$ . Surprisingly, relative to  $JH^+_{OXPHOS}$ ,

FCCP-stimulated respiration was substantially blunted in the presence of high ATP free energy across all three leukemia cell lines (**Figure 2E**), as well as healthy bone marrow cells (**Supplementary Figure 2C**), resulting in a near 2-fold difference in the  $\text{FCCP}_{\Delta\text{G}_{\text{ATP}}}/\text{JH}^{\text{+OXPHOS}}$  ratio, termed ‘FCCP Effect’ throughout (**Figure 2H**). Importantly, in the absence of ATP, the addition of CK and PCR up to 21mM did not impact FCCP-supported flux in permeabilized MV-4-11 cells (**Supplementary Figure 2E**). To determine the sensitivity of ETS inhibition by  $\Delta\text{G}_{\text{ATP}}$ , FCCP-supported flux in MV-4-11 cells was assessed at defined ATP free energies. In these experiments, extramitochondrial  $\Delta\text{G}_{\text{ATP}}$  was administered after CV inhibition with oligomycin, followed by FCCP titration. Results revealed a dose-dependent decrease in uncoupled respiration in response to increasing  $\Delta\text{G}_{\text{ATP}}$  (**Figure 2I**), confirming that ATP free energy is both necessary and sufficient to induce direct ETS flux inhibition in leukemia.

Inhibition of respiratory flux mediated by  $\Delta\text{G}_{\text{ATP}}$  could reflect a number of potential mechanisms ranging from cytoskeletal alterations, direct inhibition of the matrix dehydrogenase network (e.g., inhibitory phosphorylation of pyruvate dehydrogenase), and/or ETS inhibition (Fisher-Wellman et al., 2018). To differentiate between these potential outcomes, mitochondria were isolated from PBMC and each of the three leukemia cell lines and similarly assessed for OXPHOS kinetics. In mitochondria energized with saturating carbon, increasing  $\Delta\text{G}_{\text{ATP}}$  led to a more pronounced decrease in respiration in mitochondria of all three leukemia cell lines (**Figure 3A**). The ability of FCCP to restore maximal respiratory flux was also once again blunted in leukemic mitochondria (**Figure 3A-B**), consistent with lower fractional OXPHOS (**Figure 2G**). Evidence of ATP-dependent inhibition of ETS flux using both isolated mitochondria and permeabilized cells was used as criteria to rule out any involvement of the cytoskeleton. To differentiate between respiratory flux inhibition localized to the matrix dehydrogenases or the ETS,

NADH/NAD<sup>+</sup> redox poise was measured in substrate-replete isolated mitochondria exposed to an identical  $\Delta G_{ATP}$  span. Results are depicted as a percentage of complete reduction, where 0% reduction reflects isolated mitochondria at 37°C without added substrates and 100% reduction is recorded at the end of the assay with the addition of the CIV inhibitor cyanide. Except for a slight hyper-reduction in HL-60 mitochondria, NADH/NAD<sup>+</sup> redox was similar across groups (**Figure 3C**), indicating that ATP-mediated respiratory flux inhibition in leukemia is not due to a generalized impairment in carbon substrate uptake and/or dehydrogenase flux. Having eliminated the cytoskeleton and the dehydrogenase network as potential sites of inhibition, we next turned our attention to the ETS. To determine if flux inhibition induced by  $\Delta G_{ATP}$  was specific to a given respiratory complex, OXPHOS kinetics were assessed in isolated mitochondria energized with either complex I (CI)- or CII-linked substrate combinations. Note, the presence of saturating malate in the CI substrate mix results in CII inhibition via malate-fumarate equilibration (**Figure 3D**). Likewise, the addition of rotenone in the presence of succinate eliminates residual CI-supported flux by downstream products of succinate oxidation (**Figure 3D**). Using either CI- or CII-linked substrates, we once again observed a more pronounced decrease in respiration in response to  $\Delta G_{ATP}$  titration in leukemic mitochondria, as well as a relative inability of FCCP to restore maximal respiratory flux (**Figure 3E-H**). Taken together these findings demonstrate that leukemic mitochondria are characterized by a unique form of OXPHOS regulation involving ETS inhibition by ATP free energy.

***Subcellular proteomics reveals unique isoform expression of the adenine nucleotide translocase (ANT) in leukemia.***

To identify potential protein mediators responsible for OXPHOS insufficiency in leukemia, we conducted a proteomics screen using TMT-labeled peptides prepared from the same isolated mitochondria samples used for functional characterization. To control for group differences in percent mitochondrial enrichment, nLC-MS/MS raw data were searched using the MitoCarta 2.0 database, as previously described (McLaughlin et al., 2020). Using this approach, total mitochondrial protein abundance was similar between groups, thus allowing for intrinsic mitochondrial signatures to be identified across leukemia. In total, 135 differentially expressed mitochondrial proteins (adjusted P value < 0.01) were identified comparing PBMC to each of the three leukemia lines (**Figure 4A**). With respect to the shared differentially expressed proteins, several of these proteins have previously been implicated in cancer biology, such as decreased MAOB (Ryu et al., 2018) and HK1 (Rai et al., 2019), and increased MTHFD1L (Lee et al., 2017), and COX17 (Singh et al., 2020) (**Figure 4A**).

Focusing on the OXPHOS proteome, we assessed the abundance of the individual protein subunits that comprise CI, CII, CIII, and CIV, as well as the protein components of the phosphorylation system which include ATP synthase (CV), the phosphate carrier (SLC25A3), and ANT (**Figure 4B**). Although considerable heterogeneity was present across groups, comparing protein expression profiles of the individual subunits that comprise CI-CV and SLC25A3 (**Supplementary Figure 3A-D**) revealed that only 6 of the 110 subunits were similarly altered in leukemia. With the exception of COX6A1, all protein subunits were involved in the assembly of CI (NDUFB10), CIV (COA4, COA7, COX17) or CV (ATPAF2). In stark contrast, the expression profiles of the three main ANT isoforms were entirely distinct between PBMC and leukemia mitochondria, highlighted by reduced ANT1 (SLC25A4) and increased ANT2 (SLC25A5) and ANT3 (SLC25A6) in leukemia (**Figure 4D**).

***Inhibition of ETS flux by  $\Delta G_{ATP}$  is a result of matrix ATP consumption in leukemia.***

Given that ATP free energy was required to induce ETS flux inhibition, we hypothesized that this effect may be mediated by ATP transport into the matrix, facilitated by dominant ANT2/3 expression in leukemia (Chevrollier et al., 2011). To test this hypothesis, FCCP-supported respiration was assessed in permeabilized MV-4-11 and HL-60 cells exposed to  $\Delta G_{ATP}$  of -61.49 kJ/mol in the absence and presence of the ANT inhibitor carboxyatractyloside (CAT) (Maldonado et al., 2016). Consistent with our prior findings, the addition of FCCP in the presence of  $\Delta G_{ATP}$  was incapable of restoring flux to levels obtained with minimal ATP free energy in leukemia (**Figure 5A-B**; ' $\Delta G_{ATP}$  (-61.49 kJ/mol)'). However, relative to no adenylates, as well as minimal  $\Delta G_{ATP}$  (e.g., - 54.16 kJ/mol), the addition of CAT restored maximal FCCP-supported ETS flux in the presence of maximal ATP free energy (**Figure 5A-C**). Similar experiments performed in MV-4-11 isolated mitochondria (**Figure 5D**), as well as with the ANT inhibitor bongkreikic acid (**Supplementary Figure 4A**) revealed nearly identical results, indicating that ETS flux inhibition by  $\Delta G_{ATP}$  requires matrix ATP uptake via ANT.

As a component of OXPHOS, ANT functions to exchange matrix ATP for cytosolic ADP in a process that consumes (i.e., depolarizes) the electrochemical proton gradient across the inner membrane. It is critical to point out that the directionality of transport by ANT is dependent on inner membrane polarization. Based on this, if indeed ANT2/3 were favoring matrix ATP uptake in leukemia then chemical inhibition of the phosphorylation system should depolarize, rather than hyperpolarize, membrane potential in leukemic isolated mitochondria. To test this, we quantified mitochondrial membrane potential in substrate-replete isolated mitochondria from HL-60 and KG-1, as well as PBMC, across a  $\Delta G_{ATP}$  span and then assessed the impact of ANT inhibition with

CAT or CV inhibition with oligomycin. Contrary to that seen in PBMC (**Figure 5E**), the addition of CAT or oligomycin caused a near complete elimination of mitochondrial membrane potential in HL-60 and KG-1 (**Supplementary Figure 4B**), indicative of matrix ATP uptake/consumption. Interestingly, in similar experiments with MV-4-11 mitochondria, the addition of oligomycin partially polarized membrane potential (**Figure 5H**), presumably due to the higher ETS capacity of MV-4-11 compared to HL-60 or KG-1 (**Figure 2B**). However, in the absence of any carbon substrates (i.e., no forward electron transport), membrane potential generated exclusively by  $\Delta G_{ATP}$  was ~2-fold more polarized in all AML lines compared to PBMC (**Figure 5I**). In fact, for each AML line, membrane potential generated by ATP consumption was comparable to that generated during forward electron transport with saturating carbon substrates (**Figure 5J**). Together, these data indicate that leukemic mitochondria are particularly poised to consume, rather than produce, ATP. Such a mechanism appears mediated by the dominant expression of ANT2/3 in AML and once inside the matrix, ATP exerts a direct inhibitory effect on ETS flux.

***Low fractional OXPHOS in AML is reversed by small-molecule inhibitors of TRAP1.***

Having established that extramitochondrial  $\Delta G_{ATP}$  must gain access to the matrix space to inhibit ETS flux in leukemia, we next set out to elucidate the potential protein mediator(s) of this effect. To do this, we searched our proteomics dataset for mitochondrial proteins with known kinase and/or ATPase function that were substantially upregulated across all three leukemia lines and identified mitochondrial TRAP1 (**Figure 6A**). TRAP1 is the mitochondrial paralog of the heat shock protein 90 (HSP90) family and is widely recognized as a potential anti-cancer drug target across multiple human malignancies, including leukemia (Bryant et al., 2017; Kim et al., 2020; Li et al., 2020; Sanchez-Martin et al., 2020a, 2020b; Sciacovelli et al., 2013; Yoshida et al., 2013).

Given that ATPase activity is required for TRAP1 function (Ramkumar et al., 2020), we hypothesized that  $\Delta G_{\text{ATP}}$ -mediated ETS inhibition may be driven by acute activation of TRAP1. To test this hypothesis, OXPHOS kinetics were assessed in permeabilized MV-4-11 cells in the absence and presence of the purported TRAP1 inhibitor 17-AAG (Kamal et al., 2003). In substrate-replete permeabilized MV-4-11 cells, acute exposure to 17-AAG had no impact on maximal FCCP-supported respiration in the absence of adenylates (**Supplementary Figure 5A**). Remarkably, the presence of 17-AAG increased  $JH^+_{\text{OXPHOS}}$  and calculated fractional OXPHOS relative to vehicle control and completely restored FCCP-supported respiration in the presence of ATP free energy (**Figure 6B-D**). Similar results were observed using permeabilized HL-60 cells (**Supplementary Figure 5B-D**), as well as using the mitochondrial-targeted TRAP1 inhibitor gamitrinib (**Supplementary Figure 4A**). Using both MV-4-11 and KG-1 permeabilized cells, the ability of 17-AAG to restore OXPHOS flux was similar in the presence of CI or CII-based carbon substrates (**Supplementary Figure 5E-F**).

Although ATP is widely understood to be the universal energy currency in cells, it is critical to consider that ATP alone has minimal bio-synthetic power; rather, its utilization as a common energy currency is solely a function of the remarkable displacement of the molecule from equilibrium ( $\sim 10$  orders of magnitude) (Willis et al., 2016). This means that biological processes driven by ATP hydrolysis are presumably fueled by ATP free energy, rather than ATP levels per se. The primary advantage of the CK clamp technique is that it allows for mitochondrial bioenergetics to be evaluated across a physiological  $\Delta G_{\text{ATP}}$  span without appreciable changes in ATP concentration (**Supplementary Figure 5G**). Thus, we reasoned that the CK clamp could be utilized to assess 17-AAG effectiveness across a  $\Delta G_{\text{ATP}}$  span under conditions in which free [ATP] is not rate-limiting. For contrast, we compared the respiratory impact of 17-AAG to that of the

commonly used ETC inhibitor antimycin A. Although antimycin A decreased respiratory flux in permeabilized MV-4-11 cells, percent inhibition by the compound was largely insensitive to  $\Delta G_{ATP}$ , consistent with its known mechanism of action at CIII (**Supplementary Figure 5H**). In contrast, across all leukemia cell lines, restoration of respiratory flux by 17-AAG was exquisitely sensitive to  $\Delta G_{ATP}$  (**Figure 6E**, **Supplementary Figure 5I-J**).

***OXPHOS restoration by 17-AAG and Gamitrinib is independent of TRAP1.***

To control for potential off-target effects mediated by 17-AAG or gamitrinib, MV-4-11 cells were infected with lentivirus containing pooled short hairpin RNA (shRNA) against TRAP1. Control cells were infected with lentivirus containing scrambled shRNA. All constructs encoded GFP, as well as a puromycin selection gene to allow for stable selection. Following 24hr exposure to lentiviral particles and multiple rounds of puromycin selection, shRNA against TRAP1 led to a > 90% reduction in TRAP1 mRNA (**Figure 6F**). Consistent with prior reports (Laquatra et al., 2021; Sciacovelli et al., 2013), TRAP1 knockdown increased basal respiration in intact cells (**Figure 6G**). To determine the impact of TRAP1 knockdown on OXPHOS kinetics,  $JH^{+}_{Total}$  and  $JH^{+}_{OXPHOS}$  were assessed in substrate-replete permeabilized cells. Despite no change in  $JH^{+}_{Total}$  (**Supplementary Figure 5K**), TRAP1 knockdown decreased  $JH^{+}_{OXPHOS}$  and exacerbated the ability of ATP free energy to blunt ETS flux (**Figure 6H-J**). This was surprising, given that acute administration of 17-AAG/gamitrinib consistently increased fractional OXPHOS across all AML lines (**Figure 6C**, **Supplementary Figure 5C**). Based on this, we hypothesized that the ability of 17-AAG and/or gamitrinib to bolster OXPHOS kinetics may be independent of TRAP1. To test this, we repeated the  $JH^{+}_{OXPHOS}$  experiments in control and TRAP1 knockdown cells in the presence of either 17-AAG or gamitrinib. In control cells, acute administration of 17-AAG and

gamitrinib once again increased fractional OXPHOS and restored the FCCP effect and near identical results were also apparent in TRAP1 knockdown cells (**Figure 6I-J, Supplementary Figure 5L**). Such findings indicated that OXPHOS restoration by 17-AAG/gamitrinib occurs independent of TRAP1 and is thus attributable to an ‘off-target’ mechanism. One such off-target effect documented for 17-AAG relates to the ability of the compound to bind voltage dependent anion transporter (VDAC) (Xie et al., 2011), the principal gatekeeper to adenylate transport across the outer mitochondrial membrane. A similar mechanism has also been described for the anti-cancer compound curcumin (Tewari et al., 2015); however, the implications of these interactions on cellular bioenergetics remain incompletely understood. Interestingly, nearly identical to the effect observed in the presence of 17-AAG/gamitrinib, acute exposure to curcumin also reversed  $\Delta G_{ATP}$ -mediated ETS inhibition in MV-4-11 cells (**Figure 6K**). Based on the striking functional similarities between 17-AAG, gamitrinib and curcumin, such findings suggest a potential novel mechanism whereby these small molecules are uniquely capable of selectively blocking matrix ATP uptake, while remaining permissive to ADP uptake, presumably via interaction with the VDAC-ANT axis (**Figure 6L**). In support of this, curcumin-VDAC interaction is known to lock VDAC in the ‘closed’ confirmation, in turn making it partially selective for cation (i.e.,  $ADP^{3-}$ ), rather than anion (i.e.,  $ATP^{4-}$ ), transport (Tewari et al., 2015).

To investigate the relationship between mitochondrial fractional OXPHOS and AML biology, we assessed cellular proliferation and viability in control and TRAP1 knockdown cells exposed to gamitrinib, curcumin, or vehicle control. In the absence of any small-molecule intervention, cellular proliferation was higher in TRAP1 knockdown cells (**Figure 6M**), consistent with low fractional OXPHOS being advantageous to AML growth. To determine the therapeutic efficacy of restoring fractional OXPHOS in AML, cells were exposed for 24 hrs to either

gamitrinib or curcumin, either alone or in combination with the front-line AML chemotherapeutic cytarabine (Ara-C). Compared to marginal cytotoxicity in response to Ara-C dose escalation, 24hr exposure to either gamitrinib or curcumin decreased cell viability by as much as 60% (**Figure 6N**). Note, identical cytotoxicity was observed in control and TRAP1 knockdown cells, and the additional presence of Ara-C had no further impact (**Figure 6N**).

***Intrinsic limitations in OXPHOS characterize human primary leukemia.***

To determine if the bioenergetic phenotypes present in leukemia cell lines translated to the clinic, we recruited patients diagnosed with leukemia and comprehensively evaluated mitochondrial bioenergetic function in mononuclear cells isolated from bone marrow aspirates. All patients had confirmed leukemia at the time of sample acquisition. Biochemical results were compared to PBMC isolated from age-matched participants without a prior history of leukemia. As additional controls, OXPHOS kinetics were assessed in mononuclear cells isolated from bone marrow aspirates of healthy subjects ( $BM_{\text{Healthy}}$ ), as well as purified CD34<sup>+</sup> hematopoietic stem cells. To ascertain the impact of clonal cell expansion on the underlying mitochondrial network, experiments in unstimulated (i.e., quiescent) CD34<sup>+</sup> cells were also performed following chronic exposure to proliferative stimuli (e.g., TPO, SCF, FLT-3; 'CD34<sup>+</sup>GFs'). Relative to PBMC,  $BM_{\text{Healthy}}$ , and quiescent CD34<sup>+</sup>, intact basal respiration was elevated in primary leukemia, as well as clonally expanding CD34<sup>+</sup> (**Figure 7A**), reminiscent of that seen in AML cell lines and entirely consistent with their proliferative phenotypes. Relative to quiescent CD34<sup>+</sup>,  $JH^+_{\text{Total}}$  in substrate-replete permeabilized cells was ~ 2-fold higher in PBMC, CD34<sup>+</sup>GFs and primary leukemia (**Figure 7B**), consistent with higher cellular mitochondrial density. Despite this apparent increase in mitochondrial content,  $JH^+_{\text{OXPHOS}}$  remained elevated above quiescent CD34<sup>+</sup> only in PBMC, as

OXPHOS kinetics were completely unaltered comparing clonally expanding CD34<sup>+</sup> or primary leukemia to quiescent CD34<sup>+</sup> (**Figure 7C**). As seen in the AML cell lines, calculated fractional OXPHOS was decreased in clonally expanding CD34<sup>+</sup> and primary leukemia, entirely consistent with low fractional OXPHOS being required for hematopoietic clonal expansion (**Figure 7D**). To determine the impact of 17-AAG on OXPHOS kinetics, CK clamp experiments were performed in a separate cohort of primary AML samples, as well as clonally expanding CD34<sup>+</sup> cells. Relative to vehicle control, 17-AAG increased  $JH^{+}_{OXPHOS}$  and restored FCCP-stimulated respiration in the presence of  $\Delta G_{ATP}$  in primary AML and CD34<sup>+</sup><sub>GFs</sub> (**Figure 7E-F**). Of note, acute 17-AAG had no impact on OXPHOS kinetics in PBMC or BM<sub>Healthy</sub> and 24hr exposure of PBMC to 17-AAG or gamitrinib did not impact cell viability (**Supplementary Figure 6A-C**).

***Intrinsic limitations in OXPHOS power output characterize venetoclax resistance in AML.***

The preponderance of evidence related to mitochondrial bioenergetics in AML indicates that active repression of OXPHOS is advantageous to the leukemia phenotype. Related to this, although several reports have linked AML chemoresistance to apparent increases in ‘OXPHOS reliance’ (Farge et al., 2017; Guièze et al., 2019; Liu et al., 2020; Roca-Portoles et al., 2020), such conclusions are based largely on intact cellular respirometry in which OXPHOS kinetics are not directly quantified. To address the specific role for OXPHOS in AML chemoresistance, we conducted a series of experiments in chemosensitive HL-60 cells and compared the results to HL-60 cells made to be refractory to venetoclax (**Figure 8A-B**). In these experiments,  $JH^{+}_{Total}$  and  $JH^{+}_{OXPHOS}$  were determined as described above. In addition, OXPHOS kinetic data generated using the CK clamp was integrated with parallel analysis of OXPHOS efficiency (mitochondrial ATP synthesis relative to oxygen consumption; quantified as the P/O ratio). By incorporating

empirically derived P/O, respiratory flux at each  $\Delta G_{\text{ATP}}$  can be converted to ATP production rate. Assuming extra-mitochondrial force applied via the CK clamp is fixed at each titration step, ATP production rate can be used to quantitate OXPHOS power output in Watts ( $\text{J}\cdot\text{s}^{-1}$ ). Power is an extremely useful parameter because it encompasses thermodynamic, kinetic, as well as stoichiometric descriptions that effectively report on the actual quantities of OXPHOS work performed across the demand range. Looking first at intact cellular respirometry, both basal and maximal respiratory capacity were elevated in venetoclax-resistant HL-60 (HL60<sub>VR</sub>) (**Figure 8C**). Remarkably, despite a near ~2-fold increase in cellular respiratory capacity, OXPHOS kinetics were in fact decreased in HL60<sub>VR</sub>, such that  $JH^+_{\text{OXPHOS}}$  failed to reach the respiratory rates observed under basal conditions prior to digitonin permeabilization (**Figure 8D**). Of note, the addition of extramitochondrial cytochrome C did not impact  $JH^+_{\text{OXPHOS}}$  in either cell type (**Figure 8E**). The combination of increased maximal respiratory capacity combined with decreased  $JH^+_{\text{OXPHOS}}$  translated to a striking decrease in both fractional OXPHOS (**Figure 8F**), as well as OXPHOS power output in HL60<sub>VR</sub> (**Figure 8G-I**), indicating that intrinsic OXPHOS insufficiency also underlies cellular bioenergetics in chemoresistant AML.

## Discussion

Increased mitochondrial oxidative metabolism, an established metabolic hallmark of leukemia (Byrd et al., 2013; Kuntz et al., 2017; Lee et al., 2015; Sriskanthadevan et al., 2015; Suganuma et al., 2010), has been historically interpreted to reflect an increased reliance on mitochondrial ATP production. However, fractional OXPHOS kinetics had not been empirically evaluated in leukemia at the onset of this project. Thus, it remained to be determined whether higher basal respiration in leukemia reflected accelerated demand for ATP regeneration or intrinsic

OXPHOS insufficiency. Both conditions would be expected to similarly restrict cellular ATP/ADP equilibrium displacement (i.e.,  $\Delta G_{ATP}$  charge) and thus could potentially result in identical respiratory profiles in intact cells. For example, a small network of mitochondria each respiring near maximal capacity could in theory produce an identical ‘basal’ oxygen consumption rate to that of a comparatively larger mitochondrial network in which forward respiratory flux was constrained across each mitochondrial unit. Our findings provide definitive support for the latter scenario in AML, as application of our diagnostic biochemical workflow revealed that intrinsic limitations in fractional OXPHOS characterize an expansive mitochondrial network in human leukemia. In fact, a substantial portion of the AML mitochondrial network is incapable of contributing to oxidative ATP production, as leukemic mitochondria primarily consume, rather than produce, ATP across a physiological  $\Delta G_{ATP}$  span. Intrinsic OXPHOS limitations in AML appear to derive from a unique biochemical mechanism whereby extra-mitochondrial ATP gains access to the matrix space, where it then directly inhibits electron transport flux in a  $\Delta G_{ATP}$  dependent manner. Such inhibition is independent of ATP synthase (i.e., CV) and presumably localized to the respiratory complexes downstream of the ubiquinone pool (i.e., CIII, Cyt C, CIV). Given that evidence for this effect was also observed in bone marrow-derived CD34<sup>+</sup> stem cells, allosteric and/or post-translation regulation of ETS flux is likely a primary mode of OXPHOS regulation in hematopoietic progenitors that is maintained during leukemogenesis. Importantly, reversal of this effect was strongly cytotoxic to AML, indicating that direct OXPHOS regulation by  $\Delta G_{ATP}$  confers a survival advantage during hematopoietic clonal cell expansion. Although additional work will be required to fully elucidate the mechanism(s) by which ATP uptake directly inhibits OXPHOS flux in AML, our preliminary findings leveraging gamitrinib and curcumin provide proof-of-principle that such regulation can indeed be targeted therapeutically.

While prior work has implicated ANT2 (Chevrollier et al., 2011; Lee et al., 2019; Maldonado et al., 2016) in cancer biology, we present for the first time here a potential mechanism whereby ANT2/3 regulate leukemic cell metabolism via  $\Delta G_{ATP}$ . Specifically, our findings inform a model of leukemia bioenergetics in which decreased ANT1, and increased ANT2/3 favor the uptake of extra-mitochondrial ATP into the matrix space. The transfer of  $\Delta G_{ATP}$  from the cytosol to the matrix in turn constrains OXPHOS via direct inhibition of the ETS. Direct ETS inhibition by  $\Delta G_{ATP}$  could derive from multiple sources, such as adenylate-mediated allosteric regulation (Kadenbach, 2020), inhibitory phosphorylation of the respiratory complexes (Helling et al., 2012), or chaperone mediated protein-protein interactions (Sciacovelli et al., 2013). In either case, the exquisite sensitivity of the ETS to  $\Delta G_{ATP}$  likely prevents the mitochondrial network from contributing to the cellular  $\Delta G_{ATP}$  charge in the leukemic blasts. Consequentially, maintenance of a low cellular  $\Delta G_{ATP}$  would be predicted to maximize both glycolytic and mitochondrial metabolism, entirely consistent with the known hyper-metabolic phenotype of human leukemia (Goto et al., 2014a, 2014b; Sukanuma et al., 2010). Such conditions are likely advantageous to proliferating leukemic blasts, as insufficient ATPase activity has been demonstrated to be rate-limiting for cellular proliferation (Luengo et al., 2020).

Currently, there is great interest in developing novel pharmacotherapies that target mitochondrial OXPHOS in leukemia (Farge et al., 2017; Guièze et al., 2019; Kuntz et al., 2017; Lee et al., 2015; Panina et al., 2020). Yet, a large caveat of targeting mitochondria is the ubiquitous necessity of OXPHOS for healthy cellular metabolism. If indeed the proliferative potential of leukemia depends upon mitochondrial ATP consumption, rather than production, it is tempting to speculate that a pharmaceutical intervention designed to restore OXPHOS kinetics and/or  $\Delta G_{ATP}$  could effectively halt cell proliferation, in turn allowing for proliferating blasts to succumb to

apoptosis. Such a targeted approach would be expected to minimize secondary toxicity as increased OXPHOS efficiency is likely advantageous across non-cancerous, highly metabolic tissues (e.g., brain, heart, muscle), as well as in the context of adaptive cellular immunity (Buck et al., 2016; Vardhana et al., 2020). Based upon our proposed model, targeting the acute OXPHOS regulating capabilities of  $\Delta G_{ATP}$  through the VDAC-ANT axis provides an appealing, leukemia-specific target for pharmaceutical intervention, as small-molecule interference of this pathway restored OXPHOS kinetics in leukemic mitochondria and induced cytotoxicity (**Figure 6**). Although prior work has identified TRAP1 (Bryant et al., 2017; Ramkumar et al., 2020) as a potential anti-cancer target in leukemia, genetic knockdown in MV-4-11 cells increased, rather than decreased, cellular proliferation in the present study. Of note, the mitochondrial-localized TRAP1 inhibitor gamitrinib is currently being evaluated in a first-in-human phase I clinical trial for treatment of advanced cancers (ClinicalTrials.gov Identifier: NCT04827810). It is currently unclear how much of the cytotoxicity induced by 17-AAG and/or gamitrinib is attributable to on-target TRAP1 inhibition vs off-target interference with ATP exchange via VDAC-ANT. Moreover, the mechanism of cytotoxicity induced by 17-AAG/gamitrinib/curcumin requires additional experimentation. Although speculative, it is possible that the ability of these compounds to selectively block matrix ATP uptake acutely restores full respiratory competence of the expansive AML mitochondrial network, in turn increasing redox pressure across the ETS and boosting ROS production above a cytotoxic threshold.

Taken together, the present findings provide novel insight into the hyper-metabolic phenotype characteristic of human leukemia. With respect to the mitochondria, it bears repeating that heightened basal respiration in AML is almost exclusively assumed to reflect an increased reliance on oxidative ATP synthesis (i.e., OXPHOS). Although this assumption largely

underscores the growing interest in targeting mitochondrial oxidative metabolism in cancer, direct interrogation of the mitochondrial network herein consistently revealed active OXPHOS repression in AML. Representative of this phenotype, TRAP1 knockdown and venetoclax resistance both resulted in an increase in basal respiration that was subsequently linked to decreased, not increased, OXPHOS kinetics. Such findings highlight the diagnostic limitations of metabolic measurements made in intact cells and suggest that too much reliance on binary readouts of respiration versus glycolysis may in fact be masking ‘actionable’ cancer-specific mitochondrial biology. By leveraging comprehensive mitochondrial diagnostics, our collective findings inform a model whereby intrinsic OXPHOS limitations support aggressive disease dissemination in leukemia and raise the intriguing possibility that pharmaceutical interventions aimed at blocking mitochondrial ATP uptake/consumption warrants further exploration. Given that increased OXPHOS efficiency is advantageous across non-cancerous tissues, a potential benefit to this novel treatment paradigm is the minimization of secondary toxicity (i.e., a wide therapeutic window).

## **Methods**

### ***Ethical approval of human subject research***

All procedures involving human subjects were approved by the Institutional Review Board of the Brody School of Medicine at East Carolina University (study ID: UMCIRB 18-001328, UMCIRB 19-002331).

### ***Blood collection and isolation of PBMCs.***

For PBMC samples, healthy subjects (ages 18-70 years), without a prior history of hematological malignancy, were recruited from the surrounding area. Following informed consent

(study ID: UMCIRB 18-001328), venous blood from the brachial region of the upper arm was collected. Whole blood was collected in sodium-heparinized Cell Preparation Tubes (CPT) (BD Biosciences, Franklin Lakes, NJ) and centrifuged at 1,800 x g for 15 min. Prior to experimentation, mononuclear cells were washed in ammonium-chloride-potassium (ACK) lysis buffer to remove red blood cells and either used immediately for experiments or cultured overnight in IMDM (Thermo Fisher Scientific, Waltham, MA) supplemented with glutamine, 10% FBS, and 1% penicillin/streptomycin.

### ***Mononuclear cell isolation from bone marrow aspirates***

For primary leukemia samples, bone marrow aspirates were collected from patients undergoing confirmatory diagnosis for a range of hematological malignancies as a component of an already scheduled procedure. All patients provided informed consent prior to study enrollment (study ID: UMCIRB 19-002331). Type of leukemia ranged from acute myeloid leukemia (AML, N=14), chronic myeloid leukemia (CML, N=2), and granular lymphocytic leukemia (N=1). Patient age ranged from 32-78 years (male/female, 8/9). Bone marrow aspirates were collected in sodium-heparinized Cell Preparation Tubes (CPT) (BD Biosciences, Franklin Lakes, NJ) and centrifuged at 1,800 x g for 15 min. Mononuclear cells were isolated and then washed in ACK lysis buffer to remove red blood cells and used immediately for experiments. In addition to primary leukemia samples, bone marrow aspirates were collected from healthy donors, ages 26-33, supplied by HemaCare (Northridge, CA).

### ***CD34<sup>+</sup> Stem/Progenitor cell collection and culture***

CD34<sup>+</sup> cells were purchased from HemaCare (Northridge, CA). These cells were isolated and purified from bone marrow aspirates of healthy donors, ages 20-39. A portion from each vial was cultured in IMDM supplemented with 15% HyClone FBS, recombinant human SCF (25ng/mL), TPO (50ng/mL), and FLT-3 (50ng/mL).

### ***AML cell line culture***

HL-60, KG-1, and MV-4-11 (ATCC, Manassas, VA) human leukemia cells were cultured in IMDM (Thermo Fisher Scientific, Waltham, MA) supplemented with glutamax, 10% FBS, and 1% penicillin/streptomycin and incubated at 37°C in 5% CO<sub>2</sub>. All cell lines were obtained from ATCC (Manassas, VA). Cell lines were not tested or authenticated over and above documentation provided by ATCC, which included antigen expression, DNA profile, short tandem repeat profiling, and cytogenetic analysis. For experiments involving venetoclax resistance, HL-60 cells were cultured in RPMI-1640, supplemented with glutamax, 10% FBS, and 1% penicillin/streptomycin. To model venetoclax resistance, HL-60 cells were conditionally adapted over time to 1µM venetoclax in a manner previously described for other chemotherapy drugs (L. P. Kao et al., 2019). Upon reaching an average cell density of 1.5x10<sup>6</sup>cell/mL the cells were harvested and used for whole cell, permeabilized cell, and isolated mitochondria experiments. Primary human muscle progenitor cells (human myoblasts, ‘HMB’) were derived from fresh muscle biopsy samples, as described previously (Ryan et al., 2018). Cells were cultured on collagen-coated flasks using HMB growth medium (GM: Ham’s F10, supplemented with 20% FBS and 1% penicillin/streptomycin, and supplemented immediately prior to use with 5 ng/ml basic FGF).

### ***Cell viability assays***

Cell viability was determined by viable cell count using Trypan Blue (0.4%). Where indicated, viability was determined by fluorescence measurement as previously described (L.-P. Kao et al., 2019). Briefly, cells were seeded in black-wall, 96-well plates, in growth medium. After addition of agents (0.1 ml final well volume), cells were incubated at 37° C, 5% CO<sub>2</sub>, for the times indicated. Viability was determined using propidium iodide (PI) as follows. Positive control cells were permeabilized by addition of 10 µl of 1.0 mg/ml digitonin and incubated at 37° C, 5% CO<sub>2</sub>, for 20 min. Plates were then centrifuged at 1200 x g for 20 min, and after dumping the media, 0.1 ml of a 5.0 µM PI solution in PBS was added. The plate was again incubated for 20 min, and viability was calculated as the mean fluorescence (minus permeabilized vehicle control) at 530 nm excitation and 620 nm emission. For venetoclax induced cell death assays, cell viability was determined using a standard MTT assay and absorption was read at 570 nm. For all viability assays, each biological replicate was derived from the mean of three technical replicates.

### ***TRAP1 Knockdown in MV-4-11 cells***

MV-4-11 cells were cultured in IMDM (Thermo Fisher Scientific, Waltham, MA) supplemented with glutamax, 10% FBS, and 1% penicillin/streptomycin and incubated at 37°C in 5% CO<sub>2</sub>. Human shRNA lentiviral particles packaged from pGFP-C-shLenti vector (4 unique 29mer TRAP1-specific shRNA [ACAGCCGCAAAGTCCTCATCCAGACCAAG; ATGGTGGCTGACAGAGTGGAGGTCTATTC;GGAGACGGACATAGTCGTGGATCACTACA; TGGCTTTCAGATGGTTCTGGAGTGTTTGA], 1 scramble control; 0.5 ml each, >10<sup>7</sup> TU/ml) were purchased from Origene (CAT#: TL300868V). To facilitate infection, MV-4-11 cells and lentiviral particles were co-cultured for 24 hours in individual wells of a 96-well plate in 0.1mL

of IMDM growth media, supplemented with 4 $\mu$ g/mL polybrene (multiplicity of infection of approximately 20). At the end of the 24hrs, cells were spun down and resuspended in culture media devoid of polybrene. Cultures were then subjected to puromycin selection by continuous exposure to 2 $\mu$ g/mL puromycin in the culture media. Confirmation of TRAP1 knockdown was performed via real-time PCR. To do this, total RNA was extracted from cell pellets using Qiagen RNeasy Midi kits per manufacturer instructions. RNA was reverse transcribed using Superscript IV reverse transcriptase according to manufacturer instructions (Invitrogen). Real-time PCR on TRAP1 was performed using a Quantstudio 3 Real-Time PCR system (Applied Biosystems). Relative quantification of mRNA levels was determined using the comparative threshold cycle ( $\Delta\Delta$ CT) method using FAM-labeled Taqman gene expression assays (Applied Biosystems) specific to TRAP1 run in multiplex with a VIC-labeled 18S control primer.

### ***Confocal Microscopy***

Cells were pre-loaded with 200nM Mitotracker Green-FM dye (MTG-FM; Molecular Probes, Eugene, OR) at 37°C for 1hr. Cells were then centrifuged at 300 x g for 7min at ~25°C and resuspended in MTG-FM-free IMDM formulation media (Thermo Fisher) containing 50nM tetramethyl rhodamine methyl ester (TMRM) and 2 $\mu$ M Hoechst 33342. Cells were plated on glass-bottom dishes (MatTek, Ashland, MA) for imaging. Cells were held in place with a thin 1% agarose pad that was applied immediately prior to imaging in order to minimize rapid motion interference during imaging of live non-adherent cells (Ivanusic et al., 2017).

All imaging was performed using an Olympus FV1000 laser scanning confocal microscope (LSCM) with an onstage incubator at 37°C. Acquisition software was Olympus FluoView FSW (V4.2). The objective used was 60X oil immersion (NA=1.35, Olympus Plan Achromat

UPLSAPO60X(F)). Images were 800x800 pixel with 2 $\mu$ s/pixel dwell time, sequential scan mode, resulting in a 4X digital zoom. Hoechst 33342 was excited using the 405nm line of a multiline argon laser; emission was filtered using a 560nm dichroic mirror and 420-460nm barrier filter. MTG-FM was excited using the 488nm line of a multiline argon laser; emission was filtered using a 560nm dichroic mirror and 505-540nm barrier filter. TMRM was excited using a 559nm laser diode; emission was filtered using a 575-675nm barrier filter. Zero detector offset was used for all images and gain at the detectors was kept the same for all imaging. The pinhole aperture diameter was set to 105 $\mu$ m (1 Airy disc).

Images were analyzed using Fiji (Schindelin et al., 2012). Spatial resolution was measured using sub-resolution fluorescent beads (Thermo Fisher) and curve fitting was performed using the MetroloJ plugin in Fiji. 16-bit images were made into a composite. Circular ROIs were manually selected using the ROI manager plugin. Images were then decomposed into separate 16-bit image stacks leaving the ROI positions intact. A Huang auto-threshold was used for automated selection of signal for all three channels. Following threshold application, each signal was measured using the multi-measure feature. Only whole cells were analyzed (i.e. cells on edges of the FOV were excluded). Slices containing cells above the lowest monolayer were removed from stacks to avoid oversampling. The following calculations were performed to determine the relevant signal volumes.

$$\text{Signal Volume } (\mu\text{m}^3) = [A*Z]/N$$

Where A is the signal-positive area selected using a Huang auto-threshold ( $\mu\text{m}^2$ ), Z is the optical section thickness (axial resolution;  $\mu\text{m}$ ), and N is the number of steps within each optical section (i.e. axial resolution divided by the step size). The latter operation is necessary to correct for oversampling of the signal volumes.

### ***Respiratory flux in intact and permeabilized cells***

Approximately  $1-3 \times 10^6$  cells were used for each intact and permeabilized cell experiment. High-resolution respirometry measurements were performed using the Oroboros Oxgraph-2k (O2k; Oroboros Instruments, Innsbruck, Austria) in a 0.5 or 1.0mL reaction volume at 37°C. For normalization to total protein, at the conclusion of each experiment the cell suspension was collected from each chamber and centrifuged at 2,000 x g for 10 min at 4°C. Cells were lysed using low-percentage detergent buffer (CellLytic M) followed by a freeze-thaw cycle, and protein concentration was determined using a BCA protein assay.

Respiratory flux was measured using previously described methods (Fisher-Wellman et al., 2018). For intact cell measurements, cells were resuspended in Intact Cell Respiratory Media (17.7g/L Iscove's Modified Dulbecco's Medium (IMDM), 20mM HEPES, 1% Penicillin/Streptomycin, 10% FBS, pH 7.4). After basal respiration was established, oligomycin (Oligo; 0.02 $\mu$ M) was added followed by FCCP titration (FC; 0.5-5 $\mu$ M), rotenone (Rot; 0.5 $\mu$ M) and antimycin A (Ant; 0.5 $\mu$ M). For permeabilized cell measurements, cells were resuspended in Respiratory Buffer supplemented with creatine (105mM MES potassium salt, 30mM KCl, 8mM NaCl, 1mM EGTA, 10mM KH<sub>2</sub>PO<sub>4</sub>, 5mM MgCl<sub>2</sub>, 0.25% BSA, 5mM creatine monohydrate, pH 7.2). Cells were permeabilized with digitonin (Digi; 0.02mg/mL), and respiratory flux was measured using the creatine kinase (CK) clamp and FCCP titration assays. Within the CK clamp assay, the free energy of ATP hydrolysis ( $\Delta G_{ATP}$ ) is calculated using the equilibrium constant for the CK reaction ( $K'_{CK}$ ) and is based upon the addition of known concentrations of creatine (CR), phosphocreatine (PCR), and ATP in the presence of excess amounts of CK (Fisher-Wellman et al., 2018). Calculation of  $\Delta G_{ATP}$  at defined PCR concentrations was done using the online resource

([https://dmpio.github.io/bioenergetic-calculators/ck\\_clamp/](https://dmpio.github.io/bioenergetic-calculators/ck_clamp/)) previously described (Fisher-Wellman et al., 2018).

For all assays, various combinations of carbon substrates and inhibitors were employed. Substrates and inhibitors utilized are indicated in the figure legends: CK (20U/mL), ATP (5mM), PCR (1mM, 6mM, 15mM, 21mM), pyruvate (Pyr or P; 5mM), malate (M; 1mM), glutamate (G; 5mM), octanoyl-carnitine (O; 0.2mM), succinate (Succ or S; 5mM) cytochrome C (Cyt C, 10 $\mu$ M), oligomycin (Oligo, 0.02 $\mu$ M), FCCP (FC, 0.5-2 $\mu$ M), rotenone (Rot, 0.5 $\mu$ M), antimycin A (Ant A, 0.5 $\mu$ M), carboxyatractyloside (CAT, 1 $\mu$ M), bongkrekic acid (20 $\mu$ M), 17-AAG (sigma, #100068, 1 $\mu$ M), Gamitrinib TPP hexafluorophosphate (MedChemExpress, #HY-102007A, 1 $\mu$ M).

### ***Extracellular flux analysis***

Extracellular acidification rate (ECAR) and oxygen consumption rate (OCR) were measured using a Seahorse XF24e flux analyzer (Agilent Technologies, Santa Clara, CA). Prior to analysis, wells were coated with Cell-Tak (Corning, Cat# 354240). Cells were then seeded at 3x10<sup>5</sup> cells/well. The assay was performed in bicarbonate free IMDM, supplemented with 2mM HEPES, in the absence of FBS, pH 7.4. The flux analysis protocol was as follows: Basal OCR and ECAR were measured followed by the addition of 5 $\mu$ M Oligomycin, and 50mM 2-deoxyglucose (2-DG). All data were normalized to viable cell count.

### ***Isolation of mitochondria from PBMCs and leukemia cells***

In order to pellet cells, PBMC fractions were washed with PBS and centrifuged at 300 x g for 10 min at 4°C and leukemia cells were centrifuged at 300 x g for 10 min followed by a PBS wash. Cell pellets were resuspended in Mitochondrial Isolation Buffer with BSA (100mM KCl,

50mM MOPS, 1mM EGTA, 5mM MgSO<sub>4</sub>, 0.2% BSA, pH 7.1) and homogenized using a borosilicate glass mortar and Teflon pestle. Homogenates were centrifuged at 800 x g for 10 min at 4°C. The supernatant was collected, and the remaining pellet was resuspended in Mitochondrial Isolation Buffer with BSA, then homogenized and centrifuged again. This process was repeated a total of 3 times. The collected supernatant was centrifuged at 10,000 x g for 10 min at 4°C to pellet the mitochondrial fraction. The fraction was resuspended in Mitochondrial Isolation Buffer without BSA, transferred to a microcentrifuge tube and subjected to another spin at 10,000 x g. The mitochondrial pellet was resuspended in ~100μL of Mitochondria Isolation Buffer and protein concentration was calculated using the Pierce BCA assay. Respiration assays using isolated mitochondria were similar to that described for permeabilized cells.

### ***Mitochondrial NADH/NAD<sup>+</sup> redox in isolated mitochondria***

Fluorescent determination of NADH/NAD<sup>+</sup> was performed using a QuantaMaster Spectrofluorometer (QM-400, Horiba Scientific, Kyoto, Japan). The NADH/NAD<sup>+</sup> was detected at Ex/Em: 350/450. NADH/NAD<sup>+</sup> was measured in mitochondria isolated from PBMC and leukemia cell lines using the CK clamp assay. Experiments were performed at 37°C in a 200μL reaction volume. To start, Respiratory Buffer supplemented with creatine (200μL), Cyt C (10μM), mitochondrial lysate (100μg) were added into a glass cuvette. Mitochondria were incubated at 37°C for ~ 5 minutes in the absence of substrate to induce 0% reduction of the NADH pool. Saturating carbon substrates were added (P/M/G/S/O), and respiration was stimulated with the CK clamp. Titration of ΔG<sub>ATP</sub> was performed via PCR titration (6, 15, 21mM). Oligomycin (0.02μM) was added to inhibit ATP synthesis and cyanide (CN, 10mM) was added to induce 100% reduction

of the matrix NADH pool. The NADH/NAD<sup>+</sup> was expressed as a percentage reduction of the CN value (i.e. 100% reduction) based upon the formula % Reduction =  $(F - F_{0\%}) / (F_{100\%} - F_{0\%}) * 100$ .

### ***Mitochondrial membrane potential ( $\Delta\Psi$ ) in isolated mitochondria***

Fluorescent determination of  $\Delta\Psi$  was carried out via a QuantaMaster Spectrofluorometer (QM-400; Horiba Scientific). Determination of  $\Delta\Psi$  via TMRM was done as described previously (Fisher-Wellman et al., 2018), taking the fluorescence ratio of the following excitation/emission parameters [Ex/Em, 576/590 and 551/590]. The 576/551 ratio was then converted to millivolts via a KCl standard curve performed in the presence of valinomycin as described (Fisher-Wellman et al., 2018).

### ***Mitochondrial JATP synthesis, P/O ratio and OXPHOS power output in permeabilized cells***

Parallel respiration and fluorometric experiments were carried out in order to generate an ATP/O (P/O) ratio, as previously described (Lark et al., 2016). Experiments were performed at 37°C in a 2.5mL reaction volume in Respiratory Buffer supplemented with AP5A (0.2mM), and digitonin (0.02mg/mL). ATP synthesis and oxygen consumption were determined in permeabilized cells energized with P/M/G/S/O in the presence of 0.1mM ADP. The P/O ratio was then calculated using the ratio of the JATP and the steady state  $JO_2$ , divided by 2. Empirically derived P/O ratios were then used to convert oxygen consumption rates recorded during the CK clamp assay (using identical substrates) to ATP production rate [(oxygen consumption rate) x (P/O x 2)]. A fixed extra-mitochondrial force was assumed to be applied via the CK clamp at each PCR titration. These forces corresponded to -54.16, -58.93, -60.64, and -61.49 kJ/mol. These forces were used along with ATP production rate to quantitate OXPHOS power output in Watts (J/s)

according to the following formula [(pmol ATP/s/million cells) x (5.416 or 5.893 or 6.064 or 6.149 \* 10<sup>-8</sup> J/pmol ATP) =  $\mu$ Watts/million cells].

### ***Mitochondrial lysis, protein digestion, and peptide labeling for TMT quantitative proteomics***

Mitochondrial pellets from leukemia cells and PBMC (approximately 250  $\mu$ g of protein) were lysed in ice-cold 8 M Urea Lysis Buffer (8 M urea in 50 mM Tris, pH 8.0, 40 mM NaCl, 2 mM CaCl<sub>2</sub>, 1x cOmplete ULTRA mini EDTA-free protease inhibitor tablet), as described previously (McLaughlin et al., 2020). The samples were frozen on dry ice and thawed for three freeze-thaw cycles and further disrupted by sonication with a probe sonicator in three 5s bursts set at an amplitude of 30 (Q Sonica, Newtown, CT). Samples were centrifuged at 10,000  $\times$  g for 10 min at 4  $^{\circ}$ C to pellet insoluble material. Protein concentration was determined by BCA, and equal amounts of protein (200  $\mu$ g, adjusted to 2.5 mg/mL with Urea Lysis Buffer) were reduced with 5 mM DTT at 32  $^{\circ}$ C for 30 min, cooled to room temperature, and then alkylated with 15 mM iodoacetamide for 30 min in the dark. Unreacted iodoacetamide was quenched by the addition of DTT up to 15 mM. Initial digestion was performed with Lys C (Thermo Fisher) 1:100 w-w; 2  $\mu$ g enzyme per 200  $\mu$ g protein) for 4 hr at 32  $^{\circ}$ C. Following dilution to 1.5 M urea with 50 mM Tris (pH 8.0), 30 mM NaCl, 5 mM CaCl<sub>2</sub>, the samples were digested overnight with trypsin (Promega, Madison, WI) 50:1 w/w, protein:enzyme at 32  $^{\circ}$ C. Samples were acidified to 0.5% TFA and centrifuged at 10,000  $\times$  g for 10 min at 4  $^{\circ}$ C to pellet insoluble material. Supernatant containing soluble peptides was desalted on a 50 mg tC18 SEP-PAK solid phase extraction column (Waters, Milford, MA) and eluted (500  $\mu$ L 25% acetonitrile/0.1% TFA and 2  $\times$  500  $\mu$ L 50% acetonitrile/0.1% TFA). The 1.5 mL eluate was frozen and lyophilized.

### ***TMT labeling***

TMT labeling was performed as previously described (McLaughlin et al., 2020). The samples from isolated mitochondria were re-suspended in 100  $\mu$ L of 200 mM triethylammonium bicarbonate (TEAB), mixed with a unique 10-plex Tandem Mass Tag (TMT) reagent (0.8 mg re-suspended in 50  $\mu$ L 100% acetonitrile), and shaken for 4 hr at room temperature (Thermo Fisher). A total of 2 x 10-plex kits were used and one sample was TMT-labeled in both kits to control for quantification differences across multiplex preparations. Following quenching with 0.8  $\mu$ L 50% hydroxylamine samples were frozen, and lyophilized. Samples were re-suspended in  $\sim$ 1 mL of 0.5% TFA and again subjected to solid phase extraction, but with a 100 mg tC18 SEP-PAK SPE column (Waters). The multiplexed peptide sample was subjected to high pH reversed phase fractionation according to the manufacturer's instructions (Thermo Fisher). In this protocol, peptides (100  $\mu$ g) are loaded onto a pH-resistant resin and then desalted with water washing combined with low speed centrifugation. A step-gradient of increasing acetonitrile concentration in a high-pH elution solution is then applied to columns to elute bound peptides into 8 fractions. Following elution, fractions were frozen and lyophilized.

### ***nLC-MS/MS for TMT proteomics***

nLC-MS/MS was performed as described previously (McLaughlin et al., 2020). Peptide fractions were suspended in 0.1% formic acid at a concentration of 0.25  $\mu$ g/ $\mu$ L, following peptide quantification (ThermoFisher). All samples were subjected to nanoLC-MS/MS analysis using an UltiMate 3000 RSLCnano system (Thermo Fisher) coupled to a Q Exactive PlusHybrid Quadrupole-Orbitrap mass spectrometer (Thermo Fisher) via nanoelectrospray ionization source. For each injection of 4  $\mu$ L (1  $\mu$ g), the sample was first trapped on an Acclaim PepMap 100 20 mm

× 0.075 mm trapping column (Thermo Fisher) 5 µl/min at 98/2 v/v water/acetonitrile with 0.1% formic acid, after which the analytical separation was performed over a 90-min gradient (flow rate of 300 nanoliters/min) of 3 to 30% acetonitrile using a 2 µm EASY-Spray PepMap RSLC C18 75 µm × 250 mm column (Thermo Fisher) with a column temperature of 55 °C. MS1 was performed at 70,000 resolution, with an AGC target of  $1 \times 10^6$  ions and a maximum IT of 60 ms. MS2 spectra were collected by data-dependent acquisition (DDA) of the top 20 most abundant precursor ions with a charge greater than 1 per MS1 scan, with dynamic exclusion enabled for 30s. Precursor ions were filtered with a 1.0 m/z isolation window and fragmented with a normalized collision energy of 30. MS2 scans were performed at 17,500 resolution, AGC target of  $1 \times 10^5$  ions, and a maximum IT of 60 ms.

### ***Data analysis for TMT proteomics***

Proteome Discoverer 2.2 (PDv2.2) was used for raw data analysis, with default search parameters including oxidation (15.995 Da on M) as a variable modification and carbamidomethyl (57.021 Da on C) and TMT6plex (229.163 Da on peptide N-term and K) as fixed modifications, and 2 missed cleavages (full trypsin specificity). Data were searched against human Mito Carta 2.0 database (Calvo et al., 2016). PSMs were filtered to a 1% FDR. PSMs were grouped to unique peptides while maintaining a 1% FDR at the peptide level. Peptides were grouped to proteins using the rules of strict parsimony and proteins were filtered to 1% FDR using the Protein FDR Validator node of PD2.2. MS2 reporter ion intensities for all PSMs having co-isolation interference below 0.5 (50% of the ion current in the isolation window) and an average S/N > 10 for reporter ions were summed together at the peptide and protein level. Imputation was performed via low abundance resampling.

### ***Statistical analysis for TMT proteomic***

The protein group tab in the PDv2.2 results was exported as tab delimited.txt. files, and analyzed based on a previously described workflow (McLaughlin et al., 2020). First, M2 reporter (TMT) intensities were summed together for each TMT channel, each channel's sum was divided by the average of all channels' sums, resulting in channel-specific loading control normalization factors to correct for any deviation from equal protein input in the 10-plex experiments. Reporter intensities for proteins were divided by the loading control normalization factors for each respective TMT channel. All loading control-normalized reporter intensities were converted to  $\log_2$  space and the average value from the ten samples per kit was subtracted from each sample specific measurement to normalize the relative measurements to the mean of each kit. Data from each kit were then combined for statistical comparisons. For comparison of PBMC to leukemia cell lines, condition average, standard deviation, p-value (p, two-tailed student's t-test, assuming equal variance), and adjusted p-value ( $P_{adjusted}$ , Benjamini Hochberg FDR correction) were calculated (Benjamini and Hochberg, 1995; Naugler and Lesack, 2011). For protein-level quantification, only Master Proteins—or the most statistically significant protein representing a group of parsimonious proteins containing common peptides identified at 1% FDR—were used for quantitative comparison.

### ***Data availability***

All data from the manuscript are available upon request. In addition, all data are available in the source data files provided with this paper. All raw data for proteomics experiments is

available online using accession number “PXD020715” for Proteome Xchange (Deutsch et al., 2017) and accession number “JPST000934” for jPOST Repository (Okuda et al., 2017).

### ***Statistical Analysis and Software***

Statistical analysis was performed using GraphPad Prism 8.4. All data are represented as mean  $\pm$  SEM and analysis were conducted with a significance level set at  $p < 0.05$ . Details of statistical analysis are included within figure legends. Figures were generated using Biorender and GraphPad Prism 8.4.

### **Acknowledgements**

The work was supported by DOD-W81XWH-19-1-0213 (K.H.F.-W.) and NIH P01 CA171983 (M.C.C). This project used the North Carolina Tissue Consortium (NCTC) shared resource which is supported in part by the University Cancer Research Fund (UCRF).

### **Ethics Declaration**

The authors of this manuscript declare no competing interests.

## Figures

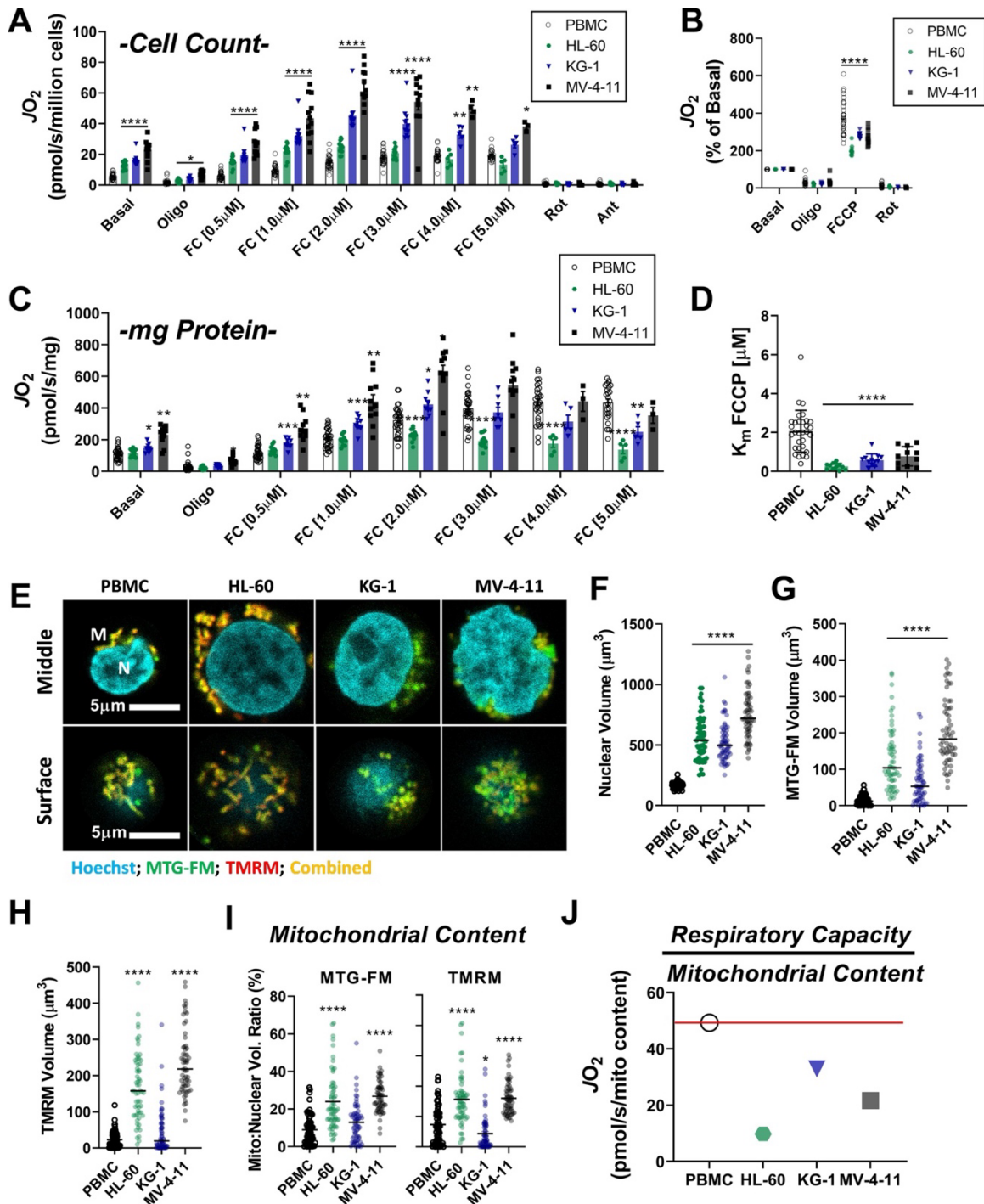


**Figure 1. Leukemia exhibits impaired cellular respiratory capacity amid an increased mitochondrial network.** All experiments were performed in intact cells. FCCP-stimulated flux

normalized to cell count (**A**) and protein concentration (**C**) and represented as percentage of basal respiration (**B**). (**D**)  $K_m$  of FCCP calculated from FCCP titration (cell lines n=12, PBMC n=31). (**E-I**) Confocal microscopy was performed using two mitochondrial targeted cationic fluorescent dyes, MitoTracker Green FM (MTG-FM) and TMRM. (**E**) Representative fluorescent images of nuclear volume (**F**) and mitochondrial volume as measured by MTG-FM (**G**) and TMRM labelling (**H**) (n=65 cells/cell type). (**I**) Ratios of mitochondrial to nuclear volumes assessed by MTG-FM and TMRM labelling. (**J**) Respiratory deficiency of cell type calculated by comparing respiratory capacity (the protein-normalized maximal respiration rate) to mitochondrial content (mitochondrial TMRM volume). Data are presented as mean  $\pm$ SEM and analyzed by two-way ANOVA (**A-D**) and one-way ANOVA (**F-I**). \* $p < 0.05$ , \*\* $p < 0.01$ , \*\*\* $p < 0.001$ , \*\*\*\* $p < 0.0001$ .

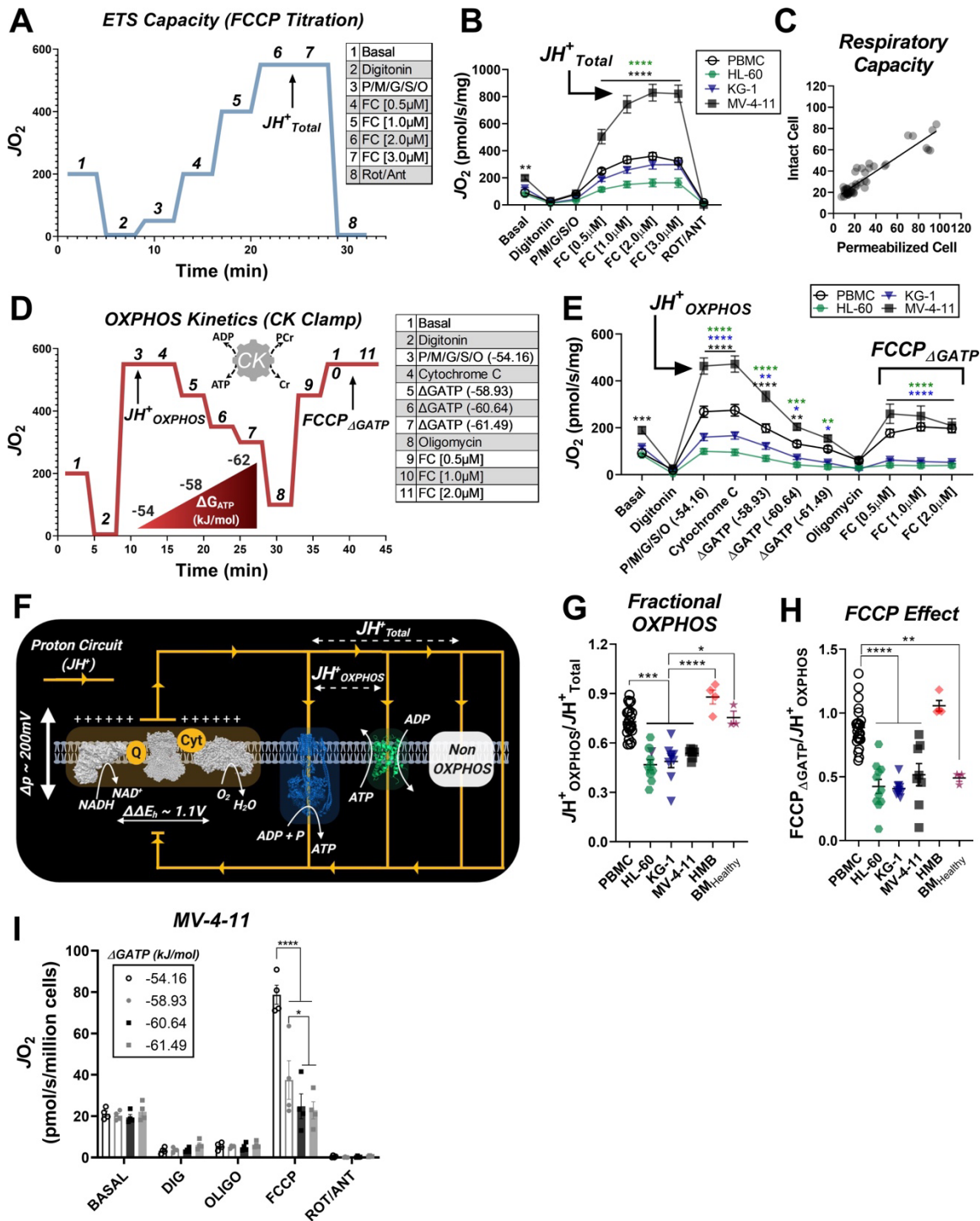


**Figure 2. Impaired OXPHOS kinetics and ATP-dependent inhibition of ETS flux are unique phenotypes of leukemic mitochondria.** All experiments were performed using digitonin-permeabilized cells. (A) Schematic depicting changes in oxygen consumption ( $JO_2$ ) during an

ETS capacity protocol (FCCP titration) where points 6-7 represent the maximum proton conductance of the respiratory system ( $JH^+_{\text{Total}}$ ). **(B)** ETS capacity protocol measured in leukemia cell lines and PBMC. **(C)** Comparison of respiratory capacity between intact and permeabilized experimental conditions across cell types. **(D)** Schematic depicting  $JO_2$  during an OXPHOS kinetics protocol ( $\Delta G_{\text{ATP}}$  titration) where point 3 represents maximum proton conductance by the OXPHOS system ( $JH^+_{\text{OXPHOS}}$ ) and point 10-11 represents maximum proton conductance of the respiratory system in the presence of  $\Delta G_{\text{ATP}}$  (FCCP  $\Delta G_{\text{ATP}}$ ). **(E)** OXPHOS capacity protocol measured in leukemia cell lines and PBMC. **(F)** Illustration detailing maximal proton current generated by the electron transport system ( $JH^+_{\text{Total}}$ ) and proportion of current harnessed by the phosphorylation system ( $JH^+_{\text{OXPHOS}}$ ). **(G)** Comparison of fractional OXPHOS calculated as the ratio of  $JH^+_{\text{OXPHOS}}$  to  $JH^+_{\text{Total}}$ . **(H)** Comparison of FCCP Effect calculated as the ratio of FCCP  $\Delta G_{\text{ATP}}$  to  $JH^+_{\text{OXPHOS}}$ . For all experiments, n=10 for leukemia cell lines, n=22 for PBMC, n=4 for HMB, and n=3 for BM<sub>Healthy</sub>. **(I)** FCCP-stimulated flux was measured under four ATP-free energy ( $\Delta G_{\text{ATP}}$ ) conditions in permeabilized MV-4-11 cells; n=4 independent experiments. Data are presented as mean  $\pm$ SEM and analyzed by two-way ANOVA in **(B, E, I)** and one-way ANOVA in **(G-H)**. \*p<0.05, \*\*p<0.01, \*\*\*p<0.001, \*\*\*\*p<0.0001.

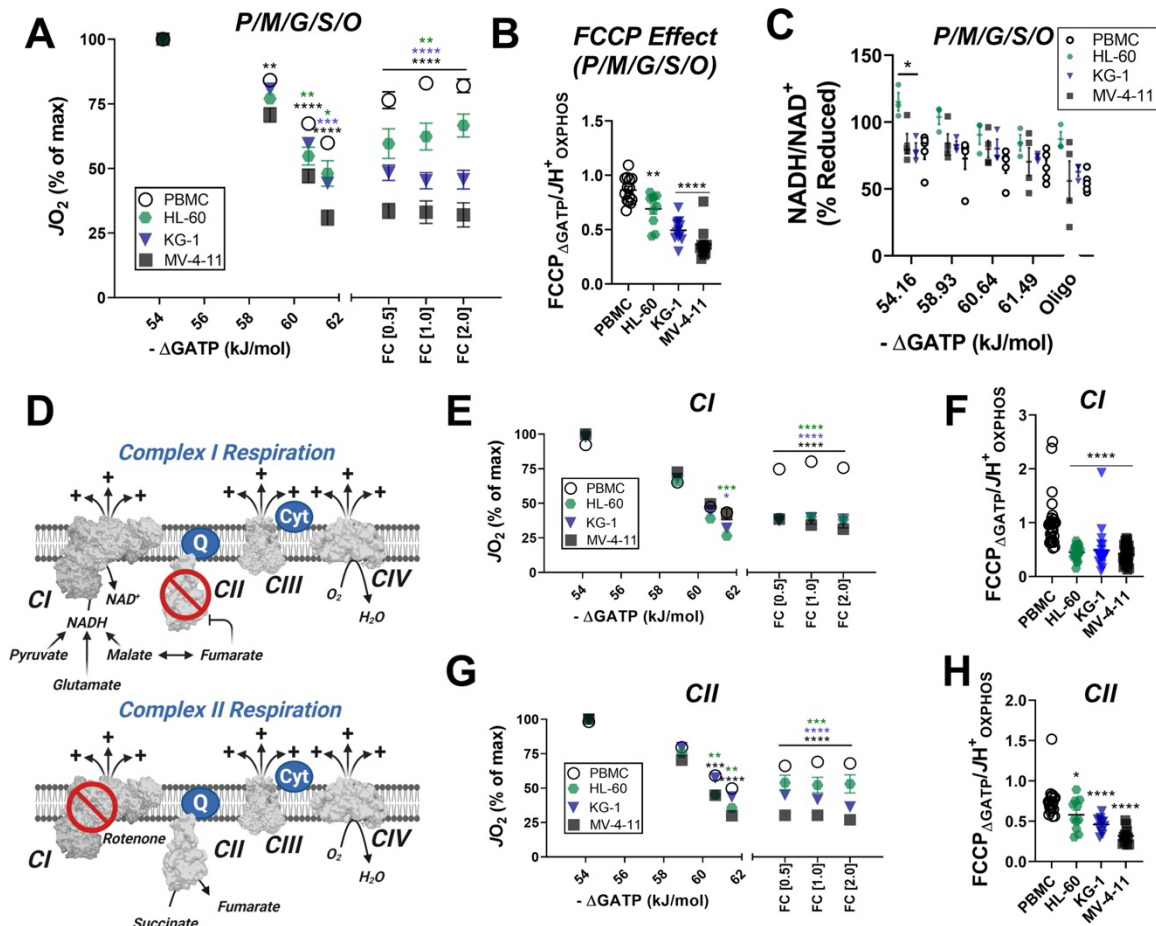


**Figure 3. In leukemic mitochondria  $\Delta G_{ATP}$  regulates ETS flux independent of substrate condition.** (A) OXPHOS kinetics supported by P/M/G/S/O in mitochondria isolated from PBMC and leukemia cells. (B) Comparison of FCCP Effect calculated as the ratio of FCCP  $\Delta G_{ATP}$  to  $JH^{+}_{OXPHOS}$  from B. (C) Relationship between  $\Delta G_{ATP}$  and NADH/NAD<sup>+</sup> redox supported by P/M/G/S/O in mitochondria isolated from leukemia cell lines and PBMC. (D) Schematic depicting CI supported respiration driven by pyruvate/glutamate/malate and inhibition of CII by equilibration of malate/fumarate (top) and CII supported respiration driven by succinate and inhibition of CI by rotenone (bottom). OXPHOS kinetics of mitochondria isolated from PBMC and leukemia cells and supported by Complex I substrates (E) and Complex II substrates (G). FCCP Effect of complex I (F) and complex II (H) supported respiration. (A, B, E-H) n=7-10 for

leukemia cell lines and n=22 for PBMC. (C) n=3-5 independent experiments. Data are mean  $\pm$ SEM and analyzed by one-way ANOVA in (A) and two-way ANOVA in (B-C, E-H). \*p<0.05, \*\*p<0.01, \*\*\*p<0.001, \*\*\*\*p<0.0001.

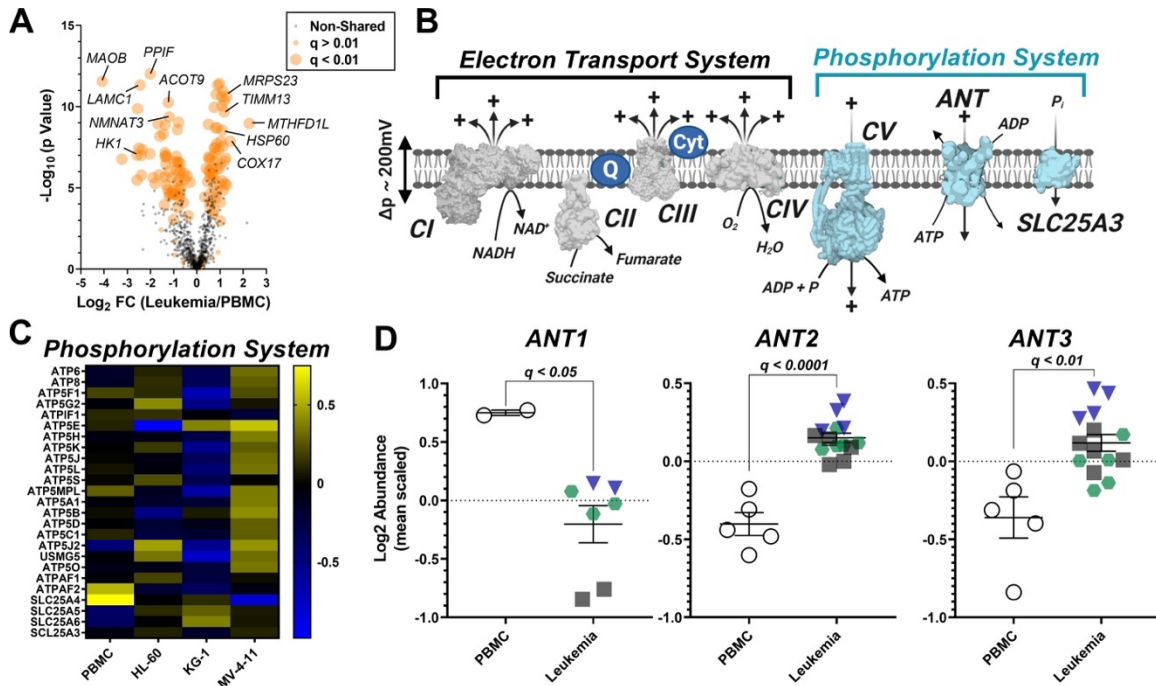


**Figure 4. Analysis of mitochondrial proteome reveal disparate expression of ANT isoforms in leukemia.** TMT-labelled nLC-MS/MS was performed on mitochondrial lysates from each cell type. (A) Volcano plot depicting changes in proteome between leukemia cell lines and PBMC with mitochondrial proteins shown in orange. Significance is indicated by size of each circle with changes in significance ( $p < 0.01$ ) represented by larger circles. (B) Schematic depicting the OXPHOS system with enzymes integral to the ETS shown in gray and the phosphorylation system shown in blue. (C) Heat map displaying the common differentially expressed proteins across the phosphorylation system of leukemia and PBMC. Data are displayed as  $\text{Log}_2$  protein intensity of all quantified master proteins. (D) Comparison of  $\text{log}_2$  abundance of ANT isoforms in leukemia and PBMC; n=4-6 mitochondrial preparations per cell lines. Data are presented as

mean  $\pm$ SEM and analyzed by unpaired t-tests with multiple hypothesis correction ( $P_{adjusted}$ , Benjamini Hochberg FDR correction, significance cutoff of  $q < 0.1$ ).

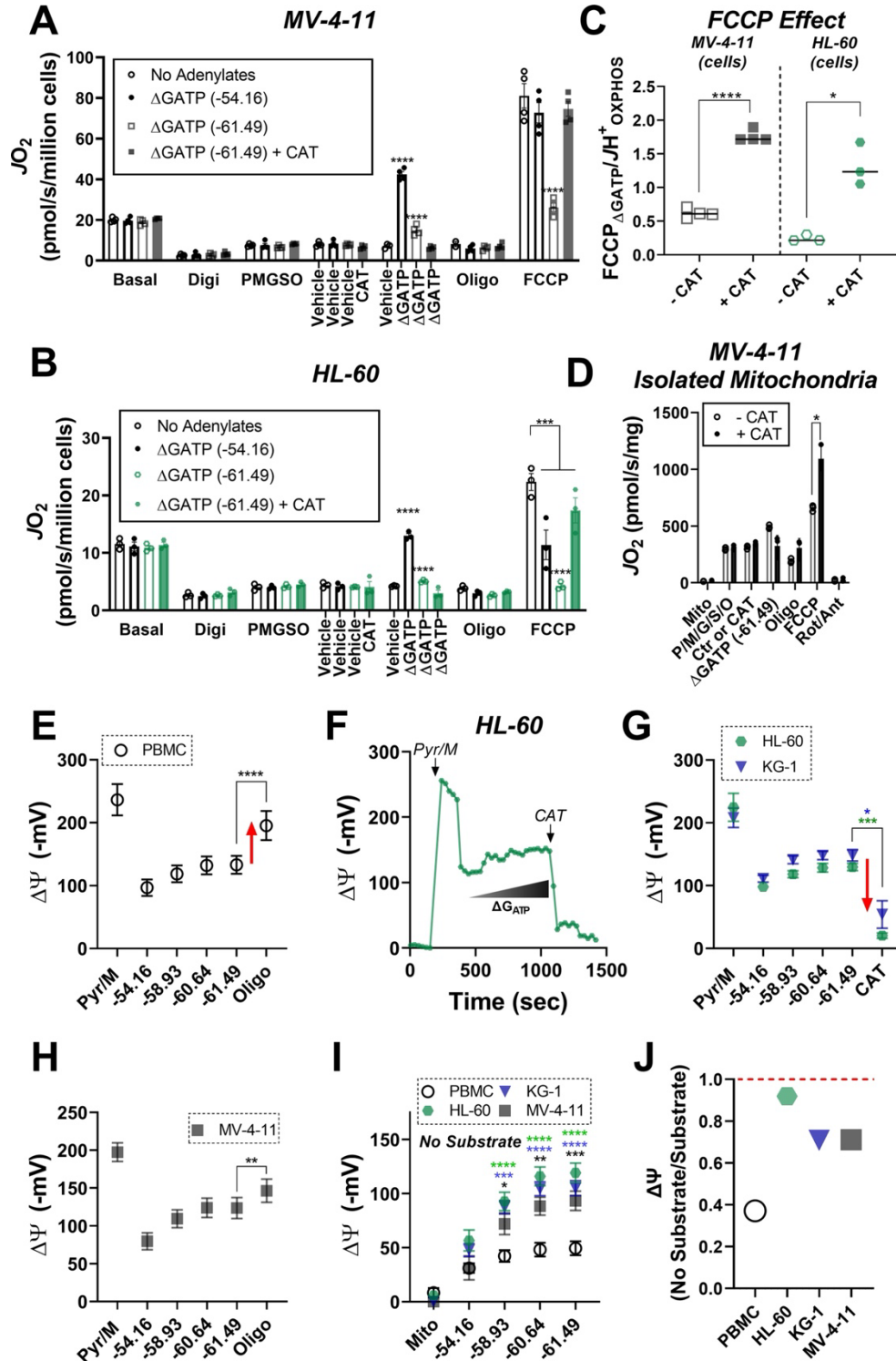


**Figure 5. ETS flux inhibition by  $\Delta G_{ATP}$  links to matrix ATP consumption in leukemia. (A-B)** OXPHOS kinetics (via CK clamp) were assessed in the absence of adenylates or in the presence of minimal  $\Delta G_{ATP}$  (-54.16), maximal  $\Delta G_{ATP}$  (-61.49), or maximal  $\Delta G_{ATP}$  + CAT (Carboxyatractyloside; ANT inhibitor). Comparison of OXPHOS kinetics in MV-4-11 (**A**) and HL-60 cells (**B**). (**C**) Ratio of FCCP <sub>$\Delta G_{ATP}$</sub>  to  $JH^+$ <sub>OXPHOS</sub> with and without CAT in MV-4-11 and HL-60 cells. (**D**) OXPHOS kinetics measured in the presence of CAT in mitochondria isolated from MV-4-11. (**A-D**) n=4 independent experiments per cell type. (**E**) Mitochondrial membrane potential ( $\Delta\Psi$ ) in PBMC isolated mitochondria across a  $\Delta G_{ATP}$  span, followed by CV inhibition with oligomycin; n=8 independent experiments. (**F**) Representative trace of  $\Delta\Psi$  in HL-60 isolated mitochondria across a  $\Delta G_{ATP}$  span, followed by ANT inhibition with CAT. (**G**) Quantification of the experiment depicted in panel **F** in HL-60 and KG-1 isolated mitochondria; n=3 independent experiments. (**H**) Mitochondrial  $\Delta\Psi$  in MV411 isolated mitochondria across a  $\Delta G_{ATP}$  span, followed by CV inhibition with oligomycin; n=9 independent experiments. (**I**) Mitochondrial  $\Delta\Psi$  in isolated mitochondria across a  $\Delta G_{ATP}$  span in the absence of any carbon substrates; n=4 independent experiments. (**J**) Ratio of group mean  $\Delta\Psi$  generated at  $\Delta G_{ATP} = -61.49$  kJ/mol in the absence versus presence of carbon substrates (pyruvate, malate). Data are presented as mean  $\pm$ SEM and analyzed by two-way ANOVA (**A-B, I**) or paired t-tests (**C-E, G-H**). \*p<0.05, \*\*p<0.01, \*\*\*p<0.001, \*\*\*\*p<0.0001.



(TRAP1 KD) or scrambled shRNA (Control). **(I-J)** Fractional OXPHOS and FCCP Effect measured in the presence of vehicle (DMSO), 17-AAG (15 $\mu$ M), or gamitrinib (1 $\mu$ M) in control and TRAP1 KD cells. **(K)** OXPHOS kinetics in permeabilized MV-4-11 cells in the presence of DMSO or curcumin (10-20 $\mu$ M). FCCP Effect is graphed to the right. **(L)** Schematic depicting the presumed mechanism of action of 17-AAG, gamitrinib and curcumin in which the compounds selectively block ATP uptake via the VDAC-ANT axis to restore OXPHOS kinetics. **(M)** Cell proliferation expressed as a percentage of Control. **(N)** Cell viability in MV-4-11 cells infected with lentivirus encoding shRNA targeted to TRAP1 or scrambled shRNA and treated for 24 hours with increasing concentrations of Ara-C. Additional treatments included gamitrinib (1 $\mu$ M), 17-AAG (15 $\mu$ M) or curcumin (10-20 $\mu$ M) either alone or plus Ara-C (20 $\mu$ M). Data depicted as viability based on the percentage of vehicle using the propidium iodide assay. **(A)** n=4/6/group; **(B-D)** n=4 independent experiments; **(E-K)** n=3 independent experiments; **(M)** n=8 independent experiments; **(N)** n=4-6 independent experiments. Data are presented as mean  $\pm$  SEM analyzed by unpaired t-tests **(F-H, M)** two-way ANOVA **(B, K)**, one-way ANOVA **(A, I, J, N)**, paired t-tests **(B-E)**. \*p<0.05, \*\*p<0.01, \*\*\*p<0.001, \*\*\*\*p<0.0001.

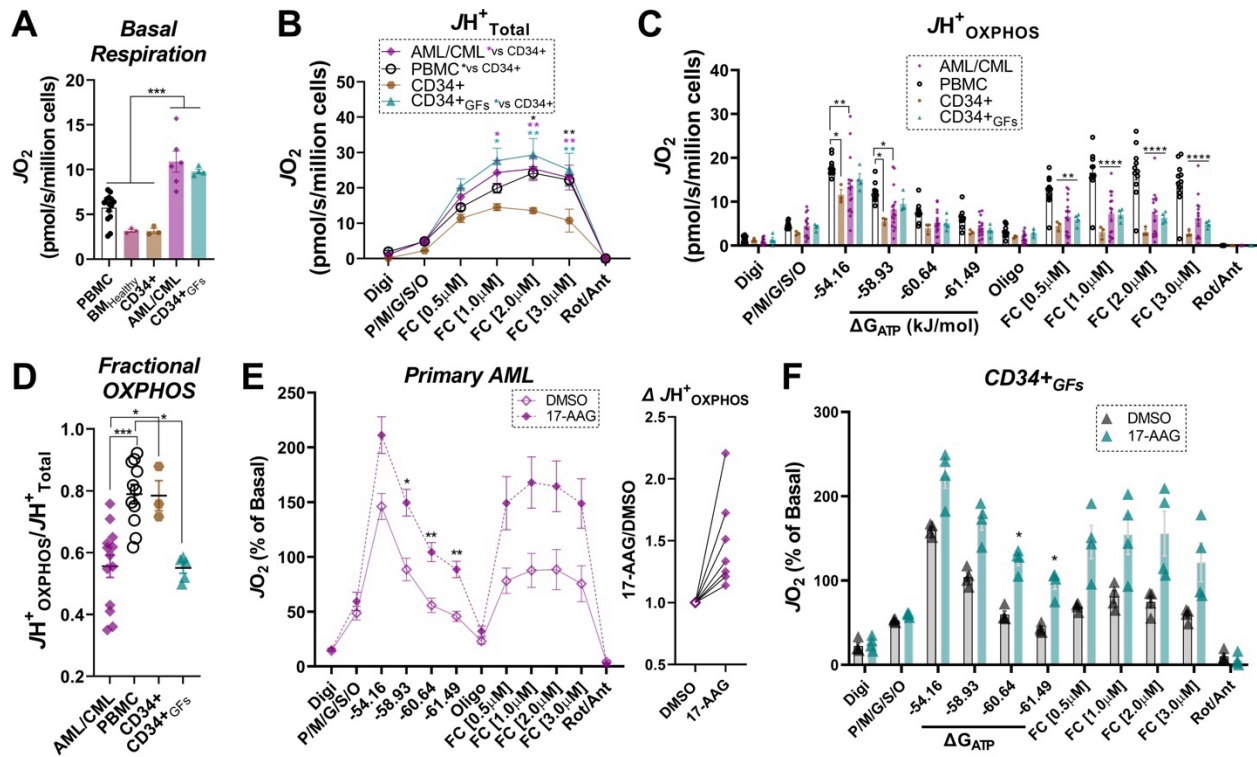
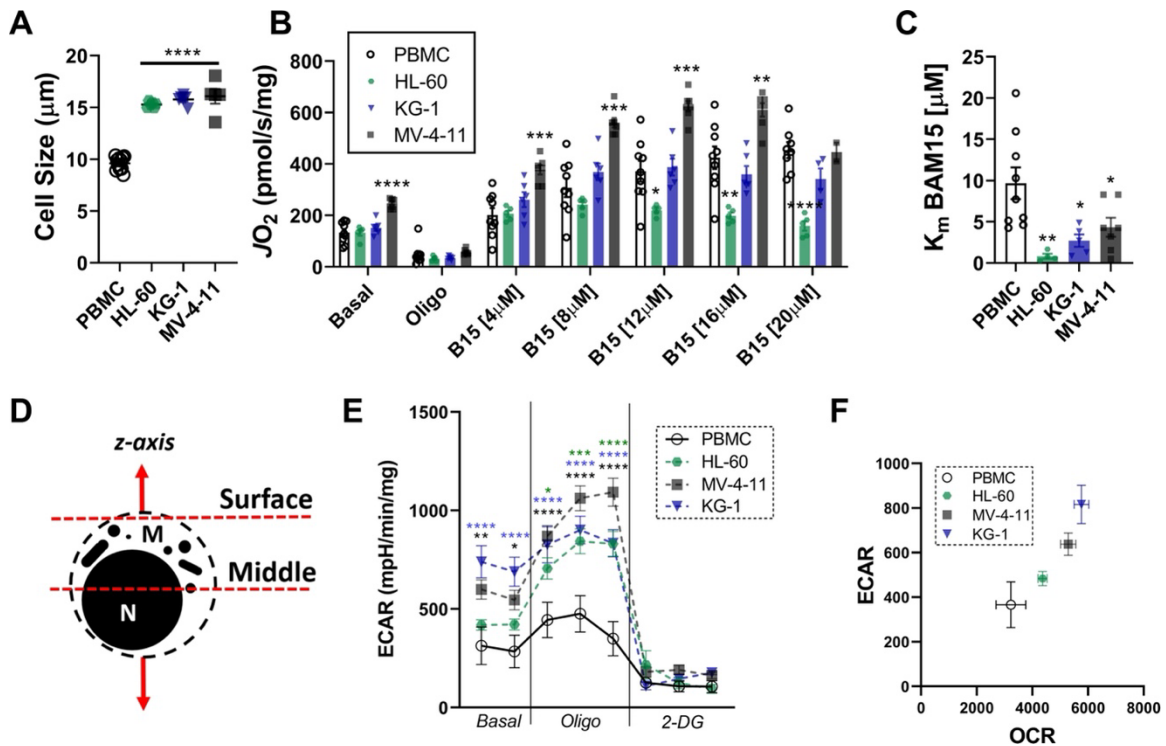


**Figure 7. Human primary leukemia is characterized by low Fractional OXPHOS.**

(A) Basal respiration in intact cells – ‘PBMC’ (age-matched to the primary leukemia samples); ‘BM<sub>Healthy</sub>’ (bone marrow mononuclear cells); ‘CD34+’ (pure CD34+ cells not exposed to growth factors); ‘P. Leukemia’ (mononuclear cells isolated from bone marrow of patients with confirmed leukemia); ‘CD34+GFs’ (pure CD34+ cells stimulated to undergo clonal expansion in culture). (B) ETS capacity assay in permeabilized cells. (C) OXPHOS kinetics in permeabilized cells. (D) Fractional OXPHOS. (A-D) n=3-15 independent experiments. (E) Comparison of OXPHOS kinetics in the presence of DMSO or 17-AAG (15μM) in a cohort of patients with confirmed AML. Graph to the right depicts  $JH^+_{OXPHOS}$  depicted as a fold change from DMSO; n=7 independent cell experiments. (F) Comparison of OXPHOS kinetics in the presence of DMSO or 17-AAG (15μM) in CD34+GFs; n=4 independent cell experiments. (E-F) Data depicted as a percentage of basal respiration based on oxygen consumption rates obtained in intact cells. Data are presented as mean



free RPMI media. (D) OXPPOS kinetics in permeabilized cells. (E) Effect of cytochrome C addition on  $JH^+_{\text{OXPPOS}}$ . Data expresses as fold change from rates obtained prior to cytochrome C addition. (F) Fractional OXPPOS - note,  $JH^+_{\text{Total}}$  was calculated from the intact cell assay in C using the maximal rate stimulated by FCCP. (G) Rate of ATP synthesis ( $J_{\text{ATP}}$ ) and oxygen consumption ( $J_{\text{O}_2}$ ) in permeabilized cells energized with P/M/G/S/O. (H) Calculated P/O ratio. (I) Calculated OXPPOS power output. (C-I) n=4 independent experiments. Data are presented as mean  $\pm$  SEM analyzed by unpaired t-tests. \*p<0.05, \*\*p<0.01, \*\*\*p<0.001, \*\*\*\*p<0.0001.



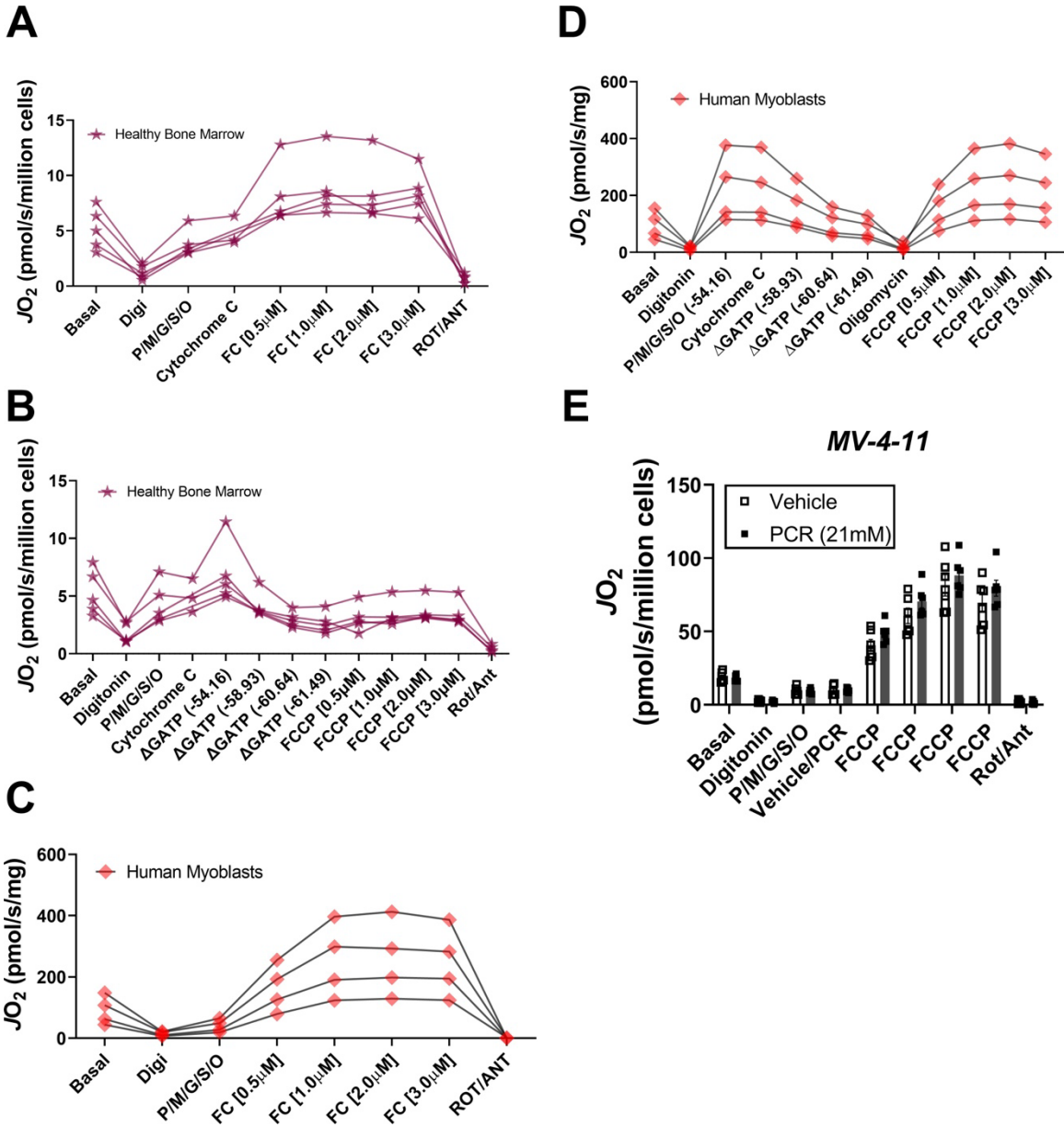
**Supplementary Figure 1. Morphology of leukemia and respiratory flux stimulated by BAM15, a mitochondrial uncoupler. (A) Comparison of cell size of leukemia cells and PBMC.**

Respiratory flux driven by BAM15 (B15), a mitochondrial uncoupler (B) and observed  $K_m$  (C).

(D) Cellular focal planes used to obtain confocal images. (E) Extracellular acidification rate

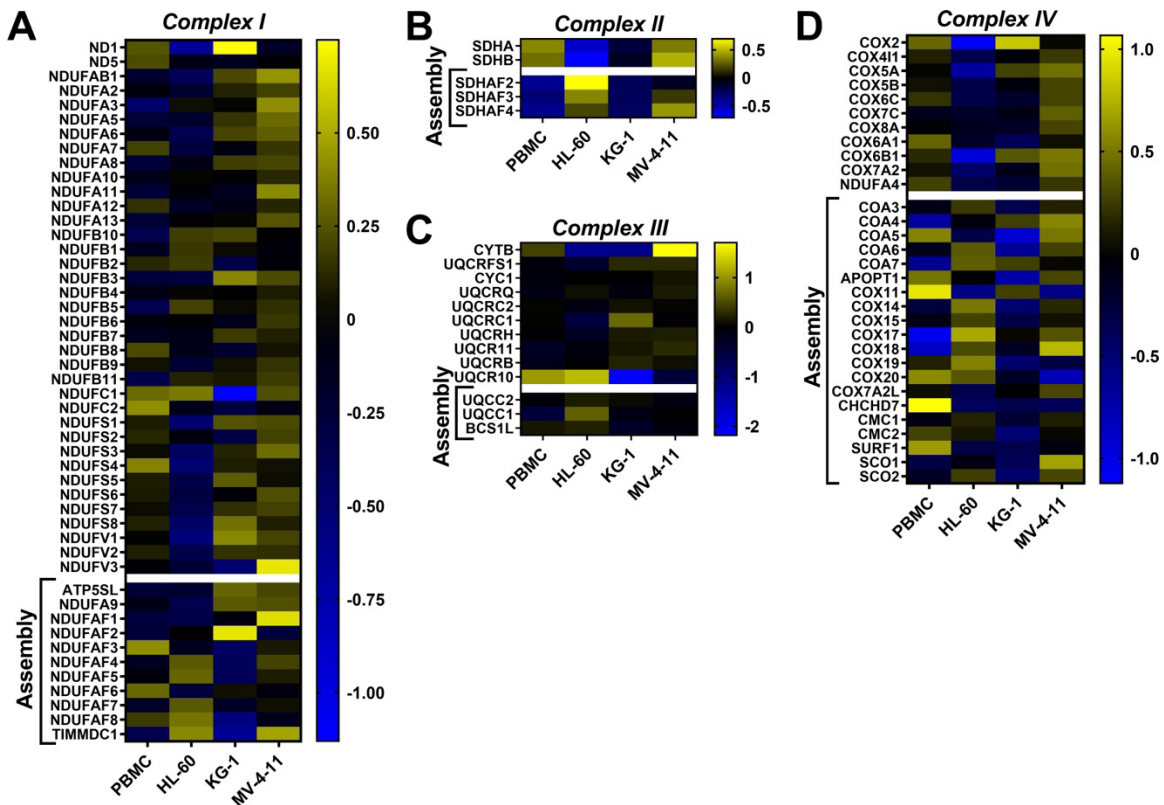
(ECAR) in intact cell. (F) Relationship between ECAR and OCR in intact cells under basal

conditions. Data are presented as mean  $\pm$ SEM and analyzed by one-way ANOVA (A, C), two-way ANOVA (B), or unpaired t-tests (E). n= 5-7 independent experiments. \*p<0.05, \*\*p<0.01, \*\*\*p<0.001, \*\*\*\*p<0.0001.

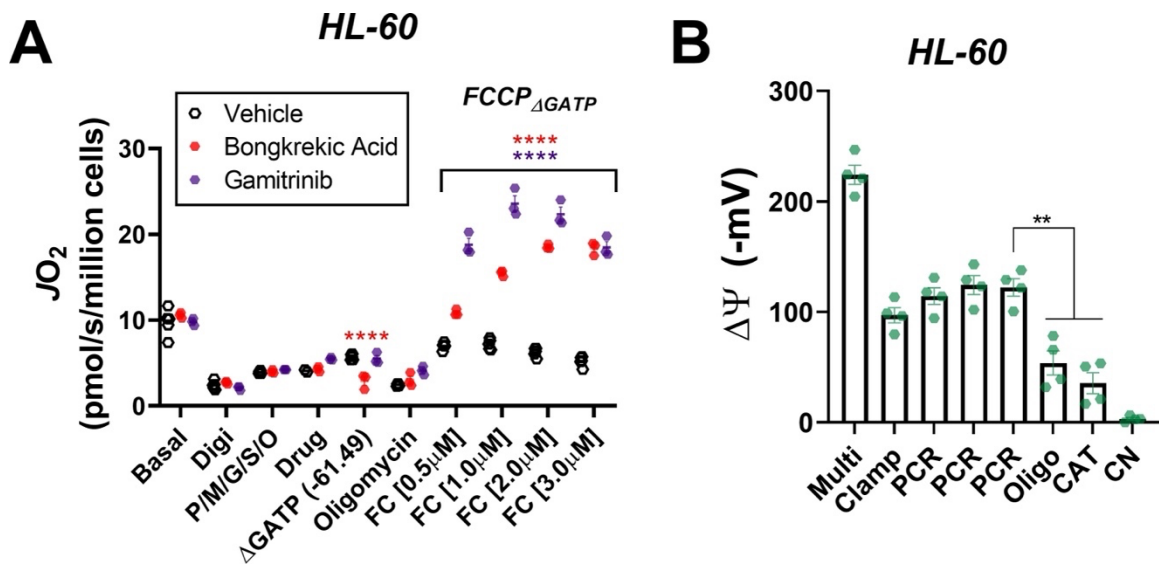


**Supplementary Figure 2. Respiratory profile of healthy bone marrow mononuclear cells and primary human myoblasts.** (A-E) Permeabilized cells were used for all experiments. ETS

capacity (A) and OXPHOS kinetic (B) protocols were performed in permeabilized BM<sub>Healthy</sub>. Data depict results from each replicate across samples from three independent donors. ETS capacity (C) and OXPHOS kinetic (D) protocols were performed in permeabilized primary human myoblasts; n=4 independent experiments. (E) OXPHOS kinetics were performed with PCr and creatine kinase but in the absence of ATP in permeabilized MV-4-11 cells; n=6 independent experiments. Data are presented as mean  $\pm$ SEM and analyzed by paired t-test (E). \*p<0.05

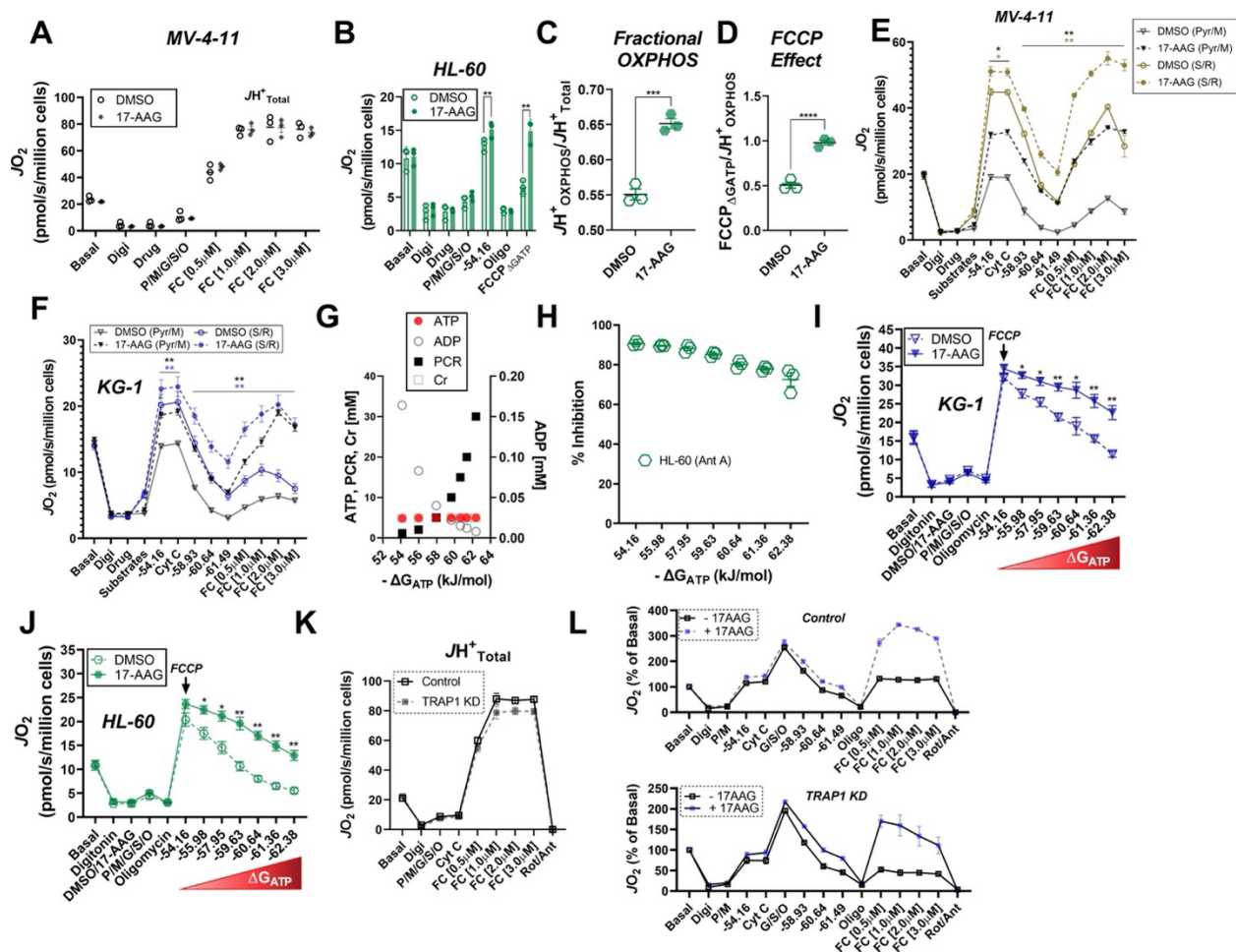


**Supplementary Figure 3. Heatmap analysis depicting abundance of subunits and assembly factors that comprise the ETS complexes.** Heatmap displaying relative protein abundance of the individual subunits and assembly factors belonging to (A) complex I (B) complex II (C) Complex III and (D) Complex IV.



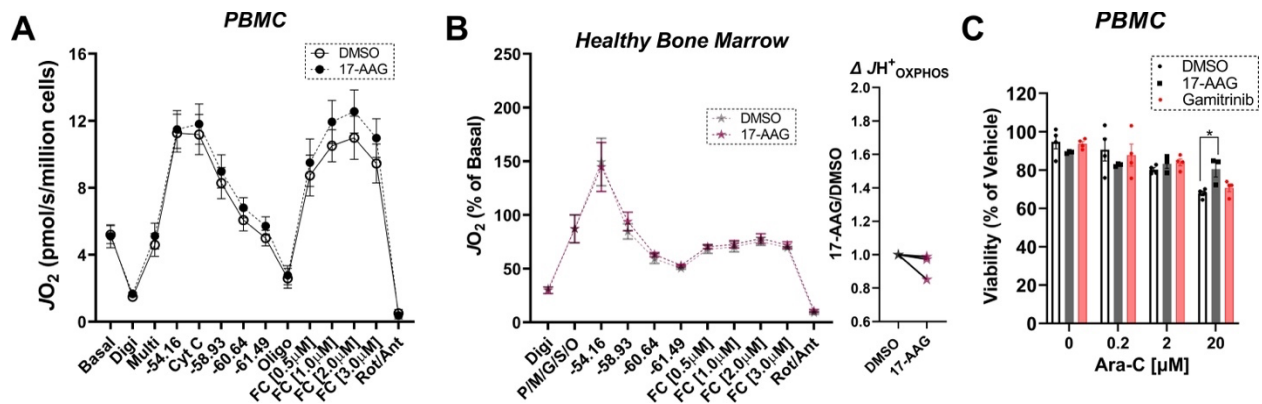
**Supplementary Figure 4. ETS flux in the presence of  $\Delta G_{ATP}$  is restored by ANT inhibition**

*ANT*. (A) OXPHOS kinetics in permeabilized HL-60 cells in the presence of DMSO (vehicle), bongkreikic acid (20  $\mu$ M; ANT inhibitor) or gamitrinib (1  $\mu$ M; TRAP1 inhibitor with mitochondria-targeted moiety); n=3 independent experiments. (B) Mitochondrial membrane potential ( $\Delta\Psi$ ) in HL-60 isolated mitochondria across a  $\Delta G_{ATP}$  span, followed by CV inhibition with oligomycin; n=3 independent experiments.. Data are presented as mean  $\pm$ SEM and analyzed by two-way ANOVA (A) or paired t-test (B). \*p<0.05, \*\*p<0.01, \*\*\*p<0.001, \*\*\*\*p<0.0001.



**Supplementary Figure 5. Effects of 17-AAG on OXPHOS kinetics.** (A) Comparison of FCCP-stimulated respiration with the addition of 17-AAG (15 $\mu$ M) in permeabilized MV-4-11 cells; n=3 independent experiments. (B-D) OXPHOS kinetics in permeabilized HL-60 cells in the presence of DMSO or 17-AAG (15 $\mu$ M); n=3 independent experiments. (E-F) OXPHOS kinetics in permeabilized MV-4-11 or KG-1 cells in the presence of DMSO or 17-AAG (15 $\mu$ M). Cell were energized with either CI (Pyr/M) or CII linked substrates (S/R); n=3 independent experiments. (G) Schematic of changes in ATP, ADP, PCR and CR concentrations across a range of  $\Delta G_{ATP}$ . (H) Inhibition of respiration by antimycin A (ANT) across a range of  $\Delta G_{ATP}$  in permeabilized HL-60 cells; n=3 independent experiments. (I-J) Comparison of respiratory flux inhibition within permeabilized AML cells across a range of  $\Delta G_{ATP}$  induced by functional

TRAP1. Respiration was stimulated by the addition of FCCP (1 $\mu$ M), followed by PCR titration to manipulate  $\Delta G_{ATP}$ ; n=3 independent experiments. **(K)** ETS capacity assay in permeabilized MV-4-11 cells infected with lentivirus encoding shRNA targeted to TRAP1 (TRAP1 KD) or scrambled shRNA (Control); n=3 independent experiments. **(L)** Comparison of OXPHOS kinetics in the presence of DMSO, 17-AAG (15 $\mu$ M), or gamitrinib (1 $\mu$ M) in Control and TRAP1 KD cells. Data depicted as a percentage of basal respiration based on oxygen consumption rates obtained prior to digitonin permeabilization; n=3 independent experiments. Data are presented as mean  $\pm$ SEM and analyzed by paired t-tests (**A-F, H-J**) or unpaired t-tests (**K-L**). \*p<0.05, \*\*p<0.01, \*\*\*p<0.001, \*\*\*\*p<0.0001.



**Supplementary Figure 6. Effects of 17-AAG on OXPHOS kinetics and cell viability in PBMC**

**and healthy bone marrow mononuclear cells.** **(A)** Comparison of OXPHOS kinetics in the presence of DMSO or 17-AAG (15 $\mu$ M) in permeabilized PBMC from healthy donors; n=5 independent experiments. **(B)** Comparison of OXPHOS kinetics in the presence of DMSO or 17-AAG (15 $\mu$ M) in permeabilized BM<sub>Healthy</sub>. Graph to the right depicts  $\Delta JH^+_{OXPHOS}$  depicted as a fold change from DMSO. Data depicted as a percentage of basal respiration based on oxygen consumption rates obtained in intact cells; n=3 independent cell experiments. **(C)** Cell viability in PBMC from healthy donors cultured for 24 hours in the presence of vehicle (DMSO), 17-

AAG (15 $\mu$ M), or gamitrinib (1 $\mu$ M) plus increasing concentrations of Ara-C. Data depicted as viability based on the percentage of vehicle using the propidium iodide assay; n=3-4 independent experiments. Data are presented as mean  $\pm$ SEM and analyzed by paired t-test (**A-B**) or two-way ANOVA (**C**). \*p<0.05

## REFERENCES

- Benjamini Y, Hochberg Y. 1995. Controlling the false discovery rate: a practical and powerful approach to multiple testing. *J R Stat Soc Ser B*. doi:10.2307/2346101
- Bryant KG, Chae YC, Martinez RL, Gordon JC, Elokely KM, Kossenkov A V., Grant S, Childers WE, Abou-Gharbia M, Altieri DC. 2017. A Mitochondrial-targeted purine-based HSP90 antagonist for leukemia therapy. *Oncotarget*. doi:10.18632/oncotarget.23097
- Buck MDD, O'Sullivan D, Klein Geltink RII, Curtis JDD, Chang CH, Sanin DEE, Qiu J, Kretz O, Braas D, van der Windt GJJW, Chen Q, Huang SCC, O'Neill CMM, Edelson BTT, Pearce EJJ, Sesaki H, Huber TBB, Rambold ASS, Pearce ELL. 2016. Mitochondrial Dynamics Controls T Cell Fate through Metabolic Programming. *Cell*. doi:10.1016/j.cell.2016.05.035
- Byrd JC, Furman RR, Coutre SE, Flinn IW, Burger JA, Blum KA, Grant B, Sharman JP, Coleman M, Wierda WG, Jones JA, Zhao W, Heerema NA, Johnson AJ, Sukbuntherng J, Chang BY, Clow F, Hedrick E, Buggy JJ, James DF, O'Brien S. 2013. Targeting BTK with ibrutinib in relapsed chronic lymphocytic leukemia. *N Engl J Med*. doi:10.1056/NEJMoa1215637
- Calvo SE, Clauser KR, Mootha VK. 2016. MitoCarta2.0: An updated inventory of mammalian mitochondrial proteins. *Nucleic Acids Res*. doi:10.1093/nar/gkv1003

- Chevrollier A, Loiseau D, Reynier P, Stepien G. 2011. Adenine nucleotide translocase 2 is a key mitochondrial protein in cancer metabolism. *Biochim Biophys Acta - Bioenerg.*  
doi:10.1016/j.bbabi.2010.10.008
- Cohen BH. 2010. Pharmacologic effects on mitochondrial function. *Dev Disabil Res Rev.*  
doi:10.1002/ddrr.106
- Deutsch EW, Csordas A, Sun Z, Jarnuczak A, Perez-Riverol Y, Ternent T, Campbell DS, Bernal-Llinares M, Okuda S, Kawano S, Moritz RL, Carver JJ, Wang M, Ishihama Y, Bandeira N, Hermjakob H, Vizcaíno JA. 2017. The ProteomeXchange consortium in 2017: Supporting the cultural change in proteomics public data deposition. *Nucleic Acids Res.*  
doi:10.1093/nar/gkw936
- Dykens JA, Will Y. 2007. The significance of mitochondrial toxicity testing in drug development. *Drug Discov Today.* doi:10.1016/j.drudis.2007.07.013
- Farge T, Saland E, de Toni F, Aroua N, Hosseini M, Perry R, Bosc C, Sugita M, Stuani L, Fraisse M, Scotland S, Larrue C, Boutzen H, Féliu V, Nicolau-Travers ML, Cassant-Sourdy S, Broin N, David M, Serhan N, Sarry A, Tavitian S, Kaoma T, Vallar L, Iacovoni J, Linares LK, Montersino C, Castellano R, Griessinger E, Collette Y, Duchamp O, Barreira Y, Hirsch P, Palama T, Gales L, Delhommeau F, Garmy-Susini BH, Portais JC, Vergez F, Selak M, Danet-Desnoyers G, Carroll M, Récher C, Sarry JE. 2017. Chemotherapy-resistant human acute myeloid leukemia cells are not enriched for leukemic stem cells but require oxidative metabolism. *Cancer Discov* 7:716–735. doi:10.1158/2159-8290.CD-16-0441
- Fisher-Wellman KH, Davidson MT, Narowski TM, Lin C Te, Koves TR, Muoio DM. 2018. Mitochondrial Diagnostics: A Multiplexed Assay Platform for Comprehensive Assessment of Mitochondrial Energy Fluxes. *Cell Rep* Sep 25;24:3593–3606.

doi:10.1016/j.celrep.2018.08.091

- Fisher-Wellman KH, Draper JA, Davidson MT, Williams AS, Narowski TM, Slentz DH, Ilkayeva OR, Stevens RD, Wagner GR, Najjar R, Hirschey MD, Thompson JW, Olson DP, Kelly DP, Koves TR, Grimsrud PA, Muoio DM. 2019. Respiratory Phenomics across Multiple Models of Protein Hyperacetylation in Cardiac Mitochondria Reveals a Marginal Impact on Bioenergetics. *Cell Rep*. doi:10.1016/j.celrep.2019.01.057
- Glancy B, Willis WT, Chess DJ, Balaban RS. 2013. Effect of calcium on the oxidative phosphorylation cascade in skeletal muscle mitochondria. *Biochemistry* **52**:2793–2809. doi:10.1021/bi3015983
- Goto M, Miwa H, Shikami M, Tsunekawa-Imai N, Suganuma K, Mizuno S, Takahashi M, Mizutani M, Hanamura I, Nitta M. 2014a. Importance of glutamine metabolism in leukemia cells by energy production through TCA cycle and by redox homeostasis. *Cancer Invest* **32**:241–247. doi:10.3109/07357907.2014.907419
- Goto M, Miwa H, Suganuma K, Tsunekawa-Imai N, Shikami M, Mizutani M, Mizuno S, Hanamura I, Nitta M. 2014b. Adaptation of leukemia cells to hypoxic condition through switching the energy metabolism or avoiding the oxidative stress. *BMC Cancer* **14**:1–9. doi:10.1186/1471-2407-14-76
- Guièze R, Liu VM, Rosebrock D, Jourdain AA, Hernández-Sánchez M, Martínez Zurita A, Sun J, Ten Hacken E, Baranowski K, Thompson PA, Heo JM, Cartun Z, Aygün O, Iorgulescu JB, Zhang W, Notarangelo G, Livitz D, Li S, Davids MS, Biran A, Fernandes SM, Brown JR, Lako A, Ciantra ZB, Lawlor MA, Keskin DB, Udeshi ND, Wierda WG, Livak KJ, Letai AG, Neuberg D, Harper JW, Carr SA, Piccioni F, Ott CJ, Leshchiner I, Johannessen CM, Doench J, Mootha VK, Getz G, Wu CJ. 2019. Mitochondrial Reprogramming Underlies

- Resistance to BCL-2 Inhibition in Lymphoid Malignancies. *Cancer Cell* **36**:369-384.e13.  
doi:10.1016/j.ccell.2019.08.005
- Helling S, Hüttemann M, Ramzan R, Kim SH, Lee I, Müller T, Langenfeld E, Meyer HE, Kadenbach B, Vogt S, Marcus K. 2012. Multiple phosphorylations of cytochrome c oxidase and their functions. *Proteomics* **12**:950–959. doi:10.1002/pmic.201100618
- Inoue T, Swain A, Nakanishi Y, Sugiyama D. 2014. Multicolor analysis of cell surface marker of human leukemia cell lines using flow cytometry *Anticancer Research*.
- Ivanusic D, Madela K, Denner J. 2017. Easy and cost-effective stable positioning of suspension cells during live-cell imaging. *J Biol Methods* **4**:80. doi:10.14440/jbm.2017.203
- Jitschin R, Hofmann AD, Bruns H, Gießl A, Bricks J, Berger J, Saul D, Eckart MJ, Mackensen A, Mougiakakos D. 2014. Mitochondrial metabolism contributes to oxidative stress and reveals therapeutic targets in chronic lymphocytic leukemia. *Blood* **123**:2663–2672.  
doi:10.1182/blood-2013-10-532200
- Kadenbach B. 2020. Complex IV– the regulatory center of mitochondrial oxidative phosphorylation. *Mitochondrion*. doi:10.1016/j.mito.2020.10.004
- Kamal A, Thao L, Sensintaffar J, Zhang L, Boehm MF, Fritz LC, Burrows FJ. 2003. A high-affinity conformation of Hsp90 confers tumour selectivity on Hsp90 inhibitors. *Nature* **425**:407–410. doi:10.1038/nature01913
- Kao L-P, Morad SAF, Davis TS, MacDougall MR, Kassai M, Abdelmageed N, Fox TE, Kester M, Loughran TP, Abad JL, Fabrias G, Tan S-F, Feith DJ, Claxton DF, Spiegel S, Fisher-Wellman KH, Cabot MC. 2019. Chemotherapy selection pressure alters sphingolipid composition and mitochondrial bioenergetics in resistant HL-60 cells. *J Lipid Res* **60**.  
doi:10.1194/jlr.RA119000251

- Kao LP, Morad SAF, Davis TS, MacDougall MR, Kassai M, Abdelmageed N, Fox TE, Kester M, Loughran TP, Abad JL, Fabrias G, Tan SF, Feith DJ, Claxton DF, Spiegel S, Fisher-Wellman KH, Cabot MC. 2019. Chemotherapy selection pressure alters sphingolipid composition and mitochondrial bioenergetics in resistant HL-60 cells. *J Lipid Res*. doi:10.1194/jlr.RA119000251
- Kim Darong, Kim SY, Kim Dongyoung, Yoon NG, Yun J, Hong KB, Lee C, Lee JH, Kang BH, Kang S. 2020. Development of pyrazolo[3,4-d]pyrimidine-6-amine-based TRAP1 inhibitors that demonstrate in vivo anticancer activity in mouse xenograft models. *Bioorg Chem* **101**:103901. doi:10.1016/j.bioorg.2020.103901
- Kuntz EM, Baquero P, Michie AM, Dunn K, Tardito S, Holyoake TL, Helgason GV, Gottlieb E. 2017. Targeting mitochondrial oxidative phosphorylation eradicates therapy-resistant chronic myeloid leukemia stem cells. *Nat Med* **23**:1234–1240. doi:10.1038/nm.4399
- Lagadinou ED, Sach A, Callahan K, Rossi RM, Neering SJ, Minhajuddin M, Ashton JM, Pei S, Grose V, O'Dwyer KM, Liesveld JL, Brookes PS, Becker MW, Jordan CT. 2013. BCL-2 inhibition targets oxidative phosphorylation and selectively eradicates quiescent human leukemia stem cells. *Cell Stem Cell* **12**:329–341. doi:10.1016/j.stem.2012.12.013
- Laquatra C, Sanchez-Martin C, Dinarello A, Cannino G, Minervini G, Moroni E, Schiavone M, Tosatto S, Argenton F, Colombo G, Bernardi P, Masgras I, Rasola A. 2021. HIF1 $\alpha$ -dependent induction of the mitochondrial chaperone TRAP1 regulates bioenergetic adaptations to hypoxia. *Cell Death Dis* **12**:434. doi:10.1038/s41419-021-03716-6
- Lark DS, Torres MJ, Lin C Te, Ryan TE, Anderson EJ, Neuffer PD. 2016. Direct real-time quantification of mitochondrial oxidative phosphorylation efficiency in permeabilized skeletal muscle myofibers. *Am J Physiol - Cell Physiol*. doi:10.1152/ajpcell.00124.2016

- Lee CH, Kim MJ, Lee HH, Paeng JC, Park YJ, Oh SW, Chai YJ, Kim YA, Cheon GJ, Kang KW, Youn H, Chung JK. 2019. Adenine Nucleotide Translocase 2 as an Enzyme Related to [18F] FDG Accumulation in Various Cancers. *Mol Imaging Biol* **21**:722–730. doi:10.1007/s11307-018-1268-x
- Lee D, Xu IMJ, Chiu DKC, Lai RKH, Tse APW, Li LL, Law CT, Tsang FHC, Wei LL, Chan CYK, Wong CM, Ng IOL, Wong CCL. 2017. Folate cycle enzyme MTHFD1L confers metabolic advantages in hepatocellular carcinoma. *J Clin Invest*. doi:10.1172/JCI90253
- Lee EA, Angka L, Rota SG, Hanlon T, Mitchell A, Hurren R, Wang XM, Gronda M, Boyaci E, Bojko B, Minden M, Sriskanthadevan S, Datti A, Wrana JL, Edginton A, Pawliszyn J, Joseph JW, Quadriatero J, Schimmer AD, Spagnuolo PA. 2015. Targeting mitochondria with avocatin B induces selective leukemia cell death. *Cancer Res* **75**:2478–2488. doi:10.1158/0008-5472.CAN-14-2676
- Li XT, Li YS, Shi ZY, Guo XL. 2020. New insights into molecular chaperone TRAP1 as a feasible target for future cancer treatments. *Life Sci* **254**:117737. doi:10.1016/j.lfs.2020.117737
- Liu F, Kalpage HA, Wang D, Edwards H, Hüttemann M, Ma J, Su Y, Carter J, Li X, Polin L, Kushner J, Dzinic SH, White K, Wang G, Taub JW, Ge Y. 2020. Cotargeting of mitochondrial complex i and bcl-2 shows antileukemic activity against acute myeloid leukemia cells reliant on oxidative phosphorylation. *Cancers (Basel)* **12**:1–19. doi:10.3390/cancers12092400
- Luengo A, Li Z, Gui D, Sullivan L, Zagorulya M, Do B, Ferreira R, Naamati A, Ali A, Lewis C, Thomas C, Spranger S, Matheson N, Vander Heiden M. 2020. Increased demand for NAD<sup>+</sup> relative to ATP drives aerobic glycolysis. *Mol Cell* 1–17. doi:10.1101/2020.06.08.140558

- Luptak I, Sverdlov AL, Panagia M, Qin F, Pimentel DR, Croteau D, Siwik DA, Ingwall JS, Bachschmid MM, Balschi JA, Colucci WS. 2018. Decreased ATP production and myocardial contractile reserve in metabolic heart disease. *J Mol Cell Cardiol* **116**:106–114. doi:10.1016/j.yjmcc.2018.01.017
- Maldonado EN, DeHart DN, Patnaik J, Klatt SC, Gooz MB, Lemasters JJ. 2016. ATP/ADP turnover and import of glycolytic ATP into mitochondria in cancer cells is independent of the adenine nucleotide translocator. *J Biol Chem* **291**:19642–19650. doi:10.1074/jbc.M116.734814
- Martínez-Reyes I, Cardona LR, Kong H, Vasani K, McElroy GS, Werner M, Kihshen H, Reczek CR, Weinberg SE, Gao P, Steinert EM, Piseaux R, Budinger GRS, Chandel NS. 2020. Mitochondrial ubiquinol oxidation is necessary for tumour growth. *Nature*. doi:10.1038/s41586-020-2475-6
- McLaughlin KL, Kew KA, McClung JM, Fisher-Wellman KH. 2020. Subcellular proteomics combined with bioenergetic phenotyping reveals protein biomarkers of respiratory insufficiency in the setting of proofreading-deficient mitochondrial polymerase. *Sci Rep*. doi:10.1038/s41598-020-60536-y
- McLaughlin KL, McClung JM, Fisher-Wellman KH. 2018. Bioenergetic consequences of compromised mitochondrial DNA repair in the mouse heart. *Biochem Biophys Res Commun* **3**–9. doi:10.1016/j.bbrc.2018.09.022
- Messer JJ, Jackman MR, Willis WT. 2004. Pyruvate and citric acid cycle carbon requirements in isolated skeletal muscle mitochondria. *Am J Physiol Cell Physiol* **286**:C565-572. doi:10.1152/ajpcell.00146.2003
- Mirali S, Botham A, Voisin V, Xu C, St-Germain J, Sharon D, Hoff FW, Qiu Y, Hurren R,

- Gronda M, Jitkova Y, Nachmias B, MacLean N, Wang X, Arruda A, Minden MD, Horton TM, Kornblau SM, Chan SM, Bader GD, Raught B, Schimmer AD. 2020. The mitochondrial peptidase, neurolysin, regulates respiratory chain supercomplex formation and is necessary for AML viability. *Sci Transl Med* **12**:1–17.  
doi:10.1126/scitranslmed.aaz8264
- Mrózek K, Tanner SM, Heinonen K, Bloomfield CD. 2003. Molecular cytogenetic characterization of the KG-1 and KG-1a acute myeloid leukemia cell lines by use of spectral karyotyping and fluorescence in situ hybridization. *Genes Chromosom Cancer* **38**:249–252. doi:10.1002/gcc.10274
- Naugler C, Lesack K. 2011. An open-source software program for performing Bonferroni and related corrections for multiple comparisons. *J Pathol Inform.* doi:10.4103/2153-3539.91130
- Okuda S, Watanabe Y, Moriya Y, Kawano S, Yamamoto T, Matsumoto M, Takami T, Kobayashi D, Araki N, Yoshizawa AC, Tabata T, Sugiyama N, Goto S, Ishihama Y. 2017. JPOSTrepo: An international standard data repository for proteomes. *Nucleic Acids Res.* doi:10.1093/nar/gkw1080
- Panina SB, Pei J, Baran N, Konopleva M, Kirienko N V. 2020. Utilizing Synergistic Potential of Mitochondria-Targeting Drugs for Leukemia Therapy. *Front Oncol* **10**.  
doi:10.3389/fonc.2020.00435
- Rai Y, Yadav P, Kumari N, Kalra N, Bhatt AN. 2019. Hexokinase II inhibition by 3-bromopyruvate sensitizes myeloid leukemic cells K-562 to anti-leukemic drug, daunorubicin. *Biosci Rep.* doi:10.1042/bsr20190880
- Ramkumar B, Dharaskar SP, Mounika G, Paithankar K, Sreedhar AS. 2020. Mitochondrial

- chaperone, TRAP1 as a potential pharmacological target to combat cancer metabolism. *Mitochondrion* **50**:42–50. doi:10.1016/j.mito.2019.09.011
- Roca-Portoles A, Rodriguez-Blanco G, Sumpton D, Cloix C, Mullin M, Mackay GM, O'Neill K, Lemgruber L, Luo X, Tait SWG. 2020. Venetoclax causes metabolic reprogramming independent of BCL-2 inhibition. *Cell Death Dis* **11**. doi:10.1038/s41419-020-02867-2
- Roth K, Weiner MW. 1991. Determination of cytosolic ADP and AMP concentrations and the free energy of ATP hydrolysis in human muscle and brain tissues with <sup>31</sup>P NMR spectroscopy. *Magn Reson Med*. doi:10.1002/mrm.1910220258
- Rücker FG, Sander S, Döhner K, Döhner H, Pollack JR, Bullinger L. 2006. Molecular profiling reveals myeloid leukemia cell lines to be faithful model systems characterized by distinct genomic aberrations. *Leukemia*. doi:10.1038/sj.leu.2404235
- Ryan TE, Yamaguchi DJ, Schmidt CA, Zeczycki TN, Shaikh SR, Brophy P, Green TD, Tarpey MD, Karnekar R, Goldberg EJ, Sparagna GC, Torres MJ, Annex BH, Neuffer PD, Spangenburg EE, McClung JM. 2018. Extensive skeletal muscle cell mitochondriopathy distinguishes critical limb ischemia patients from claudicants. *JCI insight*. doi:10.1172/jci.insight.123235
- Ryu I, Ryu MJ, Han J, Kim SJ, Lee MJ, Ju X, Yoo BH, Lee YL, Jang Y, Song IC, Chung W, Oh E, Heo JY, Kweon GR. 2018. L-Deprenyl exerts cytotoxicity towards acute myeloid leukemia through inhibition of mitochondrial respiration. *Oncol Rep* **40**:3869–3878. doi:10.3892/or.2018.6753
- Sanchez-Martin C, Menon D, Moroni E, Ferraro M, Masgras I, Elsey J, Arbiser JL, Colombo G, Rasola A. 2020a. Honokiol Bis-Dichloroacetate Is a Selective Allosteric Inhibitor of the Mitochondrial Chaperone TRAP1. *Antioxid Redox Signal* **00**:1–13.

doi:10.1089/ars.2019.7972

- Sanchez-Martin C, Moroni E, Ferraro M, Laquatra C, Cannino G, Masgras I, Negro A, Quadrelli P, Rasola A, Colombo G. 2020b. Rational Design of Allosteric and Selective Inhibitors of the Molecular Chaperone TRAP1. *Cell Rep* **31**:107531. doi:10.1016/j.celrep.2020.107531
- Schindelin J, Arganda-Carreras I, Frise E, Kaynig V, Longair M, Pietzsch T, Preibisch S, Rueden C, Saalfeld S, Schmid B, Tinevez JY, White DJ, Hartenstein V, Eliceiri K, Tomancak P, Cardona A. 2012. Fiji: An open-source platform for biological-image analysis. *Nat Methods*. doi:10.1038/nmeth.2019
- Sciacovelli M, Guzzo G, Morello V, Frezza C, Zheng L, Nannini N, Calabrese F, Laudiero G, Esposito F, Landriscina M, Defilippi P, Bernardi P, Rasola A. 2013. The mitochondrial chaperone TRAP1 promotes neoplastic growth by inhibiting succinate dehydrogenase. *Cell Metab* **17**:988–999. doi:10.1016/j.cmet.2013.04.019
- Singh RP, Jeyaraju D V., Voisin V, Hurren R, Xu C, Hawley JR, Barghout SH, Khan DH, Gronda M, Wang X, Jitkova Y, Sharon D, Liyanagae S, MacLean N, Seneviratene AK, Mirali S, Borenstein A, Thomas GE, Soriano J, Orouji E, Minden MD, Arruda A, Chan SM, Bader GD, Lupien M, Schimmer AD. 2020. Disrupting Mitochondrial Copper Distribution Inhibits Leukemic Stem Cell Self-Renewal. *Cell Stem Cell* **26**:926-937.e10. doi:10.1016/j.stem.2020.04.010
- Škrtić M, Sriskanthadevan S, Jhas B, Gebbia M, Wang X, Wang Z, Hurren R, Jitkova Y, Gronda M, Maclean N, Lai CK, Eberhard Y, Bartoszko J, Spagnuolo P, Rutledge AC, Datti A, Ketela T, Moffat J, Robinson BH, Cameron JH, Wrana J, Eaves CJ, Minden MD, Wang JCY, Dick JE, Humphries K, Nislow C, Giaever G, Schimmer AD. 2011. Inhibition of Mitochondrial Translation as a Therapeutic Strategy for Human Acute Myeloid Leukemia.

*Cancer Cell* **20**:674–688. doi:10.1016/j.ccr.2011.10.015

- Sriskanthadevan S, Jeyaraju D V., Chung TE, Prabha S, Xu W, Skrtic M, Jhas B, Hurren R, Gronda M, Wang X, Jitkova Y, Sukhai MA, Lin FH, Maclean N, Laister R, Goard CA, Mullen PJ, Xie S, Penn LZ, Rogers IM, Dick JE, Minden MD, Schimmer AD. 2015. AML cells have low spare reserve capacity in their respiratory chain that renders them susceptible to oxidative metabolic stress. *Blood* **125**:2120–2130. doi:10.1182/blood-2014-08-594408
- Suganuma K, Miwa H, Imai N, Shikami M, Gotou M, Goto M, Mizuno S, Takahashi M, Yamamoto H, Hiramatsu A, Wakabayashi M, Watarai M, Hanamura I, Imamura A, Mihara H, Nitta M. 2010. Energy metabolism of leukemia cells: Glycolysis versus oxidative phosphorylation. *Leuk Lymphoma* **51**:2112–2119. doi:10.3109/10428194.2010.512966
- Tewari D, Ahmed T, Chirasani VR, Singh PK, Maji SK, Senapati S, Bera AK. 2015. Modulation of the mitochondrial voltage dependent anion channel (VDAC) by curcumin. *Biochim Biophys Acta - Biomembr* **1848**:151–158. doi:10.1016/j.bbamem.2014.10.014
- Vardhana SA, Hwee MA, Berisa M, Wells DK, Yost KE, King B, Smith M, Herrera PS, Chang HY, Satpathy AT, van den Brink MRM, Cross JR, Thompson CB. 2020. Impaired mitochondrial oxidative phosphorylation limits the self-renewal of T cells exposed to persistent antigen. *Nat Immunol*. doi:10.1038/s41590-020-0725-2
- Veech RL, Kashiwaya Y, Gates DN, King MT, Clarke K. 2002. The energetics of ion distribution: The origin of the resting electric potential of cells. *IUBMB Life* **54**:241–252. doi:10.1080/15216540215678
- Willis WT, Jackman MR, Messer JI, Kuzmiak-Glancy S, Glancy B. 2016. A simple hydraulic analog model of oxidative phosphorylation. *Med Sci Sports Exerc*. doi:10.1249/MSS.0000000000000884

- Xiang W, Cheong JK, Ang SH, Teo B, Xu P, Asari K, Sun WT, Than H, Bunte RM, Virshup DM, Chuah C. 2015. Pyrvinium selectively targets blast phase-chronic myeloid leukemia through inhibition of mitochondrial respiration. *Oncotarget*. doi:10.18632/oncotarget.5615
- Xie Q, Wondergem R, Shen Y, Cavey G, Ke J, Thompson R, Bradley R, Daugherty-Holtrop J, Xu Y, Chen E, Omar H, Rosen N, Wenkert D, Xu HE, Vande Woud GF. 2011. Benzoquinone ansamycin 17AAG binds to mitochondrial voltage-dependent anion channel and inhibits cell invasion. *Proc Natl Acad Sci U S A* **108**:4105–4110. doi:10.1073/pnas.1015181108
- Yoshida S, Tsutsumi S, Muhlebach G, Sourbier C, Lee MJ, Lee S, Vartholomaiou E, Tatokoro M, Beebe K, Miyajima N, Mohny RP, Chen Y, Hasumi H, Xu W, Fukushima H, Nakamura K, Koga F, Kihara K, Trepel J, Picard D, Neckers L. 2013. Molecular chaperone TRAP1 regulates a metabolic switch between mitochondrial respiration and aerobic glycolysis. *Proc Natl Acad Sci U S A* **110**. doi:10.1073/pnas.1220659110

## **CHAPTER 4: CHARACTERIZATION OF THE MITOCHONDRIAL PHENOTYPE OF HEPATOCELLULAR CARCINOMA**

The previous chapter identified unique mitochondrial properties of acute myeloid leukemia compared to healthy cells from the hematopoietic lineage, addressing part of the first aim of this dissertation. To evaluate whether there were any common aspects of the mitochondrial phenotypes across diverse cancers, we applied similar methods to models of a solid tumor, hepatocellular carcinoma, as described in the following chapter. These data describe an inhibition of mitochondrial respiration by ATP free energy that is comparable between hepatocellular carcinoma and leukemia. However, this effect is not dependent upon ATP entry into the mitochondrial matrix in hepatocellular carcinoma as was found in leukemia. Hepatocellular carcinoma also displayed a distinct limitation to Complex I-supported respiration that was not previously seen in leukemia.

**Bioenergetic phenotyping of DEN-induced hepatocellular carcinoma reveals link between adenylate kinase expression and reduced complex I-supported respiration.** (To be submitted as a manuscript to Hepatology).

Kelsey L. McLaughlin<sup>1,2</sup>, Margaret A.M. Nelson<sup>1,2</sup>, Hannah S. Coalson<sup>1,2</sup>, James T. Hagen<sup>1,2</sup>, McLane Montgomery<sup>1,2</sup>, and Kelsey H. Fisher-Wellman<sup>1,2\*</sup>

<sup>1</sup>Department of Physiology, Brody School of Medicine, East Carolina University, Greenville, NC, <sup>2</sup>East Carolina Diabetes and Obesity Institute, East Carolina University, Greenville, NC

\* To whom correspondence should be addressed:

Kelsey H. Fisher-Wellman [fisherwellmank17@ecu.edu](mailto:fisherwellmank17@ecu.edu)

East Carolina Diabetes and Obesity Institute, 115 Heart Drive, Greenville, NC 27834 USA

Telephone: 252-744-2585

Fax: 252-744-0462

## **Abstract**

Hepatocellular carcinoma (HCC) is a common form of liver cancer with poor clinical prognosis. Increasing evidence suggests that mitochondria play a central role in malignant metabolic reprogramming in HCC, which may promote disease progression. To comprehensively evaluate the mitochondrial phenotype present in HCC, we applied a recently developed diagnostic workflow that combines high-resolution respirometry, fluorometry, and mitochondrial-targeted nLC-MS/MS proteomics to cell culture and mouse models of HCC. Diethylnitrosamine (DEN) was used to induce HCC in C3H mice. Across both models, CI-linked respiration was significantly decreased in HCC compared to nontumor, though this did not have an impact on oxidative phosphorylation. Interestingly, CI-linked respiration was found to be partially restored in DEN-induced tumor mitochondria through inhibition of adenylate kinases by P1, P5-di(adenosine-5') pentaphosphate (Ap5A). DEN-induced tumor mitochondria also displayed a reduced ability to retain calcium and generate  $\Delta\Psi$  across a physiological span of ATP demand states compared to DEN-treated nontumor or saline-treated liver mitochondria. Our findings support the utility of mitochondrial phenotyping in identifying novel regulatory mechanisms governing cellular bioenergetics.

## **Introduction**

Hepatocellular carcinoma (HCC) is the most common form of primary liver cancer worldwide (Villanueva, 2019) and among the top 5 causes of cancer-related death in men of all ages in the United States (Siegel et al., 2021). Although early detection and resection of small neoplasms may improve 5-year survival above 50% (Forner et al., 2012), the most recent U.S. estimates put the average 5-year survival at around 20%, making liver cancer the second deadliest

cancer behind pancreatic cancer (Siegel et al., 2021). The burden of this disease is likely to continue to grow as HCC commonly develops in the context of existing chronic liver (i.e., hepatitis, cirrhosis) and metabolic diseases (i.e., fatty liver disease, diabetes), the latter of which remains a growing health issue for Americans (Villanueva, 2019).

Emerging evidence from human, rodent, and cell models of HCC suggests that mitochondrial reprogramming plays an important role in HCC metabolism and disease progression (García-Chávez et al., 2021; Lee et al., 2021). HCC tumors commonly present with marked upregulation of glycolytic enzymes and metabolites (Cassim et al., 2018; Lee et al., 2018, 2017), decreased mitochondrial DNA (mtDNA) copy number (Yamada et al., 2006; Yin et al., 2004), and increased mtDNA mutational burden (Corral et al., 1989a, 1989b; Lee et al., 2004; Yin et al., 2010). Together, these findings are suggestive of a metabolic phenotype in which mitochondrial respiration is impaired to promote an increase in glycolysis despite the availability of oxygen, commonly described as the Warburg effect (vander Heiden et al., 2009). Further, a recent longitudinal, multi-omic study in a rat model of HCC induced by the carcinogen diethylnitrosamine (DEN) has demonstrated that changes to mitochondrial metabolism precede tumor formation, highlighting that mitochondrial metabolism is integral to the tumorigenic process (García-Chávez et al., 2021).

Despite this growing interest in mitochondria, most studies to date have focused primarily on genomic, proteomic, or metabolomic assessments of HCC metabolism, with little emphasis on the functional consequences of these findings in mitochondria (Aleksic et al., 2011; Chen et al., 2020; García-Chávez et al., 2021; Wurmbach et al., 2007). The few studies that have assessed aspects of mitochondrial function have been limited in scope. For instance, evaluations of mitochondrial respiration in DEN-induced rodent models of HCC have almost exclusively been

limited comparisons of mitochondrial respiratory control ratios between healthy and malignant liver (Boitier et al., 1995; Chavez et al., 2017). In some cases, mitochondrial function was extrapolated solely from measurements of the individual activities of TCA cycle enzymes or mitochondrial respiratory complexes (Santos et al., 2012; Suresh et al., 2013). Additionally, DEN-induced tumors were not isolated from the surrounding tissue prior to assessment, preventing any comparisons between tumor and nontumor mitochondria within the same animal (Boitier et al., 1995; Chavez et al., 2017; Santos et al., 2012; Suresh et al., 2013). These experimental limitations make it difficult to interpret the functional implications of previously reported mitochondrial differences in HCC and to define which intrinsic properties of mitochondria are altered to support in tumor metabolism.

We sought to address this gap in the field by applying a recently developed comprehensive diagnostic workflow that combines high-resolution respirometry, fluorometry, and mitochondrial-targeted nLC-MS/MS proteomics (Fisher-Wellman et al., 2018, 2019) to both a cell culture and mouse model of HCC. We first applied an abbreviated version of the workflow to mitochondria isolated from mouse HCC-derived cells (Hepa 1-6) and a nontumorigenic mouse hepatocyte cell line (AML12). Hepa 1-6 mitochondria were found to have decreased Complex I-linked respiration, though there was no corresponding decrease in Complex-I dependent ATP production. We then isolated mitochondria from tumor and nontumor liver tissues from DEN-treated C3H mice and age-matched controls and subjected them to the full battery of assays including assessments of mitochondrial respiration, membrane potential ( $\Delta\Psi$ ), NAD<sup>+</sup>/NADH redox poise, ATP production rates, and calcium retention. Consistent with the cell culture experiments, DEN-induced tumor mitochondria displayed a reduced capacity to respire when fueled by Complex I-linked carbon substrates. Interestingly, this respiratory deficit could be partially restored through inhibition of

adenylate kinase activity by P<sub>1</sub>, P<sub>5</sub>-di(adenosine-5') pentaphosphate (Ap<sub>5</sub>A). DEN-induced tumor mitochondria also displayed a reduced ability to retain calcium and generate  $\Delta\Psi$  across a physiological span of ATP demand states compared to DEN-treated nontumor or saline-treated liver mitochondria. Overall, our data highlights that most measures of maximal mitochondrial capacity were comparable between HCC and hepatocytes, but our diagnostic workflow was able to highlight more nuanced differences that may be physiologically relevant to HCC metabolism.

## Results

### *Cells derived from hepatocellular carcinoma display a profound reduction in Complex I-supported respiration.*

We first sought to define the bioenergetic impact of hepatocellular carcinoma (HCC) malignancy using commercially available cell lines derived from mouse HCC (Hepa 1-6) and healthy, immortalized hepatocytes (AML12). All experiments were performed in isolated mitochondria, and the purity of these mitochondrial isolations was found to be comparable using the citrate synthase (CS) activity assay (Figure 1A). Three unique respiratory stimuli—chemical uncoupling (Figure 1B), manipulation of ATP free energy ( $\Delta G_{ATP}$ ; Figure 1D), and supramaximal ADP (Figure 1H)—were then used to evaluate specific parameters of mitochondrial function.

First, the maximal respiratory capacity of the electron transport system (ETS) was determined through titration of the uncoupler carbonyl cyanide-4-phenylhydrazone (FCCP), as depicted in Figure 1B. Saturating amounts of carbon substrates were provided sequentially such that pyruvate (P), malate (M), glutamate (G), and octanoyl-L-carnitine (O)—all of which primarily introduce electrons into the ETS at Complex I (CI)—were added together, and the Complex II

(CII)-specific substrate succinate (S) was added following the first FCCP titration point (Figure 1B). This allowed for comparison of CI-supported oxygen consumption ( $JO_2$ ) in addition to that supported by the whole ETS within the same assay. Both CI-linked  $JO_2$  and the maximal FCCP-stimulated rate ( $JH^+_{TOTAL}$ ) were comparable between AML12 and Hepa 1-6 mitochondria (Figure 1C), suggesting similar ETS capacities.

We then compared the ability of AML12 and Hepa 1-6 mitochondria to kinetically respond to a more physiological stimulus for respiration:  $\Delta GATP$ , or the demand for ATP resynthesis through oxidative phosphorylation (OXPHOS). Using the creatine kinase (CK) energetic clamp (Figure 1D), we titrated  $\Delta GATP$  across a physiological span from maximal ATP demand ( $\Delta GATP = -12.94\text{kcal/mol}$ ) to minimal demand ( $\Delta GATP = -14.7\text{kcal/mol}$ ). As in the ETS capacity assay, carbon substrates were added sequentially (Figure 1D), allowing for separate measurements of maximal CI-supported (P/M) and whole ETS-supported (P/M/G/S/O) respiration. The  $JH^+_{OXPHOS}$  corresponded to the maximal  $JO_2$  stimulated by  $\Delta GATP$  in the presence of all substrates. Interestingly, the maximal  $\Delta GATP$ -stimulated rate fueled by CI substrates P/M alone was decreased in Hepa 1-6 mitochondria compared to AML12 ('P/M<sub>12.94</sub>', Figure 1E), but this difference was no longer significant when additional substrates were added ('G/S/O<sub>12.94</sub>', Figure 1E).

When looking at the respiratory response to  $\Delta GATP$  titration, absolute  $JO_2$  was lower in Hepa 1-6 mitochondria toward the end of the  $\Delta GATP$  titration. However, the respiratory conductance, quantified as the slope of the linear portion of the  $JO_2/\Delta GATP$  relationship (dotted lines, Figure 1E), was not significantly different between AML12 and Hepa 1-6 mitochondria (Figure 1F). This suggests that both groups are equally able to kinetically adjust oxygen consumption to ATP demand. Following the titration of  $\Delta GATP$ , we again titrated the uncoupler

FCCP to assess whether there were any inhibitory effects of the presence of  $\Delta$ GATP on ETS flux (Figure 1D). For simplicity, only the maximal FCCP-stimulated rate under these conditions was graphed as the  $\text{FCCP}_{\Delta\text{GATP}}$  (Figure 1D-E). Both AML12 and Hepa 1-6 mitochondria were able to attain a  $JO_2$  equivalent to their  $JH^+_{\text{OXPHOS}}$  when FCCP was added at the end of the CK clamp assay, suggesting a lack of inhibition by  $\Delta$ GATP for both cell types.

As both the ETS capacity and OXPHOS kinetics assays ultimately use the same combination of carbon substrates (P/M/G/S/O), we can compare the maximal  $JO_2$  that was stimulated by ATP demand ( $JH^+_{\text{OXPHOS}}$ ) to the total respiratory capacity of the ETS elicited by FCCP ( $JH^+_{\text{TOTAL}}$ ) as an estimate of how much of the total capacity is able to contribute to OXPHOS. We have previously termed this ratio ‘Fractional OXPHOS’ (Figure 1G). Fractional OXPHOS was found to be equivalent between AML12 and Hepa 1-6 mitochondria, with both able to draw on approximately 74% of their  $JH^+_{\text{TOTAL}}$  in response to elevated ATP demand. This may reflect a small amount of inefficiency in both cell types that prevents them from fully activating all mitochondrial complexes when stimulated by  $\Delta$ GATP.

To further explore the CI limitation that was revealed in the OXPHOS kinetics assay and its potential impact upon mitochondrial ATP phosphorylation, we then incorporated an assay in which ADP-stimulated respiration and ATP production rate ( $J_{\text{ATP}}$ ) could be determined in parallel under identical assay conditions (Figure 1H). Mitochondria were incubated with a supraphysiological concentration of ADP (500 $\mu$ M), which was maintained using the hexokinase (HK) enzymatic clamp. Both CI-linked flux (P/M) and CII-linked flux (S) were assessed independently within the assay using the addition of CI inhibitor rotenone (Rot) after P/M. ADP-linked respiration was then inhibited by the addition of oligomycin, and FCCP was titrated to elicit the maximal S/Rot-supported  $JO_2$ , here defined as  $\text{FCCP}_{\text{HK}}$  (Figure 1H). Once again, it was found

that P/M-supported respiration was lower in Hepa 1-6 mitochondria than AML12 ('P/M', Figure 1I), but respiration was no longer different when fueled by S/Rot and stimulated by either ADP or FCCP ('S', 'FCCP<sub>HK</sub>', Figure 1I). Surprisingly, *J*ATP did not differ significantly between Hepa 1-6 and AML12 mitochondria under either substrate condition (Figure 1J), suggesting that although respiration was lower in Hepa 1-6 when fueled by P/M, the ability to phosphorylate ATP was retained. As a result, the efficiency of ATP production, defined as the amount of ATP produced per molecule of oxygen consumed, or ATP/O, was significantly higher for Hepa 1-6 mitochondria fueled by P/M (Figure 1K).

***Induction of hepatocellular carcinoma in mice using diethylnitrosamine resulted in clearly defined tumors for mitochondrial isolation.***

To follow up on the interesting finding of a potential limitation to CI-supported respiration in HCC mitochondria, particularly when fueled by P/M, we next employed a mouse model of HCC development that would allow mitochondrial isolation from fresh tumors. As depicted in Figure 2A, male C3H mice were given a single IP injection of diethylnitrosamine (DEN; 25mg/kg) or vehicle control (Saline) at postnatal day 14 (P14). Mice would then be sacrificed after tumor development at about 27 weeks of age. At the time of sacrifice, there was a small but significant decrease in body mass in DEN-treated mice compared to Saline (Figure 2B). Saline-treated livers had almost no visible abnormalities (Figure 2C), whereas DEN-treated livers displayed numerous, clearly demarcated tumors surrounded by nontumor liver tissue (white arrows point to tumors; Figure 2D).

For optimal experimental contrast, mitochondria were isolated from 3 distinct tissue types: saline-treated liver (referred to throughout as Saline), DEN-treated nontumor tissue (DEN-NT),

and DEN-induced tumor tissue (DEN-T). A subset of mitochondrial preparations from these tissues were subjected to mitochondrial-targeted, label-free, quantitative nLC-MS/MS proteomics. Overall, 2,512 proteins were identified and quantified, and 810 of these were identified to be mitochondrial using the mouse MitoCarta 3.0 database (Rath et al., 2021). Supporting the effective separation of DEN-T from DEN-NT tissue during mitochondrial isolation, principal component analysis of the 3 groups of proteomics samples revealed that DEN-T samples clustered together away from both DEN-NT and Saline samples, with DEN-NT samples nearly clustering with Saline (Figure 2E). Differences in protein expression between the mitochondrial proteomes of Saline, DEN-NT, and DEN-T preparations were also quantified (Supplemental Figure 1A-C).

As purity can affect the interpretation of mitochondrial outcome measures normalized to total or crude mitochondrial protein amount, we compared the purity of our mitochondrial isolations using two separate methods. First, mitochondrial purity was estimated using the CS activity assay, a common surrogate for mitochondrial content. DEN-NT mitochondria had significantly greater CS activity than both DEN-T and Saline mitochondria (Figure 2F), though there was no difference between Saline and DEN-T. Higher CS activity would suggest a higher mitochondrial purity for DEN-NT isolations. To confirm this finding, we also empirically derived the mitochondrial enrichment factor (MEF) for each tissue by quantifying the summed abundances of all proteins identified to be mitochondrial using the MitoCarta 3.0 database relative to the total protein abundance, as previously described (McLaughlin et al., 2020). Consistent with the CS activity assay, the MEF for DEN-NT mitochondria was significantly greater than both DEN-T and Saline (Figure 2G). DEN-T mitochondria also had a significantly lower MEF than Saline mitochondria (Figure 2G). In support of our previous findings in liver mitochondria (McLaughlin et al., 2020), MEF was significantly correlated with CS activity (Figure 2H). Given the significant

differences in the purity of mitochondrial isolations across tissues identified through both CS activity and MEF, all functional outcome measures were normalized to MEF unless otherwise specified.

***Broad characterization of DEN-induced tumor mitochondria reveals reduced mitochondrial membrane potential as well as increased sensitivity to FCCP and calcium.***

Before evaluating any complex-specific deficiencies, we first sought to characterize several aspects of general mitochondrial functionality, including respiration, NADH/NAD<sup>+</sup> redox poise, membrane potential ( $\Delta\Psi$ ), ATP production ( $J_{ATP}$  and ATP/O), and calcium retention. Total ETS capacity ( $JH^+_{TOTAL}$ ) when fueled by saturating carbon substrates (P/M/G/S/O) was determined using an FCCP titration as described above (Figure 1B). Although the maximal FCCP-stimulated  $JO_2$  was not different between groups (Figure 3B), the shape of the FCCP titration curve was drastically different between mitochondria isolated from DEN-induced tumors and the two non-tumor tissues (Figure 3A). DEN-T mitochondria appeared more sensitive to smaller amounts of FCCP, as evident in their significantly lower  $K_m$  for FCCP compared to the other two tissues (Figure 3C).

OXPHOS kinetics were quantified using the CK clamp as described above (Figure 1D). The maximal  $JO_2$  stimulated by  $\Delta GATP$  ( $JH^+_{OXPHOS}$ ) was significantly higher for DEN-T mitochondria than both nontumor tissues, and  $JO_2$  remained significantly elevated in DEN-T mitochondria across the remainder of the  $\Delta GATP$  titration (Figure 3D). Interestingly, fractional OXPHOS was significantly greater in mitochondria isolated from both DEN-treated tissues compared to Saline mitochondria (Figure 3E), and there was a trend for higher fractional OXPHOS in DEN-T mitochondria over DEN-NT ( $p=0.0658$ ; Figure 3E). Taken alone, these data would

imply that DEN-T mitochondria may be more robust than nontumor mitochondria as they appear to be able to contribute a higher fraction of their total respiratory capacity to OXPHOS. However, other outcomes from the OXPHOS kinetics assay suggest a more nuanced interpretation is necessary. For instance, the respiratory conductance calculated from the linear portion of the OXPHOS kinetics assay, which would commonly be considered a measure of sensitivity to dynamic changes in  $\Delta$ GATP, was equivalent between all 3 mitochondrial preparations (Supplementary Figure 2A). However, when the data was graphed as a percentage of the  $JH^+$ <sub>OXPHOS</sub> (Figure 3F), DEN-T mitochondria did not proportionally reduce their respiration to the same degree as the nontumor mitochondria in response to changes to  $\Delta$ GATP.

Additionally, DEN-T mitochondria displayed a significantly reduced ability to respond to FCCP following  $\Delta$ GATP titration ( $FCCP_{\Delta$ GATP}) compared to both nontumor tissues (Figure 3F), which may imply a degree of ETS inhibition in the presence of  $\Delta$ GATP. We have previously reported this phenomenon, termed the ‘FCCP effect’, in leukemia (Nelson et al., 2021). As in leukemia, DEN-T mitochondria could not recover their  $JH^+$ <sub>OXPHOS</sub> respiration rate when stimulated by FCCP in the presence of  $\Delta$ GATP whereas the  $FCCP_{\Delta$ GATP of nontumor mitochondria surpassed their  $JH^+$ <sub>OXPHOS</sub> (Figure 3G). Our previous work in leukemia had found that *in vitro* treatment of mitochondria with the heat shock protein 90 (HSP90) inhibitor 17AAG or the adenine nucleotide translocase (ANT) inhibitor carboxyatractyloside (CAT) would rescue the FCCP effect in leukemic cells (Nelson et al., 2021). However, neither 17AAG nor CAT had any effect on the  $FCCP_{\Delta$ GATP of DEN-T (Supplementary Figure 2B). Interestingly, 17AAG did increase Fractional OXPHOS through an increase in  $JH^+$ <sub>OXPHOS</sub> in both DEN-NT and Saline mitochondria, with no effect on DEN-T (Supplementary Figure 2C-F). The magnitude of this effect was similar in Saline

and DEN-NT mitochondria despite only DEN-NT exhibiting a significant increase in the abundance of TRAP1, the purported mitochondrial target of 17AAG (Supplementary Figure 2G).

Parallel fluorometric experiments were conducted to compare additional driving forces underlying OXPHOS kinetics, NADH/NAD<sup>+</sup> redox poise (Figure 3H) and  $\Delta\Psi$  (Figure 3I), across the same  $\Delta$ GATP titration. NADH/NAD<sup>+</sup> redox poise, expressed as a percentage of the maximal reduction induced by Complex IV inhibitor cyanide (CN), was nearly identical between the 3 tissues when all 5 carbon substrates were present ('G/S/O<sub>12.94</sub>') to the end of the assay, Figure 3H). Interestingly, redox poise was significantly more reduced in DEN-T mitochondria compared to Saline when P/M was the sole carbon substrate ('P/M<sub>12.94</sub>'), Figure 3H). Relative hyper-reduction may suggest a reduced ability of DEN-T mitochondria to transfer electrons from NADH into the ETS at CI. However, this observation is difficult to interpret because there was no difference in redox poise between the two DEN-treated tissues, and the effect was only present at this single point. In contrast, there were large differences in tetramethyl rhodamine methyl ester (TMRM)-derived  $\Delta\Psi$  between DEN-T and the two nontumor tissues across the  $\Delta$ GATP span (Figure 3I). Saline mitochondria were able to drive the highest  $\Delta\Psi$  at each titration point compared to the two DEN-treated tissues, and DEN-T mitochondria were only able to match the DEN-NT  $\Delta\Psi$  at the final  $\Delta$ GATP titration point (Figure 3I). The combination of high respiration and low membrane potential that was observed in DEN-T mitochondria across the  $\Delta$ GATP span may indicate some degree of uncoupling of respiration from OXPHOS. Importantly, the mV values reported in Figure 3I were derived using tissue-specific TMRM standard curves, and these standard curves were significantly different from one another (Supplementary Figure 2H), a caveat that makes interpretation of this  $\Delta\Psi$  data difficult. However, it is possible that these tissue-specific differences were real, as there was considerable variability in the raw TMRM traces across tissues

(Supplementary Figure 2I). Additionally, our group has previously found similar  $\Delta\Psi$  values across the same  $\Delta G_{ATP}$  span in human HCC-derived HepG2 cells, supporting the possibility that this is a real effect (Schmidt et al., 2021).

To empirically test the coupling between respiration and ATP phosphorylation across tissues, a variation of the HK clamp-based assay described in Figure 1H was used. Mitochondria were energized with saturating carbon substrates (P/M/G/S/O), followed by a two-point ADP titration to the sub- $K_m$  concentration of  $10\mu\text{M}$  and the supraphysiological concentration of  $500\mu\text{M}$ . The  $\text{FCCP}_{\text{HK}}$  rate was obtained by adding oligomycin to inhibit ADP-stimulated respiratory flux and titrating FCCP. DEN-T mitochondria exhibited significantly higher  $JO_2$  than both nontumor tissues following the addition of substrate alone ('P/M/G/S/O', Figure 3J), as well as both ADP titration points (Figure 3J). Interestingly, all 3 tissues displayed similar FCCP-stimulated respiration, suggesting that ADP is not as powerful as a stimulus as FCCP for Saline and DEN-NT mitochondria under this assay condition (Figure 3J). In a parallel fluorometric assay,  $J_{ATP}$  was determined to be higher in DEN-T mitochondria than nontumor tissues at both ADP concentrations, and higher in DEN-NT mitochondria than Saline (Figure 3K). When phosphorylation efficiency was quantified from these two assays, all tissues had a comparable ATP/O ratio at  $500\mu\text{M}$  ADP, but the ATP/O for DEN-NT was significantly greater than the other two tissues at  $10\mu\text{M}$  ADP (Figure 3L). An improvement in phosphorylation efficiency may be adaptive in DEN-NT tissue, which would likely need to compete with adjacent tumor tissue for nutrients. Notably, DEN-NT also had greater relative expression of all respiratory complexes except for Complex IV (CIV) compared to Saline mitochondria, and greater relative expression of CII and Complex III than DEN-T (Supplementary Figure 2J).

Mitochondrial calcium uptake is an essential mitochondrial function that has been linked to cell fate decisions about apoptosis and survival. To evaluate whether tumor status affects this ability, we included the fluorometry-based calcium retention assay in our interrogation of DEN-induced HCC. Mitochondria were energized with S/Rot in the presence of the HK clamp and 50 $\mu$ M ADP, then calcium was titrated in 30 $\mu$ M increments until the mitochondrial permeability transition pore (MPTP) opened (representative trace in Figure 3M). Maximal calcium uptake was similar between Saline and DEN-NT mitochondria, but DEN-T mitochondria were only able to take up roughly 1/3 the calcium of the nontumor tissues prior to MPTP opening (Figure 3N).

***Complex I-linked respiratory deficiency is present in DEN-induced tumor mitochondria.***

Until this point, our assessment of DEN-induced tumor mitochondria has consisted of maximal capacity assays under saturating levels of carbon substrates that would feed electrons to multiple sites across the ETS. Although this strategy is effective for identifying broad mitochondrial deficiencies, it may obscure subtle but meaningful differences in the regulation of substrate utilization. We next shifted our focus to evaluating mitochondrial function under varying combinations of respiratory challenges and substrate conditions, beginning with a generalized substrate preference assay (Figure 4A).

Mitochondria were energized with saturating ADP (500 $\mu$ M) maintained by the HK clamp, then exposed to a series of carbon substrates and corresponding inhibitors. CI-linked substrates were layered in first, including  $\alpha$ -ketoglutarate (AKG), P/M, and G. When fueled by AKG, DEN-T mitochondria were able to match the  $JO_2$  of both nontumor tissues, though respiration was greater in DEN-NT than Saline mitochondria ('AKG', Figure 4A). The addition of P/M normalized respiration between Saline and DEN-NT, but it stimulated no further increase in DEN-T

mitochondria, leading to a significantly lower  $JO_2$  ('P/M', Figure 4A). Subsequent addition of G did not lead to a meaningful increase in respiration for any of the tissues, and the cumulative CI-supported respiration was greater in Saline and DEN-NT mitochondria than DEN-T ('G', Figure 4A). NADH-linked respiration was then inhibited using Rot, and S was then added to initiate CII-supported flux. Consistent with our findings in cells, respiration fueled by S was not different between tumor and nontumor mitochondria ('S', Figure 4A). The competitive CII inhibitor malonate (Malo) was then added, followed by dihydroorotate (DHO). DHO is the substrate for dihydroorotate dehydrogenase (DHODH), which feeds electrons directly into the quinone (Q) pool of the ETS from the outer surface of the inner mitochondrial membrane and plays an important role in pyrimidine nucleotide biosynthesis. Although it might be expected that nucleotide synthesis would be important to growing tumors, here DHO-supported respiration was significantly decreased in DEN-T mitochondria compared to both nontumor tissues ('DHO', Figure 4A). This difference was still present after the addition of DHODH inhibitor teriflunomide (TF), the implications of which are unclear ('TF', Figure 4A). Finally, respiration was stimulated with a combination of calcium and glycerol-3-phosphate (G3P), which similarly feeds electrons directly into the Q pool through glycerol-3-phosphate dehydrogenase (GPDH). There was no difference between tumor and nontumor G3P-supported respiration, though Saline was able to respire at a higher rate than DEN-NT ('G3P', Figure 4A).

As there was a consistent decrease in CI-supported respiration seen in both the HCC cell model and DEN-induced tumors, we decided to explore this phenotype further with additional respiratory stimuli. First, we repeated the OXPHOS kinetics assay experiments with G/M/O provided as carbon substrates. This combination was chosen because the contribution of G was hidden within the other CI substrates in the substrate preference assay, and lipid substrates such as

O had been excluded. In contrast to the robust  $JH^+_{\text{OXPHOS}}$  attained by DEN-T under a multi-complex stimulating substrate condition (P/M/G/S/O), the G/M/O-supported  $JH^+_{\text{OXPHOS}}$  was significantly lower compared to both nontumor tissues (Figure 4B). Although by the end of the  $\Delta\text{GATP}$  titration respiration was equivalent between all tissues, DEN-T mitochondria were again less responsive to FCCP in the presence of  $\Delta\text{GATP}$  ('FCCP $_{\Delta\text{GATP}}$ ', Figure 4B). Both Saline and DEN-NT tissues were able to double their G/M/O-supported  $JH^+_{\text{OXPHOS}}$  following FCCP titration, but DEN-T mitochondria were only able to match it (Figure 4B).

Although there were striking differences in CI-linked respiration between DEN-T and nontumor mitochondria present in both the substrate preference and G/M/O OXPHOS kinetics assays, it was still unclear whether these differences reflected a global CI deficiency or a deficiency in other enzymatic processes (i.e., dehydrogenase activity, beta-oxidation). To address this limitation, a small subset of DEN-treated mice was used to assess FCCP- and  $\Delta\text{GATP}$ -stimulated respiration under 4 substrate conditions: P/M, G/M, O/M, and palmitoyl-carnitine (PC)/M. This mixture of substrate conditions spanned the most common CI-linked metabolism products of glucose, glutamine, and fatty acid oxidation that may be utilized for mitochondrial respiration. Only DEN-NT and DEN-T tissues were considered for this evaluation as Saline mitochondrial respiration was typically equivalent to DEN-NT. Data from this later subset of mice was normalized to CS activity rather than MEF, as it was found that CS activity from several of these mitochondrial preparations was higher than the averages from earlier in the study (data not shown). When stimulated with FCCP, respiration supported by P/M, O/M, and PC/M substrates were all significantly greater in DEN-NT mitochondria than DEN-T, though there was no difference between tumor and nontumor for the G/M condition (Figure 4C). Indeed, both tissues achieved their lowest FCCP-stimulated  $JO_2$  when G/M was used to fuel respiration (Figure 4C).

To determine whether ATP free energy had any effect on CI substrate utilization, the same 4 substrate conditions were then used in conjunction with the CK-based OXPHOS kinetics assay as described above (Figure 4D). Consistent with limited CI-linked flux in DEN-T mitochondria,  $JH^{+}_{OXPHOS}$  was reduced under all substrate conditions compared to DEN-NT (Figure 4D). OXPHOS kinetics appeared most impaired in DEN-T mitochondria when fueled with P/M, as this was the only substrate condition in which respiration was significantly lower across the entire  $\Delta G_{ATP}$  titration. Additionally, as previously seen with the multi-substrate (P/M/G/S/O) and G/M/O kinetic clamps,  $FCCP_{\Delta G_{ATP}}$  was significantly decreased in DEN-T mitochondria for all conditions.

Together, the data from each of these assays strongly suggested that DEN-T mitochondria had a lower capacity to support respiration using CI-linked carbon substrates, though the nature of this limitation remained unclear. Given that we had previously observed comparable NADH/NAD<sup>+</sup> redox poise between tumor and nontumor tissues (Figure 3H), we did not expect the issue to be within the matrix dehydrogenase network. The next possible explanation would be differential expression of the complex itself. We returned to our mitochondrial proteomics data and used the summed abundances of all identified CI subunits to estimate the relative expression of CI in Saline, DEN-NT, and DEN-T mitochondria (Figure 4E). Although relative CI expression was found to be greater in DEN-NT than Saline mitochondria, there was no difference between DEN-T and the two nontumor tissues (Figure 4E). When we compared the abundance of the individual subunits, however, the majority appeared have decreased expression in DEN-T mitochondria (Figure 4F). In fact, of all protein subunits with significant differences in abundance between tumor and nontumor, only 4 were significantly upregulated in DEN-T: Ndufa13, Ndufs3, Ndufs8, and Ndufv2 (Figure 4F). Interestingly, 2 of the 4 identified mitochondrial DNA-encoded

CI subunits, ND2 and ND3, which are integral to the catalytic activity of CI, were found to have significantly decreased expression in DEN-T mitochondria compared to DEN-NT (Figure 4F).

The functional implications of altering the expression of individual subunits within mitochondrial respiratory complexes have not well been defined to date. We decided to directly test the respiratory capacity of CI in tumor and nontumor mitochondria using a recently published method for respiratory experiments in frozen mitochondria (Acin-Perez et al., 2020)(Figure 4G). Freeze-thawed mitochondria were stimulated using the HK clamp, and NADH, S/Rot, and Malo/TMPD were added sequentially to stimulate CI-, CII-, and CIV-linked respiration, respectively. Intriguingly, NADH-supported respiration was significantly lower in DEN-T mitochondria than DEN-NT, though there was no significant difference between Saline and DEN-T. Consistent with our findings in fresh mitochondria, there were no differences in respiration between any of the groups when fueled by S/Rot or Malo/TMPD.

***Upregulation of adenylate kinase 4 (AK4) in DEN-induced tumor mitochondria contributes to altered Complex I-linked respiratory flux.***

Although there was a clear deficit in CI-supported respiration in DEN-T mitochondria, it was still unclear whether this would have a meaningful impact on other important mitochondrial functions such as ATP production. To test this, parallel assessments of respiration and *J*ATP were again conducted under CI-specific (P/M) and CII-specific (S/Rot) substrate conditions and saturating ADP (Figure 5A-B). As seen in earlier experiments, S/Rot-supported respiration was similar across all 3 tissues when stimulated by both ADP and FCCP ('FCCP<sub>HK</sub>', Figure 5A). Unexpectedly, P/M-supported respiration was significantly greater in DEN-T mitochondria compared to both nontumor tissues under these assay conditions (Figure 5A). DEN-T

mitochondria also generated the greatest *J*ATP of all 3 tissues when fueled by P/M, while DEN-NT mitochondria had the greatest S/Rot-supported *J*ATP (Figure 5B). Of note, both Saline and DEN-NT mitochondria were able to attain only about 50% of their S/Rot-supported *J*ATP when fueled by P/M, whereas *J*ATP was nearly equivalent under both conditions for DEN-T mitochondria (Figure 5C). Phosphorylation efficiency was greater for both DEN-NT and DEN-T mitochondria compared to Saline under the P/M condition, but there were no differences in efficiency for S/Rot (Figure 5D).

The results of this assay demonstrated that ATP production was not compromised in DEN-T mitochondria, though the most surprising outcome was that P/M-supported respiration no longer appeared impaired. This was perplexing, as the respiratory stimulus—500 $\mu$ M ADP—was the same as that used in the substrate preference assay, with seemingly different effects. One important addition that was absent from the substrate preference assay was the adenylate kinase (AK) inhibitor, P1, P5-di(adenosine-5') pentaphosphate (Ap5A). Ap5A is included in assessments of phosphorylation efficiency as it eliminates ATP production by AK that might confound estimates of oxidative *J*ATP. We repeated the same HK-based respiration assay in the presence and absence of Ap5A and found that P/M-supported respiration was unaffected in Saline and DEN-NT mitochondria, but it was significantly decreased in the absence of Ap5A in DEN-T mitochondria (Figure 5E). Conversely, there were no significant effects of Ap5A on FCCP<sub>HK</sub> in any tissue, though there was a trend for decreased S/Rot-supported respiration in the absence of Ap5A for Saline mitochondria (Figure 5E). To understand why DEN-T mitochondria may be particularly sensitive to the presence of Ap5A, we searched our proteomics for expression of AK isoforms. Interestingly, AK4 was found to be overexpressed in DEN-T mitochondria compared to Saline and DEN-NT, while the AK2 and AK3 isoforms were equivalent between the tissues (Figure 5F).

Given that Ap5A was able to significantly improve P/M-supported respiration for DEN-T mitochondria stimulated with ADP, we were curious whether Ap5A might similarly improve CI-linked OXPHOS kinetics. Using the same 4 substrate conditions as before—P/M, G/M, O/M, and PC/M—we repeated our CK-clamp based experiments in the presence of Ap5A in DEN-NT and DEN-T mitochondria (Figure 5G). Interestingly, Ap5A was able to rescue the  $JH^+_{OXPHOS}$  of DEN-T mitochondria to a rate equivalent to DEN-NT mitochondria for all 4 substrates, though the P/M-supported  $JH^+_{OXPHOS}$  trended toward respiration being lower in DEN-T (Figure 5G). Additionally, for every substrate condition except for P/M, respiration across the  $\Delta GATP$  titration was equivalent between DEN-NT and DEN-T. Inclusion of Ap5A did not rescue the  $FCCP_{\Delta GATP}$ , however, and DEN-NT mitochondria were able to attain a significantly higher FCCP-stimulated rate under every substrate condition (Figure 5G).

## Discussion

Through application of our comprehensive mitochondrial diagnostic workflow, we sought to evaluate the functional impact of the metabolic, proteomic, and genomic shifts that have been reported in hepatocellular carcinoma (HCC). Our experiments leveraged a variety of respiratory stimuli and carbon substrate conditions *in vitro*, which allowed us to identify a consistent reduction in CI-supported respiration across two distinct models of HCC, cultured cells and diethylnitrosamine-induced tumors (DEN). Further, the pairing of mitochondrial-enriched proteomics and targeted inhibitor use revealed a potential regulatory role of adenylate kinase 4 (AK4) in limiting CI-linked respiratory flux. To our knowledge, this was the first study to combine mitochondrial-targeted proteomics with comprehensive biochemical measures of mitochondrial performance in any model of hepatocellular carcinoma.

Given previous reports of compromised mitochondrial respiration and reduced expression of respiratory complexes in HCC tumors (Boitier et al., 1995; Chavez et al., 2017; Santos et al., 2012), we expected to find large differences in intrinsic mitochondrial function in the present study. However, both models of HCC demonstrated that the total respiratory capacity of HCC was equivalent or greater to nontumor mitochondria when energized with a mixture of carbon substrates that activated the entire respiratory chain (P/M/G/S/O) across multiple respiratory stimuli (uncoupling, clamped ATP free energy, and ADP). This suggests that the manifestation of reduced mitochondrial flux in HCC may not be due to a loss of capacity, but rather an increase in extramitochondrial regulation *in vivo*.

As has been reported by others (Boitier et al., 1995; Chavez et al., 2017; Santos et al., 2012), we found a CI-specific deficit in respiration in both models of HCC. In DEN-induced tumors, this was found to be due to two separate mechanisms: a reduced capacity of CI to directly oxidize NADH, as well as regulation by adenylate kinase activity. The largest of the respiratory complexes, CI is made up of a total of 45 protein subunits encoded in both the nuclear and mitochondrial genomes. The 7 CI genes contained within mitochondrial DNA (mtDNA) are the most hydrophobic and integral to its proper assembly and catalytic activity (Falkenberg et al., 2007). Interestingly, the reduced functionality of CI in DEN tumors was not linked to an overall loss of abundance of CI-related proteins. However, we did find a specific loss of two mtDNA-encoded subunits, ND2 and ND3, between DEN-induced tumor mitochondria and their adjacent nontumor tissue that may have contributed to reduced CI capacity. This finding supports those of other groups who have found a high mutational burden in HCC mtDNA (Corral et al., 1989b; Hsu et al., 2013; Lee et al., 2010; Sloan et al., 2012; Yin et al., 2010), including the discovery of a mutation in human HCC that would introduce a premature stop codon into the gene for ND1 (Yin

et al., 2010). The loss of these subunits did not appear to affect the ability of the ETS to phosphorylate ATP under any combination of respiratory substrates, which may suggest that CI respiratory capacity is in fact separate from phosphorylation capacity.

DEN-induced tumors were also found to have increased expression of AK4 compared to nontumor tissues. AK4 is a mitochondrial matrix protein that has previously been shown to be upregulated in response to stressors such as hypoxia (Chen et al., 2006; Wujak et al., 2019). In support of our findings, AK4 has also been found to be overexpressed in human HCC-derived HepG2 cells (Kong et al., 2013), as well as other cancer types from a diverse group of tissues (Fujisawa et al., 2016; Jan et al., 2019, 2012; Xin et al., 2019; Zhang et al., 2019). In cancer, AK4 has been suggested to contribute to the progression and metastasis of cancer, though the exact mechanism is not clear. Our findings demonstrate that in DEN-induced HCC, AK4 appears to have a role in regulating respiratory flux through CI, and these effects were particularly pronounced in the presence of ATP free energy that mimics physiological demands on mitochondria. This may have important implications for mitochondrial metabolism in the context of the whole cell. For instance, limiting the oxidation of NADH at Complex I may also slow the oxidation of pyruvate, leading to an increased rate of conversion to lactate and a preservation of carbon backbones for biosynthesis (vander Heiden et al., 2009).

Consistent with our previously published work in leukemia (Nelson et al., 2021), DEN-induced tumor mitochondria displayed a reduced capacity to respond to the uncoupler FCCP in the presence of ATP free energy across all substrate conditions tested. As both leukemic and HCC mitochondria were unable to attain the respiration rate from earlier in the same assay, it appears that the FCCP effect is due in some part to direct inhibition of the respiratory complexes. In leukemia, this effect was found to be dependent upon the entry of ATP into the mitochondrial

matrix, as the addition of the adenine nucleotide translocase (ANT) inhibitor carboxyatractyloside (CAT) restored FCCP-stimulated flux in the presence of ATP free energy (Nelson et al., 2021). Interestingly, we found that CAT had no effect on the FCCP response in HCC tumor mitochondria, suggesting that the effector of the inhibition was not located within the matrix. This finding is intriguing as the same phenotype appears to be caused by two separate mechanisms, suggesting that it may have an important physiological role in cancer.

We did see limitations to mitochondrial membrane potential ( $\Delta\Psi$ ) in DEN-induced tumor mitochondria, consistent with other findings in DEN-treated rodents (Chavez et al., 2017) and our own results in HepG2 cells (Schmidt et al., 2021). Depolarization of  $\Delta\Psi$  was evident across a physiological span of ATP free energy despite the availability of all respiratory substrates (P/M/G/S/O). Although surprising, this relative depolarization may explain two other effects that were seen in DEN tumor mitochondria: the reduced  $K_m$  for FCCP and their reduced ability to retain calcium. In the case of FCCP, respiration is dependent upon the import of respiratory substrates into the mitochondrial matrix, which is dependent upon a polarized inner mitochondrial membrane. As FCCP uncoupling already induces a slight depolarization, the reduced respiration seen in DEN tumor mitochondria stimulated by FCCP was likely caused by more rapid loss of  $\Delta\Psi$  and subsequent substrate transport.

Similarly, calcium cations require mitochondrial membrane polarization for their accumulation in the matrix, and reduced membrane potential has been linked to increased sensitivity of the mitochondrial transition pore opening (Camara et al., 2009; Nicholls, 2005). The physiological relevance of reduced calcium uptake in HCC is supported by previous reports of elevated cytosolic calcium levels in cell models of HCC with low mitochondrial activity (Lee et al., 2015). Interestingly, increased intracellular calcium was shown to induce nuclear transcription

of NUPR1, a promoter of cancer progression (Lee et al., 2015). This may imply that low mitochondrial membrane potential and calcium uptake could be a means of retrograde signaling to the nucleus in HCC. This is an interesting avenue to explore further as HCC tumors may be particularly sensitive to treatments designed to manipulate intracellular calcium levels.

Our findings support the utility of mitochondrial phenotyping in identifying novel regulatory mechanisms governing cellular bioenergetics. As all measurements were made in isolated mitochondria, the influence of cytosolic and cytoskeletal regulation on metabolic fluxes was removed to evaluate the intrinsic properties of the mitochondria. Future studies incorporating whole cell or tissue measurements of flux will help to increase understanding of the physiological impact of these differences in HCC.

## **Methods**

### ***Materials and Reagents***

Unless indicated, all chemicals and reagents were purchased from Sigma-Aldrich (St. Louis, MO).

### ***Animal Treatment***

All animal experiments were conducted in C3H/HeJ mice (The Jackson Laboratory, stock #000,659) according to the guidelines approved by the East Carolina University Institutional Animal Care and Use Committee. Mice were housed under controlled temperature (22°) and light (12h light/12h dark) conditions with free access to food and water. Induction of hepatocellular carcinoma was achieved using a single injection of diethylnitrosamine (DEN), as previously described (Tolba et al., 2015). DEN (25mg/kg) or saline (0.9%) was injected interperitoneally at

14 days postnatal. As mice were not weaned, all littermates received the same treatment. Both DEN (n=23) and saline (n=27) mice were sacrificed after tumor development at ~27 weeks of age. At the time of sacrifice, 12h-fasted mice were anesthetized with isoflurane and exsanguinated prior to tissue removal.

### ***Cell culture***

Mouse hepatocellular carcinoma cells (Hepa 1-6) and mouse immortalized hepatocytes (AML12) were purchased from ATCC (Manassas, VA). Hepa 1-6 cells were cultured in Dulbecco's Modified Eagle's Medium (DMEM; Thermo Fisher Scientific, Waltham, MA) containing 4mM L-glutamine, 4.5g/L glucose, 1mM sodium pyruvate, and 1.5g/L sodium bicarbonate, supplemented with 10% fetal bovine serum (FBS; Gibco) and 1% penicillin/streptomycin as recommended by ATCC. AML12 cells were cultured in DMEM: F-12 Medium containing 2.5mM L-glutamine, 15mM HEPES, 0.5mM sodium pyruvate, and 1200mg/L sodium bicarbonate, supplemented with 10% FBS, 1% penicillin/streptomycin, 10µg/ml insulin, 5.5µg/ml transferrin, 5ng/ml selenium, and 40ng/ml dexamethasone.

### ***Isolation of mitochondria from cultured cells and mouse tissues***

Mitochondrial isolation from cultured cells was performed as previously described (Schmidt et al., 2021) with slight modifications. Briefly, cells were trypsinized, centrifuged at 300xg at room temperature, resuspended in phosphate-buffered saline (PBS), and again centrifuged at 300 x g. This pellet was resuspended in ice-cold Buffer A (50mM MOPS, 100mM KCl, 1mM EGTA, 5mM MgSO<sub>4</sub>, 2g/L bovine serum albumin; pH=7.1) and homogenized via a Teflon pestle and borosilicate glass vessel for 40 passes, then centrifuged at 800 x g for 10min at

4°C. The supernatant was saved on ice, and the pellet was resuspended in Buffer A, homogenized, and centrifuged at 800 x g. Both supernatants were pooled and centrifuged at 10,000 x g for 10min at 4°C. The mitochondrial pellet was then washed in Buffer B (Buffer A with no bovine serum albumin), transferred to a microcentrifuge tube, and centrifuged again at 10,000 x g for 10min at 4°C. Final mitochondrial pellets were resuspended in 100-150µL of Buffer A and protein content was determined via the Pierce BCA protein assay.

Livers from DEN- and saline-treated mice were excised, rinsed in ice cold (4°C) PBS to remove excess blood, and placed on ice in Buffer C (7.23mM K<sub>2</sub>EGTA, 2.77mM CaK<sub>2</sub>EGTA, 20mM imidazole, 20mM taurine, 6.56mM MgCl<sub>2</sub>·6H<sub>2</sub>O, and 50mM K-MES; pH 7.4). Tumors were separated from nontumor adjacent liver tissue under a dissecting microscope. Nontumor tissue was only selected for mitochondrial isolation if there were no visible abnormalities present. Following separation, tissues were transferred to Buffer B, minced, and homogenized via Teflon pestle and borosilicate glass for 8 passes, then centrifuged at 800 x g for 10min at 4°C. Supernatants were passed through gauze to remove lipid and then centrifuged at 10,000 x g for 10min at 4°C. This mitochondrial pellet was washed in Buffer A, transferred to a microcentrifuge tube and again centrifuged at 10,000 x g. Final mitochondrial pellets were resuspended in 200-300µL of Buffer A and protein content was determined via the Pierce BCA protein assay.

### ***Citrate Synthase Activity***

Citrate synthase activity was determined using a plate-based colorimetric assay as previously described (McLaughlin et al., 2020).

### ***Mitochondrial Respiration Assessment***

High-resolution oxygen consumption rate ( $JO_2$ ) was assessed via the Oroboros Oxygraph-2K (Oroboros Instruments, Innsbruck, Austria) as previously described (McLaughlin et al., 2020), with minor adjustments. Respiration media was Buffer D (105mM K-MES, 30mM KCl, 10mM  $KH_2PO_4$ , 5mM  $MgCl_2$ , 1mM EGTA, 2.5g/L bovine serum albumin; pH=7.2), with additions as noted. All respiration experiments were conducted in a 1mL reaction volume at 37°C. All respiration assays conducted with cell mitochondria were performed with the addition of 10 $\mu$ M cytochrome C.

A variety of carbon substrates and inhibitors were used to support respiration, with assay-specific substrate conditions defined in figure legends. General substrate concentrations were as follows: pyruvate (P; 5mM), malate (M; 1mM), glutamate (G; 5-10mM), octanoyl-L-carnitine (O; 0.2mM), succinate (S; 5-10mM), palmitoyl-carnitine (PC; 20 $\mu$ M),  $\alpha$ -ketoglutarate (AKG; 10mM), dihydroorotate (DHO; 10mM); glycerol-3-phosphate (5mM), calcium (1.2mM), malonate (Malo; 20mM), oligomycin (0.02 $\mu$ M), carbonyl cyanide-4-phenylhydrazone (FCCP; 0.25-4 $\mu$ M), rotenone (Rot; 0.5 $\mu$ M), antimycin A (0.5 $\mu$ M), carboxyatractyloside (CAT, 1 $\mu$ M), 17-AAG (1 $\mu$ M), teriflunomide (TF; 20 $\mu$ M), P1, P5-di(adenosine-5') pentaphosphate (Ap5A; 0.2mM), creatine kinase (CK; 20U/mL), ATP (5mM), phosphocreatine (PCR; 1mM, 6mM, 15mM, 21mM), hexokinase (HK; 1U/mL), glucose (5mM), ADP (10-500 $\mu$ M).

Electron transport system (ETS) capacity was determined through titration of chemical uncoupler FCCP using 25 $\mu$ g cell mitochondria and 50-100 $\mu$ g tissue mitochondria. Buffer D was supplemented with 5mM creatine monohydrate (Cr), and FCCP was titrated from 0.5-4 $\mu$ M in multi-substrate assays, and from 0.25-4 $\mu$ M for the Complex-I specific assays.

Oxidative phosphorylation (OXPHOS) kinetics were determined using the creatine kinase (CK) clamp as previously described (Fisher-Wellman et al., 2018; Glancy et al., 2013, 2008). The

equilibrium constant of the CK reaction ( $K'_{CK}$ ) was used to calculate the free energy of ATP hydrolysis ( $\Delta G_{ATP}$ ) in the presence of known quantities of Cr, PCr, and ATP via an online resource ([https://dmpio.github.io/bioenergetic-calculators/ck\\_clamp/](https://dmpio.github.io/bioenergetic-calculators/ck_clamp/)) described previously (Fisher-Wellman et al., 2018). Assay buffer was Buffer D supplemented with 5mM Cr, and experiments were conducted using 50 $\mu$ g cell mitochondria and 100-150 $\mu$ g tissue mitochondria. Following the titration of  $\Delta G_{ATP}$ , FCCP was titrated from 0.5-4 $\mu$ M in multi-substrate assays, and from 0.25-4 $\mu$ M for the Complex-I specific assays.

The substrate preference assay was conducted using Buffer D supplemented with 5mM Cr and the hexokinase (HK) clamp components (1U/mL HK, and 5mM glucose) using 150-200 $\mu$ g tissue mitochondria.

ADP-stimulated respiration assays were performed using Buffer D supplemented with HK (1U/mL), glucose (5mM), glucose-6-phosphate dehydrogenase (2U/mL), NADP<sup>+</sup> (4mM), and Ap5A. Mitochondrial loading was 50 $\mu$ g cell mitochondria and 100-150 $\mu$ g tissue mitochondria. ADP-linked respiration was inhibited at the end of each assay using oligomycin, then FCCP was titrated from 0.5-3 $\mu$ M. All mitochondrial respiration was inhibited by the addition of complex III inhibitor antimycin A.

### ***Mitochondrial NAD(P)H/NAD(P)<sup>+</sup> redox and membrane ( $\Delta\Psi$ ) potential***

NADH/NAD<sup>+</sup> and  $\Delta\Psi$  were determined simultaneously using a QuantaMaster Spectrofluorometer (QM-400, Horiba Scientific, Kyoto, Japan) as previously described (Nelson et al., 2021), with some modifications. Experiments were performed with tissue mitochondria (20 $\mu$ g) in a 200 $\mu$ L reaction volume at 37°C. Assay buffer was Buffer D supplemented with Cr (5mM) and tetramethyl rhodamine methyl ester (TMRM; 0.2  $\mu$ M). Mitochondria were stimulated using the

creatine kinase clamp and  $\Delta G_{\text{ATP}}$  was titrated via PCr (6, 15, 21mM). Oligomycin (0.02 $\mu$ M) was added to inhibit ATP synthesis and cyanide (CN, 10mM) was added to induce 100% reduction of the matrix NADH pool, followed by isocitrate (5mM) to induce 100% reduction of the matrix NADPH pool. NADH/NAD<sup>+</sup> was detected at Ex/Em: 350/450 and ultimately expressed as a percentage reduction of the CN value as previously described (Nelson et al., 2021). TMRM-derived  $\Delta\Psi$  was quantified by taking the fluorescence ratio of Ex/Em: 576/590 to 551/590 and converting this to mV values using a tissue-specific standard curve determined as previously described (Fisher-Wellman et al., 2018).

### ***JATP synthesis using the hexokinase ADP clamp***

ATP production rate (JATP) was determined fluorometrically as previously described (McLaughlin et al., 2020). Experiments with cell mitochondria were performed with the addition of 10 $\mu$ M cytochrome C.

### ***Frozen mitochondrial respiration***

Experiments using frozen mitochondria were performed using a protocol adapted from Acin-Perez et al. (2020). Mitochondrial pellets were frozen on dry ice, then thawed on wet ice and resuspended in Buffer B. Protein concentration was determined using a Pierce BCA Assay. Respiration assay buffer was Buffer D supplemented with 5mM creatine, 2mM NAD<sup>+</sup>, 0.1mM coenzyme A, 0.3mM thiamine pyrophosphate, 10 $\mu$ M cytochrome C, 1U/L HK, and 5mM glucose. Mitochondria (40 $\mu$ g) were added to the chamber, followed by ADP (500 $\mu$ M). Complex I-linked respiration was stimulated with NADH (2mM), then inhibited with Rot (0.5 $\mu$ M). Complex II-linked respiration was then stimulated with S (10mM) and inhibited by Malo (20mM), followed

by antimycin A (0.5 $\mu$ M) to inhibit Complex III. Complex IV-linked respiration was then stimulated with N,N,N',N'-tetramethyl-*p*-phenylenediamine (TMPD; 0.5mM dissolved in 2mM ascorbate) and ascorbate (2mM). Respiration in the presence of any of the inhibitors was considered to be non-mitochondrial and subtracted (ex. Final NADH-stimulated  $JO_2 = \text{NADH } JO_2 - \text{Rot } JO_2$ ).

### ***Calcium retention assay***

Calcium retention was evaluated fluorometrically in a 200 $\mu$ L reaction volume at 37°C as previously described (Sloan et al., 2012), with some modification. Assay buffer was Buffer E (0.25M sucrose, 10mM Trizma-HCl, 20mM Trizma-base, 10mM  $KH_2PO_4$ , 0.5mg/mL bovine serum albumin, 5mM Cr, 40 $\mu$ M EGTA, 1U/mL HK, 5mM glucose) supplemented with 1 $\mu$ M calcium green 5N to fluorescently measure extracellular calcium (Ex/Em: 506/532). Mitochondria (50 $\mu$ g) were energized with S/Rot and 50 $\mu$ M ADP, then calcium was titrated in 30 $\mu$ M additions until mitochondrial permeability transition pore opening (rapid increase in fluorescence trace). Additional 30 $\mu$ M and 100 $\mu$ M additions were made following MPTP opening to confirm no additional calcium uptake. The assay was then ended with the addition of 10mM EGTA. Calcium retention capacity was considered the amount of calcium added prior to MPTP opening.

### ***nLC-MS/MS for label-free proteomics***

Mitochondria were lysed, digested, and lyophilized for proteomics as previously described (McLaughlin et al., 2020). Samples were then resuspended in 0.1% formic acid for peptide quantification (ThermoFisher Cat# 23275) and dilution to a final concentration of 0.25 $\mu$ g/ $\mu$ L. nanoLC-MS/MS analysis was performed using an UltiMate 3000 RSLCnano system

(ThermoFisher) coupled to a Q Exactive Plus Hybrid Quadrupole-Orbitrap mass spectrometer (ThermoFisher) via a nanoelectrospray ionization source as previously described (McLaughlin et al., 2020). MS1 was performed at 70,000 resolution, with an AGC target of  $3 \times 10^6$  ions and a maximum injection time (IT) of 100ms. Data-dependent acquisition (DDA) was used to collect MS2 spectra of the top 15 most abundant precursor ions with a charge  $> 1$  per MS1 scan, with dynamic exclusion enabled for 20s. Precursor ions isolation window was 1.5m/z and normalized collision energy was 27. MS2 scans were performed at 17,500 resolution, maximum IT of 50ms, and AGC target of  $1 \times 10^5$  ions.

### ***Data analysis for label-free proteomics***

Proteome Discoverer 2.2 (PDv2.2) was used for raw data analysis. Default search parameters included oxidation as a variable modification and carbamidomethyl (57.021 Da on C) as a fixed modification. Data were searched against both the Uniprot Mus musculus reference proteome (Proteome ID: UP000000589) and mouse Mito Carta 3.0 database (Rath et al., 2021). As previously described (McLaughlin et al., 2020), PSMs were filtered to a 1% FDR and grouping to unique peptides was also maintained at a 1% FDR at the peptide level. Strict parsimony was used to group peptides to proteins, and proteins were again filtered to 1% FDR. MS1 precursor intensity was used for peptide quantification, and low abundance resampling was used for imputation. As previously described (McLaughlin et al., 2020), high confidence master proteins were used to determine mitochondrial enrichment factor (MEF) by comparing mitochondrial protein abundance (identified by the MitoCarta 3.0 database) to total protein abundance.

### ***Statistical analysis***

Statistical analysis of label-free proteomics was performed as described previously (McLaughlin et al., 2020). All functional assays were analyzed using Prism 9, and results are all presented as mean  $\pm$  SEM (error bars). Data were normalized to mitochondrial enrichment factor (MEF) as previously described (McLaughlin et al., 2020) or citrate synthase (CS) activity as indicated in individual figures. Statistical significance was set at  $p < 0.05$ , and details of statistical analysis are included within figure legends.

## Figures

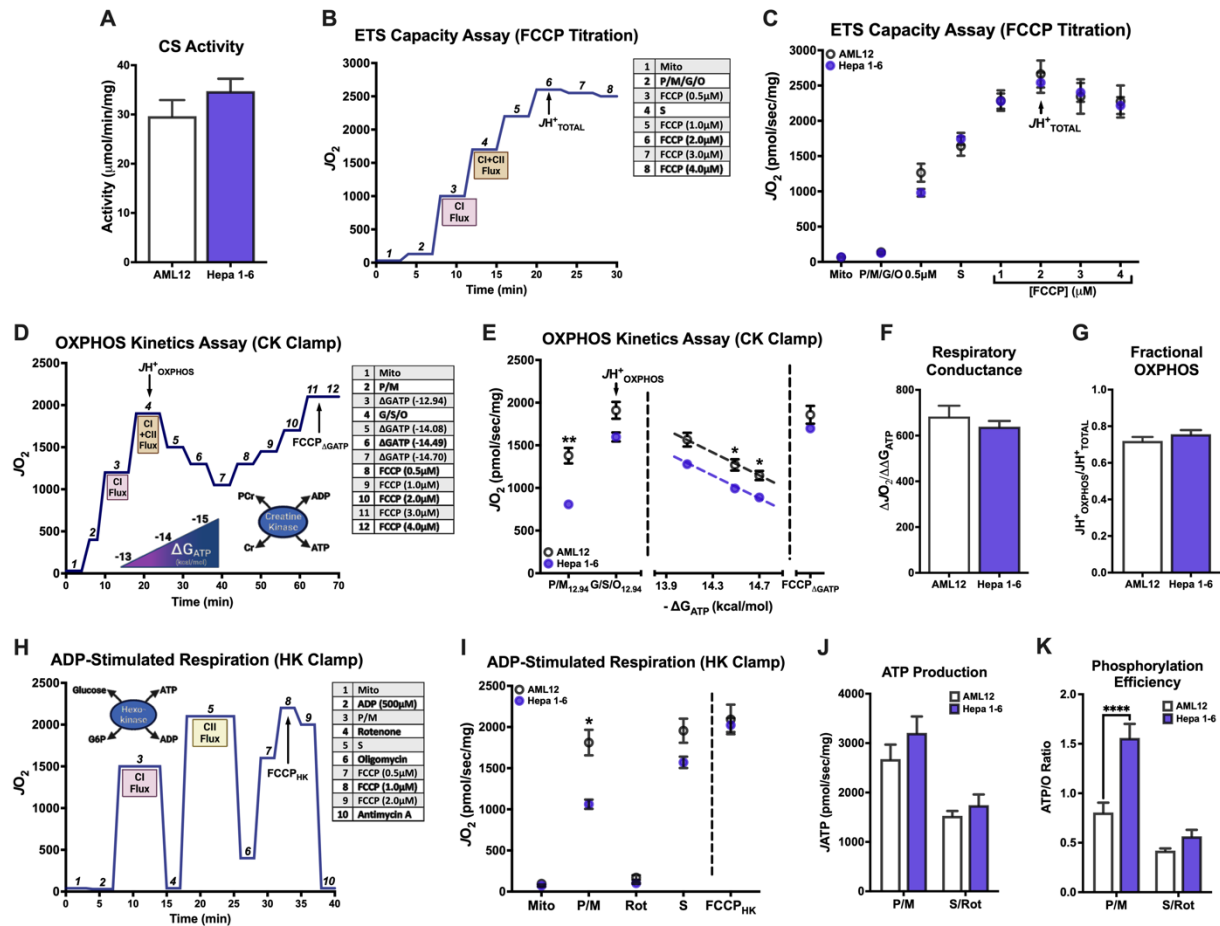


**Figure 1. Hepatocellular carcinoma-derived (Hepa 1-6) cells display profound impairment in Complex I-supported respiration compared to non-tumorigenic immortalized hepatocytes**

(*AML12*). All experiments were performed using isolated mitochondria and normalized to mitochondrial protein (mg). (A) Citrate synthase (CS) activity. (B) Schematic depicting oxygen consumption ( $JO_2$ ) during the ETS Capacity Assay (FCCP titration) where point 3 represents FCCP-stimulated flux in the presence of Complex I substrates pyruvate/malate (P/M), point 4 represents FCCP-stimulated flux in the presence of Complex I and II substrates P, M, glutamate, succinate, octanoyl-L-carnitine (P/M/G/S/O), and point 6-7 represents the maximal proton conductance of the electron transport system ( $JH^+_{TOTAL}$ ). (C) ETS capacity protocol measured in *AML12* and Hepa 1-6. (D) Schematic depicting  $JO_2$  during the OXPHOS Capacity Assay ( $\Delta GATP$  titration) where point 3 represents  $\Delta GATP$ -stimulated flux with P/M, point 4 represents  $\Delta GATP$ -stimulated flux with P/M/G/S/O or the maximal proton conductance by the OXPHOS system ( $JH^+_{OXPHOS}$ ), and point 11-12 represents the maximum proton conductance in the presence of  $\Delta GATP$  (FCCP $_{\Delta GATP}$ ). (E) OXPHOS capacity protocol measured in *AML12* and Hepa 1-6. (F) Comparison of respiratory conductance from dotted lines in (E). (G) Comparison of fractional OXPHOS calculated as the ratio of  $JH^+_{OXPHOS}$  to  $JH^+_{TOTAL}$ . (H) Schematic depicting  $JO_2$  during the ADP-stimulated Respiration where point 3 represents ADP-stimulated flux with P/M, point 5 represents ADP-stimulated flux with S/rotenone (Rot), and point 8 represents maximal proton conductance in the presence of ADP and oligomycin (FCCP $_{HK}$ ). (I) ADP-stimulated protocol with *AML12* and Hepa 1-6. (J) ATP production rate ( $JATP$ ) fueled by P/M and S/Rot. (K) Phosphorylation efficiency, quantified as the ATP/O ratio, fueled by P/M and S/Rot. Data are presented as mean  $\pm$  SEM and analyzed by unpaired t-test (A, F-G) and two-way ANOVA (C, E, I-K). \* $p < 0.05$ , \*\* $p < 0.01$ , \*\*\* $p < 0.001$ , \*\*\*\* $p < 0.0001$ .

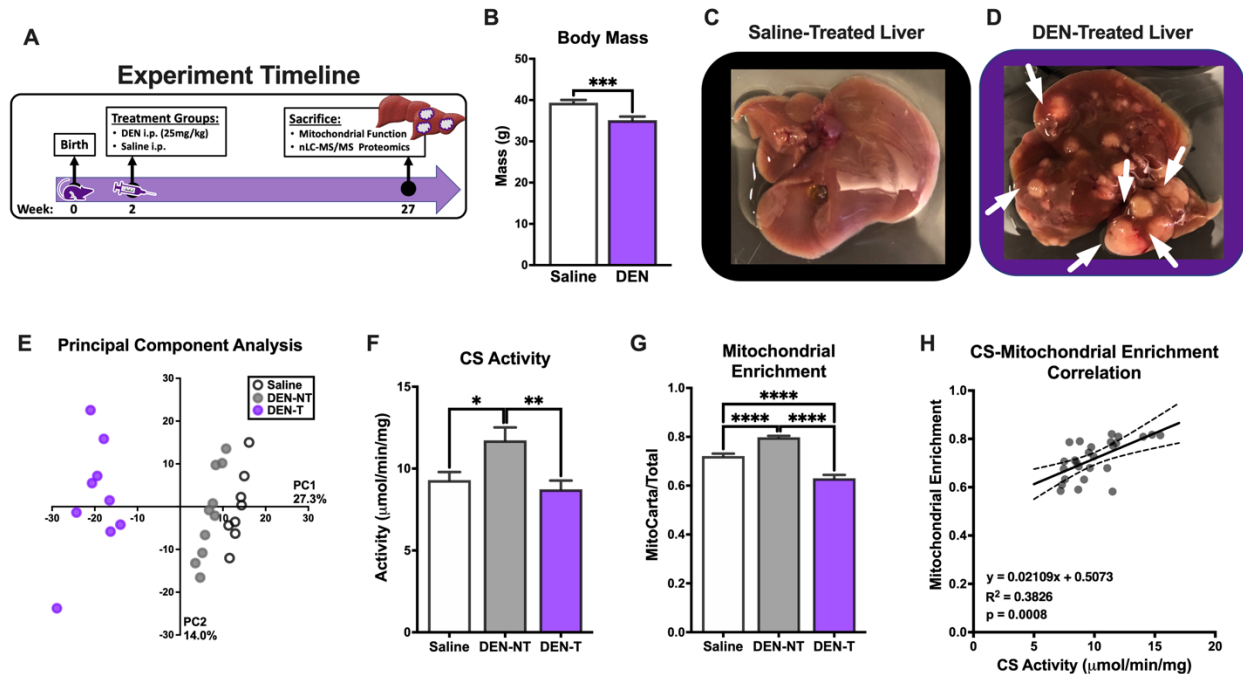


**Figure 2. Induction of hepatocellular carcinoma in C3H mice using diethylnitrosamine (DEN) and the purity of the resultant isolated mitochondrial preparations.** (A) Experiment timeline of DEN treatment. (B) Body weight (g) of saline and DEN-treated mice at time of sacrifice. (C,D) Images of saline (C) and DEN-treated livers (D); white arrows denote tumors. (E) Principal component analysis (PCA) of isolated mitochondrial preparations from saline treated liver (Saline), DEN-treated nontumor (DEN-NT), and DEN-induced tumor (DEN-T). (F) Citrate synthase (CS) activity of isolated mitochondria. (G) Comparison of mitochondrial enrichment calculated of the ratio of mitochondrial (MitoCarta) to total protein abundance. (H) Linear correlation between CS activity and mitochondrial enrichment. Data are presented as mean  $\pm$  SEM and analyzed by unpaired t-test (B) and one-way ANOVA (F,G). \* $p < 0.05$ , \*\* $p < 0.01$ , \*\*\* $p < 0.001$ , \*\*\*\* $p < 0.0001$ .

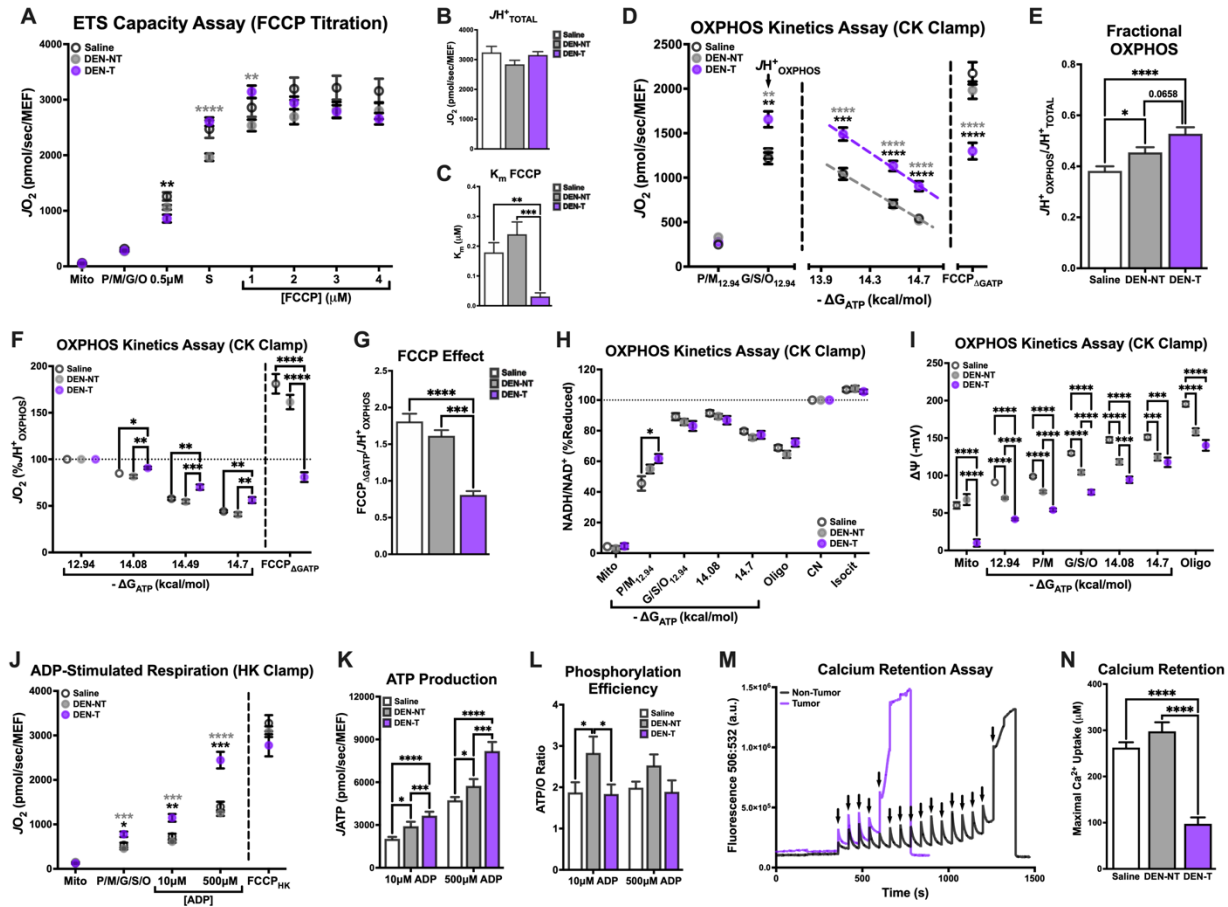


**Figure 3. Broad characterization of DEN-induced tumor mitochondria across diverse biochemical stimuli.** All experiments were performed using isolated mitochondria and normalized to mitochondrial enrichment factor (MEF). (A) ETS capacity protocol measured in Saline, DEN-NT, and DEN-T, significant differences from DEN-T denoted by black asterisks for Saline, gray for DEN-NT. (B) Comparison of  $JH^+_{TOTAL}$  from (A). (C) Comparison of  $K_m$  of FCCP from (A). (D) OXPHOS capacity protocol measured in Saline, DEN-NT, and DEN-T, significant differences from DEN-T denoted by black asterisks for Saline, gray for DEN-NT. (E) Comparison of fractional OXPHOS from (D). (F) OXPHOS capacity protocol from (D), graphed as  $\% JH^+_{OXPHOS}$ . (G) Comparison of FCCP effect, quantified as the ratio of  $FCCP_{\Delta GATP}$  to  $JH^+_{OXPHOS}$ . (H) Relationship between  $\Delta GATP$  and NADH/NAD<sup>+</sup> redox poise as  $\%$  cyanide-induced reduction (CN). (I) Mitochondrial membrane potential across a  $\Delta GATP$  span. (J) ADP-stimulated protocol

measured in Saline, DEN-NT, and DEN-T fueled by P/M/G/S/O, significant differences from DEN-T denoted by black asterisks for Saline, gray for DEN-NT. (K) Comparison of  $J_{ATP}$  when stimulated with  $10\mu\text{M}$  and  $500\mu\text{M}$  ADP. (L) ATP/O ratio when stimulated with  $10\mu\text{M}$  and  $500\mu\text{M}$  ADP. (M) Representative fluorometric trace of calcium retention assay (Ex/Em: 506/532); black arrows represent  $30\mu\text{M}$  additions of calcium; sharp increase in fluorescence was considered MPTP opening. (N) Comparison of maximal calcium uptake ( $\mu\text{M}$ ) prior to MPTP opening. Data are presented as mean  $\pm$  SEM and analyzed by two-way ANOVA (A,D, F, H-L) and one-way ANOVA (B-C, E, G, N). \* $p < 0.05$ , \*\* $p < 0.01$ , \*\*\* $p < 0.001$ , \*\*\*\* $p < 0.0001$ .

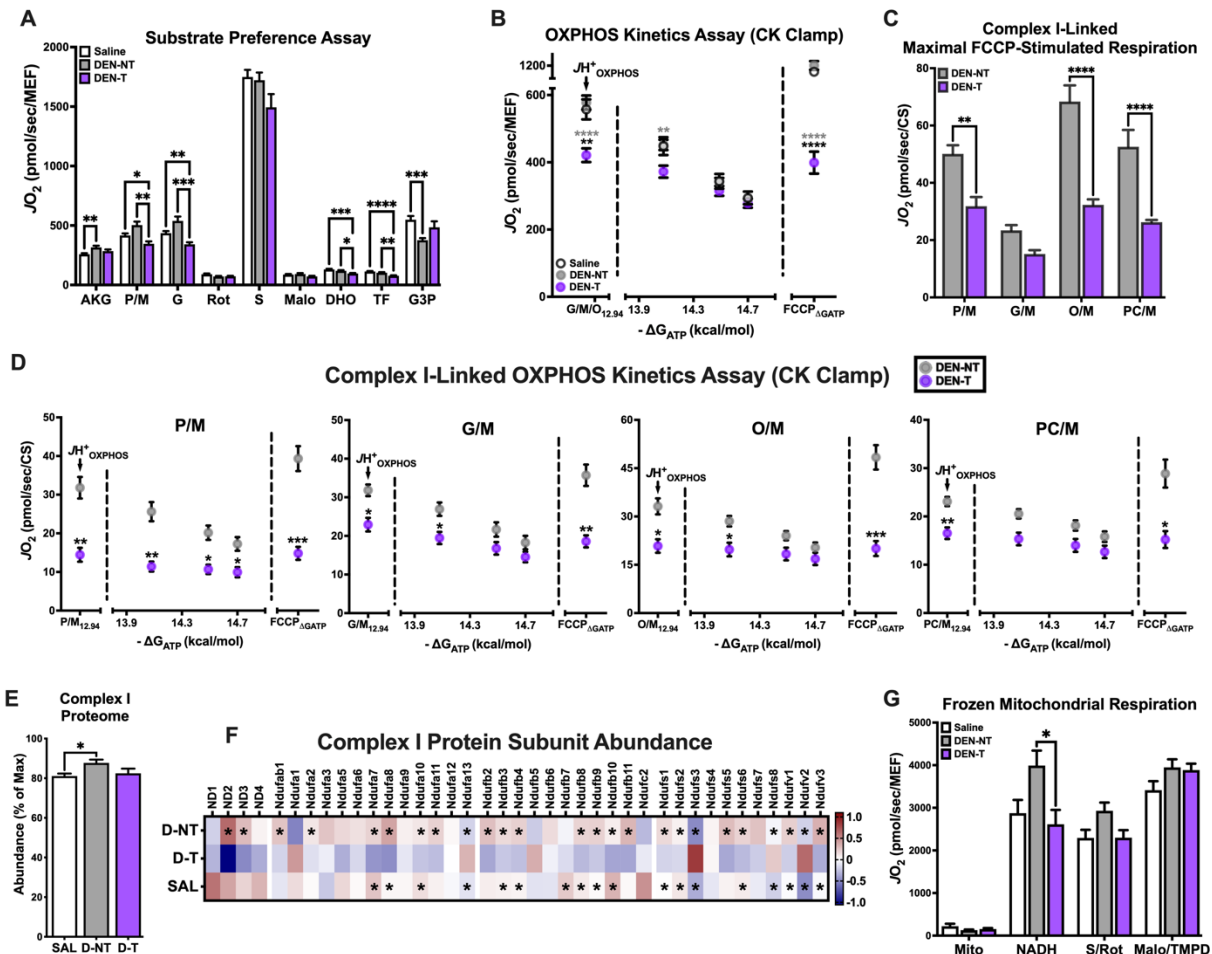


**Figure 4. DEN tumor-derived mitochondria exhibit Complex I-linked respiratory deficiency.**

(A) Substrate preference assay stimulated with 500 $\mu$ M ADP clamped by HK clamp. Substrate/inhibitor additions were as follows: AKG (10mM), P/M (5/1mM), G (10mM), Rot (0.5 $\mu$ M), S (10mM), Malo (20mM), DHO (10mM), TF (20 $\mu$ M), G3P (5mM). (B) OXPHOS kinetics protocol fueled by G/M/O. (C) Maximal FCCP-stimulated rates when fueled by 4 different Complex I-linked carbon substrates (P/M, G/M, O/M, PC/M); data normalized to CS activity. (D) OXPHOS kinetics protocols fueled by P/M, G/M, O/M, PC/M; data normalized to CS activity. (E) Relative abundance of Complex I subunits expressed as % of highest summed abundance. (F) Heatmap of Complex I protein subunit expression; asterisks denote significant difference from DEN-T ( $q < 0.1$ ). (G) Respiration in freeze-thawed mitochondrial preparations. Data are presented as mean  $\pm$  SEM and analyzed by two-way ANOVA (A-D, G) and one-way ANOVA (E). \* $p < 0.05$ , \*\* $p < 0.01$ , \*\*\* $p < 0.001$ , \*\*\*\* $p < 0.0001$ .

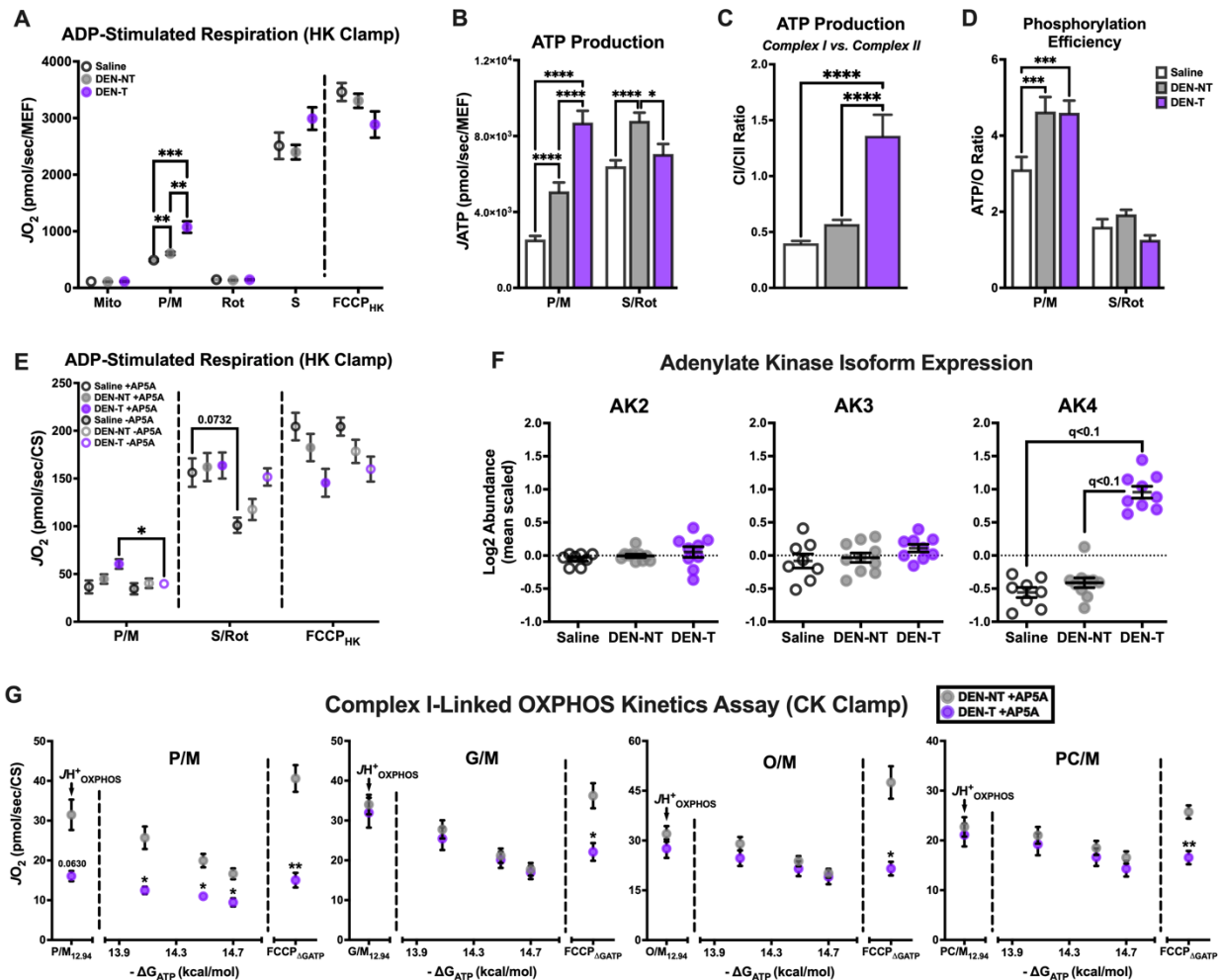
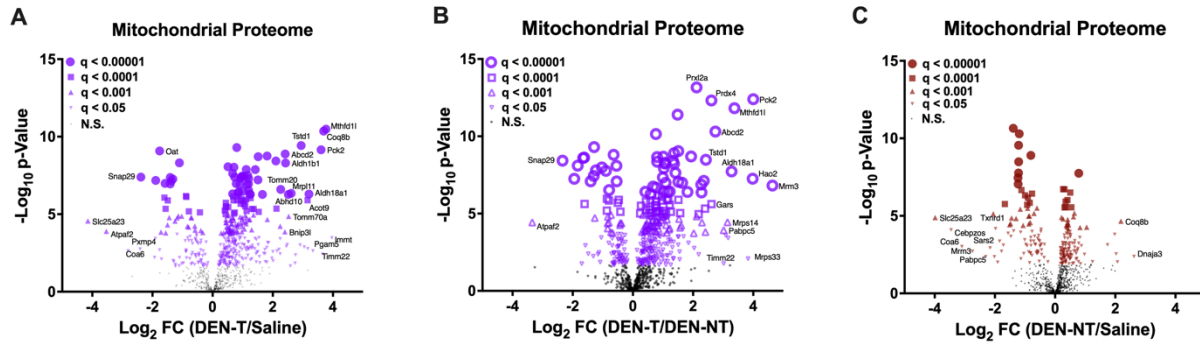


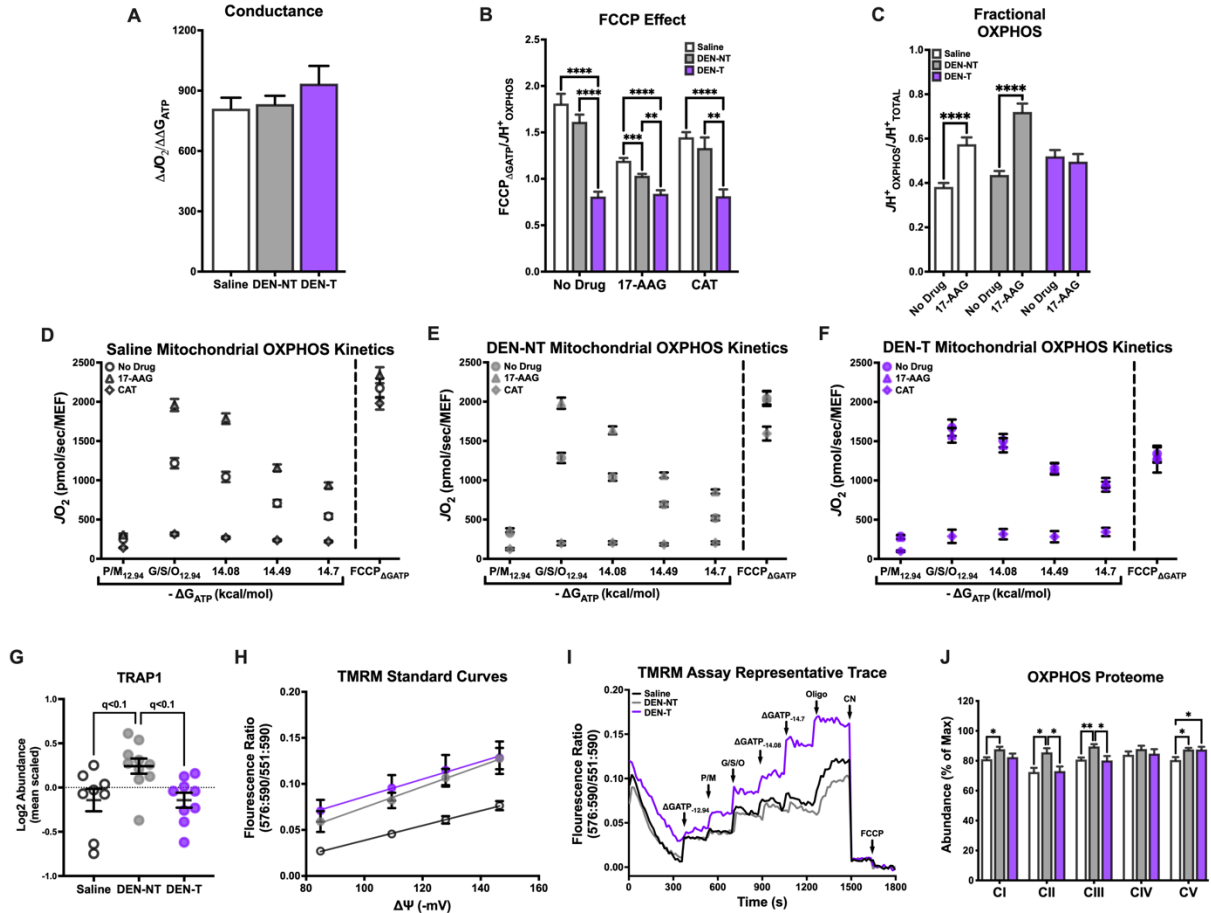
**Figure 5. Upregulation of adenylate kinase 4 (AK4) in DEN-induced tumor mitochondria contributes to altered Complex I-linked respiratory flux.** (A) ADP-stimulated protocol fueled by P/M and S/Rot. (B) Comparison of JATP fueled by P/M and S/Rot. (C) Ratio of CI-supported (P/M) JATP to CII-supported (S/Rot) JATP from (B). (D) Comparison of ATP/O ratios fueled by P/M and S/Rot. (E) ADP-stimulated protocol fueled by P/M and S/Rot in the presence (+) and absence (-) of adenylate kinase (AK) inhibitor Ap5A; data normalized to CS activity. (F) Relative expression of AK isoforms 2-4. (G) OXPHOS kinetics protocols in the presence of Ap5A fueled by P/M, G/M, O/M, PC/M; data normalized to CS activity. Data are presented as mean  $\pm$  SEM and

analyzed by two-way ANOVA (A-B, D-E, G) and one-way ANOVA (C). \* $p < 0.05$ , \*\* $p < 0.01$ , \*\*\* $p < 0.001$ , \*\*\*\* $p < 0.0001$ .



**Supplementary Figure 1. Pairwise mitochondrial proteome volcano plot comparisons. (A-C)**

Volcano plots of differentially expressed mitochondrial proteins identified using the mouse MitoCarta 3.0 database. Plots depict differences between tumor (DEN-T) and saline-treated liver (Saline; A), tumor and DEN-treated nontumor liver (DEN-NT; B), and DEN-NT and Saline tissues (C). Significance is denoted by the size and color of each symbol, as indicated in the legend. Gray symbols indicate adjusted  $p$  value  $> 0.1$ .



**Supplementary Figure 2. *Trap1* and OXPHOS complex expression and effects of 17AAG and CAT on OXPHOS kinetics.** (A). Comparison of respiratory conductance (dotted lines in Figure 3E). (B) Comparison of FCCP effect in the presence of no drug, HSP90 inhibitor 17AAG, and adenine dinucleotide transporter inhibitor CAT. (C) Comparison of Fractional OXPHOS in the presence and absence of 17AAG. (D-F) OXPHOS kinetics protocols in the presence of no drug, 17AAG, or CAT for Saline (D), DEN-NT (E), and DEN-T (F). (G) Comparison of relative TRAP1 abundance. (H) Plotted TMRM standard curves for Saline, DEN-NT, and DEN-T. (I) Representative fluorometric trace of TMRM membrane potential assay. (J) Relative abundance of OXPHOS complex protein subunits, presented as % maximal summed abundance per complex.

Data are presented as mean  $\pm$  SEM and analyzed by two-way ANOVA (B-F, J) and one-way ANOVA (A). \* $p < 0.05$ , \*\* $p < 0.01$ , \*\*\* $p < 0.001$ , \*\*\*\* $p < 0.0001$ .

## References:

- Acin-Perez R, Benador IY, Petcherski A, Veliova M, Benavides GA, Lagarrigue S, Caudal A, Vergnes L, Murphy AN, Karamanlidis G, Tian R, Reue K, Wanagat J, Sacks H, Amati F, Darley-Usmar VM, Liesa M, Divakaruni AS, Stiles L, Shirihai OS. 2020. A novel approach to measure mitochondrial respiration in frozen biological samples. *The EMBO Journal* **39**:e104073. doi:<https://doi.org/10.15252/emj.2019104073>
- Aleksic K, Lackner C, Geigl JB, Schwarz M, Auer M, Ulz P, Fischer M, Trajanoski Z, Otte M, Speicher MR. 2011. Evolution of genomic instability in diethylnitrosamine-induced hepatocarcinogenesis in mice. *Hepatology* **53**:895–904. doi:10.1002/hep.24133
- Boitier E, Merad-Boudia M, Guguen-Guillouzo C, Defer N, Ceballos-Picot I, Leroux JP, Marsac C. 1995. Impairment of the Mitochondrial Respiratory Chain Activity in Diethylnitrosamine-induced Rat Hepatomas: Possible Involvement of Oxygen Free Radicals. *Cancer Research* **55**:3028–3035.
- Camara Y, Mampel T, Armengol J, Villarroya F, Dejean L. 2009. UCP3 Expression in Liver Modulates Gene Expression and Oxidative Metabolism in Response to Fatty Acids, and Sensitizes Mitochondria to Permeability Transition. *Cellular Physiology and Biochemistry* **24**:243–252. doi:10.1159/000233249
- Cassim S, Raymond VA, Lacoste B, Lapierre P, Bilodeau M. 2018. Metabolite profiling identifies a signature of tumorigenicity in hepatocellular carcinoma. *Oncotarget* **9**:26868–26883. doi:10.18632/oncotarget.25525

- Chavez E, Lozano-Rosas MG, Dominguez-Lopez M, Velasco-Loyden G, Rodriguez-Aguilera JR, Jose-Nunez C, Tuena de Gomez-Puyou M, Chagoya de Sanchez V. 2017. Functional, metabolic, and dynamic mitochondrial changes in the rat cirrhosis-hepatocellular carcinoma model and the protective effect of IFC-305. *Journal of Pharmacology and Experimental Therapeutics* **jpet.116.239301**. doi:10.1124/jpet.116.239301
- Chen L, Fink T, Ebbesen P, Zachar V. 2006. Temporal transcriptome of mouse ATDC5 chondroprogenitors differentiating under hypoxic conditions. *Experimental Cell Research* **312**:1727–1744. doi:https://doi.org/10.1016/j.yexcr.2006.02.013
- Chen Z, Li S, Shen M, Lu X, Bao C, Chen D, Ding J, Wang Q, Huang S, Cong W, Han L, He X. 2020. The Mutational and Transcriptional Landscapes of Hepatocarcinogenesis in a Rat Model. *iScience* **23**:101690. doi:10.1016/j.isci.2020.101690
- Corral M, Kitzis A, Baffet G, Paris B, Tichonicky L, Kruh J, Guguen-Guillouzo C, Defer N. 1989a. RNAs containing mitochondrial ND6 and COI sequences present an abnormal structure in chemically induced rat hepatomas. *Nucleic acids research* **17**:5191–5206. doi:10.1093/nar/17.13.5191
- Corral M, Paris B, Baffet G, Tichonicky L, Guguen-Guillouzo C, Kruh J, Defer N. 1989b. Increased level of the mitochondrial ND5 transcript in chemically induced rat hepatomas. *Experimental cell research* **184**:158–166. doi:10.1016/0014-4827(89)90374-1
- Falkenberg M, Larsson N-G, Gustafsson CM. 2007. DNA Replication and Transcription in Mammalian Mitochondria. *Annual Review of Biochemistry* **76**:679–699. doi:10.1146/annurev.biochem.76.060305.152028

- Fisher-Wellman K, Davidson M, Narowski T, Lin C-T, Koves TR, Muoio DM. 2018. Mitochondrial diagnostics: A multiplexed assay platform for comprehensive assessment of mitochondrial energy fluxes. *Cell Reports* **24**:3593–3606.
- Fisher-Wellman KH, Draper JA, Davidson MT, Williams AS, Narowski TM, Slentz DH, Ilkayeva OR, Stevens RD, Wagner GR, Najjar R, Hirschey MD, Thompson JW, Olson DP, Kelly DP, Koves TR, Grimsrud PA, Muoio DM. 2019. Respiratory Phenomics across Multiple Models of Protein Hyperacetylation in Cardiac Mitochondria Reveals a Marginal Impact on Bioenergetics. *Cell Reports* **26**:1557-1572.e8. doi:10.1016/j.celrep.2019.01.057
- Forner A, Llovet JM, Bruix J. 2012. Hepatocellular carcinoma. *The Lancet* **379**:1245–1255. doi:10.1016/S0140-6736(11)61347-0
- Fujisawa K, Terai S, Takami T, Yamamoto N, Yamasaki T, Matsumoto T, Yamaguchi K, Owada Y, Nishina H, Noma T, Sakaida I. 2016. Modulation of anti-cancer drug sensitivity through the regulation of mitochondrial activity by adenylate kinase 4. *Journal of Experimental and Clinical Cancer Research* **35**:1–15. doi:10.1186/s13046-016-0322-2
- García-Chávez JN, Vásquez-Garzón VR, López MG, Villa-Treviño S, Montiel R. 2021. Integration of chronological omics data reveals mitochondrial regulatory mechanisms during the development of hepatocellular carcinoma. *Plos One* **16**:e0256016. doi:10.1371/journal.pone.0256016
- Glancy B, Barstow T, Willis WT. 2008. Linear relation between time constant of oxygen uptake kinetics, total creatine, and mitochondrial content in vitro. *AJP: Cell Physiology* **294**:C79–C87. doi:10.1152/ajpcell.00138.2007

- Glancy B, Willis WT, Chess DJ, Balaban RS. 2013. Effect of calcium on the oxidative phosphorylation cascade in skeletal muscle mitochondria. *Biochemistry* **52**:2793–2809. doi:10.1021/bi3015983
- Hsu CC, Lee HC, Wei YH. 2013. Mitochondrial DNA alterations and mitochondrial dysfunction in the progression of hepatocellular carcinoma. *World Journal of Gastroenterology* **19**:8880–8886. doi:10.3748/wjg.v19.i47.8880
- Jan Y-H, Lai T-C, Yang C-J, Lin Y-F, Huang M-S, Hsiao M. 2019. Adenylate kinase 4 modulates oxidative stress and stabilizes HIF-1 $\alpha$  to drive lung adenocarcinoma metastasis. *Journal of Hematology & Oncology* **12**:12. doi:10.1186/s13045-019-0698-5
- Jan Y-H, Tsai H-Y, Yang C-J, Huang M-S, Yang Y-F, Lai T-C, Lee C-H, Jeng Y-M, Huang C-Y, Su J-L, Chuang Y-J, Hsiao M. 2012. Adenylate Kinase-4 Is a Marker of Poor Clinical Outcomes That Promotes Metastasis of Lung Cancer by Downregulating the Transcription Factor ATF3. *Cancer Research* **72**:5119 LP – 5129. doi:10.1158/0008-5472.CAN-12-1842
- Kong F, Binas B, Moon JH, Kang SS, Kim HJ. 2013. Differential expression of adenylate kinase 4 in the context of disparate stress response strategies of HEK293 and HepG2 cells. *Archives of Biochemistry and Biophysics* **533**:11–17. doi:https://doi.org/10.1016/j.abb.2013.02.014
- Lee HC, Chang CM, Chi CW. 2010. Somatic mutations of mitochondrial DNA in aging and cancer progression. *Ageing Research Reviews* **9**:S47–S58. doi:10.1016/j.arr.2010.08.009
- Lee HC, Li SH, Lin JC, Wu CC, Yeh DC, Wei YH. 2004. Somatic mutations in the D-loop and decrease in the copy number of mitochondrial DNA in human hepatocellular carcinoma. *Mutation Research* **547**:71–78. doi:10.1016/j.mrfmmm.2003.12.011

- Lee HY, Nga HT, Tian J, Yi HS. 2021. Mitochondrial metabolic signatures in hepatocellular carcinoma. *Cells* **10**:1–15. doi:10.3390/cells10081901
- Lee NCW, Carella MA, Papa S, Bubici C. 2018. High Expression of Glycolytic Genes in Cirrhosis Correlates With the Risk of Developing Liver Cancer. *Frontiers in cell and developmental biology* **6**:138. doi:10.3389/fcell.2018.00138
- Lee Y-K, Jee BA, Kwon SM, Yoon Y-S, Xu WG, Wang H-J, Wang XW, Thorgeirsson SS, Lee J, Woo HG, Yoon G. 2015. Identification of a mitochondrial defect gene signature reveals NUPR1 as a key regulator of liver cancer progression. *Hepatology* **62**:1174–1189. doi:10.1002/hep.27976
- Lee Y-K, Lim JJ, Jeoun U-W, Min S, Lee E-B, Kwon SM, Lee C, Yoon G. 2017. Lactate-mediated mitoribosomal defects impair mitochondrial oxidative phosphorylation and promote hepatoma cell invasiveness. *The Journal of biological chemistry* **292**:20208–20217. doi:10.1074/jbc.M117.809012
- McLaughlin KL, Hagen JT, Coalson HS, Nelson MAM, Kew KA, Wooten AR, Fisher-Wellman KH. 2020. Novel approach to quantify mitochondrial content and intrinsic bioenergetic efficiency across organs. *Scientific Reports* **10**:1–15. doi:10.1038/s41598-020-74718-1
- Nelson MAM, McLaughlin KL, Hagen JT, Coalson HS, Schmidt C, Kassai M, Kew KA, McClung JM, Neuffer PD, Brophy P, Vohra NA, Liles D, Cabot MC, Fisher-Wellman KH. 2021. Intrinsic oxphos limitations underlie cellular bioenergetics in leukemia. *eLife* **10**:1–31. doi:10.7554/eLife.63104
- Nicholls DG. 2005. Mitochondria and calcium signaling. *Cell Calcium* **38**:311–317. doi:https://doi.org/10.1016/j.ceca.2005.06.011

Rath S, Sharma R, Gupta R, Ast T, Chan C, Durham TJ, Goodman RP, Grabarek Z, Haas ME, Hung WHW, Joshi PR, Jourdain AA, Kim SH, Kotrys A v, Lam SS, McCoy JG, Meisel JD, Miranda M, Panda A, Patgiri A, Rogers R, Sadre S, Shah H, Skinner OS, To T-L, Walker MA, Wang H, Ward PS, Wengrod J, Yuan C-C, Calvo SE, Mootha VK. 2021. MitoCarta3.0: an updated mitochondrial proteome now with sub-organelle localization and pathway annotations. *Nucleic Acids Research* **49**:D1541–D1547. doi:10.1093/nar/gkaa1011

Santos NP, Pereira IVOC, Pires MJ, Lopes C, Andrade R, Oliveira MM, Colaço A, Peixoto F, Oliveira PA. 2012. Histology, Bioenergetics and Oxidative Stress in Mouse Liver Exposed to N-Diethylnitrosamine. *In Vivo* **26**:921 LP – 929.

Schmidt CA, McLaughlin KL, Boykov IN, Mojalagbe R, Ranganathan A, Buddo KA, Lin C-T, Fisher-Wellman KH, Neuffer PD. 2021. Aglycemic growth enhances carbohydrate metabolism and induces sensitivity to menadione in cultured tumor-derived cells. *Cancer & Metabolism* **9**:1–21. doi:10.1186/s40170-021-00241-0

Siegel RL, Miller KD, Fuchs HE, Jemal A. 2021. Cancer Statistics, 2021. *CA: A Cancer Journal for Clinicians* **71**:7–33. doi:10.3322/caac.21654

Sloan RC, Moukdar F, Frasier CR, Patel HD, Bostian PA, Lust RM, Brown DA. 2012. Mitochondrial permeability transition in the diabetic heart: Contributions of thiol redox state and mitochondrial calcium to augmented reperfusion injury. *Journal of Molecular and Cellular Cardiology* **52**:1009–1018. doi:10.1016/j.yjmcc.2012.02.009

Suresh V, Anbazhagan C, Thangam R, Senthilkumar D, Senthilkumar N, Kannan S, Rengasamy R, Palani P. 2013. Stabilization of mitochondrial and microsomal function of fucoidan from *Sargassum plagiophyllum* in diethylnitrosamine induced hepatocarcinogenesis. *Carbohydrate Polymers* **92**:1377–1385. doi:https://doi.org/10.1016/j.carbpol.2012.10.038

- Tolba R, Kraus T, Liedtke C, Schwarz M, Weiskirchen R. 2015. Diethylnitrosamine (DEN)-induced carcinogenic liver injury in mice. *Laboratory Animals* **49**:59–69.  
doi:10.1177/0023677215570086
- vander Heiden MG, Cantley LC, Thompson CB. 2009. Understanding the Warburg Effect: The Metabolic Requirements of Cell Proliferation. *Science* **324**:1029–1033.  
doi:10.1126/science.1160809
- Villanueva A. 2019. Hepatocellular Carcinoma. *New England Journal of Medicine* **380**:1450–1462. doi:10.1056/NEJMra1713263
- Wujak M, Wilke T, Weiss A, Brosien M, Wu C-Y, Schermuly RT, Ghofrani HA, Seeger W, Grimminger F, Pak O, Weissmann N. 2019. Role of adenylate kinase 4 as a new metabolic regulator of pulmonary artery smooth muscle cells under hypoxia. *European Respiratory Journal* **54**:PA5044. doi:10.1183/13993003.congress-2019.PA5044
- Wurmbach E, Chen YB, Khitrov G, Zhang W, Roayaie S, Schwartz M, Fiel I, Thung S, Mazzaferro V, Bruix J, Bottinger E, Friedman S, Waxman S, Llovet JM. 2007. Genome-wide molecular profiles of HCV-induced dysplasia and hepatocellular carcinoma. *Hepatology* **45**:938–947. doi:10.1002/hep.21622
- Xin F, Yao D-W, Fan L, Liu J-H, Liu X-D. 2019. Adenylate kinase 4 promotes bladder cancer cell proliferation and invasion. *Clinical and Experimental Medicine* **19**:525–534.  
doi:10.1007/s10238-019-00576-5
- Yamada S, Nomoto S, Fujii T, Kaneko T, Takeda S, Inoue S, Kanazumi N, Nakao A. 2006. Correlation between copy number of mitochondrial DNA and clinico-pathologic parameters of hepatocellular carcinoma. *European Journal of Surgical Oncology* **32**:303–307.  
doi:10.1016/j.ejso.2006.01.002

Yin PH, Lee HC, Chau GY, Wu YT, Li SH, Lui WY, Wei YH, Liu TY, Chi CW. 2004.

Alteration of the copy number and deletion of mitochondrial DNA in human hepatocellular carcinoma. *British Journal of Cancer* **90**:2390–2396. doi:10.1038/sj.bjc.6601838

Yin PH, Wu CC, Lin JC, Chi CW, Wei YH, Lee HC. 2010. Somatic mutations of mitochondrial genome in hepatocellular carcinoma. *Mitochondrion* **10**:174–182.

doi:10.1016/j.mito.2009.12.147

Zhang J, Yin YT, Wu CH, Qiu RL, Jiang WJ, Deng XG, Li ZX. 2019. AK4 Promotes the Progression of HER2-Positive Breast Cancer by Facilitating Cell Proliferation and Invasion.

*Disease Markers* **2019**. doi:10.1155/2019/8186091

## **CHAPTER 5: DISCUSSION**

### **Mitochondrial Enrichment Factor**

Appropriate data normalization is central to the ability of researchers to interpret differences within their data. Particularly for comparing the intrinsic properties of mitochondria across tissues and malignancies, an unbiased assessment of mitochondrial content that could be broadly applied was necessary. As the data were able to demonstrate, there is no single protein that can predict mitochondrial content across tissues. The availability of the MitoCarta database (Calvo et al., 2016; Rath et al., 2021) as a resource for identifying proteins with known mitochondrial localization provided an excellent opportunity to quantify mitochondrial purity using mitochondrial-targeted proteomics. The mitochondrial enrichment factor proved to be useful for normalizing mitochondrial function data obtained from diethylnitrosamine (DEN)-induced liver tumors, as there was great variability in mitochondrial content between tumor and nontumor tissues that might otherwise have altered the outcome of the findings.

### **Mitochondrial Phenotype of Acute Myeloid Leukemia**

The primary purpose of this work was to determine whether there exists a common mitochondrial phenotype of cancer. This question was addressed by comparing multiple models within the same cancer type as well as across two types of cancer. Acute myeloid leukemia and hepatocellular carcinoma were chosen because they both represent exceptionally heterogeneous patient populations, have poor prognoses (5-year survival of 20-25%), and limited curative treatment options (Döhner et al., 2015; Villanueva, 2019).

Within models of AML, it was found that mitochondrial phenotype was highly consistent. For instance, despite differences in oncogenic driver mutations, differentiation state, and basal respiration rate, all 3 leukemia cell lines tested (HL-60, KG-1, MV-4-11) showed consistent limitations to  $\Delta G_{ATP}$ -stimulated respiratory flux that was not present in terminally differentiated peripheral blood cells or quiescent CD34<sup>+</sup> hematopoietic progenitors. This limitation was revealed to be due to inhibition of respiration by increasing  $\Delta G_{ATP}$ , which mimicked the effect of a low demand for ATP resynthesis. Written another way, the in vitro conditions created an elevation of the concentration of ATP relative to ADP, and this ATP was found to be transported into the mitochondrial matrix to effect respiratory inhibition. This effect was found to be present regardless of the carbon substrate that was used to fuel respiration, suggesting that there is not an independent limitation to respiratory complexes I or II.

Supporting a possible therapeutic application for this finding, when leukemic cells were forced to use OXPHOS for energy transduction through treatments with inhibitors that disrupted mitochondrial ATP import, proliferation was reduced, and cells became more sensitive to chemotherapy. Even more compelling, this phenotype was replicated in fresh primary human leukemia samples, demonstrating that these mitochondrial adaptations were not induced by the cell culture process but were present in the true presentation of the disease. Interestingly, a similar phenotype was also seen in CD34<sup>+</sup> hematopoietic progenitors that were stimulated with growth factors, suggesting that this mitochondrial rewiring may also be a feature of white blood cell clonal expansion. Research into healthy versus malignant proliferation will be needed to determine whether there are any targetable differences between these two processes.

Supportive of previous work by others (Farge et al., 2017), venetoclax-resistant HL-60 cells were shown to have elevated basal and FCCP-stimulated respiration rates compared to normal

HL-60 cells when intact cell respiration was measured. However, when respiration was stimulated with physiological  $\Delta G_{ATP}$ , it was revealed that the  $\Delta G_{ATP}$ -stimulated impairment to respiration was actually more pronounced in the venetoclax-resistant cells and was associated with a lower rate of ATP production ( $J_{ATP}$ ) across the entire physiological span of  $\Delta G_{ATP}$ . This finding suggests that intact cell measurement of respiration may be overestimating the contribution of mitochondrial respiration to the cellular energy charge, as well as erroneously classifying these cells as “OXPHOS-reliant”.

### **Mitochondrial Phenotype of Hepatocellular Carcinoma**

Comparison of mouse HCC-derived Hepa 1-6 cell mitochondria to those obtained from diethylnitrosamine (DEN)-induced tumors in mice yielded a consistent mitochondrial phenotype of repressed Complex I (CI) respiration with normal ATP production rates. Although not evaluated in Hepa 1-6 cells, adenylate kinase activity, likely adenylate kinase 4 (AK4) specifically, was found to mediate this effect under most CI-linked substrate conditions in DEN-induced tumor mitochondria. Despite this respiration-specific limitation to CI in HCC tumors, it was shown that respiratory flux that was supported by a multi-complex-stimulating mixture of carbon substrates was similar or greater in both HCC models compared to their respective nontumor controls. This finding contradicts the work of others who have reported overall impairments to mitochondrial respiration and ATP production in DEN-induced HCC models (Boitier et al., 1995; Chavez et al., 2017). However, this discrepancy is likely due to the fact that the majority of respiration experiments performed in DEN-induced tumor mitochondria to date were fueled using primarily CI substrates such as glutamate/malate or  $\alpha$ -ketoglutarate (Boitier et al., 1995; Chavez et al., 2017).

Interestingly, although high  $\Delta G_{ATP}$  was found to inhibit respiration in DEN-induced tumors, as assessed by FCCP titration under low ATP resynthesis demand states, this effect was not present in the Hepa 1-6 cells. This may be related to the etiology of HCC in each model, as Hepa 1-6 cells are derived from a spontaneous mouse tumor rather than carcinogen exposure (Lacoste et al., 2017). It is not clear whether this phenotype would be seen in other types of hepatocellular carcinoma of different origins, or if this is an adaptation specific to cultured HCC cells rather than fresh HCC tumors. This is an important distinction as cultured cells are frequently used to model HCC in screens of potential new treatments, and successful translation of these results depends upon the ability of cells to replicate the phenotype of human disease (Heindryckx et al., 2009).

There were also two interesting characteristics of DEN-induced tumors that were not evaluated in Hepa 1-6 cells. For instance, DEN-induced tumors were found to have both reduced membrane potential ( $\Delta\Psi$ ) across the  $\Delta G_{ATP}$  span and reduced capacities for calcium retention. Decreased membrane potential has been reported in other models of DEN-induced (Boitier et al., 1995) and cell culture models of HCC (Schmidt et al., 2021b). Low mitochondrial respiratory chain activity, and thus possibly lower  $\Delta\Psi$ , has also been linked to higher intracellular calcium concentrations in HCC-derived cells (Lee et al., 2015). The same study demonstrated that elevated cytosolic calcium was associated with upregulated expression of NUPR1, a promoter of cancer progression, supporting the possible relevance of both decreased membrane potential and decreased mitochondrial calcium uptake to HCC malignancy.

### **Consistencies in Cancer Mitochondrial Phenotype**

Between AML and HCC mitochondria, there was a consistent signature of inhibition of respiration by  $\Delta G_{ATP}$ , at least in DEN-induced tumors. Interestingly, the underlying mechanism of this inhibition appeared to differ between AML and HCC. Whereas ATP entry into the mitochondrial matrix was necessary for  $\Delta G_{ATP}$ -induced respiratory inhibition in AML, inhibition appeared to occur outside of the matrix in HCC, possibly in the intermembrane space. Respiratory inhibition was also found to be rescued with the HSP90 inhibitor 17AAG in AML, though 17AAG had no effect on respiration in HCC tumor mitochondria. Together, these data support our initial hypothesis that reprogramming of metabolism in cancer mitochondria may arise from unique protein expression profiles and regulatory mechanisms, but ultimately lead to the same functional mitochondrial phenotype. Importantly, this phenotype may not in fact be specific to cancer but may be a general feature of proliferation, as illustrated by the data in CD34<sup>+</sup> progenitor cells stimulated with growth factors. The detection of this phenotype was entirely dependent upon the use of mitochondrial interrogation methods that simulate *in vivo* energy states, supporting the tremendous importance of the integration of bioenergetics with physiology.

### **Future Directions**

To expand upon the findings described herein and better understand the implications for cancer biology and treatment, two main issues will need to be addressed: 1) the impact of CI-linked respiratory deficiency on tumor growth needs to be evaluated in additional models of HCC, and 2) the mitochondrial phenotypes of healthy proliferation versus tumorigenic proliferation need more comprehensive definition.

Several models may be utilized to address the relationship between deficient CI expression/activity and tumorigenesis in HCC. First, CI may be manipulated in nontumorigenic

cultured hepatocytes—such as AML12 cells or primary liver cells—to determine whether this induces tumor-like proliferation or colony formation. CI manipulation could be in the form of exposure to inhibitors such as rotenone, which would allow titration of inhibition from partial to complete loss of activity. Alternatively, expression of integral CI subunits could be reduced in these cells using siRNA. Decreased expression of CI-linked subunits GRIM-19 and NDUFS3 has been shown to be an effective means of reducing CI function in HeLa cells, with implications for metastatic capability (He et al., 2013). Additionally, the impact of altered CI expression on susceptibility to tumor growth can be investigated using the NDUFS4 knockout mouse (Ingraham et al., 2009). These mice are heterozygous for a point mutation in the gene of CI subunit NDUFS4 that creates a truncated, dysfunctional protein, leading to a deficiency in CI activity without changes to downstream respiratory complexes or severe systemic complications (Ingraham et al., 2009). Importantly, these mice were generated on a C57BL/6 background, a strain that has been shown to be resistant to DEN-induced tumor formation (Diwan et al., 1986; Tolba et al., 2015). Using this mouse model would thus simultaneously allow for evaluation of mitochondrial phenotype in DEN-resistant mice, evaluation of the role of CI deficiency in tumorigenesis, and would provide validation of the DEN-induced tumor findings reported here in a separate mouse strain.

The utility of mitochondrial phenotyping for identifying potential new therapeutic targets in cancer is dependent upon the specificity of this mitochondrial phenotype. Healthy proliferation is an important feature of both hematopoietic stem cells and hepatocytes that becomes dysregulated during tumorigenesis in AML and HCC (Döhner et al., 2015; Forner et al., 2018). Previous work comparing tumors from several tissues of origin has demonstrated that the transcriptomic features of these tumors are more closely related to their native tissue than other types of cancer (Hoadley

et al., 2018). Thus, an important control for any assessment of tumor metabolic properties is healthy progenitors from the same tissue lineage. In AML, the inclusion of a model of healthy proliferation revealed similar sensitivities to  $\Delta G_{ATP}$  as leukemic models. However, other distinctive features of leukemia, including a tendency to import ATP into the mitochondrial matrix, have yet to be explored in proliferating CD34<sup>+</sup> cells. Repeating the full panel of experiments, including proteomics, in CD34<sup>+</sup> cells in the presence and absence of growth factors would help address this gap in the knowledge.

There was no inclusion of a model for healthy liver proliferation in this study, limiting the conclusions that can be drawn about the specificity of our findings to HCC. Ideally, mitochondrial phenotyping experiments would be repeated in models of liver proliferation during liver development and liver repair. One possible model would be mouse weanlings, as mouse liver remains in a proliferative state until ~14 days of age (Bakiri and Wagner, 2013). Alternatively, liver regeneration and proliferation can be stimulated through partial hepatectomy or pharmacological stimulation with phenobarbital (Hall et al., 2021). Interestingly, both of these methods have previously been shown to be associated with similar lipid accumulation profiles to mouse models of HCC including DEN treatment (Hall et al., 2021). This may suggest a common metabolic phenotype for healthy and malignant proliferation in the liver, which would be exciting to investigate using the comprehensive approach that has been described in this work.

### **Public Health Significance**

Cancer represents an immense public health burden for which treatment options remain limited. The most common treatment, chemotherapy, is associated with appreciable secondary toxicity due to its inability to discriminate between cancerous and healthy proliferating cells. The

design of more cancer-specific therapies depends upon improved understanding of the mechanisms that support cancer growth and progression. The work of this dissertation provides a framework for evaluating intrinsic differences in the mitochondrial networks of cancerous and noncancerous tissues, applied to two separate cancer models, that may help identify metabolic vulnerabilities that are unique to cancer.

## REFERENCES

- Ahn CS, Metallo CM. 2015. Mitochondria as biosynthetic factories for cancer proliferation. *Cancer & Metabolism* **3**:1–10. doi:10.1186/s40170-015-0128-2
- Arber DA, Orazi A, Hasserjian R, Thiele J, Borowitz MJ, le Beau MM, Bloomfield CD, Cazzola M, Vardiman JW. 2016. The 2016 revision to the World Health Organization classification of myeloid neoplasms and acute leukemia. *Blood* **127**:2391–2405. doi:https://doi.org/10.1182/blood-2016-03-643544
- Bakiri L, Wagner EF. 2013. Mouse models for liver cancer. *Molecular Oncology* **7**:206–223. doi:https://doi.org/10.1016/j.molonc.2013.01.005
- Balogh J, Victor III D, Gordon S, Li X, Ghobrial RM, Jr HPM. 2016. Hepatocellular Carcinoma: a review. *Journal of Hepatocellular Carcinoma* **Volume 3**:41–53.
- Bayley J-P, Devilee P. 2010. Warburg tumours and the mechanisms of mitochondrial tumour suppressor genes. Barking up the right tree? *Current Opinion in Genetics & Development* **20**:324–329. doi:https://doi.org/10.1016/j.gde.2010.02.008
- Boitier E, Merad-Boudia M, Guguen-Guillouzo C, Defer N, Ceballos-Picot I, Leroux JP, Marsac C. 1995. Impairment of the Mitochondrial Respiratory Chain Activity in Diethylnitrosamine-induced Rat Hepatomas: Possible Involvement of Oxygen Free Radicals. *Cancer Research* **55**:3028–3035.
- Brand MD, Nicholls DG. 2011. Assessing mitochondrial dysfunction in cells. *Biochemical Journal* **435**:297–312. doi:10.1042/BJ20110162
- Calderwood SK, Bump EA, Stevenson MA, van Kersen I, Hahn GM. 1985. Investigation of adenylate energy charge, phosphorylation potential, and ATP concentration in cells stressed

- with starvation and heat. *Journal of cellular physiology* **124**:261–268.  
doi:10.1002/jcp.1041240214
- Calvo SE, Clauser KR, Mootha VK. 2016. MitoCarta2.0: An updated inventory of mammalian mitochondrial proteins. *Nucleic Acids Research* **44**:D1251–D1257. doi:10.1093/nar/gkv1003
- Carew JS, Huang P. 2002. Mitochondrial defects in cancer. *Molecular Cancer* **1**:1–12.
- Chavez E, Lozano-Rosas MG, Dominguez-Lopez M, Velasco-Loyden G, Rodriguez-Aguilera JR, Jose-Nunez C, Tuena de Gomez-Puyou M, Chagoya de Sanchez V. 2017. Functional, metabolic, and dynamic mitochondrial changes in the rat cirrhosis-hepatocellular carcinoma model and the protective effect of IFC-305. *Journal of Pharmacology and Experimental Therapeutics* jpet.116.239301. doi:10.1124/jpet.116.239301
- Cortes JE, Kantarjian H, Foran JM, Ghirdaladze D, Zodelava M, Borthakur G, Gammon G, Trone D, Armstrong RC, James J, Levis M. 2013. Phase I study of quizartinib administered daily to patients with relapsed or refractory acute myeloid leukemia irrespective of FMS-like tyrosine kinase 3-internal tandem duplication status. *Journal of clinical oncology : official journal of the American Society of Clinical Oncology* **31**:3681–3687. doi:10.1200/JCO.2013.48.8783
- Dai Z, Shestov AA, Lai L, Locasale JW. 2016. A Flux Balance of Glucose Metabolism Clarifies the Requirements of the Warburg Effect. *Biophysical Journal* **111**:1088–1100.  
doi:https://doi.org/10.1016/j.bpj.2016.07.028
- Diebold LP, Gil HJ, Gao P, Martinez CA, Weinberg SE, Chandel NS. 2019. Mitochondrial complex III is necessary for endothelial cell proliferation during angiogenesis. *Nature metabolism* **1**:158–171. doi:10.1038/s42255-018-0011-x
- DiNardo CD, Pratz K, Pullarkat V, Jonas BA, Arellano M, Becker PS, Frankfurt O, Konopleva M, Wei AH, Kantarjian HM, Xu T, Hong W-J, Chyla B, Potluri J, Pollyea DA, Letai A. 2019.

- Venetoclax combined with decitabine or azacitidine in treatment-naive, elderly patients with acute myeloid leukemia. *Blood* **133**:7–17. doi:<https://doi.org/10.1182/blood-2018-08-868752>
- Ding L, Ley TJ, Larson DE, Miller CA, Koboldt DC, Welch JS, Ritchey JK, Young MA, Lamprecht T, McLellan MD, McMichael JF, Wallis JW, Lu C, Shen D, Harris CC, Dooling DJ, Fulton RS, Fulton LL, Chen K, Schmidt H, Kalicki-Veizer J, Magrini VJ, Cook L, McGrath SD, Vickery TL, Wendl MC, Heath S, Watson MA, Link DC, Tomasson MH, Shannon WD, Payton JE, Kulkarni S, Westervelt P, Walter MJ, Graubert TA, Mardis ER, Wilson RK, DiPersio JF. 2012. Clonal evolution in relapsed acute myeloid leukaemia revealed by whole-genome sequencing. *Nature* **481**:506–510. doi:10.1038/nature10738
- Diwan BA, Rice JM, Ohshima M, Ward JM. 1986. Interstrain differences in susceptibility to liver carcinogenesis initiated by N-nitrosodiethylamine and its promotion by phenobarbital in C57BL/6NCr, C3H/HeNCrMTV- and DBA/2NCr mice. *Carcinogenesis* **7**:215–220. doi:10.1093/carcin/7.2.215
- Döhner H, Estey E, Grimwade D, Amadori S, Appelbaum FR, Büchner T, Dombret H, Ebert BL, Fenaux P, Larson RA, Levine RL, Lo-Coco F, Naoe T, Niederwieser D, Ossenkoppele GJ, Sanz M, Sierra J, Tallman MS, Tien H-F, Wei AH, Löwenberg B, Bloomfield CD. 2017. Diagnosis and management of AML in adults: 2017 ELN recommendations from an international expert panel. *Blood* **129**:424–447. doi:10.1182/blood-2016-08-733196
- Döhner H, Estey EH, Amadori S, Appelbaum FR, Büchner T, Burnett AK, Dombret H, Fenaux P, Grimwade D, Larson RA, Lo-Coco F, Naoe T, Niederwieser D, Ossenkoppele GJ, Sanz MA, Sierra J, Tallman MS, Löwenberg B, Bloomfield CD. 2010. Diagnosis and management of acute myeloid leukemia in adults: recommendations from an international expert panel, on

- behalf of the European LeukemiaNet. *Blood* **115**:453–474. doi:10.1182/blood-2009-07-235358
- Döhner H, Weisdorf DJ, Bloomfield CD. 2015. Acute Myeloid Leukemia. *New England Journal of Medicine* **373**:1136–1152. doi:10.1056/NEJMra1406184
- Dyson J, Jaques B, Chattopadhyay D, Lochan R, Graham J, Das D, Aslam T, Patanwala I, Gaggari S, Cole M, Sumpter K, Stewart S, Rose J, Hudson M, Manas D, Reeves HL. 2014. Hepatocellular cancer: the impact of obesity, type 2 diabetes and a multidisciplinary team. *Journal of hepatology* **60**:110–117. doi:10.1016/j.jhep.2013.08.011
- Estey E, Döhner H. 2006. Acute myeloid leukaemia. *The Lancet* **368**:1894–1907. doi:https://doi.org/10.1016/S0140-6736(06)69780-8
- European Association for the Study of the Liver. 2018. EASL Clinical Practice Guidelines: Management of hepatocellular carcinoma. *Journal of Hepatology* **69**:182–236. doi:https://doi.org/10.1016/j.jhep.2018.03.019
- Falkenberg M, Larsson N-G, Gustafsson CM. 2007. DNA Replication and Transcription in Mammalian Mitochondria. *Annual Review of Biochemistry* **76**:679–699. doi:10.1146/annurev.biochem.76.060305.152028
- Farge T, Saland E, de Toni F, Aroua N, Hosseini M, Perry R, Bosc C, Sugita M, Stuani L, Fraise M, Scotland S, Larrue C, Boutzen H, Féliu V, Nicolau-Travers ML, Cassant-Sourdy S, Broin N, David M, Serhan N, Sarry A, Tavitian S, Kaoma T, Vallar L, Iacovoni J, Linares LK, Montersino C, Castellano R, Griessinger E, Collette Y, Duchamp O, Barreira Y, Hirsch P, Palama T, Gales L, Delhommeau F, Garmy-Susini BH, Portais JC, Vergez F, Selak M, Danet-Desnoyers G, Carroll M, Récher C, Sarry JE. 2017. Chemotherapy-resistant human acute

- myeloid leukemia cells are not enriched for leukemic stem cells but require oxidative metabolism. *Cancer Discovery* **7**:716–735. doi:10.1158/2159-8290.CD-16-0441
- Faubert B, Solmonson A, DeBerardinis RJ. 2020. Metabolic reprogramming and cancer progression. *Science* **368**:1–5. doi:10.1126/science.aaw5473
- Figueroa ME, Abdel-Wahab O, Lu C, Ward PS, Patel J, Shih A, Li Y, Bhagwat N, Vasanthakumar A, Fernandez HF, Tallman MS, Sun Z, Wolniak K, Peeters JK, Liu W, Choe SE, Fantin VR, Paietta E, Löwenberg B, Licht JD, Godley LA, Delwel R, Valk PJM, Thompson CB, Levine RL, Melnick A. 2010. Leukemic IDH1 and IDH2 Mutations Result in a Hypermethylation Phenotype, Disrupt TET2 Function, and Impair Hematopoietic Differentiation. *Cancer Cell* **18**:553–567. doi:https://doi.org/10.1016/j.ccr.2010.11.015
- Fisher-Wellman K, Davidson M, Narowski T, Lin C-T, Koves TR, Muoio DM. 2018. Mitochondrial diagnostics: A multiplexed assay platform for comprehensive assessment of mitochondrial energy fluxes. *Cell Reports* **24**:3593–3606.
- Forner A, Reig M, Bruix J. 2018. Hepatocellular carcinoma. *The Lancet* **391**:1301–1314. doi:10.1016/S0140-6736(18)30010-2
- Gaidzik V, Döhner K. 2008. Prognostic implications of gene mutations in acute myeloid leukemia with normal cytogenetics. *Seminars in oncology* **35**:346–355. doi:10.1053/j.seminoncol.2008.04.005
- Gammage PA, Frezza C. 2019. Mitochondrial DNA: the overlooked oncogenome? *BMC Biology* **17**:53. doi:10.1186/s12915-019-0668-y
- Gerencser AA, Neilson A, Choi SW, Edman U, Yadava N, Oh RJ, Ferrick DA, Nicholls DG, Brand MD. 2009. Quantitative microplate-based respirometry with correction for oxygen diffusion. *Analytical chemistry* **81**:6868–6878. doi:10.1021/ac900881z

- Glancy B, Willis WT, Chess DJ, Balaban RS. 2013. Effect of calcium on the oxidative phosphorylation cascade in skeletal muscle mitochondria. *Biochemistry* **52**:2793–2809. doi:10.1021/bi3015983
- Gorelick AN, Kim M, Chatila WK, La K, Hakimi AA, Berger MF, Taylor BS, Gammage PA, Reznik E. 2021. Respiratory complex and tissue lineage drive recurrent mutations in tumour mtDNA. *Nature Metabolism* **3**:558–570. doi:10.1038/s42255-021-00378-8
- Guièze R, Liu VM, Rosebrock D, Jourdain AA, Hernández-Sánchez M, Martínez Zurita A, Sun J, ten Hacken E, Baranowski K, Thompson PA, Heo J-M, Cartun Z, Aygün O, Iorgulescu JB, Zhang W, Notarangelo G, Livitz D, Li S, Davids MS, Biran A, Fernandes SM, Brown JR, Lako A, Ciantra ZB, Lawlor MA, Keskin DB, Udeshi ND, Wierda WG, Livak KJ, Letai AG, Neuberg D, Harper JW, Carr SA, Piccioni F, Ott CJ, Leshchiner I, Johannessen CM, Doench J, Mootha VK, Getz G, Wu CJ. 2019a. Mitochondrial Reprogramming Underlies Resistance to BCL-2 Inhibition in Lymphoid Malignancies. *Cancer cell* **36**:369-384.e13. doi:10.1016/j.ccell.2019.08.005
- Guièze R, Liu VM, Rosebrock D, Jourdain AA, Hernández-Sánchez M, Martínez Zurita A, Sun J, ten Hacken E, Baranowski K, Thompson PA, Heo JM, Cartun Z, Aygün O, Iorgulescu JB, Zhang W, Notarangelo G, Livitz D, Li S, Davids MS, Biran A, Fernandes SM, Brown JR, Lako A, Ciantra ZB, Lawlor MA, Keskin DB, Udeshi ND, Wierda WG, Livak KJ, Letai AG, Neuberg D, Harper JW, Carr SA, Piccioni F, Ott CJ, Leshchiner I, Johannessen CM, Doench J, Mootha VK, Getz G, Wu CJ. 2019b. Mitochondrial Reprogramming Underlies Resistance to BCL-2 Inhibition in Lymphoid Malignancies. *Cancer Cell* **36**:369-384.e13. doi:10.1016/j.ccell.2019.08.005

- Hall Z, Chiarugi D, Charidemou E, Leslie J, Scott E, Pellegrinet L, Allison M, Mocciaro G, Anstee QM, Evan GI, Hoare M, Vidal-Puig A, Oakley F, Vacca M, Griffin JL. 2021. Lipid Remodeling in Hepatocyte Proliferation and Hepatocellular Carcinoma. *Hepatology* **73**:1028–1044. doi:10.1002/hep.31391
- Hatzivassiliou G, Zhao F, Bauer DE, Andreadis C, Shaw AN, Dhanak D, Hingorani SR, Tuveson DA, Thompson CB. 2005. ATP citrate lyase inhibition can suppress tumor cell growth. *Cancer cell* **8**:311–321. doi:10.1016/j.ccr.2005.09.008
- He X, Zhou A, Lu H, Chen Y, Huang G, Yue X, Zhao P, Wu Y. 2013. Suppression of Mitochondrial Complex I Influences Cell Metastatic Properties. *PLOS ONE* **8**:e61677.
- Heindryckx F, Colle I, van Vlierberghe H. 2009. Experimental mouse models for hepatocellular carcinoma research. *International Journal of Experimental Pathology* **90**:367–386. doi:10.1111/j.1365-2613.2009.00656.x
- Higuchi M. 2007. Regulation of mitochondrial DNA content and cancer. *Mitochondrion* **7**:53–57. doi:10.1016/j.mito.2006.12.001
- Higuchi M, Kudo T, Suzuki S, Evans TT, Sasaki R, Wada Y, Shirakawa T, Sawyer JR, Gotoh A. 2006. Mitochondrial DNA determines androgen dependence in prostate cancer cell lines. *Oncogene* **25**:1437–1445. doi:10.1038/sj.onc.1209190
- Hinkle PC. 2005. P/O ratios of mitochondrial oxidative phosphorylation. *Biochimica et biophysica acta* **1706**:1–11. doi:10.1016/j.bbabbio.2004.09.004
- Hoadley KA, Yau C, Hinoue T, Wolf DM, Lazar AJ, Drill E, Shen R, Taylor AM, Cherniack AD, Thorsson V, Akbani R, Bowlby R, Wong CK, Wiznerowicz M, Sanchez-Vega F, Robertson AG, Schneider BG, Lawrence MS, Noushmehr H, Malta TM, The Cancer Genome Atlas Network, Stuart JM, Benz CC, Laird PW. 2018. Cell-of-Origin Patterns Dominate the

- Molecular Classification of 10,000 Tumors from 33 Types of Cancer. *Cell* **173**:291-304.e6.  
doi:<https://doi.org/10.1016/j.cell.2018.03.022>
- Ingraham CA, Burwell LS, Skalska J, Brookes PS, Howell RL, Sheu S-S, Pinkert CA. 2009. NDUFS4: creation of a mouse model mimicking a Complex I disorder. *Mitochondrion* **9**:204–210. doi:[10.1016/j.mito.2009.02.001](https://doi.org/10.1016/j.mito.2009.02.001)
- Ishizawa T, Hasegawa K, Aoki T, Takahashi M, Inoue Y, Sano K, Imamura H, Sugawara Y, Kokudo N, Makuuchi M. 2008. Neither Multiple Tumors Nor Portal Hypertension Are Surgical Contraindications for Hepatocellular Carcinoma. *Gastroenterology* **134**:1908–1916. doi:[10.1053/j.gastro.2008.02.091](https://doi.org/10.1053/j.gastro.2008.02.091)
- Khutornenko AA, Roudko V v, Chernyak B v, Vartapetian AB, Chumakov PM, Evstafieva AG. 2010. Pyrimidine biosynthesis links mitochondrial respiration to the p53 pathway. *Proceedings of the National Academy of Sciences* **107**:12828 LP – 12833. doi:[10.1073/pnas.0910885107](https://doi.org/10.1073/pnas.0910885107)
- King A, Selak MA, Gottlieb E. 2006. Succinate dehydrogenase and fumarate hydratase: linking mitochondrial dysfunction and cancer. *Oncogene* **25**:4675–4682. doi:[10.1038/sj.onc.1209594](https://doi.org/10.1038/sj.onc.1209594)
- Kirtonia A, Pandya G, Sethi G, Pandey AK, Das BC, Garg M. 2020. A comprehensive review of genetic alterations and molecular targeted therapies for the implementation of personalized medicine in acute myeloid leukemia. *Journal of Molecular Medicine* **98**:1069–1091. doi:[10.1007/s00109-020-01944-5](https://doi.org/10.1007/s00109-020-01944-5)
- Koppenol WH, Bounds PL, Dang C v. 2011. Otto Warburg's contributions to current concepts of cancer metabolism. *Nature Reviews Cancer* **11**:325–337. doi:[10.1038/nrc3038](https://doi.org/10.1038/nrc3038)

- Lacoste B, Raymond V-A, Cassim S, Lapierre P, Bilodeau M. 2017. Highly tumorigenic hepatocellular carcinoma cell line with cancer stem cell-like properties. *PLoS one* **12**:e0171215. doi:10.1371/journal.pone.0171215
- Lark DS, Torres MJ, Lin C-T, Ryan TE, Anderson EJ, Neuffer PD. 2016. Direct real-time quantification of mitochondrial oxidative phosphorylation efficiency in permeabilized skeletal muscle myofibers. *American Journal of Physiology - Cell Physiology* **311**:C239–C245. doi:10.1152/ajpcell.00124.2016
- Lee HC, Li SH, Lin JC, Wu CC, Yeh DC, Wei YH. 2004. Somatic mutations in the D-loop and decrease in the copy number of mitochondrial DNA in human hepatocellular carcinoma. *Mutation Research* **547**:71–78. doi:10.1016/j.mrfmmm.2003.12.011
- Lee Y-K, Jee BA, Kwon SM, Yoon Y-S, Xu WG, Wang H-J, Wang XW, Thorgeirsson SS, Lee J, Woo HG, Yoon G. 2015. Identification of a mitochondrial defect gene signature reveals NUPR1 as a key regulator of liver cancer progression. *Hepatology* **62**:1174–1189. doi:10.1002/hep.27976
- Llovet JM, Brú C, Bruix J. 1999. Prognosis of Hepatocellular Carcinoma: The BCLC Staging Classification. *Seminars Liver Disease* **19**:329–338.
- Llovet JM, Mas X, Aponte JJ, Fuster J, Navasa M, Christensen E, Rodés J, Bruix J. 2002. Cost effectiveness of adjuvant therapy for hepatocellular carcinoma during the waiting list for liver transplantation. *Gut* **50**:123–128. doi:10.1136/gut.50.1.123
- Llovet JM, Villanueva A, Lachenmayer A, Finn RS. 2015. Advances in targeted therapies for hepatocellular carcinoma in the genomic era. *Nature Reviews Clinical Oncology* **12**:408–424. doi:10.1038/nrclinonc.2015.103

- Luptak I, Sverdlov AL, Panagia M, Qin F, Pimentel DR, Croteau D, Siwik DA, Ingwall JS, Bachschmid MM, Balschi JA, Colucci WS. 2018. Decreased ATP production and myocardial contractile reserve in metabolic heart disease. *Journal of Molecular and Cellular Cardiology* **116**:106–114. doi:10.1016/j.yjmcc.2018.01.017
- Martínez-Reyes I, Cardona LR, Kong H, Vasan K, McElroy GS, Werner M, Kihshen H, Reczek CR, Weinberg SE, Gao P, Steinert EM, Piseaux R, Budinger GRS, Chandel NS. 2020. Mitochondrial ubiquinol oxidation is necessary for tumour growth. *Nature* **585**:288–292. doi:10.1038/s41586-020-2475-6
- Martínez-Reyes I, Diebold LP, Kong H, Schieber M, Huang H, Hensley CT, Mehta MM, Wang T, Santos JH, Woychik R, Dufour E, Spelbrink JN, Weinberg SE, Zhao Y, DeBerardinis RJ, Chandel NS. 2016. TCA Cycle and Mitochondrial Membrane Potential Are Necessary for Diverse Biological Functions. *Molecular cell* **61**:199–209. doi:10.1016/j.molcel.2015.12.002
- Maxwell PH. 2005a. Hypoxia-inducible factor as a physiological regulator. *Experimental Physiology* **90**:791–797. doi:https://doi.org/10.1113/expphysiol.2005.030924
- Maxwell PH. 2005b. The HIF pathway in cancer. *Seminars in Cell & Developmental Biology* **16**:523–530. doi:https://doi.org/10.1016/j.semcdb.2005.03.001
- Mazzaferro V, Regalia E, Doci R, Andreola S, Pulvirenti A, Bozzetti F, Montalto F, Ammatuna M, Morabito A, Gennari L. 1996. Liver transplantation for the treatment of small hepatocellular carcinomas in patients with cirrhosis. *The New England journal of medicine* **334**:693–699. doi:10.1056/NEJM199603143341104

- McLaughlin KL, Hagen JT, Coalson HS, Nelson MAM, Kew KA, Wooten AR, Fisher-Wellman KH. 2020. Novel approach to quantify mitochondrial content and intrinsic bioenergetic efficiency across organs. *Scientific Reports* **10**:1–15. doi:10.1038/s41598-020-74718-1
- Molina JR, Sun Y, Protopopova M, Gera S, Bandi M, Bristow C, McAfoos T, Morlacchi P, Ackroyd J, Agip A-NA, Al-Atrash G, Asara J, Bardenhagen J, Carrillo CC, Carroll C, Chang E, Ciurea S, Cross JB, Czako B, Deem A, Daver N, de Groot JF, Dong J-W, Feng N, Gao G, Gay J, Do MG, Greer J, Giuliani V, Han J, Han L, Henry VK, Hirst J, Huang S, Jiang Y, Kang Z, Khor T, Konoplev S, Lin Y-H, Liu G, Lodi A, Lofton T, Ma H, Mahendra M, Matre P, Mullinax R, Peoples M, Petrocchi A, Rodriguez-Canale J, Serreli R, Shi T, Smith M, Tabe Y, Theroff J, Tiziani S, Xu Q, Zhang Q, Muller F, DePinho RA, Toniatti C, Draetta GF, Heffernan TP, Konopleva M, Jones P, di Francesco ME, Marszalek JR. 2018. An inhibitor of oxidative phosphorylation exploits cancer vulnerability. *Nature Medicine* **24**:1036–1046. doi:10.1038/s41591-018-0052-4
- Montero J, Morales A, Llacuna L, Lluís JM, Terrones O, Basañez G, Antonsson B, Prieto J, García-Ruiz C, Colell A, Fernández-Checa JC. 2008. Mitochondrial cholesterol contributes to chemotherapy resistance in hepatocellular carcinoma. *Cancer Research* **68**:5246–5256. doi:10.1158/0008-5472.CAN-07-6161
- Nault J-C. 2014. Pathogenesis of hepatocellular carcinoma according to aetiology. *Best Practice & Research Clinical Gastroenterology* **28**:937–947. doi:https://doi.org/10.1016/j.bpg.2014.08.006
- Nelson MAM, McLaughlin KL, Hagen JT, Coalson HS, Schmidt C, Kassai M, Kew KA, McClung JM, Neuffer PD, Brophy P, Vohra NA, Liles D, Cabot MC, Fisher-Wellman KH. 2021.

- Intrinsic oxphos limitations underlie cellular bioenergetics in leukemia. *eLife* 10:1–31. doi:10.7554/eLife.63104
- Newman AC, Maddocks ODK. 2017. One-carbon metabolism in cancer. *British Journal of Cancer* **116**:1499–1504. doi:10.1038/bjc.2017.118
- Norsworthy KJ, Luo L, Hsu V, Gudi R, Dorff SE, Przepiora D, Deisseroth A, Shen Y-L, Sheth CM, Charlab R, Williams GM, Goldberg KB, Farrell AT, Pazdur R. 2019. FDA Approval Summary: Ivosidenib for Relapsed or Refractory Acute Myeloid Leukemia with an Isocitrate Dehydrogenase-1 Mutation. *Clinical Cancer Research* **25**:3205 LP – 3209. doi:10.1158/1078-0432.CCR-18-3749
- Othus M, Appelbaum FR, Petersdorf SH, Kopecky KJ, Slovak M, Nevill T, Brandwein J, Larson RA, Stiff PJ, Walter RB, Tallman MS, Stenke L, Erba HP. 2015. Fate of patients with newly diagnosed acute myeloid leukemia who fail primary induction therapy. *Biology of blood and marrow transplantation: journal of the American Society for Blood and Marrow Transplantation* **21**:559–564. doi:10.1016/j.bbmt.2014.10.025
- Rath S, Sharma R, Gupta R, Ast T, Chan C, Durham TJ, Goodman RP, Grabarek Z, Haas ME, Hung WHW, Joshi PR, Jourdain AA, Kim SH, Kotrys A v, Lam SS, McCoy JG, Meisel JD, Miranda M, Panda A, Patgiri A, Rogers R, Sadre S, Shah H, Skinner OS, To T-L, Walker MA, Wang H, Ward PS, Wengrod J, Yuan C-C, Calvo SE, Mootha VK. 2021. MitoCarta3.0: an updated mitochondrial proteome now with sub-organelle localization and pathway annotations. *Nucleic Acids Research* **49**:D1541–D1547. doi:10.1093/nar/gkaa1011
- Reznik E, Miller ML, Şenbabaoglu Y, Riaz N, Sarungbam J, Tickoo SK, Al-Ahmadie HA, Lee W, Seshan VE, Hakimi AA, Sander C. 2016. Mitochondrial DNA copy number variation across human cancers. *eLife* **5**:1–20. doi:10.7554/eLife.10769

- Reznik ED, Wang Q, La K, Schultz N, Sander C. 2017. Mitochondrial respiratory gene expression is suppressed in many cancers. *eLife* **6**:1–16. doi:10.7554/eLife.21592
- Schmidt CA, Fisher-Wellman KH, Neufer PD. 2021a. From OCR and ECAR to energy: perspectives on the design and interpretation of bioenergetics studies. *Journal of Biological Chemistry* 101140. doi:10.1016/j.jbc.2021.101140
- Schmidt CA, McLaughlin KL, Boykov IN, Mojalagbe R, Ranganathan A, Buddo KA, Lin C-T, Fisher-Wellman KH, Neufer PD. 2021b. Aglycemic growth enhances carbohydrate metabolism and induces sensitivity to menadione in cultured tumor-derived cells. *Cancer & Metabolism* **9**:1–21. doi:10.1186/s40170-021-00241-0
- Schulze K, Imbeaud S, Letouzé E, Alexandrov LB, Calderaro J, Rebouissou S, Couchy G, Meiller C, Shinde J, Soysouvanh F, Calatayud A-L, Pinyol R, Pelletier L, Balabaud C, Laurent A, Blanc J-F, Mazzaferro V, Calvo F, Villanueva A, Nault J-C, Bioulac-Sage P, Stratton MR, Llovet JM, Zucman-Rossi J. 2015. Exome sequencing of hepatocellular carcinomas identifies new mutational signatures and potential therapeutic targets. *Nature Genetics* **47**:505–511. doi:10.1038/ng.3252
- Schulze K, Nault J-C, Villanueva A. 2016. Genetic profiling of hepatocellular carcinoma using next-generation sequencing. *Journal of hepatology* **65**:1031–1042. doi:10.1016/j.jhep.2016.05.035
- Shallis RM, Wang R, Davidoff A, Ma X, Zeidan AM. 2019. Epidemiology of acute myeloid leukemia: Recent progress and enduring challenges. *Blood Reviews* **36**:70–87. doi:10.1016/j.blre.2019.04.005
- Shay JW, Werbin H. 1987. Are mitochondrial DNA mutations involved in the carcinogenic process? *Mutation Research* **186**:149–160. doi:10.1016/0165-1110(87)90028-5

- Siegel RL, Miller KD, Fuchs HE, Jemal A. 2021. Cancer Statistics, 2021. *CA: A Cancer Journal for Clinicians* **71**:7–33. doi:10.3322/caac.21654
- Singal AG, Pillai A, Tiro J. 2014. Early detection, curative treatment, and survival rates for hepatocellular carcinoma surveillance in patients with cirrhosis: a meta-analysis. *PLoS medicine* **11**:e1001624. doi:10.1371/journal.pmed.1001624
- Smith CC, Wang Q, Chin C-S, Salerno S, Damon LE, Levis MJ, Perl AE, Travers KJ, Wang S, Hunt JP, Zarrinkar PP, Schadt EE, Kasarskis A, Kuriyan J, Shah NP. 2012. Validation of ITD mutations in FLT3 as a therapeutic target in human acute myeloid leukaemia. *Nature* **485**:260–263. doi:10.1038/nature11016
- Song X, Peng Y, Wang X, Chen Y, Jin L, Yang T, Qian M, Ni W, Tong X, Lan J. 2018. Incidence, Survival, and Risk Factors for Adults with Acute Myeloid Leukemia Not Otherwise Specified and Acute Myeloid Leukemia with Recurrent Genetic Abnormalities: Analysis of the Surveillance, Epidemiology, and End Results (SEER) Database, 2001–2013. *Acta Haematologica* **139**:115–127. doi:10.1159/000486228
- Stein EM, DiNardo CD, Pollyea DA, Fathi AT, Roboz GJ, Altman JK, Stone RM, DeAngelo DJ, Levine RL, Flinn IW, Kantarjian HM, Collins R, Patel MR, Frankel AE, Stein A, Sekeres MA, Swords RT, Medeiros BC, Willekens C, Vyas P, Tosolini A, Xu Q, Knight RD, Yen KE, Agresta S, de Botton S, Tallman MS. 2017. Enasidenib in mutant IDH2 relapsed or refractory acute myeloid leukemia. *Blood* **130**:722–731. doi:10.1182/blood-2017-04-779405
- Sun Y, Xu H, Chen X, Li X, Luo B. 2019. Inhibition of mitochondrial respiration overcomes hepatocellular carcinoma chemoresistance. *Biochemical and Biophysical Research Communications* **508**:626–632. doi:10.1016/j.bbrc.2018.11.182

- Sung H, Ferlay J, Siegel RL, Laversanne M, Soerjomataram I, Jemal A, Bray F. 2021. Global Cancer Statistics 2020: GLOBOCAN Estimates of Incidence and Mortality Worldwide for 36 Cancers in 185 Countries. *CA: A Cancer Journal for Clinicians* **71**:209–249. doi:<https://doi.org/10.3322/caac.21660>
- Takami A. 2018. Hematopoietic stem cell transplantation for acute myeloid leukemia. *International journal of hematology* **107**:513–518. doi:[10.1007/s12185-018-2412-8](https://doi.org/10.1007/s12185-018-2412-8)
- Teague WEJ, Golding EM, Dobson GP. 1996. Adjustment of K' for the creatine kinase, adenylate kinase and ATP hydrolysis equilibria to varying temperature and ionic strength. *The Journal of experimental biology* **199**:509–512.
- The Cancer Genome Atlas Research Network. 2013. Genomic and Epigenomic Landscapes of Adult De Novo Acute Myeloid Leukemia. *New England Journal of Medicine* **368**:2059–2074. doi:[10.1056/NEJMoa1301689](https://doi.org/10.1056/NEJMoa1301689)
- Tolba R, Kraus T, Liedtke C, Schwarz M, Weiskirchen R. 2015. Diethylnitrosamine (DEN)-induced carcinogenic liver injury in mice. *Laboratory Animals* **49**:59–69. doi:[10.1177/0023677215570086](https://doi.org/10.1177/0023677215570086)
- Totoki Y, Tatsuno K, Covington KR, Ueda H, Creighton CJ, Kato M, Tsuji S, Donehower LA, Slagle BL, Nakamura H, Yamamoto S, Shinbrot E, Hama N, Lehmkuhl M, Hosoda F, Arai Y, Walker K, Dahdouli M, Gotoh K, Nagae G, Gingras M-C, Muzny DM, Ojima H, Shimada K, Midorikawa Y, Goss JA, Cotton R, Hayashi A, Shibahara J, Ishikawa S, Guiteau J, Tanaka M, Urushidate T, Ohashi S, Okada N, Doddapaneni H, Wang M, Zhu Y, Dinh H, Okusaka T, Kokudo N, Kosuge T, Takayama T, Fukayama M, Gibbs RA, Wheeler DA, Aburatani H, Shibata T. 2014. Trans-ancestry mutational landscape of hepatocellular carcinoma genomes. *Nature Genetics* **46**:1267–1273. doi:[10.1038/ng.3126](https://doi.org/10.1038/ng.3126)

- Viale A, Pettazzoni P, Lyssiotis CA, Ying H, Sánchez N, Marchesini M, Carugo A, Green T, Seth S, Giuliani V, Kost-Alimova M, Muller F, Colla S, Nezi L, Genovese G, Deem AK, Kapoor A, Yao W, Brunetto E, Kang Y, Yuan M, Asara JM, Wang YA, Heffernan TP, Kimmelman AC, Wang H, Fleming JB, Cantley LC, DePinho RA, Draetta GF. 2014. Oncogene ablation-resistant pancreatic cancer cells depend on mitochondrial function. *Nature* **514**:628–632. doi:10.1038/nature13611
- Villanueva A. 2019. Hepatocellular Carcinoma. *New England Journal of Medicine* **380**:1450–1462. doi:10.1056/NEJMra1713263
- Warburg O. 1956. On the origin of cancer cells. *Science* **123**:309–314. doi:10.1126/science.123.3191.309
- Watt IN, Montgomery MG, Runswick MJ, Leslie AGW, Walker JE. 2010. Bioenergetic cost of making an adenosine triphosphate molecule in animal mitochondria. *Proceedings of the National Academy of Sciences of the United States of America* **107**:16823–16827. doi:10.1073/pnas.1011099107
- Weltermann A, Fonatsch C, Haas OA, Greinix HT, Kahls P, Mitterbauer G, Jäger U, Kainz B, Geissler K, Valent P, Sperr WR, Knöbl P, Schwarzinger I, Gleiss A, Lechner K. 2004. Impact of cytogenetics on the prognosis of adults with de novo AML in first relapse. *Leukemia* **18**:293–302. doi:10.1038/sj.leu.2403243
- Wheaton WW, Weinberg SE, Hamanaka RB, Soberanes S, Sullivan LB, Anso E, Glasauer A, Dufour E, Mutlu GM, Budigner GS, Chandel NS. 2014. Metformin inhibits mitochondrial complex I of cancer cells to reduce tumorigenesis. *eLife* **3**:e02242. doi:10.7554/eLife.02242

- Wu L, Zhao J, Cao K, Liu X, Cai H, Wang J, Li W, Chen Z. 2018. Oxidative phosphorylation activation is an important characteristic of DOX resistance in hepatocellular carcinoma cells. *Cell communication and signaling : CCS* **16**:6. doi:10.1186/s12964-018-0217-2
- Wu S, Akhtari M, Alachkar H. 2018. Characterization of Mutations in the Mitochondrial Encoded Electron Transport Chain Complexes in Acute Myeloid Leukemia. *Scientific Reports* **8**:13301. doi:10.1038/s41598-018-31489-0
- Yan H, Parsons DW, Jin G, McLendon R, Rasheed BA, Yuan W, Kos I, Batinic-Haberle I, Jones S, Riggins GJ, Friedman H, Friedman A, Reardon D, Herndon J, Kinzler KW, Velculescu VE, Vogelstein B, Bigner DD. 2009. IDH1 and IDH2 Mutations in Gliomas. *New England Journal of Medicine* **360**:765–773. doi:10.1056/NEJMoa0808710
- Yin PH, Wu CC, Lin JC, Chi CW, Wei YH, Lee HC. 2010. Somatic mutations of mitochondrial genome in hepatocellular carcinoma. *Mitochondrion* **10**:174–182. doi:10.1016/j.mito.2009.12.147
- Yu C, Wang X, Huang L, Tong Y, Chen L, Wu H, Xia Q, Kong X. 2018. Deciphering the Spectrum of Mitochondrial DNA Mutations in Hepatocellular Carcinoma Using High-Throughput Sequencing. *Gene expression* **18**:125–134. doi:10.3727/105221618X15185539348147
- Zong WX, Rabinowitz JD, White E. 2016. Mitochondria and Cancer. *Molecular Cell* **61**:667–676. doi:10.1016/j.molcel.2016.02.011

**APPENDIX A: IACUC APPROVAL LETTER**



July 23, 2019

Kelsey Fisher-Wellman, Ph.D.  
Department of Physiology/ECDOI  
ECHI 4<sup>th</sup> floor  
East Carolina University

Dear Dr. Fisher-Wellman:

Your Animal Use Protocol entitled, "Investigating Mitochondrial Function in Cancer" (AUP #Q359) was reviewed by this institution's Animal Care and Use Committee on July 23, 2019. The following action was taken by the Committee:

"Approved as submitted"

**\*Please contact Aaron Hinkle at 744-2997 prior to hazard use\***

A copy is enclosed for your laboratory files. Please be reminded that all animal procedures must be conducted as described in the approved Animal Use Protocol. Modifications of these procedures cannot be performed without prior approval of the ACUC. The Animal Welfare Act and Public Health Service Guidelines require the ACUC to suspend activities not in accordance with approved procedures and report such activities to the responsible University Official (Vice Chancellor for Health Sciences or Vice Chancellor for Academic Affairs) and appropriate federal Agencies. **Please ensure that all personnel associated with this protocol have access to this approved copy of the AUP and are familiar with its contents.**

Sincerely yours,

A handwritten signature in blue ink that reads "S. B. McRae".

Susan McRae, Ph.D.  
Chair, Animal Care and Use Committee

SM/jd

Enclosure

## **APPENDIX B: IRB APPROVAL LETTERS**



**EAST CAROLINA UNIVERSITY**  
**University & Medical Center Institutional Review Board**  
4N-64 Brody Medical Sciences Building · Mail Stop 682  
600 Moye Boulevard · Greenville, NC 27834  
Office 252-744-2914 · Fax 252-744-2284 ·  
[www.ecu.edu/ORIC/irb](http://www.ecu.edu/ORIC/irb)

## Notification of Amendment Approval

From: Biomedical IRB  
To: [Kelsey Fisher-Wellman](#)  
CC: [Kelsey Fisher-Wellman](#)  
[Patricia Brophy](#)  
Date: 12/4/2018  
Re: [Ame3\\_UMCIRB 18-001328](#)  
[UMCIRB 18-001328](#)  
Bioenergetic characterization of peripheral blood cells.

Your Amendment has been reviewed and approved using expedited review for the period of 12/3/2018 to 6/21/2019. It was the determination of the UMCIRB Chairperson (or designee) that this revision does not impact the overall risk/benefit ratio of the study and is appropriate for the population and procedures proposed.

Please note that any further changes to this approved research may not be initiated without UMCIRB review except when necessary to eliminate an apparent immediate hazard to the participant. All unanticipated problems involving risks to participants and others must be promptly reported to the UMCIRB. A continuing or final review must be submitted to the UMCIRB prior to the date of study expiration. The investigator must adhere to all reporting requirements for this study.

Approved consent documents with the IRB approval date stamped on the document should be used to consent participants (consent documents with the IRB approval date stamp are found under the Documents tab in the study workspace).

The approval includes the following items: K. McLaughlin has been added to the study.

Document	Description
There are no items to display	

The Chairperson (or designee) does not have a potential for conflict of interest on this study.



**EAST CAROLINA UNIVERSITY**  
**University & Medical Center Institutional Review Board**  
4N-64 Brody Medical Sciences Building · Mail Stop 682  
600 Moyer Boulevard · Greenville, NC 27834  
Office 252-744-2914 · Fax 252-744-2284 ·  
[rede.ecu.edu/umcirb/](http://rede.ecu.edu/umcirb/)

## Notification of Amendment Approval

From: Biomedical IRB  
To: [Kelsey Fisher-Wellman](#)  
CC: [Sue Joyner](#)  
Date: 2/17/2020  
Re: [Ame2\\_UMCIRB\\_19-002331](#)  
[UMCIRB\\_19-002331](#)  
Bioenergetic characterization of solid tumors and primary leukemias.

Your Amendment has been reviewed and approved using expedited review on 2/14/2020. It was the determination of the UMCIRB Chairperson (or designee) that this revision does not impact the overall risk/benefit ratio of the study and is appropriate for the population and procedures proposed.

Please note that any further changes to this approved research may not be initiated without UMCIRB review except when necessary to eliminate an apparent immediate hazard to the participant. All unanticipated problems involving risks to participants and others must be promptly reported to the UMCIRB. The investigator must submit a Final Report application to the UMCIRB prior to the Expected End Date provided in the IRB application. If the study is not completed by this date, an Amendment will need to be submitted to extend the Expected End Date. The investigator must adhere to all reporting requirements for this study.

Approved consent documents with the IRB approval date stamped on the document should be used to consent participants (consent documents with the IRB approval date stamp are found under the Documents tab in the study workspace).

The approval includes the following items:

Document	Description
Fisher-Wellman Review of PHI in Prep for Research Signed 05FEB2020.pdf(0.04)	HIPAA Authorization
Elizabeth Waddell, Kelsey McLaughlin, James Hagen, and Margaret Nelson are being added to the study team.	

For research studies where a waiver of HIPAA Authorization has been approved, each of the waiver criteria in 45 CFR 164.512(i)(2)(ii) has been met. Additionally, the elements of PHI to be collected as described in items 1 and 2 of the Application for Waiver of Authorization have been determined to be the minimal necessary for the specified research.

The Chairperson (or designee) does not have a potential for conflict of interest on this study.

